ORDRE : 41370

THÈSE

Présentée à

Université Lille 1 - Sciences et Technologies
(Ecole Doctorale des Sciences de la Matière, du Rayonnement et de l'Environnement)

pour l'obtention du

Docteur

(Discipline : Molécules et Matière Condensée)

par

Aany Sofia Lilly Thankamony

SYNERGIE RMN ET RPE : DÉVELOPPEMENT DE LA DNP-RMN POUR LA CARACTERISATION DES MATERIAUX INORGANIQUES ET HYBRIDES

(Synergy NMR-EPR: Developement of the DNP NMR for the Characterization of Inorganic and Hybrid Materials)

Soutenance prévue le 24 Janvier 2014

Composition du Jury :

Directeur de Thèse :

Olivier Lafon, Professeur, Université Lille 1
Herve Vezin, Professeur, Université Lille 1 (**Co-Directeur**)

Rapporteurs :

Christian Bonhomme, Professeur, Université Paris 6
Didier Gourier, Professeur, Chimie Paris Tech

Examinateurs :

Jean-Paul Amoureux, Professeur, Université Lille 1
Arno Kentgens, Professeur, Radboud University
Anne Lesage, Ingénieur de Recherche CNRS, Ecole Normale Supérieure de Lyon

Abstract

My PhD work focused on two topics: (i) the extension of Dynamic Nuclear Polarisation (DNP) to inorganic and hybrid materials and (ii) the development of advanced NMR methods to probe the atomic-level structure of solids.

In the field of DNP NMR, my PhD work aimed at demonstrating that DNP sensitivity enhancement can provide new insights into the structure of inorganic and hybrid materials. The extension of DNP NMR to new classes of materials requires the development of novel approaches for (i) the incorporation of the polarizing agent and (ii) the polarization of the nuclei. For mesoporous silica, we demonstrated that functionalization with nitroxide radicals is an alternative to post-synthesis impregnation. This approach permits us to show that solvent-free DNP benefits from faster polarization build-up.

Furthermore, we have shown that DNP is feasible for nanoparticles dispersed a frozen solution containing exogenous radicals. This dispersion protocol is expected to become a standard for the DNP of nanoparticles, since they are often dispersed in a liquid phase to prevent their aggregation. The DNP sensitivity enhancement has allowed an easy observation of defects located on the edges or the surfaces of the nanoparticles. The complementarity of DNP cross-polarization (CP) and direct polarization (DP) has also been demonstrated.

We have also demonstrated that the DNP sensitivity enhancement has enabled the detection of Al-Al proximities and has shown the bridging role of penta-coordinated aluminium sites between tetra- and hexa-coordinated aluminium sites. We have shown also that ^{27}Al-^{13}C proximities in the microporous metalorganic framework MIL-100(Al) can be probed using advanced ^{27}Al-^{13}C NMR methods boosted by DNP.

Besides, we have also shown in the case of functionalized mesoporous silica nanoparticles loaded with surfactants that DNP CP-MAS can be used to enhance NMR signals of ^{13}C and ^{29}Si nuclei located at several hundred nanometers from the polarizing agent. The DNP-enhanced ^{1}H magnetization is transported through the mesopores via ^{1}H-^{1}H spin diffusion.

In addition, we have systematically analyzed the different contributions to the sensitivity enhancement in ^{13}C and ^{29}Si CP-MAS experiments of functionalized mesoporous silica nanoparticles. Specifically, we separated contributions due to: (i) microwave irradiation, (ii) quenching by paramagnetic effects, (iii) the presence of frozen solvent, (iv) the temperature, as well as changes in (v) relaxation and (vi) cross-polarization behavior.

The second part of the thesis focused on the development of conventional NMR methods, including (i) tunable homonuclear dipolar decoupling for ^{1}H high-resolution NMR and (ii) novel cross polarization (CP) pulse sequence to probe proximities between half-integer quadrupolar isotopes. We analyzed the performance of novel 1H homonuclear decoupling sequence, called TIMES and TIMES$_0$, under different MAS frequency regimes (from 10 to 64 kHz). In particular, we have shown that at MAS frequency of 64 kHz, efficient ^{1}H homonuclear decoupling can be achieved by moderate radiofrequency field strength (40-50 kHz). We have also developed multiple-pulse CP to probe proximities between distinct quadrupolar isotopes. This sequence is more robust with respect to offset and Rotary Resonance Recoupling detrimental effects than the conventional continuous wave CP transfer. This novel methods was applied to observe ^{27}Al-^{17}O proximities in ^{17}O-enriched alumina and ^{27}Al-^{11}B proximities in oxide glasses.

ACKNOWLEDGEMENTS

It is my great pleasure to express my heartfelt thanks to helping hands behind this work. This work would be nothing more than incomplete without attending to the task of acknowledging the overwhelming help I received from teachers, friends, near and dear ones during this endeavor.

Firstly and foremost, let me seize this opportunity to convey my prodigious gratitude and deep appreciation to my respectful supervisors, Prof. Olivier Lafon and Dr. Hervé Vezin for their keen supervision and precious advices from the initial to the final development of this thesis. Prof. Lafon has lifted my knowledge in DNP NMR and greatly inspired me to improve myself. I cannot find words to express my gratitude to him for making my research study becomes possible. I am grateful to Prof. Jean-Paul Amoureux for his great support, guidance and suggestions for the entire study.

I convey my deep sense of gratitude to director of UCCS, Prof. Lionel Montagne, Prof. Rose-Noelle Vannier, Dr. Laurent Delevoye and all other faculty members of UCCS, ENSCL, University of Lille 1, for their huge support and considerations. I am also grateful to the administrative staffs for their assistances in various ways.

I wish to express my sincere thanks to Dr. Julien Trébosc who helped me to do NMR experiments and simulations, and for teaching me the basics of NMR. I would like to thank Dr. Xingyu Lu, who as a good friend, was always willing to help me while doing the experiments and theoretical calculations and give his best suggestions. Thanks to Nadia Touati who helped me to perform the EPR experiments.

The DNP NMR experimental studies discussed in this thesis would not have been possible without the support from Prof. Geoffrey Bodenhausen and his students Dr. Diego Carnevale, Dr. Perez Linde Angel Joaquin and Dr. Veronika Vitzthum from EPFL, Lausanne, Switzerland, Dr. Fabien Aussenac from Bruker biospin, Wissembourg, France, Dr. G. de Paëpe, Dr. D. Lee, and Dr. H. Takahashi from CEA in Grenoble and Prof. M. Pruski and Dr. T. Kobayashi, from Ames laboratory, USA.

I acknowledge to all the defense committee members Prof. Christian Bonhomme from Université Paris, Prof. Didier Gourier from Chimie Paris Tech, Prof. Arno Kentgens from

Radboud University and Dr. Anne Lesage from ENS Lyon for evaluating my thesis even during their busy schedule.

I would also like to thank Dr. Frederique Pourpoint for her help, support and friendship. I gratefully acknowledge all my present and past lab mates including Ibtissem, Ming, Yixuan and Nacho for their help, support and friendship at University of Lille.

I would like to thank Dr. Chandramohana Kumar, Dr Muraleedharan Nair, Dr.Jacob Chacko and Dr. Sujatha, my respected teachers of Cochin University of Sciecnce and Technology (CUSAT), for their constant encouragement. Earnest thanks also to Dr. T G Ajithkumar, Dr. P R Rajamohanan, Dr. R Nandini Devi and Dr. Kala Raj, Scientists at National Chemical Laboratory (NCL), India for their motivational advices throughout my career. I also thank all my wonderful friends at CUSAT and NCL, who have been my strongest supporters.

I would like to thank my loving sister Dr. Roshni L T and brother Dr. Sreejith K for their strong assistance, encouragement, love, prayers and unconditional support that made my Ph.D. experience productive and stimulating. My heartfelt thanks to my fiancé Mr. Sibin Knox for his continuous encouragement, support, trust, love and care. My parents have made countless sacrifices for me, and have provided me with steady guidance and encouragement. This thesis is dedicated to them who raised me with a love of science and supported me in all my pursuits.

Finally, I am always grateful to my Lord Jesus Christ who continues to be my refuge and my guiding light.

Contents

Chapter 1

Dynamic Nuclear Polarization NMR (DNP NMR)

1.1. Solid-state NMR and sensitivity

Solid-state NMR (ssNMR) spectroscopy is a powerful technique capable of providing information regarding both the structure of materials and the dynamics of processes occurring within the materials. It has been applied to the study of a wide range of materials[1, 2] including polymers, catalysts, glasses, materials for energy (battery, solid-oxide fuell cells), biomaterials (bones, drug delivery…), minerals, pharmaceuticals, and foodstuffs. However, the poor sensitivity of ssNMR limits its ability to observe surface sites or defects containing nuclei with low gyromagnetic ratios and/or low natural abundance such as ^{29}Si and ^{13}C. This intrinsic limitation stimulated active research on methods with superior sensitivity. The sensitivity of NMR spectroscopy can be improved by either two of general routes. The first of these is to design more sensitive detection schemes, including cryoprobes[3], microcoils[4], mechanic detection by cantilever[5], optical detection by light beam[6] and magnetometer[7, 8]. The second route to more sensitive NMR is enhancing the starting polarization. This route includes the use of high magnetic fields[9] and of low temperature[10]. Nuclear polarization can also be enhanced by exciting high-γ nuclei and transferring their polarization to low-γ nuclei[11-13] gases, Nuclear polarization can also be enhanced by transferring polarization between electrons and nuclei. This transfer can be achieved during a chemical reaction namely Chemical Induced Dynamic Nuclear Polarization[14], (CIDNP) or by using microwave fields (Dynamic Nuclear Polarization, DNP[15-17]). Another strategy, Parahydrogen Induced Polarization[18] (PHIP) is based on the correlation between a particular quantum mechanical spin state and a rotational state in diatomic hydrogen. Another method, known as the Haupt effect, involves the conversion of rotational energy during a fast temperature jump into nuclear polarization[19, 20]. Furthermore, the polarization of excited electrons is transferred via spin exchange optical pumping (SEOP) to noble gas nuclei such as ^{3}He, $^{129,131}Xe$ and ^{83}Kr to generate highly polarized gases for MRI applications, characterization of porous media and surfaces[21]. Among these techniques, DNP at high magnetic field under Magic Angle Spinning (MAS) conditions benefits from sensitivity enhancement of several orders of magnitude, high spectral resolution owing to high magnetic field and MAS and is applicable for a wide range of systems, including biomolecules, small organic molecules, membrane systems, porous materials, nanomaterials.

1.2 History of DNP

DNP was discovered by Overhauser, who proposed to enhance the nuclear spin system polarization by electronic cross relaxation in 1953[16]. This prediction was later experimentally proved by Carver and Slichter in metallic lithium[15, 17] (Fig.1.1) using a static magnetic field B_0=0.003 T (corresponding to an NMR frequency of 50 kHz and an ESR frequency of 84 MHz). Afterwards, Overhauser's idea was extended to other systems like dielectric solids and electron-nuclear spin systems in liquid state[22]. For dielectric solids, additional DNP mechanisms, including solid effect, cross effect and thermal mixing, have been proposed (see section 1.4). Various papers on the solid effect involving a coupled electron and nuclear spin in a dielectric system were published by Abragam[23, 24]. During 1960s, several publications illustrated the cross effect in a system consisting of two coupled electrons and one nuclear spin[25, 26]. Polarization transfer between many coupled unpaired electrons and nuclei has been described in thermodynamic terms at the late 1970s[23, 27].

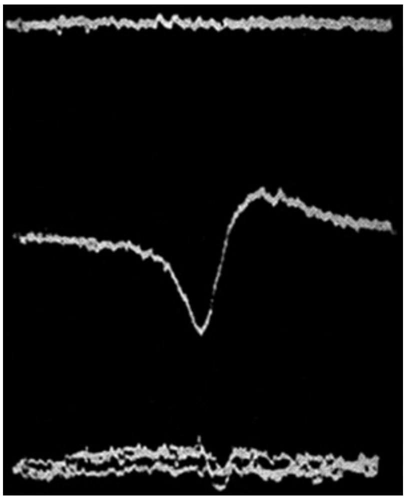

Fig.1.1. DNP experiment performed by Carver and Slichter. Top: The noisy ^{7}Li resonance. Middle: The ^{7}Li resonance enhanced by electron saturation. Bottom: Proton resonance in glycerin sample[17].

Narrow line width in solid state NMR spectra was obtained when Wind and Yanoni combined DNP with MAS and they successfully studied ^{13}C solid state NMR spectra of charcoal and diamond[28],[29]. Another milestone in the history of DNP NMR is the study of polymers using DNP by Schaefer et al.[30] They studied polymers by using DNP at 1.4 T which corresponds to 40 GHz ESR and 60 MHz ^{1}H NMR frequency. Detailed investigation on the enhancement of nuclear polarization in liquids by the Overhauser effect (OE) was done by Hausser, Stehlik and Muller Warmuth[31, 32]. They achieved high polarization at low magnetic fields which rapidly diminished when the microwave frequency exceeded the inverse rotational or translational correlation time of the radical-solvent mixture.

High-field DNP-NMR has been limited by the dearth of microwave sources operating at frequency higher than 130 GHz. After 1990s, Griffin's group at MIT regenerated the interest in DNP by using high frequency microwave sources, which are cyclotron resonance masers, also called gyrotrons,[33-35] and Gunn diodes[34]. The gyrotrons were introduced into the DNP into the early 1990s at 140 GHz[33], and more recently at 250 GHz[36-38] and 460 GHz. for enhancing the polarization in high field NMR experiments under MAS.

High-field DNP-NMR instrumention has allowed the Griffin's group to investigate biomolecular systems. In particular, they have investigated the protein T4 lysozyme in frozen glycerol-water solutions by DNP and have obtained for such system an enhancement factor of 100[39]. In 2001, Melanie et al. demonstrated that it is possible to efficiently polarize fd bacteriorhodopsin (bR) and its accompanying lipids by DNP and compared the DNP signal enhancements in the ^{15}N and ^{31}P spectra[40]. Furthermore, they have shown that ^{1}H spin diffusion can distribute the enhanced polarization inside the capsid, which is not in direct contact with the bulk solvent and thus it provides an efficient mechanism for dispersing enhanced polarization throughout a large macromolecule. In 2006, van der Wel *et al*. demonstrated the efficient transfer of DNP-enhanced ^{1}H polarization via ^{1}H-^{1}H spin diffusion from an aqueous, radical-containing solvent matrix into peptide crystals across the matrix-crystal interface[39]. The samples consist of nanocrystals of the amyloid-forming peptide GNNQQNY7-13 dispersed in a glycerol-water matrix containing a biradical polarizing agent, TOTAPOL.

In the mean time, Hu *et al* studied the important parameter which governs the efficiency of e^{-} -e^{-} dipole coupling in the three spin TM and CE processes[41]. Thus, it should be possible to optimize the enhancements in DNP experiments by constraining the distance between the two unpaired electrons. They have demonstrated the validity of this concept with experiments that employ biradical polarizing agents consisting of two 2,2,6,6- tetramethylpiperidinyl-1oxyl (TEMPO) radicals tethered by a poly- (ethylene glycol) chain. Strong arguments in favour of the 3-spin CE were advanced recently by the Griffin group[42]. Thus they could achieve the signal enhancements up to 330 even at higher magnetic fields using the cross effect with biradicals as DNP agents. They showed that the highest polarization enhancement for protons can be achieved with the use of biradicals, such as TOTAPOL and others, which provide a splitting of the EPR line due to the intramolecular ss interaction between two unpaired electrons. After this pioneering work, the innovative solid state DNP-NMR technology of Professors Robert Griffin and Richard Temkin at MIT was commercialized by Bruker. Bruker's 263 GHz DNP-NMR spectrometer was the world's first commercially available solid-state DNP-NMR systems[43]. . More recently 395 and 527 GHz DNP-NMR system has been commercialized by Bruker BioSpin. Owing to the recent availability of commercial DNP solid-state NMR instrument, this technique has been applied recently to study different materials like porous materials, pharmaceuticals, cell walls, cellulose...[44-46]. The details of recent materials study are explained in section 1.7. In just a few years we have seen a tremendous growth in DNP-NMR applications in the areas of biological solids and material science research.

Concurrently there have been theoretical works to describe DNP machanisms at high magnetic field under static and MAS conditions[42, 47-60]. Historically the DNP mechanisms have been described phenomenologically by rate equations describing the evolution of the nuclear spin magnetization of the bulk under continuous microwave irradiation[61-64]. Recent theoretical work has focused on the quantum mechanical description of the solid effect[47, 48, 54, 55], the cross effect[49, 50, 56] and the thermal mixing[57-60] under static conditions as well as that of the solid effect and the cross effect under MAS conditions[52, 53]. In 2012, Tycko's and Vega's groups have shown the difference between DNP under static and MAS conditions and the importance of time-dependent avoided energy-level crossings.

The development of DNP-NMR equipement under MAS at sub-liquid nitrogen temperatures ($T < 90$ K) is also an active field of DNP-NMR instrumentation. The group of Fujiwara has developed a solid-state NMR apparatus with DNP and MAS at 14 T, 30 K and MAS frequency of about 3 kHz for 4 mm rotors.[65] In this system, cold helium gas is used for both sample-cooling and –spinning. The group of Tycko has described a solid-state NMR spectrometer with DNP and NMR at 20–25 K, 9.4 T and MAS frequency of 6.8 kHz.[66] Their MAS NMR probe uses helium to cool the sample space and nitrogen gas for MAS drive and bearings[67]. The group of de Paëpe at CEA Grenoble (France) also develops in collaboration with Bruker BioSpin a system for solid-state DNP-NMR under MAS at $T < 90$ K. Another important development for DNP-NMR instrumention is that of low-temperature MAS DNP-

NMR probe, which are able to spin the sample at MAS frequency higher than 20 kHz. Bruker BioSpin currently develpos such probe for rotor with outer diameters of 1.9 and 1.3 mm.

1.3 EPR (Electron Paramagnetic Resonance) Spectral Parameters affecting the DNP transfer

DNP consists in the transfer of spin polarization from electrons to nuclei. This polarization transfer requires continuous microwave irradiation at a frequency close to the corresponding electron paramagnetic resonance (EPR) frequency when the electron spin system is in a thermal equilibrium. The EPR parameters which affect the DNP transfer are g-tensor hyperfine coupling tensor, the electron-electron dipolar coupling and the electron relaxation times.

Relaxation Processes

If electrons were to be continually raised from a low energy level to a high level then the populations of the two energy levels would equalize and there would be no net absorption of radiation. In order to maintain a population excess in the lower level, the odd electrons from the upper level give up the hν quantum to return to the lower level and satisfy the Maxwell – Boltzmann law. The release of this energy occurs via a spin relaxation process. These process are of two type called spin-lattice relaxation and spin-spin relaxation.

In the case of spin-lattice relaxation, the energy is degenerated within the lattice as vibrational, rotational or translational energy ie, as phonons. The mechanism by which this degeneracy occurs is known as spin-lattice relaxation characterized by an exponential decay of energy as a function of time. The exponential time constant denoted as T_{1e} and is called the spin-lattice relaxation time. In the case of spin-spin relaxation the initial equilibrium is reached by an exchange of energy between the spins without transfer of energy to the lattice. This phenomenon is characterized by a time constant T_{2e} called the spin-spin relaxation time. T_{2e} increases with decreasing spin concentration, that is, the average electron-electron distance in the system. In some cases the EPR lines are broadened beyond detection. In such cases, cooling the sample increases T_{1e} and usually leads to detectable lines as T_{1e} is inversely proportional to the absolute temperature ($T_{1e} \propto T^{n}$) with n depending on the precise relaxation mechanism. Thus, EPR experiments are often performed at liquid nitrogen (77 K) or liquid helium (4 K) temperatures. On the other hand, if the spin-lattice relaxation time is too long, electrons do not have time to return to the ground state. The populations of the two levels (α and β) tend therefore to equalize and the intensity of the signal decreases, being no longer proportional to the number of spins in the sample itself. This effect is known as saturation.

g-factor

A dimensionless scalar quantity which characterizes the magnetic moment and gyromagnetic ratio of an electron is called g-factor. The g-factor determines the center of gravity of EPR spectrum. The microwaves in Bruker DNP NMR system irradiates EPR transition at $g \approx 2$. DNP experiments are usually performed using radicals dispersed in frozen solution and hence it gives anisotropic spectra.

Hyperfine coupling

The interaction between the magnetic moments arising from the electron spin and the surrounding nuclear spins in an applied magnetic field is called hyperfine coupling. When the paramagnetic species has magnetic anisotropy the hyperfine coupling is the expressed by a 3x3 matrix. The hyperfine coupling is due to two main mechanisms which are the Fermi contact interaction (isotropic interaction) and dipolar interaction (anisotropic interaction). The combination of the g-anisotropy and the hyperfine interaction gives rise to the inhomogeneous broadening. The hyperfine coupling constant 'A' is directly related to the distance between peaks in a spectrum and its magnitude indicates the extent of delocalization of the unpaired electron over the molecule.

$$A=g\mu_e/\Delta B \qquad (1)$$

where g is g-factor, μ_e is the Bohr magneton and ΔB is difference in magnetic field strengths.

Dipolar broadening (homogeneous broadening) and g-Anisotropy (inhomogeneous broadening)

The lines of the EPR spectra can be homogeneously or inhomogeneously broadened. Depending on the radical concentration, the distance between the unpaired electrons can be short enough to observe a mutual perturbation through the electron-electron dipolar interaction. This interaction results in a broadening of the EPR lines called dipolar broadening or homogeneous broadening. A homogeneous line is a superposition of spin packets with the same resonance field and the same width.

The electron Zeeman interaction depends on the absolute orientation of the molecule with respect to the external magnetic field. An inhomogeneously broadened line consists of a superposition of spin packets with distinct, time-independent resonance fields. The sources of the inhomogeneous broadening can include inhomogeneous external magnetic field(s), *g*-strain, unresolved hyperfine structure, and anisotropy of the magnetic interactions in orientation-disordered solids. This definition of lineshapes is particularly important in pulsed EPR spectroscopy because the behaviour of the spin system in a pulsed experiment depends on the type of line broadening leading to the overall contour.

1.4 Theory of DNP

1.4.1 Polarization transfer mechanisms

The general principle of DNP mechanisms consists in the transfer of the polarization from unpaired electrons to nuclei, using the irradiation at or near the frequency of the EPR line of the electron. At sufficiently low temperatures, this process exploits around 100% polarization transfer from electrons. The concentration of unpaired electrons in NMR samples has to be dilute to reduce the paramagnetic broadening of NMR. Thus the rate of polarization transfer from electrons to bulk nuclei is slow and often regulated by the nuclear spin-lattice relaxation time T_1. At the same time, optimal electron T_{1e} and T_{2e} are required to be in the range of micro- to milliseconds to simultaneously facilitate efficient microwave saturation of electron spin polarization essential for DNP mechanisms and fast turnover rates (which require small T_{1e}) in multiple polarization transfers. Furthermore, homonuclear spin diffusion that assists polarization transfer from dilute electron spins to bulk nuclei is more effective with a long nuclear relaxation time. In addition, ^{1}H-^{1}H spin diffusion is essential when the NMR system of interest is not available to polarizing agents. The efficient ^{1}H-^{1}H spin diffusion permits separation of the nuclear spins of interest from the electron spins to maintain resolution of the enhanced NMR spectra. Additionally, for compounds with long $T_1(^1H)$, the optimal repetition delay is decreased due to spin diffusion from the fast relaxing surface coating.

The transfer of polarization is initiated by irradiation at or close to the electron Larmor frequency, and the transfer involves simultaneous nuclear and electron spin transitions, during the irradiation or induced by relaxation.

The overall Hamiltonian of an electron-nuclear spin system in a magnetic field is given by:

$$H = \omega_e S_Z + \omega_n I_Z + H_{ee} + H_{en} + H_{nn} \qquad (2)$$

The first two terms describe the electron and nuclear Zeeman interactions, respectively, with $\omega_e = -\gamma_e B_0$ and $\omega_n = -\gamma_n B_0$, where γ_e and γ_n are the gyromagnetic ratios of electrons and nuclei, respectively, and B_0 represents the external magnetic field strength. *S* and *I* are the electron and nuclear spin operators respectively. H_{ee}, H_{en} and H_{nn} denote the spin–spin interactions between electrons, electrons and nuclei and between nuclei, respectively. H_{ee} can been neglected for sufficiently dilute concentrations of electrons. It becomes relevant for the DNP mechanisms involving several electrons, such as thermal mixing and cross effect (TM and CE). The electron and nuclear relaxation times also influences the DNP transfer. The mechanisms for the microwave-driven DNP processes are specifically classified into the Overhauser effect (OE), the solid-effect (SE), the cross-effect (CE) and thermal-mixing (TM)[68-70].

1.4.2 The Overhauser effect (OE)

For metals, Albert Overhauser predicted that "*if the electron spin resonance of the conducting electrons is saturated, the nuclei will be polarized to the same degree they would if their gyromagnetic ratio were that of the electron spin*". Figure 1.1. shows the experimental verification of the Overhauser's theoretical concept by Carver and Slichter for metallic lithium dispersed in oil. This is the first DNP-enhanced NMR spectrum and the measured enhancement factor was about 100 fold. The OE DNP mechanism is a cross relaxation process which flips an electron and a nuclear spin simultaneously. The time-dependent dipolar and scalar interactions between the unpaired electrons and the nuclei are responsible for these relaxation processes. This time dependence is due to molecular motions in liquid and to motions of free electrons in solid-state conductors. If ω_{0S} is the electron Larmor frequency, the OE should satisfy the condition $\omega_{0S}\tau < 1$ with τ the rotational correlation time of the paramagnetic species. When ω_{0S} becomes large, this condition is difficult to satisfy. Thus the efficiency of the OE decreases at high magnetic fields. The principles of the OE are described below.

Fig.1.2 depicts the energy level diagram for the OE. W_0 and W_2 represent the rates of the zero- and double-quantum transitions and W_S and W_I are the rates for the EPR transitions and corresponding rates for NMR transition respectively. W^0_I is the nuclear relaxation rate in the absence of electrons. In the OE the allowed EPR transitions are saturated by microwave irradiations, while the zero- and double-quantum transitions induce changes in the nuclear spin population resulting in the DNP effect. The enhancement by OE DNP can be expressed as

$$\epsilon = 1 - \underbrace{\frac{W_2 + W_0}{W_0 + 2W_I + W_2}}_{\text{coupling parameter}} \cdot \underbrace{\frac{W_0 + 2W_I + W_2}{W_0 + 2W_I + W_2 + W_I^0}}_{\text{leackage factor}} \cdot \underbrace{\frac{\langle S_0 \rangle - \langle S_Z \rangle}{\langle S_0 \rangle}}_{\text{saturation factor}} \cdot \frac{\gamma_S}{\gamma_I} \qquad (3)$$

Where <S_0> is the equilibrium magnetization of S spin and <S_Z> are the electron transitions.

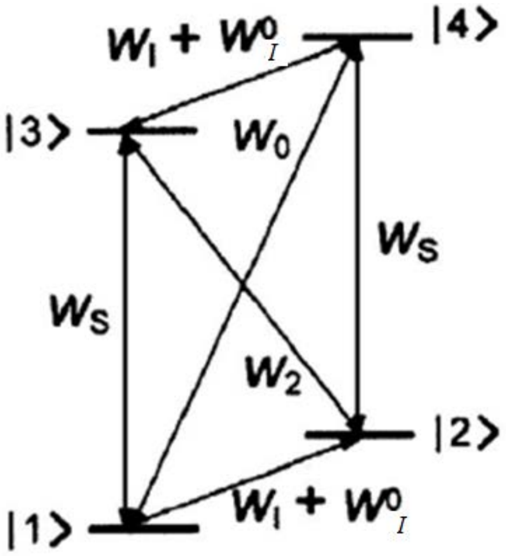

Fig 1.2. Energy level diagram for the Overhauser effect

The coupling parameter depends on the scalar and dipolar couplings between unpaired electrons and nucleus and can have the values between −1.0 (pure scalar coupling) and 0.5 (pure dipolar coupling). The leakage factor describes the nuclear spin relaxation by the electron spins and can a value between 0 (no relaxation due to the electron-nuclear coupling) and 1 (no other relaxation mechanisms). When the electron transitions are saturated completely (<S_Z> = 0), the saturation factor has a value of 1. The saturation factor depends on the relaxation of the electrons and the microwave power.

1.4.3 The solid effect (SE)

After the discovery of OE, Jeffries realized that "*the saturation of so called forbidden transitions will produce a comparable nuclear polarization directly in the sense that the applied radiofrequency field itself flips the nuclei*" in solids[71]. He mentions that this had previously been observed by Pound[72] and theoretically considered by Abragam[22], who coined the name "l'effet solide." Jeffries later described the SE theoretically[73], and reviewed the early work of DNP in 1964 [74]. SE requires the presence in the investigated solid of unpaired electrons exhibiting a homogeneous EPR linewidth (δ) and an inhomogeneous spectral breadth (Δ) smaller than the nuclear Larmor frequency ($\delta,\Delta<\omega_{0I}$). Fig.1.3. shows the energy level diagram for SE. The enhancement is driven by the forbidden flip-flop (W_0) and flip-flip (W_2) transitions using microwave irradiation at the corresponding resonance frequencies.

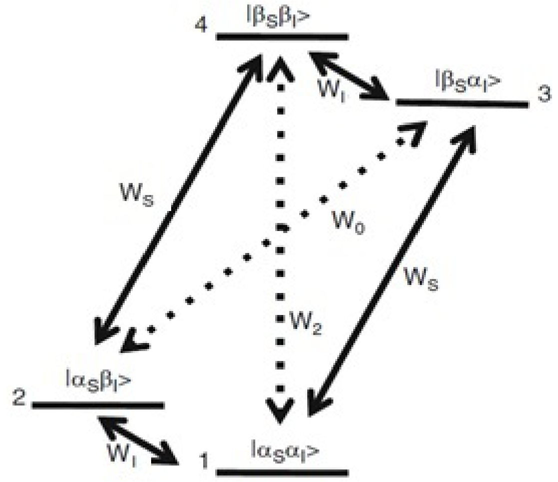

Fig1.3. Energy level diagram for the SE, which is driven by forbidden single and double quantum transitions (W_0 and W_2, dotted lines)

SE is a two spin process and it is associated with mixing of states caused by the nonsecular component (pseudo secular term) *B* of the hyperfine coupling. *B* contains the spin operators E_ZN^+ and E_ZN^- where E and N denotes electron and nuclear spin operators respectively). These terms lead to a mixing of the electron and nuclear states under the influence of microwave irradiation. The effective nutation frequency can be expressed by the

$$\omega_{\mathrm{eff}} = \sqrt{(\omega_{0\mathrm{e}} - \omega)^2 + \omega_{1\mathrm{e}}^2} \qquad (4)$$

where ω is the microwave frequency, and $(\omega_{0e} - \omega)$ represents the detuning of the microwave frequency with respect to the resonance frequency of the electron spin. ω_{0e} , and ω_{1e} is the strength of the microwave field B_1, The mixed states are generated from the original states with a coefficient *p*. This coefficient can be calculated by the first order perturbation theory and is given by

$$p = -\frac{3\gamma_e\gamma_n}{4\omega_0 N R^3} . \sin\theta \cos\theta \, e^{-i\varphi} \qquad (5)$$

where R, θ, and Φ are the polar coordinates describing the electron-nuclear vectors. γ_e and γ_n are the gyromagnetic ratios of electron and neutron. The irradiation probability of zero quantum or double quantum transitions is proportional to $4p^2$. Since p is inversely proportional to ω_{0N}, the transition probability and sensitivity enhancement will be scaled with ω_{0N}^{-2}. Thus SE is usually poorly efficient at high field. By solving the rate equations, the SE enhancement factor can be obtained by

$$\epsilon_{SE} = 1 + \frac{W_2}{W_2 + W_I} \cdot \left(\frac{\gamma_e}{\gamma_n} - 1 \right) \tag{6}$$

where W_I is the rate for NMR transition.

1.4.4 The cross effect (CE)

The CE is a three-spin process discovered by Hwang et al[25]. It involves the interaction between two dipolar coupled electrons with EPR frequencies ω_{0S1} (electron spin 1) and ω_{0S2} (electron spin 2) that satisfy the relation $\omega_{0S2} - \omega_{0S1} = \omega_{0I}$. This occurs when the inhomogeneous breadth Δ of the EPR spectrum is larger than the nuclear Larmor frequency ω_{0I} and at the same time the homogeneous width must satisfy the condition $\delta < \omega_{0I}$. The biradical polarizing agents can be used to achieve this condition and thus the efficiency of the DNP effect can be improved by the presence of a dipolar coupling between the two electrons. The energy level diagram for CE is as shown in Fig.1.4. There are mainly 8 energy levels.

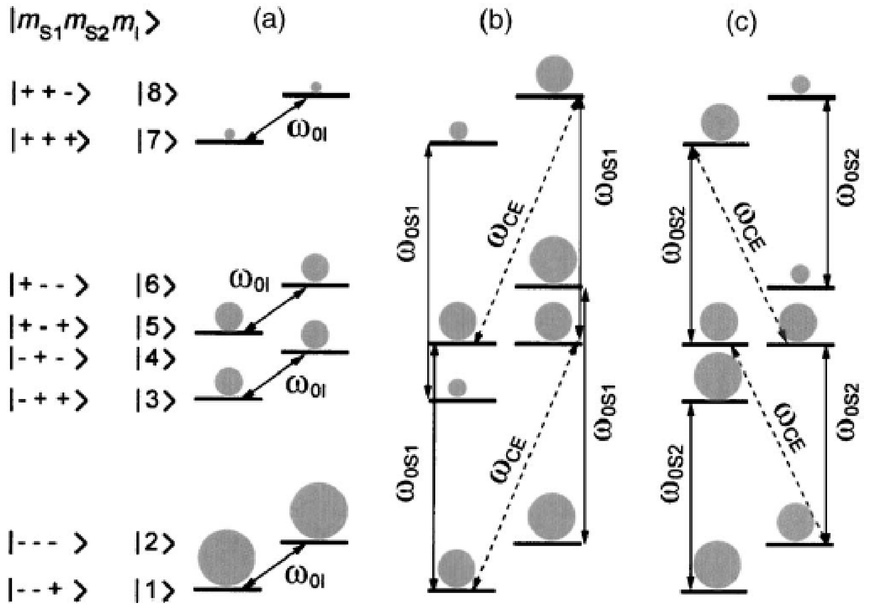

Fig: 1.4. a) Population distribution at thermal equilibrium for a three spin system, b) negative enhancement caused by the saturation of the allowed EPR transitions for one of the dipolar coupled electrons ω_{0S1} and c) Saturation of the transition corresponding to the second electron ω_{0S2} leads to positive enhancement.

Fig.1.4. a) shows the thermal equilibrium spin population for a three-spin system. The degeneracy is obtained when there are two dipolar coupled electrons separated in frequency by ω_{0I}. The microwave irradiation can the EPR transition of one of the two dipolar coupled electrons and the CE transitions. Negative (Fig. 1.4b) or positive (Fig. 1.4c) DNP enhancements are achieved depending on the electron which is saturated. The CE mechanisms have been applied successfully to polarize biological solids and inorganic materials at high magnetic fields. Additionally, CE mechanism leads to an improved polarization enhancements compared to SE and TM and nitroxide biradicals, such as TOTAPOL or bTbK, favors CE mechanism.

1.4.5 Thermal mixing (TM)

Thermal mixing is an energy exchange phenomenon between the multiple electron spins and the nuclear spin, which can enhance nuclear polarization. It requires the presence of a high concentration of paramagnetic agents with the homogeneous EPR line width larger than the nuclear Larmor frequency $\delta > \omega_{0I}$. TM is similar to the CE due to the coupling of multiple electrons and it was developed from the concept of spin temperature based on the Provotov theory[75, 76], in which spin systems are treated as thermodynamic ensembles. Based on this concept, the electron-nuclear spin system in TM can be explained as a set of three interacting baths, the electron Zeeman system (EZS), the electron dipolar system (EDS), and the nuclear Zeeman system (NZS). NZS is cooled in an energy conserving electron-electron-nuclear spin exchange process. Off resonance irradiation of the allowed EPR transition results in a large polarization gradient across the EPR line, equivalent to cooling the EDS. DNP enhancement may occur while this bath is in thermal contact with the NZS. The enhancement can be due to the direct TM of the direct coupling between the NZS and the EDS, or indirect, when both allowed and forbidden transitions are induced. The TM effect is less efficient compared to the CE. The energy level diagram for TM is as shown in Fig.1.5. A multi-spin system involving multiple electrons and one nuclear spin is sketched and the electron-nuclear transitions are indicated with dashed lines. The probability of these transitions can be large when degeneracy exists between the states with opposite nuclear spin quantum numbers.

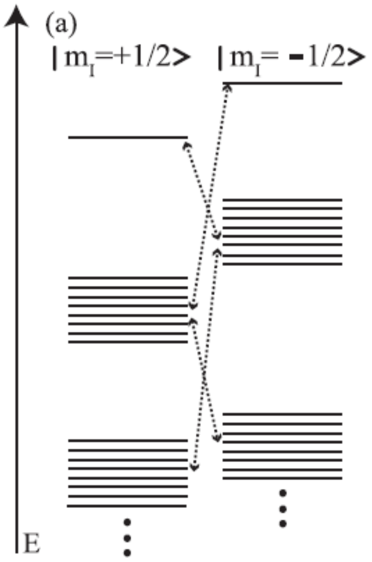

Figure 1.5: (a) Energy level diagram for thermal mixing (TM).

1.5 Polarizing agents

During the past 60-years history of DNP, CW-microwave polarization mechanisms have been categorized as belonging to the OE, the SE, CE or TM which are already explained in the above section. OE occurs with mobile electrons in gases and liquids and in conducting solids. Polarization transfer in OE relies on electron-nuclear cross relaxation, and the efficiency depends on the correlation time of the underlying stochastic modulation of electron-nuclear interactions. DNP experiments in aqueous solutions have shown unexpected OE enhancements at 3–9 T using nitroxides in aqueous systems. An enhancement factor of −20 was measured from Fremyl salt, $Na_2(SO_3)_2NO\bullet$ and typical nitroxide radicals in water. Molecular dynamics simulations of nitroxide and explicit water molecules showed unexpectedly short correlation times (< 5 ps) involving NO• … H-O-H contact[77].

Currently the DNP for non-conductive solid-state samples relies mainly on time-independent, spin-spin interactions for significant electron– nucleus polarization transfer mechanisms such as the SE, CE or TM, involving one, two or multiple electron spins, respectively. Hence, the mechanism of the DNP experiment depends on the choice of the polarizing agent and its concentration within the sample. The DNP mechanism and enhancement are also influenced by factors, such as the width of the EPR spectrum, the radical solubility and the relaxation times of the unpaired electrons. SE requires the homogeneous linewidth of the radical is less than the nuclear Larmor frequency. The TM and CE mechanisms are the dominant mechanisms when the breadth of the EPR spectrum is large compared to the nuclear Larmor frequency. If the EPR spectrum is homogeneously broadened, the TM governs the DNP process. The CE, on the other hand, is the dominant mechanism when the EPR spectrum is inhomogeneously broadened.

Furthermore, the polarizing agents are of two types. Exogenous ones include mono- or biradical or metal ion added to the system, whereas endogenous ones are paramagnetic centers present inside the sample. Endogenous polarizing agents, which have been used hitherto, include conduction electrons of metals[15], semiconductors[78] or organic conductors (*trans*-polyacetylene, (fluoranthenyl)$_2$PF$_6$)[79, 80] as well as dangling bond in coal[28, 29], diamond film[81], ceramics[82] (Si–C–N ceramic fibers formed by the pyrolysis of cured hydridopolysilazane polymer) and the stable, naturally occurring radical in a protein (the flavin mononucleotide semiquinone of flavodoxin).[83] Exogenous polarizing agents includes metal ions (Tm^{2+} in CaF_2,[84] Nd^{3+} in $La_2Mg_3(NO_3)_{12}0.24H_2O$)[85] and stable organic radicals (trityl, BDPA, nitroxide radicals). Polymers, such as polystyrene, doped with BDPA have been investigated by DNP[28, 30, 33]. However, trityl and BDPA radicals exhibit narrow EPR lines and ^1H magnetization is enhanced mainly via SE. This mechanism is less efficient than CE at high magnetic field. Nitroxide based radicals/biradicals was found to be very suitable for the CE and TM mechanisms since its EPR line is inhomogeneously broadened and exceeds the ^1H Larmor frequency. The development of exogenous polarizing agents efficient at high magnetic field is under progress for the past 10 years. Fig.1.6 shows the structure of some exogenous polarizing agents, which have been used for high-field DNP-NMR.

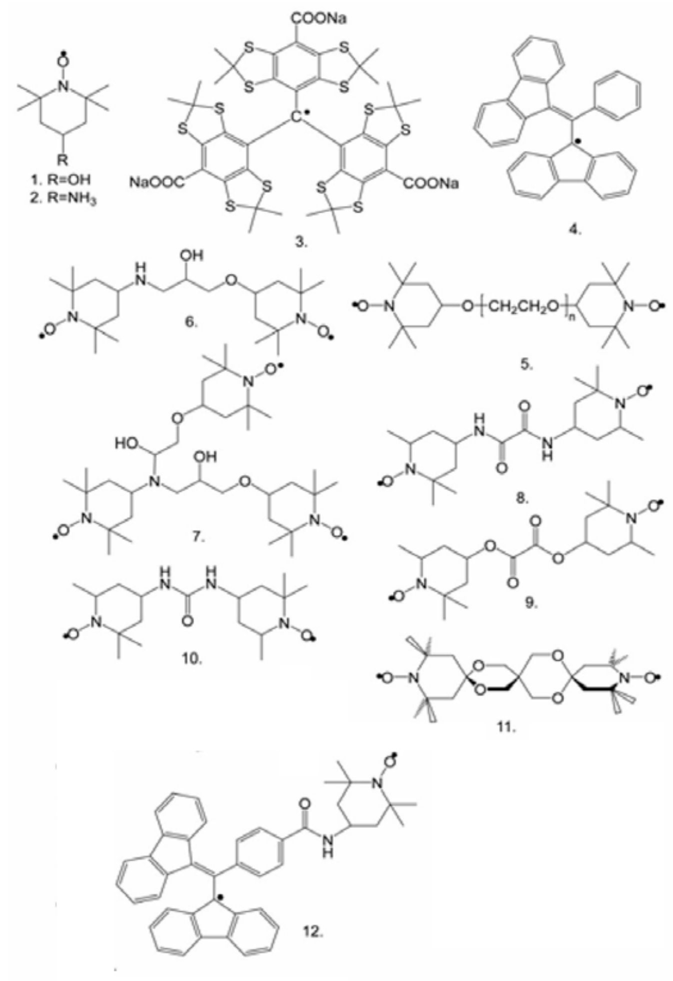

Figure 1.6. Polarizing agents: (1) 4-hydroxy-TEMPO, (2) 4-amino-TEMPO, (3) trityl (4) BDPA, (5) BTnE, n=2, 3 or 4, (6) TOTAPOL, (7) DOTOPA-TEMPO, (8) BTOXA, (9) BTOX, (10) BTurea, (11) bTbk and (12) BDPA-TEMPO.

Initially high-field DNP experiments were carried out using high concentrations (40 to 100 mM) of mono-radical nitroxide species such as TEMPO[61] ((2,2,6,6-Tetramethylpiperidin-1-yl)oxy) which employs the cross-effect (CE) polarization transfer. Griffin's group has demonstrated in 2004 that biradicals with constrained e−e distances can yield more efficient CE DNP because of increased e−e dipolar couplings. This has led to the introduction of stable nitroxide-based biradicals TOTAPOL[86] (1-(TEMPO-4-oxy)-3-(TEMPO-4-amino)propan-2-ol) which has good solubility and stability in aqueous media containing glycerol. TOTAPOL is today the most commonly used polarizing agent for DNP solid-state NMR spectroscopy in aqueous media. The applications of TOTAPOL include the successful polarization of different biological samples and DNP-enhanced NMR of surface chemistry of porous catalytic materials. In 2009, a biradical bTbk (bis-TEMPO-bis-ketal) in which the two TEMPO moieties are linked by a rigid tether was introduced by Y. Matsuki *et al*[87]. For a glassy solution of bTbK, a DNP enhancement factor of 1.4 times higher than that of TOTAPOL under similar conditions. Recently, a series of bTbK analogues like bCTbk with increased molecular weights and longer relaxation times T_{1e} and T_{2e} were developed by Tordo's group[88]. In organic solvent glasses the DNP enhancements obtained with bCTbK are 3 to 4 times higher than those obtained with bTbK. However, the applications of bTbK and bCTbK are limited to solid state DNP experiments carried out in organic solvents due to their insolubility in aqueous solutions. In 2013, Zagdoun[89] *et al* investigated series of functionalized nitroxide biradicals (derivatives of bTbK) as exogenous polarization sources for DNP NMR shown in Fig.1.7. TEKPol, a bulky derivative of bTbK with a molecular weight of 905 $g \cdot mol^{-1}$, and high saturation factor was presented by them. With TEKPOL, a proton enhancements of over 200 in both bulk and materials samples were obtained at 9.4 T and 100 K. TEKPol also can yield enhancements of 33 at 180 K and 12 at 200 K. Two bTbK derivatives (bTbtk and bTbtk-py) with better water solubility have been reported recently. Claire Sauvee[90] *et al* recently synthesized two new biradical polarizing agents PyPol and AMUPol Fig.1.8. having a high water solubility and can give around 4 times larger DNP enhancement than that of TOTAPOL free radical at 395GHz. They investigated the DNP efficiency influence of the various parameters like e–e dipolar interaction, g tensor orientations, rigidity of the molecule and electron spin relaxation times. These biradicals can be considered as promising polarizing agents for the high field DNP of complex biological systems or water soluble materials which are currently not amenable to NMR characterization.

Besides nitroxide radicals, high-field DNP-NMR has also been reported using Mn^{2+} and Gd^{3+} complexes[91] as well as mixture of SA-BDPA and trityl radicals[92].

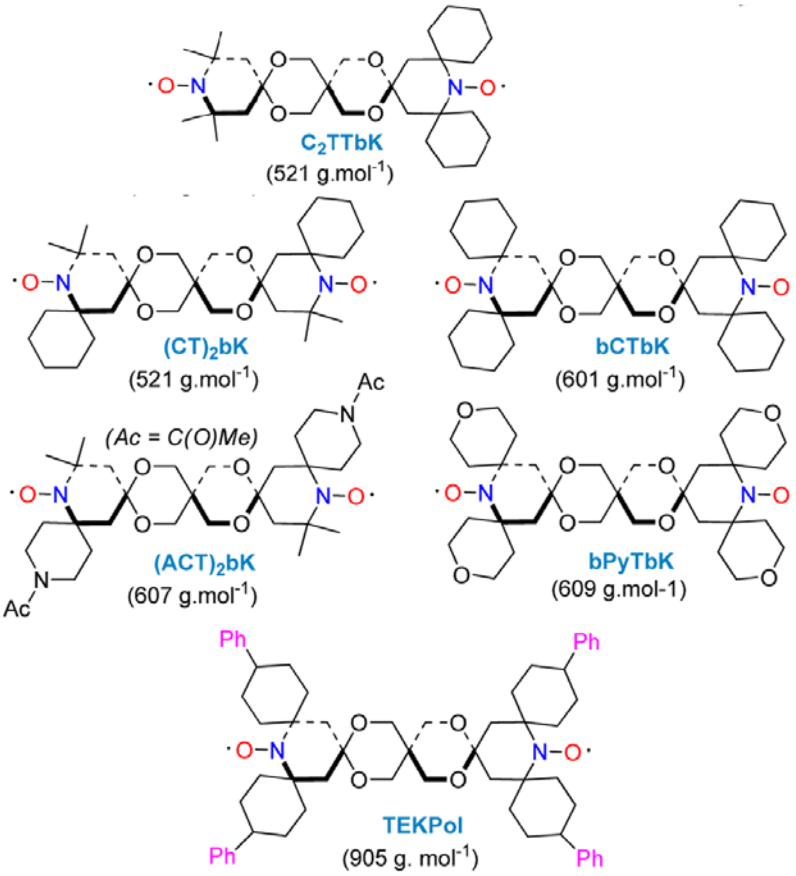

Figure 1.7. The structure, name, and molecular weight of the radicals investigated in [61] ref.

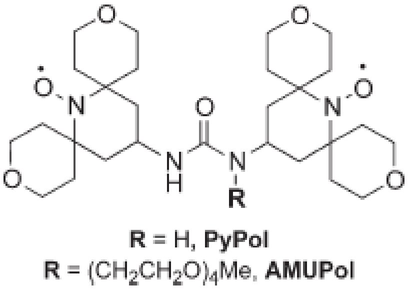

Figure 1.8. The structure of PyPol and AMUpol

1.6. Instrumentation

The high field DNP instrument consists of a NMR spectrometer connected to four additional parts: (i) a suitable microwave source with a strong oscillating field at a high frequency (140-600 GHz) which can provide continuous microwave irradiation, (ii) a wave guide to transmit the microwaves from the source to the NMR probe, (iii) a low temperature multiple frequency probe with a wave guide to irradiate the sample and (iv) cooling cabinet, which allows cooling the sample at temperature of about 100 K, since DNP enhancement increases for decreasing temperature.

1.6.1 Microwave sources

The efficiency of the DNP transfer increases with the microwave field at the sample up to a saturation level. The μw field strength ω_{1S} is directly related to the μw power, *P*, and the quality factor $Q_{\mu w}$ of the microwave circuit by

$$\omega_{1S} \propto c\sqrt{Q_{\mu w} \cdot P}. \tag{7}$$

For experiments at very low temperature or with very efficient microwave delivery to a static sample, i.e. resonant microwave cavity with high $Q_{\mu w}$, a low power microwave source may be sufficient[40, 93]. However, for MAS DNP-NMR experiments, the quality factor is lowered by the presence of rotor, the sizes of which are comparable to the wavelength of the microwave. Therefore, high power microwave sources are for MAS DNP-NMR experiments.

Two different types of high-frequency μw sources have been used for MAS DNP-NMR experiments: (i) cyclotron resonance masers, also called gyrotrons,[33,36-38] (ii) Gunn diodes[34] . The diodes deliver power ranging from 10 to 100 mW. This power is not always sufficient and the enhancements achieved using Gunn diodes are lower than those achieved using gyrotrons[34]. Gyrotrons can provide the necessary microwave power with stable continuous-wave (CW) operation.

Most gyrotrons are designed for military, radar, and plasma fusion applications typically with output frequency of up to 170 GHz and high output power, kW to MW. They are often operated with pulses of several seconds or tens of econds with low duty cycles; and minimal stability requirements. For DNP experiments, true CW operation for days with high frequency and power stability is required. This is especially important for structural studies where the DNP-enhanced NMR signal intensity must be stable over extended periods of time. Gyrotrons capable of producing tens of watts of μw power with excellent frequency stability and low phase noise have been developed for high-field DNP-NMR and EPR experiments up to 562 GHz (see Fig. 1.9A).

Gyrotrons are vaccum electronic devices , which function as an electron cyclotron resonance maser, emitting coherent radiation near the relativistic electron cyclotron frequency, or its harmonics with B_0 the magnetic field strength given by

$$\omega_c = s\frac{eB_0}{\gamma' mc} \tag{8}$$

where e the electron charge, s the harmonics of the operational mode, m the electron mass, c the speed of light, and γ' a relativistic mass factor obtained by

$$\gamma' = \frac{1}{\sqrt{1 - \upsilon^2/c^2}} \qquad (9)$$

with υ the velocity of the electron. When other experimental constraints are satisfied, the μw frequency ω_c is primarily determined by the strength of the magnetic field. A gyrotron is made of gyrotron tube placed in a superconducting solenoid. The gyrotron tube contains an electron gun, which is outside the bore and consists of an annular cathode. An electron beam is launched from the annular cathode and accelerated through the field of a superconducting magnet. The field profile is designed to compress the beam as it moves the helical motion of the electrons into microwaves. The magnetic field compresses adiabatically the electron beamlets so that they are focused into the cavity with a radius optimized to interact with the cavity mode. This compression takes place in the beam tunnel, where the generation of any spurious interaction modes that can compromise the beam quality is suppressed. Finally, a quasi-optical mode converter couples the radiation to the output window of the device and into a transmission line to the sample. After that the electron beam is collected in a water-cooled collector. For gyrotrons, the resonance condition is achieved when the cyclotron frequency of the electrons, governed by the magnetic field, is nearly equal to the frequency of the electromagnetic cavity mode. Bunching of the electrons in the beam occurs due to the relativistic dependence of the electron mass and the electron cyclotron frequency on the electron energy[43, 94].

1.6.2 Microwave waveguides

For the efficient delivery of the μw irradiation, the minimal loss of μw via transmission lines (see Fig. 1.9B) are crucial requirement. With increasing μw frequencies, fundamental waveguides become inefficient. The μw irradiation can be delivered in an oversized waveguide which is tapered down to the fundamental waveguide near to the NMR coil to minimize the loss. Corrugated overmoded or metallodielectric waveguides can be used inside the DNP probe for the transmission. These waveguides differ from classical fundamental waveguides, in that the total losses in such DNP probes are typically less than 1 – 2 dB. A dramatic increase in efficiency can be achieved by a corrugated waveguide, operating in the circular HE11 mode. Corrugated waveguide transmission lines are well-established and currently used in high frequency EPR as well as in DNP applications.

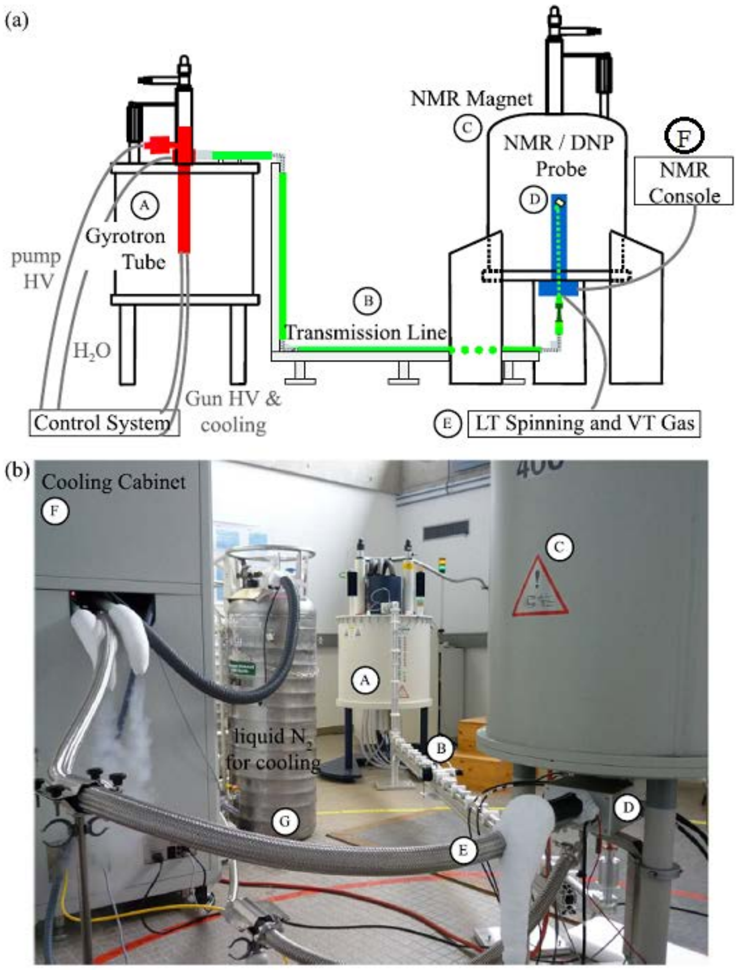

Figure 1.9: (a) A schematic diagram of DNP setup with its components and (b) a picture of the current setup at EPFL, Lausanne are shown. The microwaves are created in the gyrotron tube (A) and transmitted via the transmission line (B) into the NMR/DNP probe (D) that is installed in a NMR magnet (C). The rotor is spun at low temperature using gas flows (E) that are cooled regulated via the cooling cabinet (F) using liquid N_2 (G).

1.6.3. Multichannel low temperature MAS probe

DNP probes used for ssNMR MAS experiments cannot incorporate a μw cavity, since the rotor containing the sample, and the NMR coil spoil the $Q_{\mu w}$ of any cavity. At higher frequencies, the microwaves are usually launched between the turns of the NMR coil due to space restrictions. Figure.1.10. gives a schematic overview of a DNP low-temperature MAS (LTMAS) probe. A rotor containing the sample resides inside the MAS stator. The inner conductor of the transmission line doubles as a corrugated waveguide, and connects to a mitered, metal-mirrored assembly that terminates perpendicular to the rotor axis 1 cm from the sample. In order to achieve maximum enhancements, the microwaves delivered as a Gaussian beam in a corrugated waveguide can be focused by adjusting the miter bend on top of the probe. Tuning resonant circuit of a low temperature probe, one of the major challenges can be done by locating all variable tuning elements outside the probe at room temperatures and delivering the rf power using a transmission line. Triple channel 3.2 mm LTMAS probe have been developed by Bruker BioSpin company. These probes allow spinning rotors with 3.2 mm outer diameter up to MAS frequency of 14 kHz. Zirconia or sapphire rotors are used. Sapphire rotors are transparent and allow deeper microwave penetration. DNP LT-MAS probe for rotors with lower outer diameters (1.3 and 3.3 mm) are under development by Bruker Biospin.

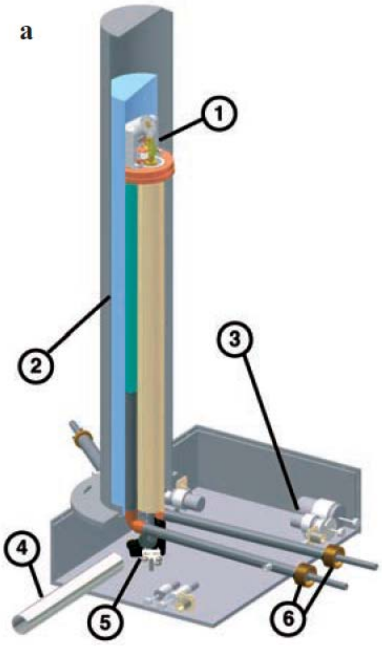

Fig.1.10. (1) probe head (2) cut-out of the vacuum dewar (3) turning elements of the RF circuit located in the box (4) corrugated waveguide from gyrotron (5) concave and flat mirrors to direct the microwaves into the vertical waveguide and (6) vacuum-jacketed transfer lines for the bearing and drive cryogens

1.6.4. Superconducting magnets

For DNP experiments, in order to obtain the maximal enhancement the μw frequency or magnetic field strength is adjusted. It is necessary to sweep the magnetic field, since gyrotrons and other high-frequency μw devices operate at a fixed frequency. The system should be equipped with a field-lock system so as to record the field profile of a polarizing agent.

1.6.5. Cooling system

Cold drive, bearing gas and the variable temperature (VT) is used for low temperature spinning. While the bearing keeps the sample on a kind of air cushion, the drive flow drives the rotor via the rotor cap like a turbine and the VT is blown through the stator to assure the low temperature. The thermal conductivity of sapphire at low temperatures insures a uniform sample temperature. The gas is cooled in a heat exchanger and the cold gas is delivered by cryogenic transfer lines. A low temperature of nearly 85 K can be achieved by using nitrogen for spinning. To attain temperatures as low as 15 K, helium gas is used. The temperatures of the three gas channels are monitored and regulated by a BVT300 LTMAS temperature control unit. The rotor-insert and eject mechanism uses nitrogen gas and is designed to operate at low temperatures. The probe is cooled for at least half an hour prior to the experiments for low temperature experiments. After inserting the sample, the experiments are started about 15 min later, in order to let the system equilibrate thermally.

1.7. Sample preparation

For successful DNP experiments, sample preparation strongly influences the sensitivity enhancement. DNP sample requires unpaired electrons within the sample for the polarization mechanisms. The radical concentration is an important parameter for a sufficient enhancement but if the concentration is too high it can lead to the paramagnetic broadening of the sample. The second critical aspect is the choice of the solvent, since the sample of interest needs to be compatible with this solvent and the choice of the solvent is important to reach a good balance between spin diffusion, ^{1}H nuclear relaxation as well as the amount of ^{1}H nuclei to polarize.

Radical concentration

Nitroxide biradicals are optimized for CE transfer from unpaired electrons to protons. For our experiments, we have used TEMPO monoradical as well as TOTAPOL and bTbK biradicals. With increasing radical concentration, the enhancement increases up to a limit, where the paramagnetic broadening prevails and decreases the signal. In addition, the increasing concentration accelerates the relaxation and shortens longitudinal relaxation T_{1H} of protons.

Furthermore, the build-up of DNP-enhanced polarization is also accelerated by higher radical concentrations, since in the case of CE the DNP build-up time τ_{DNP} is equal to the nuclear relaxation time $T_{1H.}$

Solvent choice

Right choice of a solvent is essential for a successful DNP experiment. The solubility of the radical and the sample in the solvent is an important criterion. Since a glassy matrix shows better DNP properties than crystalline matrices, the mixture should form a glass at temperatures around 100 K. For an effective enhancement, a good balance between proton relaxation, spin diffusion and the amount of ^{1}H to polarize is needed. The ^{1}H concentration in the impregnation solvent can be adjusted by mixing protonated and deuterated solvents. However, it is not always easy to find a compatible solvent for the samples of interest. This is especially the case for air- or moisture-sensitive materials.

Amount of the sample of interest

Sample preparation for DNP experiments differs from that for conventional ssNMR experiments. Conventional ssNMR is usually applied on dry powder sample. In DNP experiments, samples of interest are impregnated, dissolved or suspended in glassy chemical matrices, which can significantly reduce the effective amount of sample for DNP experiments. Thus DNP samples are often viscous mixtures or, paste like materials. It is important to pack a maximum amount of sample of interest for getting a very good signal to noise ratio. Reduction of the solvent amount is often restricted by the solubility of the compound of the interest. Low solvent amount can also contradict the formation of a homogeneous glassy matrix. Furthermore, the presence of frozen solvent within the sample can lead to line broadening owing to the conformational heterogeneity of the frozen solvent molecules. In order to optimize the sample volume and spectral resolution for MAS-DNP experiments, Takahashi *et al*[95] developed a new sample preparation procedure based on a matrix-free (MF) approach where the polarizing agent is uniformly distributed around the samples. This method maximizes the effective quantity of material observed and preserves it which in turn leads to narrower spectral lines at LT.

1.8 DNP NMR applications to materials

This section presents a brief review on the use of DNP–NMR for the characterization of materials. Wind *et. al* pioneered the study of materials by DNP NMR under MAS conditions in 1985[28]. They have used an external field of 1.4 T, corresponding to an electron Larmor frequency of 40 GHz and nuclear Larmor frequencies of 60 MHz for protons and 15 MHz for ^{13}C nuclei to perform the DNP experiments. All experiments were performed at room temperature. They illustrated DNP enhancement with ^{13}C NMR spectra obtained in a short measuring time with an outstanding signal-to-noise ratio in materials like doped polystyrene, trans poly-acetylene, coal and diamonds. The results obtained by their experiments can be briefed as follows. They used two methods: (i) indirect DNP using ^{1}H→^{13}C cross-polarization under magic angle spinning (DNP CPMAS) step, and (ii) direct DNP using ^{13}C direct polarization under MAS. In the first case, the ^{13}C nuclei of the sample were enhanced uniformly because of fast spin diffusion among the protons, whereas in the second case only the carbons close to the radicals were enhanced. Therefore it was shown that the indirect DNP technique is able to shorten the acquisition time of an experiment, and allows the acquisition of experiments, which are impossible without DNP. The ^{13}C direct DNP is especially useful for studying the environmental structure of an unpaired electron and for detecting carbons which cannot be measured via cross polarization because of the absence of protons in their surroundings. Using these techniques, they have studied the structure and dynamics of trans-polyacetylene (PA) exposed in the air[79, 80]. Trans-PA is a conductive polymer, which contains unpaired electrons, also called the solitons. These unpaired electrons move rapidly along the chains giving rise to Overhauser effect. The oxygen of air oxidizes the surface and removes unpaired electrons on the surface. Hence, direct ^{13}C DNP NMR on trans-PA exposed to air allows the observation of the carbon atoms below the surface since it can only polarize ^{13}C nuclei nearby unpaired electrons. Conversely DNP-enhanced ^{1}H→^{13}C CP allows the observation of surface carbon atoms since ^{1}H spin diffusion distributes ^{1}H polarization between the vicinity of unpaired electrons below the surface and the surface. Furthermore, it was proved that the DNP effect is useful to study the spin-density distribution of the unpaired electrons over the molecules in an organic conductor[80] (fluoranthenyl)$_2$PF$_6$. At room temperature this material behaves as a one-dimensional metal where the conduction electrons move freely along paths parallel to the molecular stacks and the electron mobility is so large that only an Overhauser effect is observed in this sample. The overall enhancement of the ^{13}C DNP CP MAS spectrum is positive due to the dominating electron–proton scalar hyperfine interaction. However, direct DNP MAS experiment on ^{13}C, shown that some lines are enhanced positively due to the dominant electron–carbon scalar interaction and one line is enhanced negatively due to a dominating electron–carbon dipolar interaction. This phenomenon arises due to the distribution of the electron density over the fluoranthenyl molecules, which is different at the different sites of the carbons, resulting in different ratios of the electron–carbon scalar and dipolar interactions. Hence, it was proved that experiments with direct DNP MAS can be used to determine the electron density distribution over the chemically different carbon sites. By discussing the results obtained on a variety of samples, they have opened new areas of ^{13}C NMR studies in solids and predicted that DNP NMR can be applied to a variety of other materials, such as polymer conductors, doped and undoped semiconductors etc and it is possible to study the surface phenomena of composite materials which contain unpaired electrons.

Later, Schaefer *et al*[30]. studied the direct electron to carbon DNP solid effect transfer for homogeneously doped polycarbonates in 1992. They could polarize the carbons that are closest to the free radicals using direct ^{13}C DNP and characterize the interfaces of heterogeneous polycarbonate/polystyrene blends using indirect ^{13}C DNP. Moreover, they were able to show that the interfacial aromatic carbons in PC have less motion than that of the bulk-PC aromatic carbons. After this study, Lock *et al* shows that indirect and direct ^{13}C DNP can be used to probe the surface of ^{13}C enriched chemical vapour deposited diamond[81]. DNP-CP-MAS ^{13}C spectra could probe the surface and intergrain boundaries of the polycrystalline sample at 1.4 T, whereas the advantage of DP-MAS ^{13}C was the increased spectral resolution at 14 T[81]. Later on, more than a decade of research was spent on the optimising conditions for DNP MAS NMR. Griffin's group developed a hardware technology to the use of high power high frequency microwave sources which are needed for high field DNP NMR. They could demonstrate a high signal enhancement at low temperature by cross effect mechanism for biological samples like amyloid-forming peptide, bacteriorhodopsin etc incorporated with biradicals at high magnetic fields[39, 40, 68, 96-98].

After the successful applications to various biomolecules at high field, there was high interest to characterize inorganic and hybrid materials using high-field DNP-NMR. This extension was pioneered by the groups of Bodenhausen, Emsley and Lafon in 2009-2010. These groups independently investigated DNP-NMR of mesoporous silica samples impregnated with radical solution. For instance, in 2010, Lesage[99] *et al*. reported a DNP signal enhancement of 50 for ^{1}H-^{13}C and ^{1}H-^{15}N CP-MAS spectra of organic groups attached to a silica surface. They used TOTAPOL as the polarizing agent, to enhance the spectra of organic groups covalently attached to the surface of porous silica. In 2011, the same group used DNP-enhanced ^{1}H-^{29}Si CP-MAS for fast characterization of the distribution of surface bonding modes and interactions in functionalized mesoporous silica[100]. In 2011, Lafon[101] *et al* showed how direct ^{29}Si DNP results in a 30-fold enhancement of ^{29}Si NMR signals from subsurface sites in mesoporous silica. In addition, they could illustrate the complementarities of indirect DNP using CP-MAS and direct DNP: the former allows the selective observation of surface sites, whereas the latter allows the observation of both surface and subsurface sites. Afterwards in 2012, Rossini[102] *et al* reported the quantitative study of ^{29}Si CP and cross-polarization Carr–Purcell Meiboom–Gill (CP/CPMG) experiments with DNP on a hybrid mesoporous silica material impregnated with aqueous biradical solutions. They have shown that the main source of loss in DNP experiments in the system is due to paramagnetic quenching. It was observed that the sample preparation which provides optimal DNP signal enhancement does not provide optimal overall signal enhancement in the system. Particularly, for CPMG acquisition of the ^{29}Si ss NMRspectra optimal signal enhancements are obtained when lower radical concentrations are employed due to slower transverse relaxation rates. In the same year, Zagdoun[103] *et al*, screened a series of non-aqueous solvents combined with the exogenous biradical bTbK. Among these organic solvents, 1,1,2,2-tetrachloroethane is one of the most promising organic solvents for the study of mesoporous solids. In 2012, Rossini[104] et al demonstrated the first application of DNP-enhanced solid-state NMR spectroscopy to functionalized indium-containing metal-oxide frameworks (MIL-68-NH_2). The MOF was impregnated by a biradical solution, bTbK. They proved that significant effective sensitivity enhancement factors can be obtained for ^{1}H-^{13}C CPMAS and reported the fast acquisition of two-dimensional ^{1}H-^{13}C correlation spectra and of ^{1}H-^{15}N CPMAS NMR spectra at natural abundance. In another study, Rossini[105] et al applied ss-DNP NMR on powdered microcrystalline solids like glucose, sulfathiazole, and paracetamol impregnated with bis-nitroxide biradical (bis-cyclohexyl-TEMPO-bisketal, bCTbK) in organic solvents. They measured for these microcrystals sensitivity enhancements on the order of 100, which allowed the rapid acquisition of ^{13}C–^{13}C correlation spectra in natural abundance. At the same time, Takahashi[95] *et al* showed that DNP-NMR allows the acquisition of 2D ^{13}C-^{13}C NMR correlation spectra in only 2 h on natural abundance microcrystalline cellulose. They have introduced a matrix-free sample preparation method to distribute the polarizing agents uniformly around the microcrystals which can allow reaching excellent absolute sensitivity. During the same year, Vitzthum[106] *et al.* studied the surface enhanced DNP NMR of γ-alumina. They combined DNP with cross-polarization and MQ-MAS to determine local symmetries of ^{27}Al sites at the surface.

In 2013, Blanc[107] *et al* studied the molecular structure of microporous organic polymers (MOP) by using natural abundance ^{13}C and ^{15}N CP MAS ss-DNP NMR spectra. They used biscyclohexyl-TEMPO-bisketal (bCTbK)2 biradical in 1,1,2,2- tetrachloroethane and low temperature (~105 K) at 14.1 T. They demonstrated that the gain of sensitivity associated with DNP NMR at 14.1 T can be used for the rapid high-throughput molecular structure determination of dozens of MOP materials. Blanc and al also reported direct and indirect DNP-NMR ^{17}O spectra of inorganic oxides and hydroxides at natural abundance[108]. They could demonstrate that ^{17}O direct and indirect NMR spectra of oxides and hydroxides at natural abundance can be acquired quickly using DNP. In the mean time, Takahashi[46] *et al* revealed the possibility of structural study on challenging nanoassemblies like diphenylalanine (FF) dipeptide. They have introduced a novel matrix free sample preparation method for DNP and performed 2D ^{13}C–^{13}C correlation experiments on unlabeled self-assembled peptide which can provide structural information such as hydrogen-bonding and p-stacking interactions. Recently Grüning[109] et al. studied the molecular structure and the intermolecular arrangement of the subunits in periodic mesoporous organosilicates (PMO) materials by using DNP NMR. Natural isotopic abundance 1D ^{13}C, ^{15}N, and ^{29}Si and 2D ^{1}H–^{13}C and ^{1}H–^{29}Si NMR spectra enhanced with DNP were recorded to distinguish outer and inner layers of the sample and to monitor the surface functionalization. Oauri[110] *et al.* presented the characterization of synthetic functional polymers by using DNP-NMR. They observed the clear signals from the polymer chain-ends which cannot be detected through conventional NMR. At the same time, Gajan[44] *et.al* demonstrated the successful use of an insoluble hybrid organic-inorganic material containing homogeneously distributed radicals as a polarization source for low temperature DNP without the requirement of a glass former such as glycerol or DMSO. They have established the design principles for such a material and also showed the polarization of substrates that impregnate the materials at ~100 K. For instance, the metabolic markers like ^{13}C-labeled pyruvate and alanine were efficiently polarized with these materials. Thus other than the surfaces and subsurfaces of silicates, the applications of DNP have been extended to inorganic polymers, nanomaterials, microporous and micro crystalline materials, mesostructured hybrid organosilica materials, on surface aluminates and metal–organic frameworks (MOFs).

In this field of DNP NMR, my PhD work aims at demonstrating new insights into the structure of the materials by the DNP sensitivity enhancement. In particular, it can permit the close observation of interfaces, diluted species (defects, dopants), or isotopes with low gyromagnetic ratio and/or low natural abundance, such as ^{29}Si, ^{13}C and ^{15}N.

References:

1 J. V. Hanna and M. E. Smith, *Solid State Nuclear Magnetic Resonance*, 2010, **38**, 1-18.

2 C. Bonhomme, C. Gervais and D. Laurencin, *Progress in Nuclear Magnetic Resonance Spectroscopy*, 2014, **77**, 1-48.

3 T. Mizuno, K. Hioka, K. Fujioka and K. Takegoshi, *Review of Scientific Instruments*, 2008, **79**.

4 D. Sakellariou, G. L. Goff and J. F. Jacquinot, *Nature*, 2007, **447**, 694-697.

5 D. RUGAR, C. S. YANNONI and J. A. SIDLES, *Nature*, 1992
360, 563 - 566.

6 I. M. Savukov, S. K. Lee and M. V. Romalis, *Nature*, 2006, **442**, 1021-1024.

7 Y. S. Greenberg, *Reviews of Modern Physics*, 1998, **70**, 175-222.

8 T. Theis, P. Ganssle, G. Kervern, S. Knappe, J. Kitching, M. P. Ledbetter, D. Budker and A. Pines, *Nature Physics*, 2011, **7**, 571-575.

9 Z. Gan, P. Gor'kov, T. A. Cross, A. Samoson and D. Massiot, *Journal of the American Chemical Society*, 2002, **124**, 5634-5635.

10 M. ConcistrÃˆ, O. G. Johannessen, E. Carignani, M. Geppi and M. H. Levitt, *Accounts of Chemical Research*, 2013, **46**, 1914-1922.

11 S. R. Hartmann and E. L. Hahn, *Physical Review*, 1962, **128**, 2042-2053.

12 Y. Ishii, J. P. Yesinowski and R. Tycko, *Journal of the American Chemical Society*, 2001, **123**, 2921-2922.

13 A. Pines, M. G. Gibby and J. S. Waugh, *The Journal of Chemical Physics*, 1972, **56**, 1776-1777.

14 R. G. Lawler, *Accounts of Chemical Research*, 1972, **5**, 25-33.

15 T. R. Carver and C. P. Slichter, *Physical Review*, 1953, **92**, 212-213.

16 A. W. Overhauser, *Physical Review*, 1953, **92**, 411-415.

17 T. R. Carver and C. P. Slichter, *Physical Review*, 1956, **102**, 975-980.

18 L. Buljubasich, I. Prina, M. B. Franzoni, K. MÃ¼nnemann, H. W. Spiess and R. H. Acosta, *Journal of Magnetic Resonance*, 2013, **230**, 155-159.

19 A. J. Horsewill, *Progress in Nuclear Magnetic Resonance Spectroscopy*, 1999, **35**, 359-389.

20 M. Icker, P. Fricke, T. Grell, J. Hollenbach, H. Auer and S. Berger, *Magnetic Resonance in Chemistry*, 2013, **51**, 815-820.

21 B. M. Goodson, *Journal of Magnetic Resonance*, 2002, **155**, 157-216.

22 A. Abragam, *Physical Review*, 1955, **98**, 1729-1735.

23 A. Abragam and M. Goldman, *Nuclear Magnetism: Order and Disorder* Oxford University Press, 1982.

24 A. Abragam and W. G. Proctor, *Physical Review*, 1958, **109**, 1441-1458.

25 C. F. Hwang and D. A. Hill, *Physical Review Letters*, 1967, **18**, 110-112.

26 A. V. Kessenikh, Manenkov, A.A., Pyatnitskii, G.I., *Sov. Phys. Solid State*, 1964, **6**, 641–643.

27 V. A. Atsarkin, *Soviet Physics Uspekhi*, 1978, **21**, 725.

28 R. A. Wind, M. J. Duljvestlicn., VAND ERL UGT, A. Manenschjn and J. Vriend, *ProgresinsN MRSp ectroscopy*, , 1985, **17**, 33-61.

29 R. A. Wind, M. J. Duijvestijn, C. van der Lugt, J. Smidt and H. Vriend, *Fuel*, 1987, **66**, 876-885.

30 M. Afeworki, R. A. McKay and J. Schaefer, *Macromolecules*, 1992, **25**, 4084-4091.

31 K. H. Hausser, Stehlik, D.:, *Concepts Magn. Reson.*, 1968, **3**, 79–139.

32 W. Müller-Warmuth, Meise-Gresch, K.: , *Adv. Magn. Reson.* , 1983, **11**, 1.

33 L. R. Becerra, G. J. Gerfen, R. J. Temkin, D. J. Singel and R. G. Griffin, *Physical Review Letters*, 1993, **71**, 3561-3564.

34 G. J. Gerfen, L. R. Becerra, D. A. Hall, R. G. Griffin, R. J. Temkin and D. J. Singel, *The Journal of Chemical Physics*, 1995, **102**, 9494-9497.

35 L. R. Becerra, G. J. Gerfen, B. F. Bellew, J. A. Bryant, D. A. Hall, S. J. Inati, R. T. Weber, S. Un, T. F. Prisner, A. E. McDermott, K. W. Fishbein, K. E. Kreischer, R. J. Temkin, D. J. Singel and R. G. Griffin, *Journal of Magnetic Resonance, Series A*, 1995, **117**, 28-40.

36 V. S. Bajaj, C. T. Farrar, M. K. Hornstein, I. Mastovsky, J. Vieregg, J. Bryant, B. ElÃ©na, K. E. Kreischer, R. J. Temkin and R. G. Griffin, *Journal of Magnetic Resonance*, 2003, **160**, 85-90.

37 V. S. Bajaj, M. K. Hornstein, K. E. Kreischer, J. R. Sirigiri, P. P. Woskov, M. L. Mak-Jurkauskas, J. Herzfeld, R. J. Temkin and R. G. Griffin, *Journal of Magnetic Resonance*, 2007, **189**, 251-279.

38 A. B. Barnes, E. A. Nanni, J. Herzfeld, R. G. Griffin and R. J. Temkin, *Journal of Magnetic Resonance*, 2012, **221**, 147-153.

39 P. C. A. van der Wel, K.-N. Hu, J. z. Lewandowski and R. G. Griffin, *Journal of the American Chemical Society*, 2006, **128**, 10840-10846.

40 M. Rosay, A.-C. Zeri, N. Astrof, S. Opella, J. Herzfeld and R. Griffin, *Journal of the American Chemical Society*, 2001, **123**, 1010-1011.

41 K.-N. Hu, H.-h. Yu, T. M. Swager and R. G. Griffin, *Journal of the American Chemical Society*, 2004, **126**, 10844-10845.

42 K.-N. Hu, G. T. Debelouchina, A. A. Smith and R. G. Griffin, *The Journal of Chemical Physics*, 2011, **134**, 125105.

43 M. Rosay, L. Tometich, S. Pawsey, R. Bader, R. Schauwecker, M. Blank, P. M. Borchard, S. R. Cauffman, K. L. Felch, R. T. Weber, R. J. Temkin, R. G. Griffin and W. E. Maas, *Physical Chemistry Chemical Physics*, 2010, **12**, 5850-5860.

44 D. Gajan, M. Schwarzwälder, M. P. Conley, W. R. Grüning, A. J. Rossini, A. Zagdoun, M. Lelli, M. Yulikov, G. Jeschke, C. Sauvée, O. Ouari, P. Tordo, L. Veyre, A.

Lesage, C. Thieuleux, L. Emsley and C. Copéret, *Journal of the American Chemical Society*, 2013, **135**, 15459-15466.

45 H. Takahashi, I. Ayala, M. Bardet, G. l. De PaÃ«pe, J.-P. Simorre and S. Hediger, *Journal of the American Chemical Society*, 2013, **135**, 5105-5110.

46 H. Takahashi, B. Viverge, D. Lee, P. Rannou and G. De Paëpe, *Angewandte Chemie International Edition*, 2013, **52**, 6979-6982.

47 Y. Hovav, A. Feintuch and S. Vega, *Journal of Magnetic Resonance*, 2010, **207**, 176-189.

48 Y. Hovav, A. Feintuch and S. Vega, *The Journal of Chemical Physics*, 2011, **134**, 074509.

49 Y. Hovav, A. Feintuch and S. Vega, *Journal of Magnetic Resonance*, 2012, **214**, 29-41.

50 D. Shimon, Y. Hovav, A. Feintuch, D. Goldfarb and S. Vega, *Physical Chemistry Chemical Physics*, 2012, **14**, 5729-5743.

51 Y. Hovav, O. Levinkron, A. Feintuch and S. Vega, *Applied Magnetic Resonance*, 2012, **43**, 21-41.

52 F. Mentink-Vigier, Ã. Akbey, Y. Hovav, S. Vega, H. Oschkinat and A. Feintuch, *Journal of Magnetic Resonance*, 2012, **224**, 13-21.

53 K. R. Thurber and R. Tycko, *The Journal of Chemical Physics*, 2012, **137**, 084508.

54 A. A. Smith, B. r. Corzilius, A. B. Barnes, T. Maly and R. G. Griffin, *The Journal of Chemical Physics*, 2012, **136**, 015101.

55 A. Karabanov, A. van der Drift, L. J. Edwards, I. Kuprov and W. Kockenberger, *Physical Chemistry Chemical Physics*, 2012, **14**, 2658-2668.

56 A. Karabanov, G. Kwiatkowski and W. KÃ¶ckenberger, *Applied Magnetic Resonance*, 2012, **43**, 43-58.

57 S. C. Serra, A. Rosso and F. Tedoldi, *Physical Chemistry Chemical Physics*, 2012, **14**, 13299-13308.

58 Y. Hovav, A. Feintuch and S. Vega, *Physical Chemistry Chemical Physics*, 2013, **15**, 188-203.

59 S. C. Serra, A. Rosso and F. Tedoldi, *Physical Chemistry Chemical Physics*, 2013, **15**, 8416-8428.

60 S. Colombo Serra, M. Filibian, P. Carretta, A. Rosso and F. Tedoldi, *Physical Chemistry Chemical Physics*, 2014, **16**, 753-764.

61 D. S. Wollan, *Physical Review B*, 1976, **13**, 3686-3696.

62 Abragam A and G. M., Rep Prog Phys. , 1978, vol. 41, p. 395.

63 M. J. Duijvestijn, R. A. Wind and J. Smidt, *Physica B+C*, 1986, **138**, 147-170.

64 C. T. Farrar, D. A. Hall, G. J. Gerfen, S. J. Inati and R. G. Griffin, *The Journal of Chemical Physics*, 2001, **114**, 4922-4933.

65 Y. Matsuki, K. Ueda, T. Idehara, R. Ikeda, I. Ogawa, S. Nakamura, M. Toda, T. Anai and T. Fujiwara, *Journal of Magnetic Resonance*, 2012, **225**, 1-9.

66 K. R. Thurber, A. Potapov, W.-M. Yau and R. Tycko, *Journal of Magnetic Resonance*, 2013, **226**, 100-106.

67 K. R. Thurber and R. Tycko, *Journal of Magnetic Resonance*, 2008, **195**, 179-186.

68 T. Maly, G. T. Debelouchina, V. S. Bajaj, K.-N. Hu, C.-G. Joo, M. L. Mak-Jurkauskas, J. R. Sirigiri, P. C. A. van der Wel, J. Herzfeld, R. J. Temkin and R. G. Griffin, *The Journal of Chemical Physics*, 2008, **128**, -.

69 A. B. Barnes, G. De Paëpe, P. C. A. van der Wel, K. N. Hu, C. G. Joo, V. S. Bajaj, M. L. Mak-Jurkauskas, J. R. Sirigiri, J. Herzfeld, R. J. Temkin and R. G. Griffin, *Applied Magnetic Resonance*, 2008, **34**, 237-263.

70 H. Heise, S. Matthews and U. L. Gunther, in *Modern NMR Methodology*, Springer Berlin Heidelberg, 2013, vol. 335, pp. 23-69.

71 C. D. Jeffries, *Physical Review*, 1957, **106**, 164-165.

72 R. V. Pound, *Physical Review*, 1950, **79**, 685-702.

73 C. D. Jeffries, *Physical Review*, 1960, **117**, 1056-1069.

74 C. D. Jeffries, *Annual Review of Nuclear Science*, 1964, **14**, 101-134.

75 A. Abragam, *Principles of Nuclear Magnetism* Oxford University Press, London, 1961.

76 M. Goldman, *Spin Temperature and Magnetic Resonance in Solids*, 1970.

77 K.-N. Hu, *Solid State Nuclear Magnetic Resonance*, 2011, **40**, 31-41.

78 A. Abragam, J. Combrisson and I. Solomon, C. R. Acad. Sci., , 1958, vol. 246, pp. 1035–1037.

79 R. A. Wind, M. J. Duijvestijn and J. Vriend, *Solid State Communications*, 1985, **56**, 713-716.

80 R. A. Wind, in *eMagRes*, John Wiley & Sons, Ltd, 2007.

81 H. Lock, R. A. Wind, G. E. Maciel and C. E. Johnson, *The Journal of Chemical Physics*, 1993, **99**, 3363-3373.

82 R. H. Lewis, R. A. Wind and G. E. Maciel, *Journal of Materials Research*, 1993, **8**, 649-654.

83 T. Maly, D. Cui, R. G. Griffin and A.-F. Miller, *The Journal of Physical Chemistry B*, 2012, **116**, 7055-7065.

84 J. F. Jacquinot, W. T. Wenckebach, M. Goldman and A. Abragam, *Physical Review Letters*, 1974, **32**, 1096-1097.

85 W. T. Wenckeback, G. M. van den Heuvel, H. Hoogstraate, T. J. B. Swanenburg and N. J. Poulis, *Physical Review Letters*, 1969, **22**, 581-583.

86 C. Song, K.-N. Hu, C.-G. Joo, T. M. Swager and R. G. Griffin, *Journal of the American Chemical Society*, 2006, **128**, 11385-11390.

87 Y. Matsuki, T. Maly, O. Ouari, H. Karoui, F. Le Moigne, E. Rizzato, S. Lyubenova, J. Herzfeld, T. Prisner, P. Tordo and R. G. Griffin, *Angewandte Chemie International Edition*, 2009, **48**, 4996-5000.

88 A. Zagdoun, G. Casano, O. Ouari, G. Lapadula, A. J. Rossini, M. Lelli, M. Baffert, D. Gajan, L. Veyre, W. E. Maas, M. Rosay, R. T. Weber, C. Thieuleux, C. Coperet, A. Lesage, P. Tordo and L. Emsley, *Journal of the American Chemical Society*, 2012, **134**, 2284-2291.

89 A. Zagdoun, G. Casano, O. Ouari, M. Schwarzwälder, A. J. Rossini, F. Aussenac, M. Yulikov, G. Jeschke, C. Copéret, A. Lesage, P. Tordo and L. Emsley, *Journal of the American Chemical Society*, 2013, **135**, 12790-12797.

90 C. Sauvée, M. Rosay, G. Casano, F. Aussenac, R. T. Weber, O. Ouari and P. Tordo, *Angewandte Chemie International Edition*, 2013, **52**, 10858-10861.

91 B. r. Corzilius, A. A. Smith, A. B. Barnes, C. Luchinat, I. Bertini and R. G. Griffin, *Journal of the American Chemical Society*, 2011, **133**, 5648-5651.

92 V. K. Michaelis, A. A. Smith, B. r. Corzilius, O. Haze, T. M. Swager and R. G. Griffin, *Journal of the American Chemical Society*, 2013, **135**, 2935-2938.

93 K. R. Thurber, W.-M. Yau and R. Tycko, *Journal of Magnetic Resonance*, 2010, **204**, 303-313.

94 Q. Z. Ni, E. Daviso, T. V. Can, E. Markhasin, S. K. Jawla, T. M. Swager, R. J. Temkin, J. Herzfeld and R. G. Griffin, *Accounts of Chemical Research*, 2013, **46**, 1933-1941.

95 H. Takahashi, D. Lee, L. Dubois, M. Bardet, S. Hediger and G. De Paëpe, *Angewandte Chemie International Edition*, 2012, **51**, 11766-11769.

96 V. S. Bajaj, M. L. Mak-Jurkauskas, M. Belenky, J. Herzfeld and R. G. Griffin, *Proceedings of the National Academy of Sciences*, 2009, **106**, 9244-9249.

97 A. B. Barnes, G. De PaÃ«pe, P. C. A. van der Wel, K. N. Hu, C. G. Joo, V. S. Bajaj, M. L. Mak-Jurkauskas, J. R. Sirigiri, J. Herzfeld, R. J. Temkin and R. G. Griffin, *Applied Magnetic Resonance*, 2008, **34**, 237-263.

98 M. L. Mak-Jurkauskas, V. S. Bajaj, M. K. Hornstein, M. Belenky, R. G. Griffin and J. Herzfeld, *Proceedings of the National Academy of Sciences*, 2008, **105**, 883-888.

99 A. Lesage, M. Lelli, D. Gajan, M. A. Caporini, V. Vitzthum, P. MiÃ©ville, J. Alauzun, A. Roussey, C. Thieuleux, A. Mehdi, G. Bodenhausen, C. Coperet and L. Emsley, *Journal of the American Chemical Society*, 2010, **132**, 15459-15461.

100 M. Lelli, D. Gajan, A. Lesage, M. A. Caporini, V. Vitzthum, P. Miéville, F. Héroguel, F. Rascón, A. Roussey, C. Thieuleux, M. Boualleg, L. Veyre, G. Bodenhausen, C. Coperet and L. Emsley, *Journal of the American Chemical Society*, 2011, **133**, 2104-2107.

101 O. Lafon, M. Rosay, F. Aussenac, X. Lu, J. Trébosc, O. Cristini, C. Kinowski, N. Touati, H. Vezin and J.-P. Amoureux, *Angewandte Chemie International Edition*, 2011, **50**, 8367-8370.

102 A. J. Rossini, A. Zagdoun, M. Lelli, D. Gajan, F. Rascon, M. Rosay, W. E. Maas, C. Coperet, A. Lesage and L. Emsley, *Chemical Science*, 2012, **3**, 108-115.

103 A. Zagdoun, A. J. Rossini, D. Gajan, A. Bourdolle, O. Ouari, M. Rosay, W. E. Maas, P. Tordo, M. Lelli, L. Emsley, A. Lesage and C. Coperet, *Chemical Communications*, 2012, **48**, 654-656.

104 A. J. Rossini, A. Zagdoun, M. Lelli, J. Canivet, S. Aguado, O. Ouari, P. Tordo, M. Rosay, W. E. Maas, C. Copéret, D. Farrusseng, L. Emsley and A. Lesage, *Angewandte Chemie International Edition*, 2012, **51**, 123-127.

105 A. J. Rossini, A. Zagdoun, F. Hegner, M. Schwarzwälder, D. Gajan, C. Copéret, A. Lesage and L. Emsley, *Journal of the American Chemical Society*, 2012, **134**, 16899-16908.

106 V. Vitzthum, P. Mieville, D. Carnevale, M. A. Caporini, D. Gajan, C. Coperet, M. Lelli, A. Zagdoun, A. J. Rossini, A. Lesage, L. Emsley and G. Bodenhausen, *Chemical Communications*, 2012, **48**, 1988-1990.

107 F. d. r. Blanc, S. Y. Chong, T. O. McDonald, D. J. Adams, S. Pawsey, M. A. Caporini and A. I. Cooper, *Journal of the American Chemical Society*, 2013, **135**, 15290-15293.

108 F. d. r. Blanc, L. Sperrin, D. A. Jefferson, S. Pawsey, M. Rosay and C. P. Grey, *Journal of the American Chemical Society*, 2013, **135**, 2975-2978.
109 W. R. Gruning, A. J. Rossini, A. Zagdoun, D. Gajan, A. Lesage, L. Emsley and C. Coperet, *Physical Chemistry Chemical Physics*, 2013, **15**, 13270-13274.
110 O. Ouari, T. Phan, F. Ziarelli, G. Casano, F. Aussenac, P. Thureau, D. Gigmes, P. Tordo and S. p. Viel, *ACS Macro Letters*, 2013, **2**, 715-719.

Chapter 2

Applications of DNP-NMR on Mesoporous Silica

Mesoporous silica nanoparticles have gained much attention due to their attractive properties, including uniform diameter of the mesopores, easy functionalization, significant biocompatibility and good control of the morphology. Thus, they are widely used in a variety of fields, like catalysis, polymer filler industries, infrared optics, bio-imaging, drug delivery, and biomedical applications.[1-3] Therefore, the molecular level characterization of both bulk and surface of the mesoporous silica materials is of great important. As mentioned in chapter 1, the DNP enhancement of NMR sensitivity is a major advantage to probe both the surface and bulk sites of mesoporous silica samples containing endogeneous or exogeneous polarizing agents. This chapter details different approaches for the incorporation of DNP polarizing agents into mesoporous silica samples. We also analyse the various contributions to DNP enhancement for these systems and the transport of DNP-enhanced ^{1}H polarization by ^{1}H-^{1}H spin diffusion.

2-1. Solvent-free DNP of mesoporous silica functionalized with TEMPO

We have demonstrated how the solvent-free high-field DNP procedure can be applied for paramagnetic materials containing endogenous radicals by using an organic–inorganic hybrid material: mesoporous silica functionalized with TEMPO moieties.[4] Based on the ^{29}Si direct and indirect DNP results it is clear that co-condensation can be employed to incorporate DNP polarizing agents into inorganic materials and the solvent-free DNP is feasible for porous materials. The ^{29}Si signals in direct experiments build up a fast polarization in a few seconds at 100 K, which improved the NMR sensitivity and facilitated the investigation of direct DNP below 100 K. The $^{1}H\rightarrow^{29}Si$ CP transfer is inefficient for this material owing to the high concentration of unpaired electrons. In 2013, Gajan et al. used this idea to covalently bound stable mono- or di-nitroxide radicals homogeneously to the silica surface of mesoporous hybrid silica-organic materials.[5]

2-2. Remote DNP using ^{1}H-^{1}H spin diffusion

We have shown how DNP can be used to enhance NMR signals of ^{13}C and ^{29}Si nuclei located in functionalized mesoporous silica nanoparticles filled with surfactant. It has been proved that the distribution of DNP-enhanced ^{1}H magnetization by ^{1}H-^{1}H spin diffusion allows enhancing the NMR signals of ^{13}C and ^{29}Si nuclei located inside the mesopores at several hundreds of nanometers from stable radicals (TOTAPOL), which are trapped in the surrounding frozen disordered water. The DNP-enhanced proton magnetization is transported into the mesopores via ^1H–^1H spin diffusion and transferred to rare spins by cross-polarization, yielding signal enhancements $\varepsilon_{on/off}$ of around 8. The propagation of DNP-enhanced ^1H polarization via ^1H spin diffusion has been demonstrated for other systems, including blends of polymers, mesocrystals of peptides and microcrystalline solids.[6-8] When the surfactant molecules are extracted, so that the radicals can enter the mesopores, the enhancements increase to $\varepsilon_{on/off} \approx 30$ for both nuclei. The difference in $\varepsilon_{on/off}$ between mesoporous silica samples with and without surfactants is consistent with predictions based on one-dimensional ^1H spin diffusion model.

2-3. Analysis of DNP enhancement for mesoporous silica nanoparticles

We also systematically analyzed the enhancement factor (per scan) and the sensitivity enhancement (per unit time) in ^{13}C and ^{29}Si cross-polarization magic angle spinning (CP-MAS) NMR boosted by DNP of functionalized mesoporous silica nanoparticles (MSNs).[9] Specifically, we separated contributions due to: (1) microwave irradiation, (2) quenching by paramagnetic effects, (3) the presence of frozen solvent, (4) the temperature, as well as changes in (5) relaxation and (6) cross polarization behaviour. This systematic study supplements previous studies, which have addressed the quantification of the DNP sensitivity enhancement for other systems.[10-13] No line-broadening effects were observed for MSNs when lowering the temperature from 300 to 100 K. Notwithstanding a significant signal reduction due to quenching by TOTAPOL radicals, DNP-CP-MAS at 100 K provided global sensitivity enhancements of 23 and 45 for ^{13}C and ^{29}Si, respectively, relative to standard CP-MAS measurements at room temperature.

The studies on the aforementioned approaches highlights the opportunities for further improvements through the development of high-field DNP, better polarizing agents, and improved capabilities for low-temperature MAS.

References:

1 E. S. Kevin, Q. Hao, Y. H. Wadood and J. M. Mark, *Nature*, 2010, **468**, 422-425.

2 C. Zhu, J. Yingbing, R. D. Darren, P. A. David, H. Carter, L. Nanguo, Z. Nan, X. George, J. Xiaozhong, N. R. Aluru, J. G. Steven, W. H. Hugh and C. J. Brinker, *Nature Materials*, 2010, **9**, 667-675.

3 Y. Wan and Zhao, *Chemical Reviews*, 2007, **107**, 2821-2860.

4 A. Lilly Thankamony, O. Lafon, X. Lu, F. Aussenac, M. Rosay, J. TrÃ©bosc, H. Vezin and J.-P. Amoureux, *Applied Magnetic Resonance*, 2012, **43**, 237-250.

5 D. Gajan, M. Schwarzwälder, M. P. Conley, W. R. Grüning, A. J. Rossini, A. Zagdoun, M. Lelli, M. Yulikov, G. Jeschke, C. Sauvée, O. Ouari, P. Tordo, L. Veyre, A. Lesage, C. Thieuleux, L. Emsley and C. Copéret, *Journal of the American Chemical Society*, 2013, **135**, 15459-15466.

6 M. Afeworki and J. Schaefer, *Macromolecules*, 1992, **25**, 4092-4096.

7 P. C. A. van der Wel, K.-N. Hu, J. z. Lewandowski and R. G. Griffin, *Journal of the American Chemical Society*, 2006, **128**, 10840-10846.

8 A. J. Rossini, A. Zagdoun, F. Hegner, M. Schwarzwälder, D. Gajan, C. Copéret, A. Lesage and L. Emsley, *Journal of the American Chemical Society*, 2012, **134**, 16899-16908.

9 T. Kobayashi, O. Lafon, A. S. Lilly Thankamony, I. I. Slowing, K. Kandel, D. Carnevale, V. Vitzthum, H. Vezin, J.-P. Amoureux, G. Bodenhausen and M. Pruski, *Physical Chemistry Chemical Physics*, 2013, **15**, 5553-5562.

10 K. R. Thurber, W.-M. Yau and R. Tycko, *Journal of Magnetic Resonance*, 2010, **204**, 303-313.

11 V. Vitzthum, F. Borcard, S. Jannin, M. Morin, P. Miéville, M. A. Caporini, A. Sienkiewicz, S. Gerber-Lemaire and G. Bodenhausen *ChemPhysChem*, 2011, **12**, 2929-2932.

12 A. J. Rossini, A. Zagdoun, M. Lelli, D. Gajan, F. Rascon, M. Rosay, W. E. Maas, C. Coperet, A. Lesage and L. Emsley, *Chemical Science*, 2012, **3**, 108-115.

13 H. Takahashi, D. Lee, L. Dubois, M. Bardet, S. Hediger and G. De Paëpe, *Angewandte Chemie International Edition*, 2012, **51**, 11766-11769.

Appl Magn Reson (2012) 43:237–250
DOI 10.1007/s00723-012-0364-3

Applied
Magnetic Resonance

Solvent-Free High-Field Dynamic Nuclear Polarization of Mesoporous Silica Functionalized with TEMPO

Aany Sofia Lilly Thankamony · Olivier Lafon ·
Xingyu Lu · Fabien Aussenac · Melanie Rosay ·
Julien Trébosc · Hervé Vezin · Jean-Paul Amoureux

Received: 7 March 2012 / Revised: 30 April 2012 / Published online: 4 June 2012

Abstract We report high-field magic-angle spinning dynamic nuclear polarization (MAS DNP) of mesoporous silica functionalized with nitroxide radicals. These results demonstrate that co-condensation can be employed to incorporate DNP polarizing agents into inorganic materials and that solvent-free DNP is feasible for porous materials. For the investigated material, the direct MAS DNP enhances the ^{29}Si nuclear magnetic resonance (NMR) spectra, whereas the indirect MAS DNP via protons is inapplicable owing to the inefficiency of $^{1}H \rightarrow {}^{29}Si$ cross polarization transfer. Furthermore, the ^{29}Si signals in direct experiments build up in a few seconds at 100 K. This fast polarization buildup improves the NMR sensitivity and will be useful for the investigation of direct DNP below 100 K.

A. S. Lilly Thankamony · O. Lafon (✉) · X. Lu · J. Trébosc · H. Vezin · J.-P. Amoureux
Univ. Lille Nord de France, 59000 Lille, France
e-mail: olivier.lafon@univ-lille1.fr

A. S. Lilly Thankamony · O. Lafon · X. Lu · J. Trébosc · J.-P. Amoureux
CNRS, UMR 8181, Unité de Catalyse et de Chimie du Solide, UCCS, Univ. Lille 1, Bât. C7, 59652 Villeneuve d'Ascq, France

F. Aussenac
Bruker BioSpin SA, 34, rue de l'Industrie, 67166 Wissembourg Cedex, France

M. Rosay
Bruker BioSpin Corporation, 15 Fortune Drive, Billerica, MA 01821, USA

H. Vezin
CNRS, UMR 8516, Laboratoire de Spectrochimie Infrarouge et Raman, LASIR, Univ. Lille 1, Bât. C4, 59652 Villeneuve d'Ascq, France

Springer

1 Introduction

Solid-state nuclear magnetic resonance (NMR) provides unique information on the atomic-scale structure and dynamics of heterogeneous, disordered or amorphous materials, such as heterogeneous catalysts [1], nuclear waste storage medium [2], battery related materials [3] and nanoobjects [4]. However, the intrinsic low sensitivity of NMR, resulting from the small nuclear magnetic moments, limits the observation of diluted species (interface sites, defects, reaction intermediates…) or of nuclei displaying low gyromagnetic ratio, low natural abundance and/or slow longitudinal nuclear relaxation. For instance, the observation of silicon sites can be limited by the low ^{29}Si natural abundance (4.7 %) and nuclear relaxation times (T_{1n}), which can reach several hours [5].

Dynamic nuclear polarization (DNP) is a promising method to enhance the NMR signal of materials by one or two orders of magnitude [6–19]. Since its invention, DNP has been applied to materials. DNP phenomenon at low static magnetic field, B^0, was initially reported in metals ($B^0 = 3$ mT) [6] and then semiconductors ($B^0 \approx 0.3$ T) [7]. For instance, low-field DNP has been applied for *n*-type silicon, amorphous silicon or hydrogenated amorphous silicon, using dangling bonds as endogenous polarizing agents [7, 9, 14]. The combination of DNP at $B^0 \approx 1.4$ T with magic-angle spinning (MAS) has allowed its application to carbonaceous materials, such as organic polymers, coals and diamonds [8, 10]. Furthermore, DNP-enhanced cross-polarization (CP) at $B^0 \approx 1.4$ T has been demonstrated in the 1990s for the selective observation of surfaces [11–13]. More recently, the development of stable high-frequency microwave (μw) source, gyrotrons [20], and the design of biradical polarizing agents [21] fostered the advent of DNP at high magnetic field with $B^0 \geq 5$ T. The improved resolution and the post-synthesis impregnation with nitroxide radical solution have permitted the extension of DNP to other material classes, including mesoporous silica [15–17], metal-oxide framework [18] and γ-alumina [19].

Dynamic nuclear polarization requires the presence of unpaired electrons in the sample. So far, high-field DNP studies of materials have mainly employed exogenous organic radicals, such as 4-amino-(2,2,6,6-tetramethylpiperidin-1-yloxyl) (4-amino-TEMPO) or 1-(TEMPO-4-oxy)-3-(TEMPO-4-amino)propan-2-ol (TOTAPOL), as a source of polarization. The radicals are introduced within the materials using post-synthesis impregnation with radical-containing solutions [15–17]. This protocol offers several advantages: (i) being a post-synthesis method, it does not alter the material preparation and can be planned for natural or already prepared samples; (ii) the protons of frozen solvents within the pores can be used for polarization distribution via ^{1}H–^{1}H spin diffusion; (iii) the presence of solvent may avoid the adsorption of the radicals onto the surface. Nevertheless, (i) it has only been demonstrated so far for materials displaying high specific surface area [15–19]; (ii) this protocol does not permit the accurate control of the position and the orientation of the paramagnetic agent with respect to the observed nuclei (only an average distance between the radical and the material surface can be inferred from the radical concentration [17]); (iii) the NMR signals of the solvents may overlap with those of the observed nuclei; (iv) the nature of the impregnation solvent affects

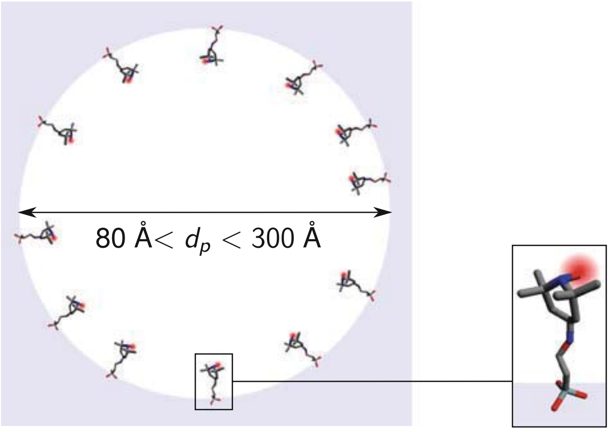

Fig. 1 Schematic structure of the material **1**

the DNP enhancements and, in practice, the sensitivity optimization still requires the test of different solvents [22].

Herein, we show how high-field DNP can be applied for paramagnetic materials containing endogenous radicals. We investigate an organic–inorganic hybrid material, which is mesoporous silica functionalized with TEMPO moieties, **1** (see Fig. 1) [23–25]. This hybrid material is a highly selective and effective oxidation heterogeneous catalyst for converting primary and secondary alcohol substrates into carbonyl derivatives and can be used for the production of pharmaceuticals, agrochemicals, flavors and fragrances [25–27]. These materials have also been used as polarizing agents for low-field DNP of flowing liquids using Overhauser effect [28, 29]. However, to the best of our knowledge, this type of material has never been studied by solid-state DNP/NMR. The TEMPO molecule is tethered to the silicon atoms during the material preparation by the sol–gel process. This co-condensation procedure can be advantageous, since: (i) it can be applied in principle to non-porous materials or microporous materials exhibiting pore aperture smaller than the smallest dimension of TEMPO and TOTAPOL (about 7 Å); (ii) it ensures a more homogeneous distribution of organic moieties within the inorganic material than post-synthesis incorporation [30]; (iii) the distance between the unpaired electrons and the silica surface cannot exceed 9 Å, the size of the organic moiety; (iv) this hybrid material allows solvent-free DNP to be tested since the xerogels are dried during the sample preparation [24]. This solvent-free DNP procedure demonstrated here for materials exhibits similarities with another solvent-free DNP protocol, which has been introduced recently for the DNP of polypeptides [31]. In this work, the molecular entities, unlabeled and labeled with nitroxide radicals, are co-condensed, whereas in reference [31], they were mixed by dissolution and solvent evaporation. In this article, the results of ^{1}H and ^{29}Si DNP experiments will be presented for **1** obtained using co-condensation. We will demonstrate that for this material, the cross-polarization (CP) transfer from ^{1}H to ^{29}Si nuclei is inefficient and hence the ^{29}Si nuclei cannot be polarized via ^{1}H (indirect DNP) [16]. Conversely, we will show that the ^{29}Si NMR signal can be enhanced by direct polarization (DP) transfer from unpaired electrons (direct DNP) [17].

2 Materials and Methods

The material **1** was purchased from Sigma-Aldrich and was used without purification. It exhibits a high specific surface area of about 450 m^2 g^{-1} and broad pore size distribution with pore diameters ranging from 80 to 300 Å [24, 25].

X-band EPR experiments were performed using a Bruker BioSpin ELEXYS E580E spectrometer operating at 9.8 GHz. The spectra were recorded with 2 mW microwave power and 0.5 G of amplitude modulation. The spin concentration of the sample was determined by full spectral integration using 4-amino-TEMPO as a reference. The EPR spectra were recorded at room temperature and the sample of mesoporous silica functionalized with TEMPO was a powder.

All solid-state DNP MAS experiments were performed on a commercial Bruker BioSpin Avance III DNP spectrometer operating at a microwave frequency of 263 GHz, a static magnetic field, $B^0 = 9.393$ T and ^{1}H and ^{29}Si Larmor frequency of 399.87 and 79.44 MHz, respectively [32]. The wide-bore NMR magnet was equipped with a double resonance ^{1}H/X 3.2 mm low-temperature DNP MAS probe. The sample was placed in a 3.2-mm ZrO$_2$ rotor. Sample temperatures of 98 K were achieved and controlled under MAS condition using a Bruker BioSpin low-temperature MAS cooling system. The sample temperature corresponds to the calibrated temperature with microwave off. All the spectra were acquired at a MAS frequency, $\nu_r = 10$ kHz. During the DNP MAS experiment, a gyrotron generated continuous microwave irradiation, which was delivered to the sample by a corrugated waveguide. The microwave power at the position of the sample was approximately 6 W [32].

The ^{1}H and ^{29}Si NMR spectra enhanced by direct DNP were recorded using the pulse sequence described in ref. [17]. First, a presaturation suppresses the equilibrium Boltzmann polarization of the detected isotope. Then, the microwave irradiation during a time, $\tau_{\mu\mathrm{w}}$, induces a transfer of longitudinal polarization between the unpaired electrons and the nuclei. The longitudinal polarization of ^{1}H or ^{29}Si nuclei is detected by tilting it into the *xy*-plane using radiofrequency pulses at the corresponding Larmor frequency. This pulse sequence relying on direct polarization (DP) is referred to as DP MAS in the following. The ^{1}H 90° pulse length was 2.5 μs in DP MAS ^{1}H experiment. All DP MAS ^{29}Si NMR spectra were recorded using a ^{29}Si 90° pulse length of 5 μs and background suppression to suppress the ^{29}Si signal of the probe [33]. The DP MAS ^{29}Si spectra of the investigated samples were unaffected by ^{1}H SPINAL-64 heteronuclear decoupling of 100 kHz amplitude [34]. Hence, no ^{1}H decoupling sequence was applied during DP MAS ^{29}Si experiments.

The indirect ^{29}Si DNP spectra were recorded using the usual $^1\mathrm{H} \rightarrow {}^{29}\mathrm{Si}$ CP MAS sequence but prior to the CP transfer, the longitudinal ^{1}H polarization was enhanced by microwave irradiation during a time, $\tau_{\mu\mathrm{w}}$ [16]. The ^{1}H 90° pulse length was 2.5 μs. The CP transfer was performed using a contact time of 2 ms, a constant ^{29}Si rf nutation frequency of 50 kHz and a linear ramp of ^{1}H rf nutation frequency

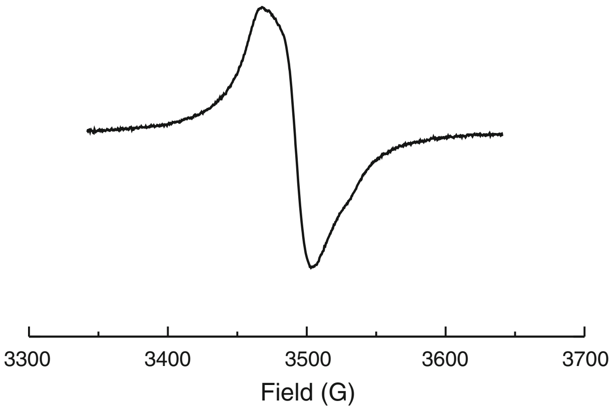

Fig. 2 X-band continuous wave EPR spectrum of the mesoporous silica functionalized with TEMPO

between 70 and 35 kHz. A SPINAL-64 decoupling with ^{1}H rf nutation frequency of 100 kHz was applied during the acquisition [34].

The ^{29}Si chemical shifts are referenced to tetramethylsilane using the shielded resonance (−9.8 ppm) in the ^{29}Si NMR spectrum of tetrakis(trimethylsilyl)silane as a secondary reference. For an isotope $X = {}^1$H or ^{29}Si, the DNP enhancement factors of the signal intensity and integral are defined as

$$\varepsilon_{\mathrm{DNP}}(X) = \frac{I(X)}{I_{\mathrm{off}}(X)} \quad \text{and} \quad \varepsilon^{A}_{\mathrm{DNP}}(X) = \frac{A(X)}{A_{\mathrm{off}}(X)}, \tag{1}$$

where the $I(X)$ and $I_{\mathrm{off}}(X)$ are the maximal intensities of X signal with and without microwave irradiation and the $A(X)$ and $A_{\mathrm{off}}(X)$ are the total integrals of X signal with and without microwave irradiation. For **1**, the intensities of ^{1}H and ^{29}Si signals peak at 0 and −66 ppm, respectively. The fit of NMR signals, as shown in Fig. 3d, was performed using Matlab software [35].

3 Results and Discussion

Figure 2 presents the EPR spectrum of the material **1** recorded at room temperature. The measured g factor is 2.0059, which is typical of nitroxide radical. The EPR spectrum of **1** displays a broad line exhibiting a shoulder at about 3,530 G. Therefore, it differs from the EPR signals of mononitroxide radicals in isotropic solution, which consist of a resolved triplet splitting produced by the isotropic hyperfine coupling with ^{14}N nucleus [21]. This difference indicates that the motions of the TEMPO moieties in material **1** are anisotropic. This is expected since the TEMPO moiety is anchored on the silica surface and its motions are limited by the covalent linkage. Furthermore, the EPR signal of **1** also differs from that of diluted mono- or bi-nitroxide radicals, which are immobilized in frozen glassy solutions or covalently linked to a peptide chain or to a silica surface [21, 23, 31, 36]. These diluted radicals show a resolved powder lineshape produced by the anisotropic

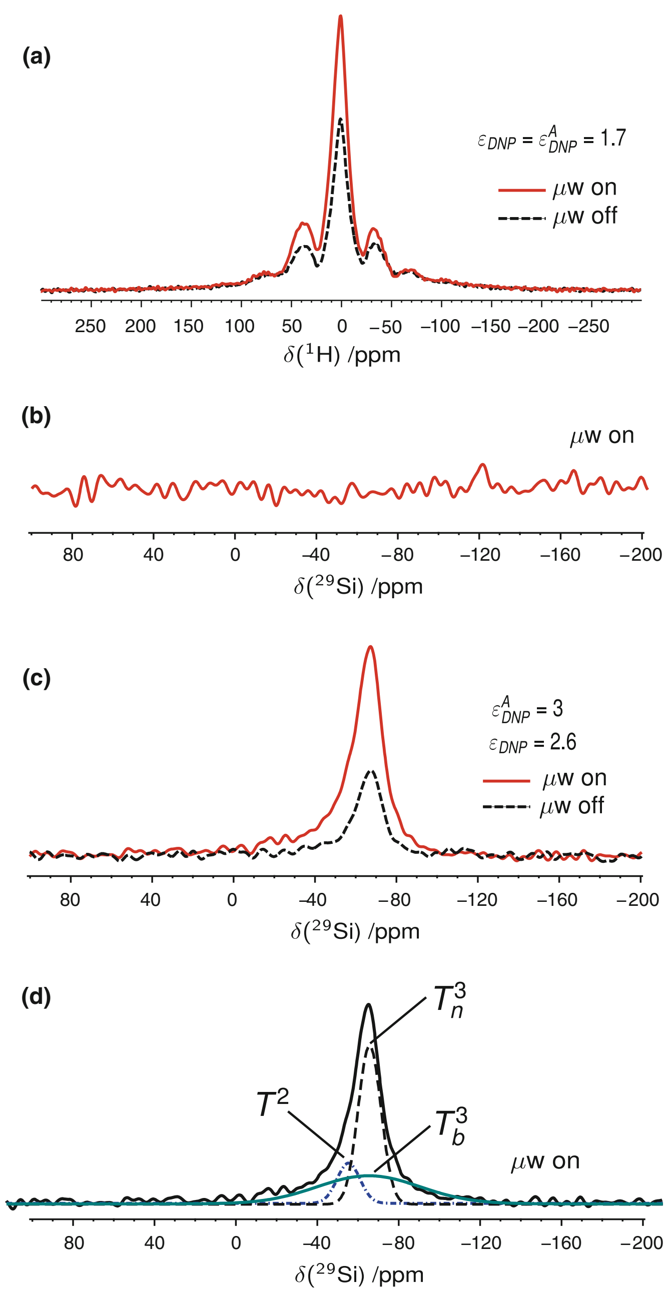

Fig. 3 Natural abundance ^{1}H and ^{29}Si NMR spectra of mesoporous silica functionalized with TEMPO. **a** DP MAS ^{1}H with (*top*) and without (*bottom*) microwave irradiation. The spectra were acquired with four scans and $\tau_{\mu w} = 5$ s. **b** CP MAS $^{1}\mathrm{H} \rightarrow {}^{29}\mathrm{Si}$ spectrum with microwave irradiation. The spectra were acquired with 64 scans and $\tau_{\mu w} = 10$ s. **c** DP MAS ^{29}Si NMR spectra with (*top*) and without (*bottom*) microwave irradiation. The spectra were acquired with 64 scans and $\tau_{\mu w} = 10$ s. **d** Deconvolution of the DP MAS ^{29}Si spectrum with microwave irradiation. The spectrum is identical to that displayed in **c**

hyperfine coupling with ^{14}N nucleus with a maximum A_{zz} component of about 65 G. For **1**, the powder lineshape is masked by the spectral broadening resulting from the extensive network of intermolecular dipolar couplings between the unpaired electrons. EPR measurements indicate that the TEMPO concentration of **1**, c_m, is about 70 mM. As the TEMPO moieties are grafted on the silica surface, it is also pertinent to estimate the TEMPO surface concentration in mol m^{-2} using

$$\Gamma = \frac{c_\mathrm{m}}{10^6 \rho a_s} \tag{2}$$

where c_m is expressed in mM, and $\rho = 0.4$ g cm^{-3} and $a_s = 456$ m^2 g^{-1} are the mass density and the specific surface area of **1**. Equation 2 yields $\Gamma = 380\,\mathrm{nmol\,m}^{-2}$. From Γ, the average distance R in Å between two TEMPO moieties can be estimated as

$$R = \left(\Gamma 10^{-20} \mathcal{N}_\mathrm{A}\right)^{-1/2} \tag{3}$$

assuming a 2-D square lattice for the positions of the TEMPO moieties. In Eq. 3, $\mathcal{N}_\mathrm{A}$ is the Avogadro number. The calculated R value is 19 Å for **1**.

The comparison of the EPR spectrum in Fig. 2 with those of diluted TEMPO moieties anchored on silica surface [23] indicates that the homogeneous spectral broadening arising from multiple dipolar couplings between electrons is comparable with the ^{29}Si Larmor frequency at 9.4 T (79.44 MHz). Therefore, the thermal mixing mechanism [8, 37, 38] can be involved in the DNP transfer for **1**, especially in the case of direct ^{29}Si DNP.

Figure 3a shows the one-dimensional (1D) ^{1}H NMR spectrum of **1** with and without microwave irradiation. For both spectra, the maximum intensity is observed at $\delta \approx 0$ ppm, which is typical of ^{1}H in alkyl groups linked to silicon atoms. As the material **1** is obtained by co-condensation of 4-oxo-TEMPO, aminopropyltrimethoxysilane and methyltrimethoxysilane [23–25], the silica surface is functionalized with methyl and (4-TEMPO)aminopropyl groups, as shown in Fig. 1. The silica surface must also contain silanol protons (Si-OH), but their ^{1}H signals between 1 and 8 ppm (2 ppm for non-hydrogen-bonded silanol) [39] is not resolved from that of alkyl protons.

The second moment, $M_2(\nu_r)$, of ^{1}H signal at MAS frequency of 10 kHz was calculated as [40, 41]

$$M_2(\nu_r) = \frac{1}{A}\int_{\nu_i}^{\nu_s} (\nu - \nu_0)^2 I(\nu)\mathrm{d}\nu \tag{4}$$

where the ν_i and ν_s frequencies are the lower and upper bounds of the frequency interval in which the ^{1}H signal intensity exceeds the noise, A the integral of ^{1}H signal between ν_i and ν_s frequencies, ν is the frequency, ν_0 is the frequency of the maximum in intensity, and $I(\nu)$ the ^{1}H signal intensity at the frequency ν. For **1**, the $M_2(\nu_r)$ value is about 300 kHz^2 and the square root of the $M_2(\nu_r)$, which is proportional to full width at half maximum for a Gaussian lineshape, is twofold lower in absolute value for **1** than those measured for 10 %-protonated frozen solvents contained within the pores of mesoporous silica. This observation is consistent with an averaging of the ^{1}H–^{1}H dipolar couplings in **1** by the threefold hopping of the methyl groups [42], the librational motion of the O–H groups about the Si–O axes [43] and the conformational changes of (4-TEMPO)aminopropyl chains [44–46]. When the pores of mesoporous silica do not contain solvents, the rate of these motions at about 100 K is faster than 1 MHz, i.e., their correlation time is below 1 μs [43–46]. As most protons experience fast librational motions and the grafted TEMPO moieties are mobile in the silica pores, the electron–proton interactions are time dependent. Nevertheless, at $B^0 = 9.393$ T and 100 K, polarization of protons via Overhauser effect [47] is unlikely since the spectral density of molecular motions in dielectric solids is very low at about 263 GHz, the electron Larmor frequency [48].

As the full width at half maximum is proportional to the square root of the $M_2(\nu_r)$ [40, 49] and the full width at half maximum of the ^{1}H signal is inversely proportional to ν_r [49, 50], the second moment under static conditions, $M_2(0)$, can be calculated as

$$M_2(0) = \frac{\nu_r}{K}[M_2(\nu_r)]^{1/2} \tag{5}$$

where the dimensionless K constant lies in the range [0.04, 0.1] [50]. The average dipolar coupling constant between protons, $\overline{b}_{\mathrm{HH}}/(2\pi)$, can be deduced from the square root of the $M_2(0)$ [51]

$$\frac{\overline{b}_{\mathrm{HH}}}{2\pi} = -\frac{2}{3}\left[\frac{M_2(0)}{\chi}\right]^{1/2} \tag{6}$$

where χ is a structural factor, which depends on the proton distribution in the sample. Here, given that (i) the protons are located on the pore surfaces, (ii) the pore average radius is much larger than the average ^{1}H–^{1}H distance between nearest neighbors, we can assume a 2-D square lattice of protons and hence $\chi = 4.77$ [51]. For the investigated systems, the electron longitudinal relaxation times, T_{1e}, are shorter than the ^{1}H transverse longitudinal relaxation times ($T_{1e} < T_{2n}(^1\mathrm{H})$), and the radius of the spin diffusion barrier, r_{d}, can be calculated as [52]

$$r_{\mathrm{d}} \approx \left[2S\frac{\gamma_e}{\gamma(^1\mathrm{H})}B_S\left(\frac{S\hbar\gamma_e B^0}{k_{\mathrm{B}}T}\right)\right]^{\alpha}\left|\frac{\mu_0}{4\pi}\frac{\gamma^2(^1\mathrm{H})\hbar}{\overline{b}_{\mathrm{HH}}}\right|^{1/3} \tag{7}$$

where $S = 1/2$ is the effective spin quantum number for the unpaired electron of TEMPO monoradical, γ_e and $\gamma(^1\mathrm{H})$ are the gyromagnetic ratios of electron and ^{1}H nucleus, B_S the Brillouin function with parameter $S, \hbar$ is the reduced Planck constant, k_{B} the Boltzmann constant, $T = 98$ K the sample temperature and $\alpha = 1/4$ using Khutsishvili's definition of the diffusion barrier [17, 52]. According to Eq. 7, the r_{d} value lies in the range [4.6, 5.4 Å], which is consistent with diffusion barrier radii reported in the literature [53]. Furthermore, the r_{d} radius is shorter than R and as the protons are located on the silica surface, the fraction, f_{d}, of protons enclosed within the diffusion barrier is given by

$$f_\mathrm{d} = \frac{\pi r_\mathrm{d}^2}{R^2}. \tag{8}$$

The calculated f_d value lies between 18 and 25 %, indicating that a significant fraction of protons is not involved in the polarization transfer via ^{1}H–^{1}H spin diffusion in the direct ^{1}H DNP.

Figure 3a shows limited DNP enhancement of ^{1}H signal intensity ($\varepsilon_\mathrm{DNP}(^1\mathrm{H}) = 1.7$). This limited enhancement mainly stems from: (i) the lower efficiency of monoradicals at high field for ^{1}H signal enhancement compared to that of biradicals [21, 54–56]; (ii) the weak ^{1}H–^{1}H dipolar couplings in **1**, which result in slow proton spin diffusion and hinder the distribution of ^{1}H polarization within the sample [57, 58]; (iii) the short electron and proton relaxation times in **1** owing to the high molecular mobility, the presence of paramagnetic molecular oxygen and the high concentration of unpaired electrons [21, 59, 60]. Short electron longitudinal relaxation times (T_{1e}) reduce the saturation of EPR transition, whereas short nuclear longitudinal relaxation times (T_{1n}) limit the time to “pump” the nuclear polarization. The ^{1}H lineshape is unaffected by the DNP transfer and the enhancement of signal integral is equal to that of signal intensity ($\varepsilon_\mathrm{DNP}(^1\mathrm{H}) = \varepsilon^A_\mathrm{DNP}(^1\mathrm{H})$). This result is consistent with the homogeneous broadening of the ^{1}H signal [61].

Figure 3b shows the 1D CP MAS $^1\mathrm{H} \rightarrow {}^{29}\mathrm{Si}$ spectrum of **1** with microwave irradiation. No ^{29}Si signal is visible after 64 scans. This observation indicates that the $^1\mathrm{H} \rightarrow {}^{29}\mathrm{Si}$ CP transfer is inefficient for **1**. This inefficiency does not stem from an interference between the conformational dynamics and the ^{1}H heteronuclear decoupling [42, 62, 63], since the ^{29}Si signal intensity in DP MAS experiment was not affected on applying a ^{1}H heteronuclear decoupling of 100 kHz amplitude. This result is consistent with conformational dynamics in **1** faster than 1 MHz at about 100 K, in the absence of solvent molecules in the silica pores [44–46]. The inefficiency of $^1\mathrm{H} \rightarrow {}^{29}\mathrm{Si}$ CP transfer mainly results from (i) the short nuclear longitudinal relaxation times in the rotating frame, $T_{1\rho}$, owing to the high concentration of TEMPO moieties [64] and (ii) the weak ^{1}H–^{29}Si dipolar couplings, which are partly averaged out by the conformational dynamics.

Conversely, as shown in Fig. 3c, the ^{29}Si direct experiments allow the detection of a ^{29}Si signal in a few minutes with and without microwave irradiation. The high sensitivity of these experiments stems from the fast polarization buildup. The fast signal buildup in direct DNP is discussed below (see Fig. 4). In the absence of microwave irradiation, the longitudinal ^{29}Si magnetization of **1** builds up in a few seconds, whereas in mesoporous silica containing frozen solvents and nitroxide radicals, the longitudinal ^{29}Si relaxation requires thousands of seconds. The faster relaxation for **1** results from (i) the shorter average distance between unpaired electrons and ^{29}Si nuclei, which is constrained by the covalent linkage [65–67] and (ii) the higher mobility at the atomic scale in the absence of frozen solvents in the pores. Furthermore, direct ^{29}Si DNP yields DNP enhancements, $\varepsilon_\mathrm{DNP}(^{29}\mathrm{Si}) = 2.6$ and $\varepsilon^A_\mathrm{DNP}(^{29}\mathrm{Si}) = 3$, which are more than 50 % higher than those measured for direct ^{1}H DNP. The higher signal enhancements in direct ^{29}Si DNP compared to direct ^{1}H DNP are consistent with the theoretical maximal enhancements [17, 68, 69], which are given by the ratios $\gamma_e/\gamma(^{29}\mathrm{Si}) \approx 3311$ for ^{29}Si and $\gamma_e/\gamma(^1\mathrm{H}) \approx 658$ for

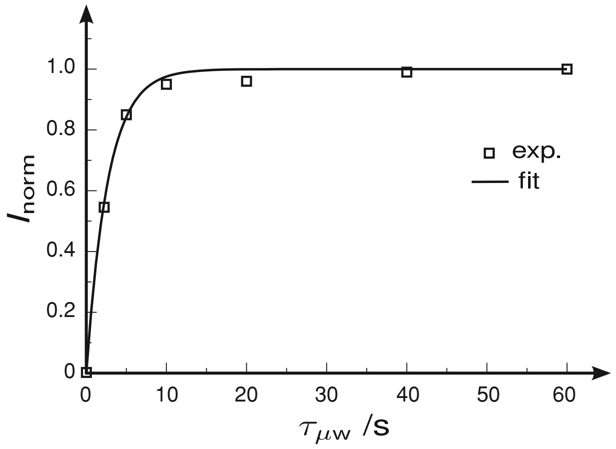

Fig. 4 Buildup curve of DP ^{29}Si signal intensity with microwave irradiation as function of $\tau_{\mu w}$ delay. The signal intensities, $I(\tau_{\mu w})$, are normalized with respect to the signal intensities at $\tau_{\mu w} = 60$ s: $I_{norm} = I(\tau_{\mu w})/I(60)$. The experimental points and the fit according to Eq. 9 are displayed as *square symbols* and *continuous line*, respectively.

^{1}H, where $\gamma(^{29}\text{Si})$ is the gyromagnetic ratio of the ^{29}Si nucleus. Nevertheless, the direct ^{29}Si DNP enhancement is lower for **1** than those measured for mesoporous silica containing frozen solutions of nitroxide radicals within its pores [17]. For instance, $|\varepsilon_{DNP}|$ values of 11 and 30 were measured for mesoporous silica containing 30 mM of 4-amino-TEMPO and 15 mM of TOTAPOL in [$^2H_6$]-DMSO/^2H_2O/H_2O frozen matrix [17]. The lower $\varepsilon_{DNP}(^{29}\text{Si})$ values for **1** stem from different factors. First, the polarization transfer in **1** relies mainly on mono-radical TEMPO, whereas the biradicals, such as TOTAPOL, are usually more efficient at high field [21, 54–56]. Second, in this work, DNP experiments were performed at a B^0 value, which is optimal for direct ^{1}H DNP employing nitroxide radicals but not optimal for the direct polarization of isotopes with low gyromagnetic ratios [17, 68, 69]. Third, as explained above for ^{1}H DNP, the electron and nuclear relaxations must be faster in **1** than in mesoporous silica impregnated with frozen solutions. However, the faster nuclear relaxation also leads to faster polarization buildup, which is a significant advantage in terms of sensitivity, as shown below.

The difference between $\varepsilon_{DNP}(^{29}\text{Si})$ and $\varepsilon^{A}_{DNP}(^{29}\text{Si})$ arises from the broader foot of the DP ^{29}Si signal with microwave irradiation compared to that without microwave irradiation. This broad ^{29}Si signal corresponds to silicon-29 nuclei experiencing large hyperfine interaction and which are located in the vicinity of the unpaired electrons. Therefore, in direct ^{29}Si DNP, the polarization of the silicon-29 nuclei close to the TEMPO moiety is higher than that of remote ^{29}Si nuclei. Similar observations have been reported for ^{13}C direct DNP at low magnetic field [8].

The DP ^{29}Si signal displays a maximum at −66 ppm, the chemical shift of $R\text{Si(OSi)}_3$ sites (T^3) with $R = \text{CH}_3$ or (4-TEMPO)aminopropyl groups [70, 71]. No ^{29}Si signal is observed in the chemical shift range, −110 to −90 ppm, corresponding to $(\text{SiO})_n\text{Si(OH)}_{4-n}$ (Q^n) sites. This observation proves that all Si atoms are covalently linked to a carbon atom in **1**, which is consistent with the preparation of **1** from aminopropyltrimethoxysilane and methyltrimethoxysilane precursors. Furthermore, the ^{29}Si signal is asymmetrical and cannot be fitted by a single Gaussian lineshape. In a phenomenological approach, the DP ^{29}Si signal with microwave irradiation has been fitted as the sum of three Gaussian lineshapes: T^3_n, T^3_b and T^2 (see Fig. 3d). Similar deconvolution has been used to fit the DP ^{29}Si signal without microwave irradiation (not shown). The T^2 contribution corresponds to the RSi(OSi)$_2$OH sites with $R = C$H$_3$ or (4-TEMPO)aminopropyl groups. In the fit, the average chemical shift of T^2 sites was fixed to -57 ppm [70, 71]. The introduction of T^3_n contribution was necessary to obtain a reasonable fit of the signal foot. The T^3_b contribution corresponds to the signal of T^3 sites close to a TEMPO moiety, whereas the T^3_n contribution subsumes the signals of other T^3 sites. The boundary between T^3_n and T^3_b sites is not well defined, since there are several sources of line broadening, including the bulk magnetic susceptibility effect, which is difficult to estimate [72]. Furthermore, to better constrain the fit, identical full widths at half maximum have been used for T^2 and T^3_n sites. The integral of T^3_n contribution is about fivefold larger than that of T^2 contribution with or without microwave irradiation. Conversely, the relative area of T^3_b contribution increases from 30 % without microwave irradiation to 40 % with microwave irradiation. This observation confirms the higher polarization of T^3_b sites close to unpaired electrons in direct ^{29}Si DNP.

Figure 4 shows that the DNP-enhanced DP ^{29}Si signal intensity builds up in less than 10 s. We propose to model the buildup of ^{29}Si signals in direct DNP experiments as a stretched exponential function

$$I_{\text{norm}} = I^{\infty}_{\text{norm}}\left\{1 - \exp\left[-\left(\frac{\tau_{\mu w}}{\tau_{\text{DNP}}}\right)^{1/2}\right]\right\} \tag{9}$$

where $\tau_{\text{DNP}} = 1.3$ s is the DNP buildup time constant and I^{∞}_{norm} is the asymptotic normalized intensity for $\tau_{\mu\text{w}} \gg \tau_{\text{DNP}}$. This model is proposed since the direct ^{29}Si DNP does not involve ^{29}Si–^{29}Si spin diffusion and the polarization is transferred directly via electron-^{29}Si hyperfine interactions. The same interactions govern the nuclear relaxation via paramagnetic centers in the absence of nuclear spin diffusion and for randomly distributed impurities in a 3-D space, this relaxation mechanism results in a buildup of nuclear polarization, which follows an exponential function of $\sqrt{t}$ [73, 74]. Therefore, it is reasonable to postulate analogous buildup in direct ^{29}Si DNP. Compared to a biexponential model employed in ref. [17], the stretched exponential model has the advantage of assuming a continuous increase of the buildup time with increasing distances to the paramagnetic centers.

The value of $\tau_{\text{DNP}} = 1.3$ s for **1** is much shorter than the buildup times reported for direct ^{29}Si DNP on mesoporous silica containing nitroxide radicals in frozen solution (about 4,000 s) [17]. This difference in τ_{DNP} values represents a sensitivity gain by a factor $(4{,}000/1.3)^{1/2} \approx 55$, which counterbalances the lower DNP enhancements for solvent-free DNP; and the global DNP enhancement [31] could be larger for **1** than for mesoporous silica containing frozen solvent.

4 Conclusion

We demonstrated that co-condensation is supplementary to post-synthesis impregnation for the incorporation of DNP polarizing agents into inorganic materials. Using this protocol, the ^{29}Si NMR signals of functionalized mesoporous silica was enhanced by high-field direct ^{29}Si DNP. We also proved the feasibility of solvent-free DNP for porous materials. The functionalization of materials with nitroxide radicals allows the removal of solvent molecules from the pores. Even if the reported DNP enhancements are limited, the polarization buildups with and without microwave irradiation are fast, which is a significant advantage in terms of sensitivity. This fast buildup is promising for DNP experiments below 100 K, since the T_{1n} times are usually long at low temperatures [75, 76]. The direct DNP is shown to be an alternative to indirect DNP, when the CP transfer is inefficient. Therefore, the direct DNP will be useful for systems featuring high atomic mobility or high concentration in unpaired electrons. The DNP enhancement for direct ^{29}Si can be improved by (i) grafting TOTAPOL derivatives, instead of TEMPO moieties, in order to benefit from the efficient cross-effect mechanism; (ii) the optimization of B^0 field and radical concentration; (iii) the use of sapphire rotor instead of ZrO_2 rotors since the sapphire is nearly transparent to the 263 GHz of microwave irradiation [32]. It would be also worth studying the influence of the nitroxide position and dynamics by varying the length and the flexibility of the linkage between the nitroxide radical and the silica surface. The impregnation of **1** with organic solvents will permit to distinguish the effects of frozen solvent presence within the pores and radical grafting on the enhancement in direct and indirect DNP experiments. The further studies proposed above are currently in progress.

Acknowledgments The authors are grateful for funding provided by Region Nord/Pas de Calais, Europe (FEDER), CNRS, French Minister of Science, FR-3050, USTL, ENSCL, Bruker BIOSPIN, and Contract No. ANR-2010-JCJC-0811-01.

References

1. K. Na, C. Jo, J. Kim, K. Cho, J. Jung, Y. Seo, R.J. Messinger, B.F. Chmelka, R. Ryoo, Science **333**, 328 (2011)
2. I. Farnan, H. Cho, W.J. Weber, Nature **445**, 190 (2007)
3. B. Key, R. Bhattacharyya, M. Morcrette, V. Seznéc, J.M. Tarascon, C.P. Grey, J. Am. Chem. Soc. **131**, 9239 (2009)
4. S. Cadars, B.J. Smith, J.D. Epping, S. Acharya, N. Belman, Y. Golan, B.F. Chmelka, Phys. Rev. Lett. **103**, 136802 (2009)
5. J.S. Hartman, A. Narayanan, Y. Wang, J. Am. Chem. Soc. **116**, 4019 (1994)
6. T.R. Carver, C.P. Slichter, Phys. Rev. **92**, 212 (1953)
7. A. Abragam, J. Combrisson, I. Solomon, C. R. Acad. Sci. **246**, 1035 (1958)
8. R. Wind, M. Duijvestijn, C. van der Lugt, A. Manenschijn, J. Vriend, Prog. Nucl. Magn. Reson. Spectrosc. **17**, 33 (1985)
9. H. Lock, R. Wind, G. Maciel, N. Zumbulyadis, Solid State Commun. **64**, 41 (1987)
10. M. Afeworki, J. Schaefer, Macromolecules **25**, 4097 (1992)
11. H. Lock, G.E. Maciel, C.E. Johnson, J. Mater. Res. **7**, 2791 (1992)
12. H. Lock, R.A. Wind, G.E. Maciel, C.E. Johnson, J. Chem. Phys. **99**, 3363 (1993)

13. R.A. Wind, in Encyclopedia of Magnetic Resonance, ed. by R.K. Harris, R.E. Wasylishen (Wiley, Ltd, Chichester, published online 15th March 2007). doi:10.1002/9780470034590.emrstm0140
14. A.E. Dementyev, D.G. Cory, C. Ramanathan, Phys. Rev. Lett. **100**, 127601 (2008)
15. A. Lesage, M. Lelli, D. Gajan, M.A. Caporini, V. Vitzthum, P. Miéville, J. Alauzun, A. Roussey, C. Thieuleux, A. Mehdi, G. Bodenhausen, C. Copéret, L. Emsley, J. Am. Chem. Soc. **132**, 15459 (2010)
16. M. Lelli, D. Gajan, A. Lesage, M.A. Caporini, V. Vitzthum, P. Miéville, F. Héroguel, F. Rascón, A. Roussey, C. Thieuleux, M. Boualleg, L. Veyre, G. Bodenhausen, C. Copéret, L. Emsley, J. Am. Chem. Soc. **133**, 2104 (2011)
17. O. Lafon, M. Rosay, F. Aussenac, X. Lu, J. Trébosc, O. Cristini, C. Kinowski, N. Touati, H. Vezin, J.P. Amoureux, Angew. Chem. Int. Ed **50**, 8367 (2011)
18. A.J. Rossini, A. Zagdoun, M. Lelli, J. Canivet, S. Aguado, O. Ouari, P. Tordo, M. Rosay, W.E. Maas, C. Copéret, D. Farrusseng, L. Emsley, A. Lesage, Angew. Chem. Int. Ed **51**, 123 (2012)
19. V. Vitzthum, P. Mieville, D. Carnevale, M.A. Caporini, D. Gajan, C. Copéret, M. Lelli, A. Zagdoun, A.J. Rossini, A. Lesage, L. Emsley, G. Bodenhausen, Chem. Commun. **48**, (2012)
20. L.R. Becerra, G.J. Gerfen, R.J. Temkin, D.J. Singel, R.G. Griffin, Phys. Rev. Lett. **71**, 3561 (1993)
21. C. Song, K.N. Hu, C.G. Joo, T.M. Swager, R.G. Griffin, J. Am. Chem. Soc. **128**, 11385 (2006)
22. A. Zagdoun, A.J. Rossini, D. Gajan, A. Bourdolle, O. Ouari, M. Rosay, W.E. Maas, P. Tordo, M. Lelli, L. Emsley, A. Lesage, C. Coperet, Chem. Commun. **48**, 654 (2012)
23. R. Ciriminna, J. Blum, D. Avnir, M. Pagliaro, Chem. Commun. pp. 1441–1442 (2000)
24. R. Ciriminna, C. Bolm, T. Fey, M. Pagliaro, Adv. Synth. Catal. **344**, 159 (2002)
25. A. Michaud, G. Gingras, M. Morin, F. Béland, R. Ciriminna, D. Avnir, M. Pagliaro, Org. Process Res. Dev. **11**, 766 (2007)
26. R. Ciriminna, M. Pagliaro, Org. Process Res. Dev. **14**, 245 (2009)
27. L. Tebben, A. Studer, Angew. Chem. Int. Ed **50**, 5034 (2011)
28. H. Dorn, T. Glass, R. Gitti, K. Tsai, Appl. Magn. Reson. **2**, 9 (1991)
29. E.R. McCarney, S. Han, J. Magn. Reson. **190**, 307 (2008)
30. M.H. Lim, A. Stein, Chem. Mater. **11**, 3285 (1999)
31. V. Vitzthum, F. Borcard, S. Jannin, M. Morin, P. Miéville, M.A. Caporini, A. Sienkiewicz, S. Gerber-Lemaire, G. Bodenhausen, ChemPhysChem **12**, 2929 (2011)
32. M. Rosay, L. Tometich, S. Pawsey, R. Bader, R. Schauwecker, M. Blank, P.M. Borchard, S.R. Cauffman, K.L. Felch, R.T. Weber, R.J. Temkin, R.G. Griffin, W.E. Maas, Phys. Chem. Chem. Phys. **12**, 5850 (2010)
33. D.G. Cory, W.M. Ritchey, J. Magn. Reson. **80**, 128 (1988)
34. B.M. Fung, A.K. Khitrin, K. Ermolaev, J. Magn. Reson. **142**, 97 (2000)
35. Mathworks Inc. http://www.mathworks.com
36. D. Baute, V. Frydman, H. Zimmermann, S. Kababya, D. Goldfarb, J. Phys. Chem. B **109**, 7807 (2005)
37. V.A. Atsarkin, Sov. Phys. Solid State **21**, 725 (1978)
38. C.T. Farrar, D.A. Hall, G.J. Gerfen, S.J. Inati, R.G. Griffin, J. Chem. Phys. **114**, 4922 (2001)
39. C.E. Bronnimann, R.C. Zeigler, G.E. Maciel, J. Am. Chem. Soc. **110**, 2023 (1988)
40. A. Abragam, The Principles of Nuclear Magnetism (Oxford University Press, Oxford, 1961)
41. D. Hirsemann, T.K.J. Koster, J. Wack, L. van Wullen, J. Breu, J. Senker, Chem. Mater. **23**, 3152 (2011)
42. V.S. Bajaj, P.C. van der Wel, R.G. Griffin, J. Am. Chem. Soc. **131**, 118 (2008)
43. T. Kobayashi, J.A. DiVerdi, G.E. Maciel, J. Phys. Chem. C **112**, 4315 (2008)
44. E.C. Kelusky, C.A. Fyfe, J. Am. Chem. Soc. **108**, 1746 (1986)
45. R.C. Zeigler, G.E. Maciel, J. Am. Chem. Soc. **113**, 6349 (1991)
46. R.C. Zeigler, G.E. Maciel, J. Phys. Chem. **95**, 7345 (1991)
47. A.W. Overhauser, Phys. Rev. **92**, 411 (1953)
48. C. Griesinger, M. Bennati, H. Vieth, C. Luchinat, G. Parigi, P. Hfer, F. Engelke, S. Glaser, V. Denysenkov, T. Prisner, Prog. Nucl. Magn. Reson. Spectrosc. (2012, in press)
49. E. Brunner, D. Freude, B. Gerstein, H. Pfeifer, J. Magn. Reson. **90**, 90 (1990)
50. V.E. Zorin, S.P. Brown, P. Hodgkinson, J. Chem. Phys. **125**, 144508 (2006)
51. D.H. Levy, K.K. Gleason, J. Phys. Chem. **96**, 8125 (1992)
52. G.R. Khutsishvili, Phys. Usp. **11**, 802 (1969)
53. C. Ramanathan, Appl. Magn. Reson. **34**, 409 (2008)
54. C.F. Hwang, D.A. Hill, Phys. Rev. Lett. **19**, 1011 (1997)

55. K.N. Hu, C. Song, H.H. Yu, T.M. Swager, R.G. Griffin, J. Chem. Phys. **128**, 052302 (2008)
56. K.N. Hu, G.T. Debelouchina, A.A. Smith, R.G. Griffin, J. Chem. Phys. **134**, 125105 (2011)
57. M. Rosay, A.C. Zeri, N.S. Astrof, S.J. Opella, J. Herzfeld, R.G. Griffin, J. Am. Chem. Soc. **123**, 1010 (2001)
58. P.C.A. van der Wel, K.N. Hu, J. Lewandowski, R.G. Griffin, J. Am. Chem. Soc. **128**, 10840 (2006)
59. K.N. Hu, Solid State Nucl. Magn. Reson. **40**, 31 (2011)
60. A. Zagdoun, G. Casano, O. Ouari, G. Lapadula, A.J. Rossini, M. Lelli, M. Baffert, D. Gajan, L. Veyre, W.E. Maas, M. Rosay, R.T. Weber, C. Thieuleux, C. Copéret, A. Lesage, P. Tordo, L. Emsley, J. Am. Chem. Soc. **134**, 2284 (2011)
61. M.M. Maricq, J.S. Waugh, J. Chem. Phys. **70**, 3300 (1979)
62. W.P. Rothwell, J.S. Waugh, J. Chem. Phys. **74**, 2721 (1981)
63. A.H. Linden, S. Lange, W.T. Franks, Ü. Akbey, E. Specker, van B.J. Rossum, H. Oschkinat, J. Am. Chem. Soc. **133**, 19266 (2011)
64. S. Lange, A.H. Linden, Akbey, W. Trent Franks, N.M. Loening, B.J.v. Rossum, H. Oschkinat, J. Magn. Reson. **216**, 209 (2012)
65. N.P. Wickramasinghe, M. Kotecha, A. Samoson, J. Past, Y. Ishii, J. Magn. Reson. **184**, 350 (2007)
66. N.P. Wickramasinghe, S. Parthasarathy, C.R. Jones, C. Bhardwaj, F. Long, M. Kotecha, S. Mehboob, L.W.M. Fung, J. Past, A. Samoson, Y. Ishii, Nat. Meth. **6**, 215 (2009)
67. P.S. Nadaud, J.J. Helmus, I. Sengupta, C.P. Jaroniec, J. Am. Chem. Soc. **132**, 9561 (2010)
68. T. Maly, L.B. Andreas, A.A. Smith, R.G. Griffin, Phys. Chem. Chem. Phys. **12**, 5872 (2010)
69. T. Maly, A.F. Miller, R.G. Griffin, ChemPhysChem **11**, 999 (2010)
70. C.A. Fyfe, Y. Zhang, P. Aroca, J. Am. Chem. Soc. **114**, 3252 (1992)
71. B. Dietrich, K. Holtin, M. Bayer, V. Friebolin, M. Kühnle, K. Albert, Anal. Bioanal. Chem. **391**, 2627 (2008)
72. G. Kervern, G. Pintacuda, Y. Zhang, E. Oldfield, C. Roukoss, E. Kuntz, E. Herdtweck, J.M. Basset, S. Cadars, A. Lesage, C. Copéret, L. Emsley, J. Am. Chem. Soc. **128**, 13545 (2006)
73. D. Tse, S.R. Hartmann, Phys. Rev. Lett. **21**, 511 (1968)
74. D. Tse, I.J. Lowe, Phys. Rev. **166**, 292 (1968)
75. K.R. Thurber, W.M. Yau, R. Tycko, J. Magn. Reson. **204**, 303 (2010)
76. Y. Matsuki, K. Ueda, T. Idehara, R. Ikeda, K. Kosuga, S. Nakamura, M. Toda, T. Anai, T. Fujiwara, in Third International DNP Symposium on dynamic nuclear polarization (Lausanne, 2011)

THE JOURNAL OF PHYSICAL CHEMISTRY C
Article
pubs.acs.org/JPCC

Mesoporous Silica Nanoparticles Loaded with Surfactant: Low Temperature Magic Angle Spinning ^{13}C and ^{29}Si NMR Enhanced by Dynamic Nuclear Polarization

Olivier Lafon,[†,‡,*] Aany S. Lilly Thankamony,[†,‡] Takeshi Kobayashi,[§] Diego Carnevale,[⊥] Veronika Vitzthum,[⊥] Igor I. Slowing,[§] Kapil Kandel,[§,∥] Hervé Vezin,[†,#] Jean-Paul Amoureux,[†,‡] Geoffrey Bodenhausen,[⊥,○] and Marek Pruski[§,∥,*]

[†]Université de Lille Nord de France, 59000 Lille, France

[‡]CNRS UMR 8181 Unité de Catalyse et de Chimie du Solide (UCCS), Ecole Nationale Supérieure de Chimie de Lille, Université de Lille 1, 59652 Villeneuve d'Ascq, France

[§]Ames Laboratory, U.S. Department of Energy, Ames, Iowa 50011, United States

[⊥]Institut des Sciences et Ingénierie Chimiques, Ecole Polytechnique Fédérale de Lausanne, EPFL, Batochime, 1015 Lausanne, Switzerland

[∥]Department of Chemistry, Iowa State University, Ames, Iowa 50011, United States

[#]CNRS UMR 8516, Laboratoire de Spectrochimie Infrarouge et Raman (LASIR), Université de Lille 1, 59652 Villeneuve d'Ascq, France

[○]Département de Chimie, Ecole Normale Supérieure, UMR 7203 CNRS/UPMC/ENS, Université Pierre et Marie Curie, 24 rue Lhomond, 75231 Paris cedex 05, France

Supporting Information

ABSTRACT: We show that dynamic nuclear polarization (DNP) can be used to enhance NMR signals of ^{13}C and ^{29}Si nuclei located in mesoporous organic/inorganic hybrid materials, at several hundreds of nanometers from stable radicals (TOTAPOL) trapped in the surrounding frozen disordered water. The approach is demonstrated using mesoporous silica nanoparticles (MSN), functionalized with 3-(*N*-phenylureido)propyl (PUP) groups, filled with the surfactant cetyltrimethylammonium bromide (CTAB). The DNP-enhanced proton magnetization is transported into the mesopores via ^{1}H−^{1}H spin diffusion and transferred to rare spins by cross-polarization, yielding signal enhancements $\varepsilon_{\text{on/off}}$ of around 8. When the CTAB molecules are extracted, so that the radicals can enter the mesopores, the enhancements increase to $\varepsilon_{\text{on/off}} \approx 30$ for both nuclei. A quantitative analysis of the signal enhancements in MSN with and without surfactant is based on a one-dimensional proton spin diffusion model. The effect of solvent deuteration is also investigated.

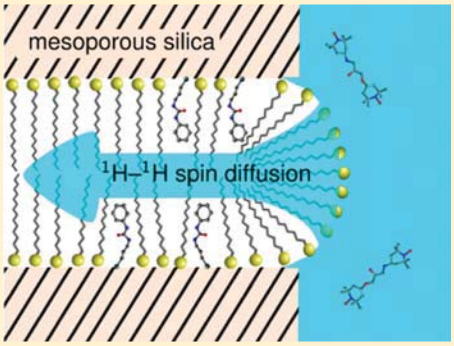

1. INTRODUCTION

The self-assembly of surfactants in the presence of silica precursors allows the synthesis of advanced materials, such as mesoporous silica[1−3] and mesoporous silica nanoparticles (MSN)[4,5] whose properties can be tailored toward applications in drug delivery,[5] sensors,[2] photonics,[1] and heterogeneous catalysis.[4] The structures of these systems depend on delicate hydrophobic−hydrophilic equilibria involving the surfactant, precursors and solvent. A better understanding of the interactions between these components should allow one to produce materials with an improved control of their composition and structure.

Because it can give information on a local atomic scale, solid-state nuclear magnetic resonance (SS-NMR) spectroscopy is very well suited to the study of mesoporous materials.[6−9] However, poor sensitivity limits the ability of conventional SS-NMR to characterize surfaces containing nuclei with low gyromagnetic ratios and/or low natural abundance, such as ^{13}C and ^{29}Si. It has been shown recently that dynamic nuclear polarization (DNP) can boost the sensitivity, particularly in conjunction with magic angle spinning (MAS) at high magnetic fields.[10−21] Sensitivity enhancements of 1−2 orders of magnitude have been achieved by impregnating dry mesoporous materials without surfactants with aqueous solutions of nitroxide biradicals, which can readily enter mesopores that have diameters of a few nanometers.[10−12,14,15]

Received: October 12, 2012
Revised: December 20, 2012
Published: December 21, 2012

dx.doi.org/10.1021/jp310109s | *J. Phys. Chem. C* 2013, 117, 1375−1382

Herein, we report enhancements achieved in MSN material containing the templating surfactant cetyltrimethylammonium bromide (CTAB) and functionalized with covalently bound 3-(*N*-phenylureido)propyl (PUP). In contrast to surfactant-free MSN, where the DNP enhancement of the ^{1}H polarization may be readily induced by radicals, such as TOTAPOL,[23] that can enter the mesopores, the radicals are prevented from entering the mesopores of MSN if they contain CTAB, so that the ^{1}H polarization must diffuse over distances up to several hundreds of nm before being transferred to ^{13}C or ^{29}Si nuclei via cross-polarization (CP). The propagation of DNP-enhanced ^{1}H polarization via ^{1}H spin diffusion has already been demonstrated for heterogeneous blends of polymers,[24] mesocrystals of peptides,[25] or very recently for microcrystalline organic solids.[20] We shall show that polarization enhancements on the order of $\varepsilon_{\mathrm{on/off}}$ ~8 can be achieved "remotely" in surfactant-filled mesopores.

2. EXPERIMENTAL SECTION

2.1. Synthesis of Materials and Structural Characterization. The MSN samples used in this study were synthesized by a previously reported co-condensation method, which includes functionalization with 3-(*N*-phenylureido)propyl (PUP) groups.[26,27] CTAB, sodium hydroxide, aniline and mesitylene were purchased from Sigma-Aldrich, whereas tetraethoxysilane (TEOS) and 3-isocyanatopropyl-triethoxysilane were acquired from Gelest. All reagents were used as received. 3-(*N*-Phenylureido)propyl triethoxysilane was obtained by mixing 3-isocyanatopropyl triethoxysilane (0.50 mL) with aniline (0.25 mL) in a screw-cap vial and stirring at room temperature for 1 h. Simultaneously, CTAB (1.02 g), NaOH (2 M, 3.5 mL), and H_2O (480 mL) were mixed and vigorously stirred in a round-bottom flask at 80 °C for 1 h. To the resulting clear solution, TEOS (5.0 mL) was added dropwise followed immediately by addition of the 3-(*N*-phenylureido)-propyl triethoxysilane, forming a cream-colored precipitate. The product was isolated by hot filtration, washed with copious amounts of water and methanol, and dried under vacuum at room temperature to yield the surfactant-containing PUP-functionalized MSN, which we shall refer to as **dry-S-MSN**. Part of the material was subjected to surfactant extraction by refluxing with methanol in a Soxhlet apparatus. The resulting surfactant-free solid product, with the PUP molecules attached, was dried under vacuum at room temperature, and will be referred to as **dry-Ex-MSN**.

The surface area and pore size distribution of **dry-Ex-MSN** were measured by nitrogen sorption isotherms using a Micromeritics Tristar analyzer, and calculated by the Brunauer−Emmett−Teller (BET) and Barrett−Joyner−Halenda (BJH) methods. The sample displayed a type IV isotherm typical of mesoporous materials (Figure S1, Supporting Information) with a surface area of 518 $m^2.g^{-1}$, a pore volume V_p = 0.59 $cm^3.g^{-1}$ and a narrow pore size distribution with a sharp maximum centered at 3.7 nm (Figure S2, Supporting Information). Small-angle powder X-ray diffraction patterns were obtained with a Rigaku Ultima IV diffractometer using a Cu target at 40 kV and 44 mA. The Cu Kβ radiation was removed using a monochromator. The pattern showed 100, 110, 200, and 210 reflections corresponding to a 2D hexagonal array of mesopores characteristic of MCM-41 type materials (Figure S3, Supporting Information). The particle size distribution of MSN was determined by dynamic light scattering in a Malvern Nano Zetasizer ZS90. The samples were prepared by suspending the particles in ethanol (100 $\mu g \cdot mL^{-1}$) and sonicating in a bath ultrasonicator for 1 min. The analysis indicated that 85% of the particles had hydrodynamic diameters between 140 and 460 nm with the maximum of the distribution centered at 220 nm (Figure S4, Supporting Information). A transmission electron microscopy (TEM) picture was obtained with a Tecnai G2 F20 electron microscope operating at 200 kV (Figure 1a).

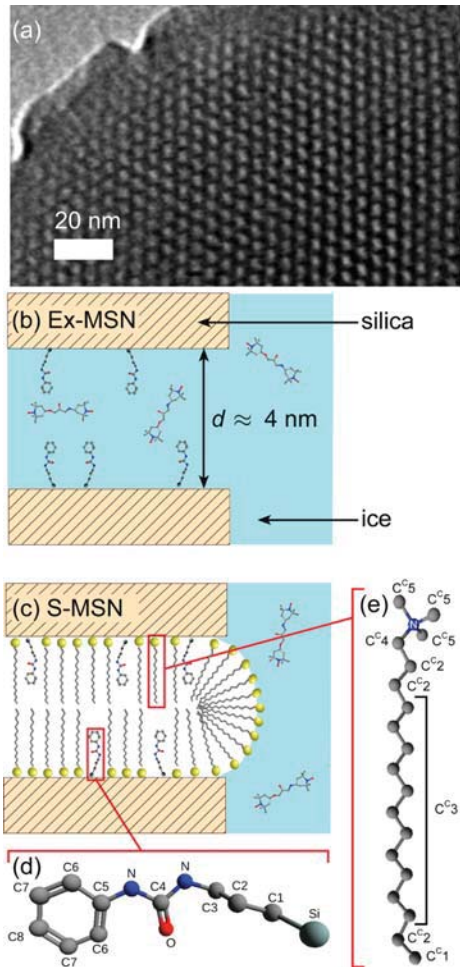

Figure 1. (a) Transmission electron micrograph of a **dry-Ex-MSN**. (b) Sketch of **Ex-MSN** where the aqueous solution of TOTAPOL can penetrate into the mesopores. (c) Sketch of **S-MSN** functionalized by covalently bound (PUP) and impregnated with the surfactant (CTAB), so that the aqueous TOTAPOL solution cannot penetrate into the mesopores. (d, e) Numbering of carbon atoms in 3-(*N*-phenylureido)propyl (PUP) and cetyltrimethylammonium bromide (CTAB).

2.2. Sample Preparation for DNP Measurements. The samples for solid-state DNP NMR experiments were prepared at room temperature by impregnating **dry-Ex-MSN** and **dry-S-MSN** with a 12.5-mM solution of TOTAPOL in H_2O without cryoprotectant such as glycerol. Water was preferred over other solvents because it does not give any signals in ^{13}C and ^{29}Si NMR. After saturating for a day, the materials were centrifuged for 5 min at 12110 × g to remove excess solution. The impregnated samples are referred to as **Ex-MSN** and **S-MSN**, and are schematically represented in Figure 1, parts b and c, respectively. A matching pair of samples, designated **Ex-MSN-90/10** and **S-MSN-90/10**, was prepared in the same way using 12.5-mM TOTAPOL dissolved in a 90/10 (w/w) mixture of ^2H_2O and H_2O. The concentration of TOTAPOL in all samples was measured on a Bruker BioSpin ELEXYS E580E X-band EPR spectrometer with 2 mW of microwave power, 0.5 G amplitude modulation, and 4-amino-TEMPO as a reference. Slow motion spectra were simulated with the EasySpin[29] program to extract the hyperfine couplings with ^{14}N nucleus, the dipolar interaction between the two electrons of TOTAPOL, and the rotation correlation time, τ_c. Longitudinal electron relaxation times (T_{1e}) were measured at 90 K using an inversion recovery sequence.

2.3. DNP Measurements.

The solid-state NMR experiments were performed at 9.4 T (400 MHz for ^1H) on a Bruker BioSpin Avance III DNP NMR spectrometer equipped with a triple resonance $^1H/X/Y$ 3.2-mm low-temperature (ca. 100 K) MAS probe and a 263-GHz gyrotron delivering a continuous microwave power of about 5 W.[18] The samples were placed in 3.2-mm sapphire rotors since this material is nearly transparent to microwaves at 263 GHz.[30] The microwave irradiation is highly nonuniform over the sample.[31] However, the regions experiencing high microwave magnetic fields have spatial dimensions ($\sim$100 μm) that are much larger than the MSN diameters (<1 μm).[28] Therefore, we can assume that (i) the regions irradiated by microwave have the same chemical composition than the whole sample and (ii) the DNP enhancement is uniform at the outer surface of S-MSN (see section 3.5).

The $^1H \rightarrow {}^{13}C$ and $^1H \rightarrow {}^{29}Si$ CPMAS spectra were acquired with the microwave irradiation "on" and "off" at a spinning frequency ν_r = 10 kHz and the temperature $T \sim 100$ K, which was controlled using a Bruker BioSpin low-temperature cooling system. The ^1H 90° pulse duration was 2.5 μs and the CP contact time was 1 ms. During the CP transfer, the ^1H RF field amplitude was linearly ramped from 53 to 59 kHz, whereas the RF amplitude was constant and equal to 46 kHz for both ^{13}C and ^{29}Si. SPINAL-64[32] proton decoupling was applied during the acquisition with an ^1H RF field amplitude of 95 kHz. The ^{13}C and ^{29}Si spectra typically resulted from the accumulation of 512 to 1024 transients with a recovery delay of 1.3 s, leading to total experimental times of 11 to 22 min. The ^{13}C and ^{29}Si chemical shifts were referenced with respect to tetramethylsilane (TMS) at 0 ppm.

3. RESULTS AND DISCUSSION

3.1. EPR Spectra of Ex-MSN and S-MSN.

Figure 2 displays the experimental EPR spectra of **Ex-MSN** and **S-MSN** taken at room temperature and the best-fit simulations. The spectra yield the overall concentration of TOTAPOL, c_m, of about 9.5 mM in both samples. The correlation times, τ_c = 410 and 63 ns for **Ex-MSN** and **S-MSN**, respectively, confirm that in **Ex-MSN** the TOTAPOL molecules are confined within the mesopores or even adsorbed on the silica surface,[12] whereas in **S-MSN** their motions are less restricted in the interparticle voids. Furthermore, the maximum coupling is 7 MHz larger for **Ex-MSN** than **S-MSN**. This coupling is equal to $2A_{zz} + D$, where A_{zz} is the secular hyperfine coupling constant with ^{14}N nucleus and D is the dipolar coupling constant between the two unpaired electrons of TOTAPOL. The EasySpin simulations indicate that the 7 MHz change in the maximum coupling stems from a change in the D value. Therefore, the distance between the two electrons is shorter in **Ex-MSN** than in **S-MSN**, which indicates a change in the conformation of TOTAPOL between the two samples. This change may be related to the adsorption of TOTAPOL on the mesopore surface in **Ex-MSN**. The T_{1e} values of TOTAPOL in **Ex-MSN** and **S-MSN** are identical and equal to 23 μs at 90 K.

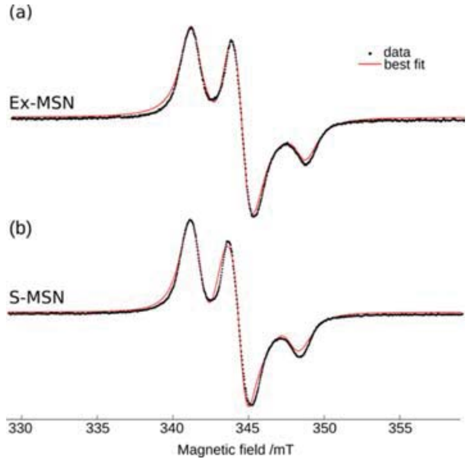

Figure 2. X-band continuous wave EPR spectra of (a) **Ex-MSN** and (b) **S-MSN** recorded at room temperature with the corresponding best fit.

3.2. ^{13}C and ^{29}Si Spectra of Ex-MSN and S-MSN.

The conventional and DNP-enhanced $^1H \rightarrow {}^{13}C$ and $^1H \rightarrow {}^{29}Si$ CPMAS spectra of **Ex-MSN** and **S-MSN** are shown in Figure 3. The ^{13}C resonances are assigned to carbon atoms of PUP and CTAB (see numbering in Figure 1). The methoxy groups (−OMe) result from washing the sample with methanol. The signals C^C3 and C^C4 in (a) represent the methylene groups in residual CTAB molecules remaining in the pores after the extraction. Other carbon resonances in CTAB, which are clearly visible in (b), are dominated in (a) by the signals of PUP. The ^{29}Si spectra feature the expected broad lines ascribed to silicon sites Q^2 ($(SiO)_2Si(OX)_2$), Q^3 ($(SiO)_3SiOX$), Q^4 ($(SiO)_4Si$), T^2 ($(SiO)_2SiROX$ with R = PUP, X = H or Me), and T^3 ($(SiO)_3SiR$ with R = PUP). No line broadening was observed in the DNP-enhanced spectra of **Ex-MSN** and **S-MSN** because in both samples the CP process is only effective for ^{13}C and ^{29}Si nuclei that are not directly affected by the unpaired electrons of TOTAPOL.[33]

Also shown in Figure 3 are the enhancement factors, $\varepsilon_{on/off}(^{13}C, {}^{29}Si)$, defined as the ratio of signal intensities with and without microwave irradiation. Furthermore, we determined that in both samples the ^1H polarization build-up time with microwave irradiation, $\tau_{DNP}(^1H)$, was identical to the ^1H longitudinal relaxation time, $T_1(^1H)$. We measured $\tau_{DNP}(^1H) = T_1(^1H)$ = 1.1 and 0.8 s for **Ex-MSN** and **S-MSN,** respectively. The fact that $\tau_{DNP}(^1H)$ is equal to $T_1(^1H)$ was observed in other systems[22,34,35] when using biradical polarizing agents such as TOTAPOL. The cross-effect (CE) DNP mechanism,[23,36] which prevails for biradicals, leads to $\tau_{DNP}(^1H) \approx T_1(^1H)$,[37] whereas $\tau_{DNP}(^1H) < T_1(^1H)$ is expected for the DNP mechanisms involving the so-called thermal mixing or solid effects.[34,37] Since the evolution of proton polarization with and without microwave irradiation is governed by the same time constant ($\tau_{DNP}(^1H) = T_1(^1H)$), the resulting CPMAS signal exhibits the same dependence with respect to the recovery delay, τ_{RD}, between two successive experiments. Hence, the

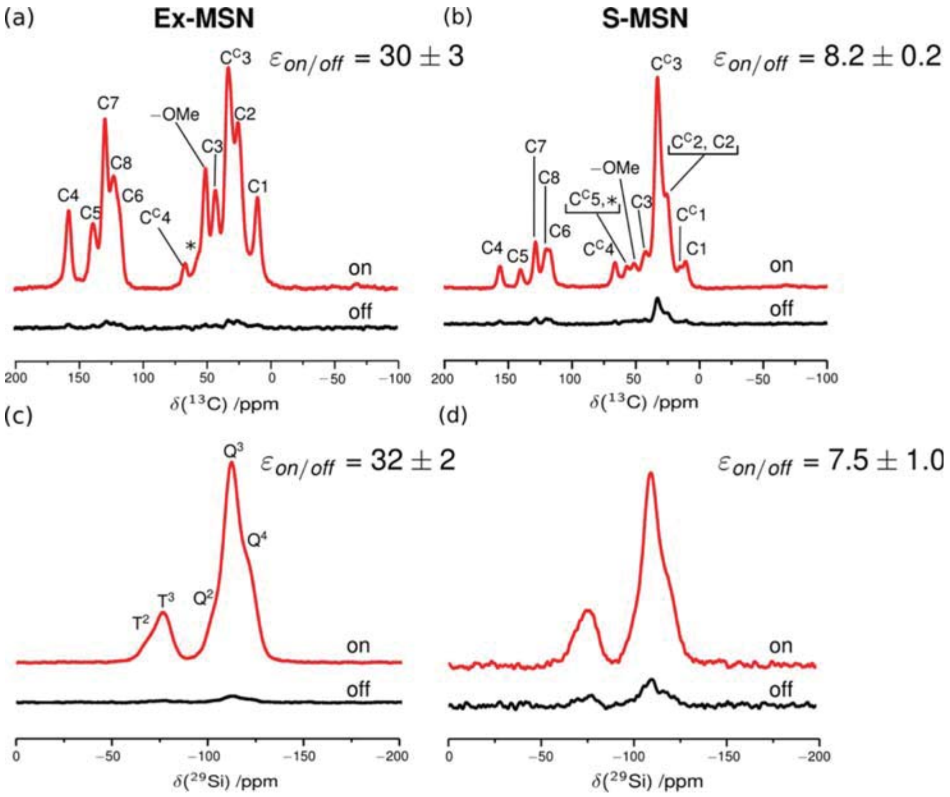

Figure 3. Natural abundance CPMAS spectra of (a, b) ^{13}C and (c, d) ^{29}Si in (a, c) **Ex-MSN** and (b, d) **S-MSN** impregnated with a 12.5 mM TOTAPOL solution in H_2O. In parts a and b, the peaks labeled with ∗ correspond to spinning sidebands. In each subfigure, the DNP-enhanced and standard spectra are labeled "on" and "off", respectively. The spectra were acquired at a temperature of about 100 K using 3.2 mm sapphire rotors spinning at 10 kHz, using a Bruker BioSpin Avance III NMR spectrometer operating at 9.4 T and equipped with a 263 GHz gyrotron. Additional experimental parameters are given in section 2.3.

enhancement factor $\varepsilon_{on/off}$ does not depend on τ_{RD}. To maximize the sensitivity, the spectra of Figure 3 were recorded with $\tau_{RD} \approx 1.3\ T_1(^1\text{H})$.[38]

All ^{13}C signals of **Ex-MSN** show the same enhancement $\varepsilon_{on/off}(^{13}\text{C}) = 30 \pm 3$. Similar ratios $\varepsilon_{on/off}(^{29}\text{Si}) = 32 \pm 2$ were obtained for all ^{29}Si signals. Since the TOTAPOL cannot penetrate into the mesopores, it is not surprising that **S-MSN** exhibits smaller enhancements, but the ratios $\varepsilon_{on/off}(^{13}\text{C}) = 8.2 \pm 0.2$ and $\varepsilon_{on/off}(^{29}\text{Si}) = 7.5 \pm 1.0$ are all the more remarkable. The large experimental errors stem from the low signal-to-noise ratio of the spectra obtained without microwave irradiation (see section II of the Supporting Information). The overall enhancements are even higher if one compares (i) the signal amplitudes of **Ex-MSN** amplified by DNP at 100 K with (ii) the conventional CPMAS spectrum of **dry-Ex-MSN** without DNP at room temperature under otherwise similar conditions. In a separate study,[39] this comparison was made per scan and for a given overall experimental time, after proper adjustments for the Boltzmann factor, paramagnetic quenching and effects of $T_1(^1\text{H})$ relaxation.

In the ensuing discussion, we first consider the enhancements $\varepsilon_{on/off}(^{13}\text{C})$ and $\varepsilon_{on/off}(^{29}\text{Si})$ in **Ex-MSN** and estimate the polarization losses during ^{1}H spin diffusion (section 3.3). In section 3.4, we present an estimate of the polarization profile within **S-MSN** based on one-dimensional ^{1}H spin diffusion in the mesopores blocked by CTAB, which accounts for the observed enhancement ratios $\varepsilon_{on/off}$. Finally, in section 3.5, we discuss the effect of diluting H_2O with ^2H_2O.

3.3. Polarization Transfer in Ex-MSN.

The spectra in Figure 3a,c show that polarization transfer by DNP enhances the ^{13}C and ^{29}Si NMR signals of **Ex-MSN** impregnated with a TOTAPOL solution by more than 1 order of magnitude.

The similarity between the $\varepsilon_{on/off}$ ratios for ^{13}C and ^{29}Si is to be expected, since they both draw their polarization from the ^{1}H bath, and polarization losses must be due to relaxation during ^{1}H spin diffusion. These losses can be estimated by assuming that microwave irradiation transfers the polarization of the unpaired electrons (via electron−proton coupling) to the ^{1}H nuclei located close to the radicals, just outside the spin diffusion barrier, r_d.[40] The DNP-enhanced ^{1}H polarization is then distributed through the glassy solvent by spin diffusion,[20,25,41] which is very efficient in **Ex-MSN** as manifested by the absence of line narrowing for increasing τ_{RD} and the monoexponential polarization build-up.[21] (In the case of vanishing spin diffusion, as in direct DNP of ^{13}C or ^{29}Si nuclei, line narrowing is usually observed upon increasing τ_{RD}, as well as stretched exponential buildup of polarization.[21,42]) We also note that at $\nu_r = 10$ kHz, ^{1}H spin diffusion is effective between water and silanol protons, since the differences in isotropic chemical shifts between these sites are much smaller than the effective $^1\text{H}-^1\text{H}$ dipolar couplings.

The pores of **Ex-MSN** contain a three-dimensional network of dipolar-coupled protons. However, for the sake of simplicity, we consider a linear chain of protons with the same isotropic chemical shift (Figure 4a) under steady-state conditions to model the ^{1}H spin diffusion between two adjacent TOTAPOL

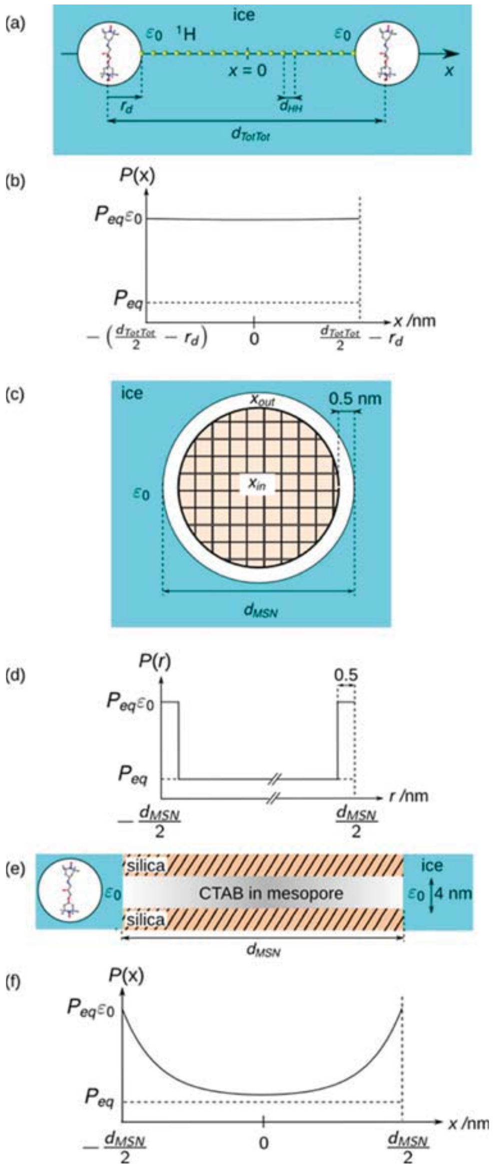

Figure 4. (a, c, e) Models of the samples; (b, d, f) corresponding proton polarization profiles. (a, b) Model and profile for a linear chain of protons between two TOTAPOL molecules in a frozen glassy solvent. The white spheres in part a represent the spin diffusion barriers surrounding the TOTAPOL molecules. The protons located inside the spin diffusion barrier are not shown, whereas small green spheres represent those located outside. (c, d) Model and profile for DNP enhancements in the 'outer crust' of the S-MSN (scenario A1). The white sphere represents the region located closer than 0.5 nm from the outer surface. The individual mesopores are not depicted in part c. In part d, the absolute value of coordinate *r* corresponds to the distance from the center of the S-MSN. (e, f) Model and profile for pseudo-one-dimensional spin diffusion along the mesopores of S-MSN (scenario A2). The schemes are not to scale. The symbols are defined in the text.

molecules in **Ex-MSN** mesopores. Assuming that $x = 0$ halfway between two TOTAPOL molecules, the edges of the spin diffusion barrier are located at $x = \pm (d_{\mathrm{TotTot}}/2 - r_{\mathrm{d}})$, where d_{TotTot} is the average distance between two TOTAPOL molecules. At these edges, the ^{1}H polarization is equal to a constant value $P_{\mathrm{eq}}\varepsilon_0$, where P_{eq} is the ^{1}H polarization at thermal equilibrium and ε_0 is the steady-state enhancement produced by microwave irradiation near the diffusion barrier. With these boundary conditions, it can be shown that the polarization $P(x)$ of the protons between the two diffusion barriers is given by[25]

$$P(x) = P_{eq}\varepsilon_0 \cosh\left(\frac{x}{\sqrt{DT_1(^1H)}}\right)/\cosh\left(\frac{d_{TotTot} - 2r_d}{2\sqrt{DT_1(^1H)}}\right) \tag{1}$$

where D is the diffusion constant and $T_1(^1H)$ is the proton spin–lattice relaxation time.

To quantify the polarization $P(0)$ in **Ex-MSN** where the radicals can penetrate into the mesopores, we estimate d_{TotTot} and the average ^{1}H–^{1}H distance d_{HH}. The average value of d_{TotTot}, in nm, is given by

$$d_{TotTot} = (c_m 10^{-27} N_{\mathrm{A}})^{-1/3} \tag{2}$$

where N_{A} is Avogadro's number and the overall TOTAPOL concentration c_m = 9.5 mM. Equation 2 yields d_{TotTot} = 5.6 nm. The average ^{1}H–^{1}H distance d_{HH} in the frozen (undeuterated) disordered water, also in nm, can be estimated as follows:

$$d_{HH} = \left[2\frac{\rho_{H_2O} n_a(^1\mathrm{H}) x(\mathrm{H_2O}) N_{\mathrm{A}}}{M(\mathrm{H_2O})} 10^{-25}\right]^{-1/3} \tag{3}$$

where the factor of 2 accounts for the number of protons in H_2O molecule, ρ_{H_2O} is the density of frozen disordered water within the **Ex-MSN** mesopores, $n_a(^1\mathrm{H})$ = 99.988% is the ^{1}H natural isotopic abundance, $x(H_2O)$ is the molar fraction of H_2O (in %) in the frozen solution and $M(\mathrm{H_2O})$ is the molar mass of water. The density of frozen water within the mesopore is identical to that of common hexagonal ice, ρ_{H_2O} = 0.93 g·cm^{-3}.[43,44] For $x(\mathrm{H_2O})$ = 100, eq 3 yields d_{HH} = 0.25 nm.

We can now evaluate the radius of the spin diffusion barrier r_d and the diffusion constant D in eq 1. Since in the MSN the longitudinal electron relaxation times, $T_{1\mathrm{e}}$, are shorter than the transverse ^{1}H relaxation times, $T_2(^1\mathrm{H})$, r_d is given by[12,40]

$$r_d \approx \left[2S\frac{\gamma_e}{\gamma_H}B_S\left(\frac{S\hbar\gamma_e B_0}{k_{\mathrm{B}}T}\right)\right]^{1/4} d_{HH} \tag{4}$$

where S is the effective quantum spin number for electrons in TOTAPOL, γ_{e} and γ_H are the gyromagnetic ratios of electrons and ^{1}H nuclei, B_S is the spin-dependent Brillouin function, $\hbar$ is the reduced Planck constant and k_{B} is the Boltzmann constant. The spin S is equal to 1/2 or 1 depending on the strength and the type of coupling between the two unpaired electrons in the TOTAPOL biradical. For **Ex-MSN**, eq 4 yields $r_d \approx$ 0.6 nm for S = 1/2 and 0.8 nm for S = 1.

The average dipolar coupling constant, b_{HH}, in rad·s^{-1} between two ^{1}H nuclei at a distance d_{HH} is given by

$$\frac{b_{HH}}{2\pi} = -\frac{\mu_0}{4\pi}\frac{{\gamma_H}^2\hbar}{{d_{HH}}^3} \tag{5}$$

where μ_0 is the vacuum permeability and all physical quantities are expressed in SI units. In a spinning sample, the corresponding effective dipolar coupling ν_{d} expressed in Hz is[25]

$$\nu_d = \frac{{b_{HH}}^2}{4\pi^2\nu_r} \tag{6}$$

The spin diffusion coefficient, D, between ^{1}H nuclei can be estimated as[24,25]

$$D = d_{HH}{}^2 \pi \nu_d \tag{7}$$

Using eqs 3, 5, 6, and 7, we obtain $D = 1.1 \times 10^3$ nm^2·s^{-1} for **Ex-MSN**, which is similar to the diffusion constants reported for fully protonated peptide nanocrystals.[25]

Returning to eq 1, we can use the above values of D, d_{TotTot}, and r_d to evaluate the polarization loss $P(0)/P_{eq}\varepsilon_0$ due to relaxation during ^{1}H spin diffusion. For **Ex-MSN**, where $T_1(^1\text{H}) = 1.1$ s, this loss is below 1%. Thus, the polarization has a very homogeneous profile throughout the sample (Figure 4b). Consequently, the enhancement factor $\varepsilon_{on/off}$, which is proportional to the average ^{1}H polarization, differs from ε_0 enhancement near spin diffusion barrier by less than 1% in **Ex-MSN**. We can conclude that losses in polarization resulting from ^{1}H spin diffusion are negligible when the TOTAPOL biradicals can penetrate into the mesopores. Furthermore, the uniform ^{1}H polarization throughout the sample entails identical ^{1}H polarizations near various ^{13}C and ^{29}Si nuclei, and hence identical $\varepsilon_{on/off}$ enhancements for ^{13}C and ^{29}Si CPMAS spectra, as observed in Figure 3, parts a and c.

3.4. Polarization Transfer in S-MSN. As already noted, long-range polarization transfer by DNP can also enhance ^{13}C and ^{29}Si NMR signals in **S-MSN**, despite the fact that the surfactant inhibits the penetration of the radicals into the mesopores (Figure 3b,d). The ^{13}C NMR spectra of **S-MSN** are dominated by a resonance at 30 ppm representing the C^C3 sites in CTAB. This demonstrates the presence of the surfactant within the mesopores, which inhibits the access of TOTAPOL, relegating it primarily to the interparticle voids. Despite the fact that the particles are several hundreds of nm across (Figure S4, Supporting Information), the ^{13}C and ^{29}Si NMR signals of **S-MSN** acquired with microwave irradiation are enhanced by surprisingly large factors $\varepsilon_{on/off}(^{13}\text{C}) = 8.2$ and $\varepsilon_{on/off}(^{29}\text{Si}) = 7.5$, respectively. In the following discussion, we show that this observation cannot be explained by a DNP enhancement of nuclei located within the ~0.5 nm thick outer layer of the MSN, but must result from spin diffusion of the DNP-enhanced proton polarization from the surrounding frozen solvent into the mesopores.

Assuming that the surfactant effectively blocks the access of TOTAPOL into the mesopores, we can calculate the distribution of DNP-enhanced ^{1}H polarization under two antithetical scenarios: (A1) no ^{1}H spin diffusion within the mesopores of **S-MSN**; (A2) ^{1}H spin diffusion through the mesopores of the **S-MSN** owing to the presence of protonated CTAB molecules.

The first scenario A1 implies that DNP can only polarize ^{1}H nuclei located outside of the nanoparticles (Figure 4c). Since the polarization transfer from ^{1}H to ^{13}C or ^{29}Si is conveyed by CP, this is limited to at most 0.5 nm in rigid spin systems, since we have used short contact times $\tau_{CP} = 1$ ms.[45] Therefore, the ^{13}C or ^{29}Si nuclei can be divided into two classes: (i) the "outer" nuclei, located at a distance less than 0.5 nm from the protons residing at the outer surface of the nanoparticles, benefit from DNP-enhanced polarization in CPMAS experiments when the microwave field is switched on, and (ii) the "inner" nuclei hidden in the depth of the mesopores, which are located at distance greater than 0.5 nm from the protons on the outer surface, are not enhanced by DNP (Figure 4d). If the MSN particles are assumed to be spherical with a diameter d_{MSN}, the molar fraction of 'outer' ^{13}C or ^{29}Si nuclei x_{out} is given by

$$x_{out} = 4\pi\left(\frac{d_{MSN}}{2}\right)^2 0.5 \Big/ \left[\frac{4\pi}{3}\left(\frac{d_{MSN}}{2}\right)^3\right] = \frac{3}{d_{MSN}} \tag{8}$$

while the fraction of 'inner' nuclei is $x_{\text{in}} = 1 - x_{\text{out}}$. The expected enhancement is thus

$$\begin{aligned}\varepsilon_{on/off}(\text{S-MSN}) &= \frac{x_{in}P_{eq} + x_{out}P_{eq}\varepsilon_{on/off}(\text{Ex-MSN})}{x_{in}P_{eq} + x_{out}P_{eq}} \\ &= 1 + x_{out}[\varepsilon_{on/off}(\text{Ex-MSN}) - 1]\end{aligned} \tag{9}$$

where $\varepsilon_{on/off}$(S-MSN) and $\varepsilon_{on/off}$(Ex-MSN) are the DNP enhancements for **S-MSN** and **Ex-MSN**, respectively. If $\varepsilon_{on/off}$(Ex-MSN) = 31, which is the average of the $\varepsilon_{on/off}(^{13}\text{C})$ and $\varepsilon_{on/off}(^{29}\text{Si})$ ratios measured in **Ex-MSN** (Figure 3a, c), eqs 8 and 9 yield $1.2 < \varepsilon_{on/off}(\text{S-MSN}) < 1.4$ for $400 > d_{MSN} > 200$ nm. Moreover, these values are upper estimates for $\varepsilon_{on/off}$(S-MSN), considering the short-range of CP transfers. Clearly, these estimates are not consistent with the experimental results shown in Figure 3b, d.

We now investigate the validity of scenario A2. In **S-MSN**, the mesopores are blocked so that TOTAPOL cannot enter the mesopores and the DNP-enhanced ^{1}H polarization can be only distributed into the bulk of the **S-MSN** via spin diffusion among the protons located in the mesopores. Again, these protons form a three-dimensional network. However, since the length of the pores is larger by about 2 orders of magnitude than their radius we can safely assume that that the penetration of DNP-enhanced ^{1}H polarization into **S-MSN** is dominated by ^{1}H spin diffusion along the pore axis. Similar pseudo-one-dimensional models have already been applied to the analysis of DNP-enhanced ^{1}H polarization in heterogeneous polymer blends or peptide mesocrystals.[24,25] To estimate the polarization losses within the mesopores, we disregard the diffusion barrier, which is much smaller than the average particle size ($r_d \approx 1$ nm $\ll d_{MSN} \approx 200-400$ nm) and assume that the ^{1}H polarization at the outer surface of the nanoparticles is identical to that at the spin diffusion barrier, $P_{eq}\varepsilon_0$. If $x = 0$ at the nanoparticle's center, we can write

$$P\left(-\frac{d_{MSN}}{2}\right) = P\left(\frac{d_{MSN}}{2}\right) = P_{eq}\varepsilon_0 \tag{10}$$

The average ^{1}H−^{1}H distance, d_{HH}, in the frozen surfactant CTAB trapped in the mesopores is calculated to be

$$d_{HH} = \left[42\frac{\rho_{CTAB} n_a(^1H) N_A}{M(CTAB)} 10^{-25}\right]^{-1/3} = 0.23 \text{ nm} \tag{11}$$

where the factor of 42 represents the number of protons per CTAB molecule, $\rho_{\text{CTAB}} = 1.17$ g.cm^{-3} is the density of CTAB,[46] and $M(\text{CTAB}) = 364.45$ g·mol^{-1} is the molar mass of CTAB. Using eqs 5, 6 and 7, we obtain a spin diffusion coefficient $D = 1.6 \times 10^3$ nm^2·s^{-1} for **S-MSN**, which is slightly larger than the value $D = 1.1 \times 10^3$ nm^2·s^{-1} calculated from eq 7 for **Ex-MSN**. In the steady state, the pseudo-one-dimensional model leads to a distribution of ^{1}H polarization in the mesopores given by an expression similar to eq 1,

$$P(x) = P_{eq}\varepsilon_0 \cosh\left(\frac{x}{\sqrt{DT_1(^1H)}}\right) \Big/ \cosh\left(\frac{d_{MSN}}{2\sqrt{DT_1(^1H)}}\right) \tag{12}$$

where $T_1(^1\mathrm{H}) = 0.8$ s for **S-MSN**. According to the above equation, we have $0.008 < P(0)/(P_{eq}\varepsilon_0) < 0.13$ for $400 > d_{MSN} > 200$ nm. In contrast to **Ex-MSN**, the ^{1}H polarization in the center of the surfactant-filled mesopores is strongly reduced compared to that at the outer surface. An expression for the average ^{1}H polarization enhancement in the entire nanoparticle is obtained by integrating $P(x)$ from $x = -d_{MSN}/2$ to $d_{MSN}/2$, which yields[13]

$$\varepsilon_{on/off}(\text{S-MSN}) = \varepsilon_0 \frac{2\sqrt{DT_1(^1H)}}{d_{MSN}} \tanh\left(\frac{d_{MSN}}{2\sqrt{DT_1(^1H)}}\right) \tag{13}$$

According to this model, the $\varepsilon_{\text{on/off}}$(S-MSN) enhancement is only 36% of ε_0 for $d_{MSN} = 200$ nm and 18% of ε_0 for $d_{MSN} = 400$ nm. As previously, no significant difference in the ^{1}H polarization is expected near the ^{29}Si and ^{13}C nuclei, as was indeed observed (Figure 3b, d). These predicted $\varepsilon_{\text{on/off}}$(S-MSN) values are also in very good agreement with the experimental data in Figure 3. Indeed, with an average particle size around $d_{MSN} = 300$ nm (Figure S4, Supporting Information), the $\varepsilon_{\text{on/off}}(^{13}\text{C})$ and $\varepsilon_{\text{on/off}}(^{29}\text{Si})$ ratios measured in **S-MSN** are about 25% of those in **Ex-MSN**. Thus, the signal enhancement observed in **S-MSN** can be rationalized by assuming that the DNP-enhanced ^{1}H magnetization is transported through the mesopores via ^{1}H−^{1}H spin diffusion before being transferred to rare spins through the CP process (scenario A2 according to the model of Figure 4, parts e and f).

3.5. Polarization Transfer in Partially Deuterated Solvents.

The **dry-Ex-MSN** and **dry-S-MSN** samples were impregnated with a 90/10 (w/w) $^2\text{H}_2\text{O}/^1\text{H}_2\text{O}$ mixture, yielding two new samples **Ex-MSN-90/10** and **S-MSN-90/10**. The observed line shapes were similar to those in Figure 3. However, we measured reduced $\varepsilon_{\text{on/off}}(^{13}\text{C}, ^{29}\text{Si})$ ratios (by about a factor of 2) and a slower polarization build-up. This is in agreement with earlier reports on similar materials,[35] but stands in contrast to the studies of small organic molecules or proteins dissolved in partially deuterated solvents, where an increased fraction of deuterium nuclei typically enhances the sensitivity by transferring the electron polarization to a smaller number of remaining ^{1}H nuclei.[18,47,48]

The reduction of $\varepsilon_{\text{on/off}}(^{13}\text{C}, ^{29}\text{Si})$ ratios induced by deuteration in **Ex-MSN-90/10** and **S-MSN-90/10** cannot be due to the reduction of the ^{1}H mole fraction. The ^{1}H concentration in pure $^1\text{H}_2\text{O}$ is about 110 M, and is estimated to be 60 M and 77 M in **Ex-MSN** and **S-MSN**, respectively, due to the presence of a silica scaffold.[28] These values exceed the ^{1}H concentration in samples of organic molecules dispersed in partially deuterated cryoprotectants, such as [$^2\text{H}_8$]-glycerol/$^2\text{H}_2\text{O}/^1\text{H}_2\text{O}$ (60/30/10 w/w/w), where DNP benefits from partial deuteration.[18] Second, the reduction of the $\varepsilon_{\text{on/off}}(^{13}\text{C}, ^{29}\text{Si})$ ratios cannot be foreseen by using eq 7 to calculate the spin diffusion coefficient and extending the analyses in sections 3.3 and 3.4 to a 90/10 mixture of $^2\text{H}_2\text{O}$ and $^1\text{H}_2\text{O}$. Indeed, for **Ex-MSN-90/10** eqs 3-7 yield $d_{HH} = 0.53$ nm, $r_d \approx 1.4$ nm (for $S = 1/2$) or 1.8 nm (for $S = 1$), and $D = 49$ nm$^2\cdot$s^{-1}. Bearing in mind the longer relaxation time $T_1(^1\text{H}) = 1.4$ s in **Ex-MSN-90/10**, we estimate from eq 1 that $P(0)$ and $P_{\text{eq}}\varepsilon_0$ differ by only ∼2%. However, the value $D = 49$ nm$^2\cdot$s^{-1} is an upper bound for proton spin diffusion coefficient since in deuterated solvent, in the absence of ^{2}H decoupling, the dipolar heteronuclear ^{1}H−^{2}H couplings reduce the spectral overlap between ^{1}H spin packets and hence hinder the flip-flop process between the ^{1}H spins.[49,50] The slower proton spin diffusion owing to dipolar ^{1}H−^{2}H couplings should result in difference larger than 2% between $P(0)$ and $P_{\text{eq}}\varepsilon_0$. Furthermore, water is a nonglass-forming solvent and the presence of crystalline domain boundaries can further impede the spin diffusion,[25,51] especially within the interparticle voids. Finally, the $T_1(^1\text{H})$ values in **Ex-MSN-90/10** and **S-MSN-90/10** are considerably shorter than those previously reported in partially deuterated cryoprotectants (about 5 s),[18,22] thereby requiring a higher ^{1}H density to ensure an efficient distribution of the polarization.

4. CONCLUSIONS

We have shown that in samples spinning at the magic angle, DNP can enhance ^{13}C and ^{29}Si signals of nuclei located within the functionalized mesoporous silica nanoparticles, despite the inability of TOTAPOL to penetrate into the mesopores. The DNP enhancements were compared to those obtained for samples where the surfactant had been extracted so that TOTAPOL is free to enter the mesopores. The DNP enhancements in the presence of surfactant were consistent with predictions based on a one-dimensional ^{1}H spin diffusion model. Similar mechanisms can be used to remotely enhance the signals in other organic−inorganic hybrid systems, at distances on the order of the characteristic diffusion length $((DT_1(^1\text{H}))^{1/2})$. The DNP enhancements can in principle be improved by using better biradicals such as bCTbk.[15] DNP thus offers new opportunities for the study of organic−inorganic hybrid materials, including the self-cooperative assembly of surfactants and the properties of catalytic centers.

■ ASSOCIATED CONTENT

Ⓢ Supporting Information

Nitrogen sorption isotherms, pore and particle size distributions, and small-angle X-ray diffraction pattern of **Ex-MSN**, error analysis of the DNP measurements, and estimates of proton concentrations in DNP samples. This material is available free of charge via the Internet at http://pubs.acs.org.

■ AUTHOR INFORMATION

Corresponding Author

*E-mail: (O.L.) olivier.lafon@univ-lille1.fr; (M.P.) mpruski@iastate.edu.

Notes

The authors declare no competing financial interest.

■ ACKNOWLEDGMENTS

This research was supported by the U.S. Department of Energy, Office of Basic Energy Sciences, Division of Chemical Sciences, Geosciences, and Biosciences through the Ames Laboratory. The Ames Laboratory is operated for the U.S. Department of Energy by Iowa State University under Contract No. DE-AC02-07CH11358. This research was also supported by the University of Lille 1, the ENSCL, the ENS, the University Pierre et Marie Curie, French CNRS, French Minister of Science, FR-3050, the Swiss National Foundation (FNS), the Swiss Commission for Technology and Innovation (CTI), Region Nord/Pas-de-Calais, Europe (FEDER), Bruker BioSpin, Contract No. ANR-2010-JCJC-0811-01 and MPNS COST Action EUROHyperPOL TD1103.

REFERENCES

(1) Shopsowitz, K. E.; Qi, H.; Hamad, W. Y.; MacLachlan, M. J. *Nature* **2010**, *468*, 422−425.

(2) Chen, Z.; Jiang, Y.; Dunphy, D. R.; Adams, D. P.; Hodges, C.; Liu, N.; Zhang, N.; Xomeritakis, G.; Jin, X.; Aluru, N. R.; et al. *Nat. Mater.* **2010**, *9*, 667−675.

(3) Wan, Y.; Zhao, D. *Chem. Rev.* **2007**, *107*, 2821−2860.

(4) Polshettiwar, V.; Cha, D.; Zhang, X.; Basset, J. M. *Angew. Chem., Int. Ed.* **2010**, *49*, 9652−9656.

(5) Folliet, N.; Roiland, C.; Begu, S.; Aubert, A.; Mineva, T.; Goursot, A.; Selvaraj, K.; Duma, L.; Tielens, F.; Mauri, F.; et al. *J. Am. Chem. Soc.* **2011**, *133*, 16815−16827.

(6) Epping, J. D.; Chmelka, B. F. *Curr. Opin. Colloid Interface Sci.* **2006**, *11*, 81−117.

(7) Blanc, F.; Coperet, C.; Lesage, A.; Emsley, L. *Chem. Soc. Rev.* **2008**, *37*, 518−526.

(8) Mao, K.; Kobayashi, T.; Wiench, J. W.; Chen, H.-T.; Tsai, C.-H.; Lin, V. S. Y.; Pruski, M. *J. Am. Chem. Soc.* **2010**, *132*, 12452−12457.

(9) Kobayashi, T.; Mao, K.; Wang, S.-G.; Lin, V. S. Y.; Pruski, M. *Solid State Nucl. Magn. Reson.* **2011**, *39*, 65−71.

(10) Lesage, A.; Lelli, M.; Gajan, D.; Caporini, M. A.; Vitzthum, V.; Mieville, P.; Alauzun, J.; Roussey, A.; Thieuleux, C.; Mehdi, A.; et al. *J. Am. Chem. Soc.* **2010**, *132*, 15459−15461.

(11) Lelli, M.; Gajan, D.; Lesage, A.; Caporini, M. A.; Vitzthum, V.; Mieville, P.; Heroguel, F.; Rascon, F.; Roussey, A.; Thieuleux, C.; et al. *J. Am. Chem. Soc.* **2011**, *133*, 2104−2107.

(12) Lafon, O.; Rosay, M.; Aussenac, F.; Lu, X.; Trebosc, J.; Cristini, O.; Kinowski, C.; Touati, N.; Vezin, H.; Amoureux, J.-P. *Angew. Chem., Int. Ed.* **2011**, *50*, 8367−8370.

(13) Rossini, A. J.; Zagdoun, A.; Lelli, M.; Canivet, J.; Aguado, S.; Ouari, O.; Tordo, P.; Rosay, M.; Maas, W. E.; Coperet, C.; et al. *Angew. Chem., Int. Ed.* **2012**, *51*, 123−127.

(14) Zagdoun, A.; Rossini, A. J.; Gajan, D.; Bourdolle, A.; Ouari, O.; Rosay, M.; Maas, W. E.; Tordo, P.; Lelli, M.; Emsley, L.; et al. *Chem. Commun.* **2012**, *48*, 654−656.

(15) Zagdoun, A.; Casano, G.; Ouari, O.; Lapadula, G.; Rossini, A. J.; Lelli, M.; Baffert, M.; Gajan, D.; Veyre, L.; Maas, W. E.; et al. *J. Am. Chem. Soc.* **2012**, *134*, 2284−2291.

(16) Hall, D. A.; Maus, D. C.; Gerfen, G. J.; Inati, S. J.; Becerra, L. R.; Dahlquist, F. W.; Griffin, R. G. *Science* **1997**, *276*, 930−932.

(17) Becerra, L. R.; Gerfen, G. J.; Temkin, R. J.; Singel, D. J.; Griffin, R. G. *Phys. Rev. Lett.* **1993**, *71*, 3561−3564.

(18) Rosay, M.; Tometich, L.; Pawsey, S.; Bader, R.; Schauwecker, R.; Blank, M.; Borchard, P. M.; Cauffman, S. R.; Felch, K. L.; Weber, R. T.; et al. *Phys. Chem. Chem. Phys.* **2010**, *12*, 5850−5860.

(19) Lee, D.; Takahashi, H.; Thankamony, A. S. L.; Dacquin, J.-P.; Bardet, M.; Lafon, O.; De Paepe, G. *J. Am. Chem. Soc.* **2012**, *134*, 18491−18494.

(20) Rossini, A. J.; Zagdoun, A.; Hegner, F.; Schwarzwalder, M.; Gajan, D.; Coperet, C.; Lesage, A.; Emsley, L. *J. Am. Chem. Soc.* **2012**, *134*, 16899−16908.

(21) Lafon, O.; Lilly Thankamony, A. S.; Rosay, M.; Aussenac, F.; Lu, X.; Trebosc, J.; Bout-Roumazeilles, V.; Vezin, H.; Amoureux, J. P. *Chem. Commun.* 2012, in press; doi: 10.1039/C2CC36170A

(22) Hu, K.-N.; Song, C.; Yu, H.-H.; Swager, T. M.; Griffin, R. G. *J. Chem. Phys.* **2008**, *128*, 052302.

(23) Song, C.; Hu, K.-N.; Joo, C.-G.; Swager, T. M.; Griffin, R. G. *J. Am. Chem. Soc.* **2006**, *128*, 11385−11390.

(24) Afeworki, M.; Schaefer, J. *Macromolecules* **1992**, *25*, 4092−4096.

(25) van der Wel, P. C. A.; Hu, K.-N.; Lewandowski, J.; Griffin, R. G. *J. Am. Chem. Soc.* **2006**, *128*, 10840−10846.

(26) Huh, S.; Wiench, J. W.; Yoo, J. C.; Pruski, M.; Lin, V. S. Y. *Chem. Mater.* **2003**, *15*, 4247−4256.

(27) Slowing, I. I.; Trewyn, B. G.; Lin, V. S. Y. *J. Am. Chem. Soc.* **2007**, *129*, 8845−8849.

(28) See Supporting Information.

(29) Stoll, S.; Schweiger, A. *J. Magn. Reson.* **2006**, *178*, 42−55.

(30) Barnes, A. B.; De Paepe, G.; van der Wel, P. C. A.; Hu, K. N.; Joo, C. G.; Bajaj, V. S.; Mak-Jurkauskas, M. L.; Sirigiri, J. R.; Herzfeld, J.; Temkin, R. J.; et al. *Appl. Magn. Reson.* **2008**, *34*, 237−263.

(31) Nanni, E. A.; Barnes, A. B.; Matsuki, Y.; Woskov, P. P.; Corzilius, B.; Griffin, R. G.; Temkin, R. J. *J. Magn. Reson.* **2011**, *210*, 16−23.

(32) Fung, B. M.; Khitrin, A. K.; Ermolaev, K. *J. Magn. Reson.* **2000**, *142*, 97−101.

(33) Lange, S.; Linden, A. H.; Akbey, U.; Franks, W. T.; Loening, N. M.; van Rossum, B.-J.; Oschkinat, H. *J. Magn. Reson.* **2012**, *216*, 209−212.

(34) Vitzthum, V.; Borcard, F.; Jannin, S.; Morin, M.; Mieville, P.; Caporini, M. A.; Sienkiewicz, A.; Gerber-Lemaire, S.; Bodenhausen, G. *ChemPhysChem* **2011**, *12*, 2929−2932.

(35) Rossini, A. J.; Zagdoun, A.; Lelli, M.; Gajan, D.; Rascon, F.; Rosay, M.; Maas, W. E.; Coperet, C.; Lesage, A.; Emsley, L. *Chem. Sci.* **2012**, *3*, 108−115.

(36) Hwang, C. F.; Hill, D. A. *Phys. Rev. Lett.* **1967**, *19*, 1011−1014.

(37) Wollan, D. S. *Phys. Rev. B* **1976**, *13*, 3671−3685.

(38) Pons, M.; Feliz, M.; Giralt, E. *J. Magn. Reson.* **1988**, *78*, 314−320.

(39) Kobayashi, T.; Lafon, O.; Lilly Thankamony, A. S.; Slowing, I. I.; Kandel, K.; Carnavale, V. V.; Vezin, H.; Amoureux, J.-P.; Bodenhausen, G.; Pruski, M. *Phys. Chem. Chem. Phys.* **2012**, Submitted.

(40) Khutsishvili, G. R. *Sov. Phys. Usp.* **1969**, *11*, 802−815.

(41) Smith, A. A.; Corzilius, B.; Barnes, A. B.; Maly, T.; Griffin, R. G. *J. Chem. Phys.* **2012**, *136*, 15101.

(42) Lilly Thankamony, A. S.; Lafon, O.; Lu, X.; Aussenac, F.; Rosay, M.; Trebosc, J.; vezin, H.; Amoureux, J.-P. *Appl. Magn. Reson.* **2012**, *43*, 237−250.

(43) Morishige, K.; Uematsu, H. *J. Chem. Phys.* **2005**, 122.

(44) Arnold, G. P.; Finch, E. D.; Rabideau, S. W.; Wenzel, R. G. *J. Chem. Phys.* **1968**, *49*, 4365−4369.

(45) Amoureux, J. P.; Pruski, M. *Mol. Phys.* **2002**, *100*, 1595−1613.

(46) Paradies, H. H.; Clancy, S. F. *Rigaku J.* **2000**, *17*, 20−34.

(47) Hu, K.-N.; Bajaj, V. S.; Rosay, M.; Griffin, R. G. *J. Chem. Phys.* **2007**, *126*, 044512−044512.

(48) Akbey, U.; Franks, W. T.; Linden, A.; Lange, S.; Griffin, R. G.; van Rossum, B.-J.; Oschkinat, H. *Angew. Chem., Int. Ed.* **2010**, *49*, 7803−7806.

(49) Kagawa, A.; Murokawa, Y.; Takeda, K.; Kitagawa, M. *J. Magn. Reson.* **2009**, *197*, 9−13.

(50) Negoro, M.; Nakayama, K.; Tateishi, K.; Kagawa, A.; Takeda, K.; Kitagawa, M. *J. Chem. Phys.* **2010**, *133*, 154504.

(51) Maly, T.; Cui, D. T.; Griffin, R. G.; Miller, A. F. *J. Phys. Chem. B* **2012**, *116*, 7055−7065.

Supporting Information

Mesoporous silica nanoparticles loaded with surfactant: low temperature magic angle spinning ^{13}C and ^{29}Si NMR enhanced by dynamic nuclear polarization

I. Materials and methods

I.1. Synthesis and structural characterization

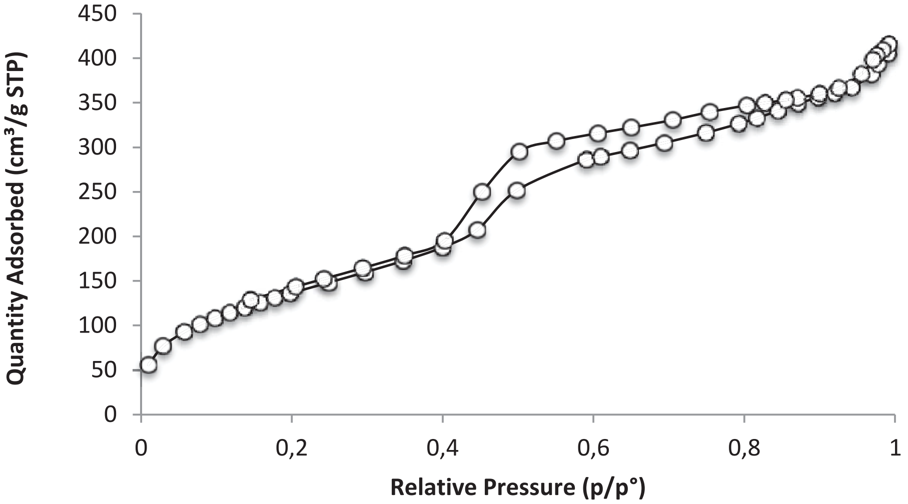

Figure S1: Nitrogen sorption isotherm of surfactant-free **dry-Ex-MSN** with 3-(N-phenylureido)propyl (PUP) groups attached to the surface.

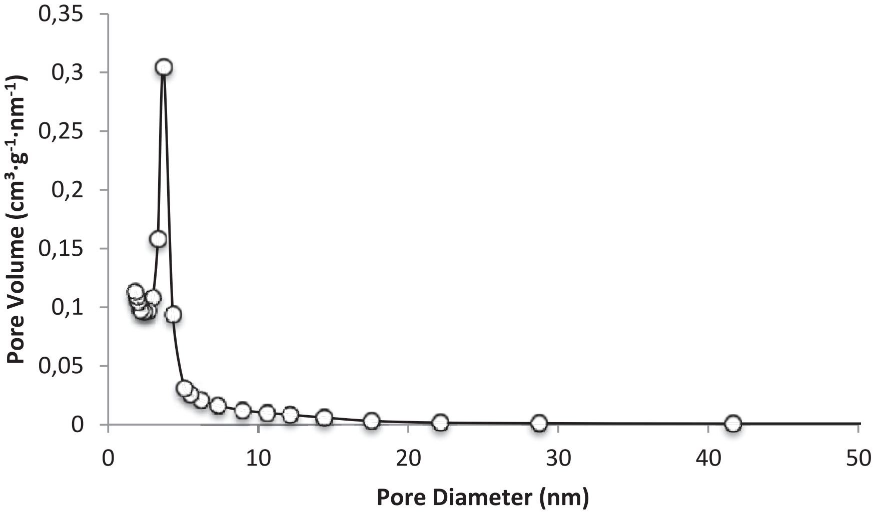

Figure S2: Pore size distribution of **dry-Ex-MSN**.

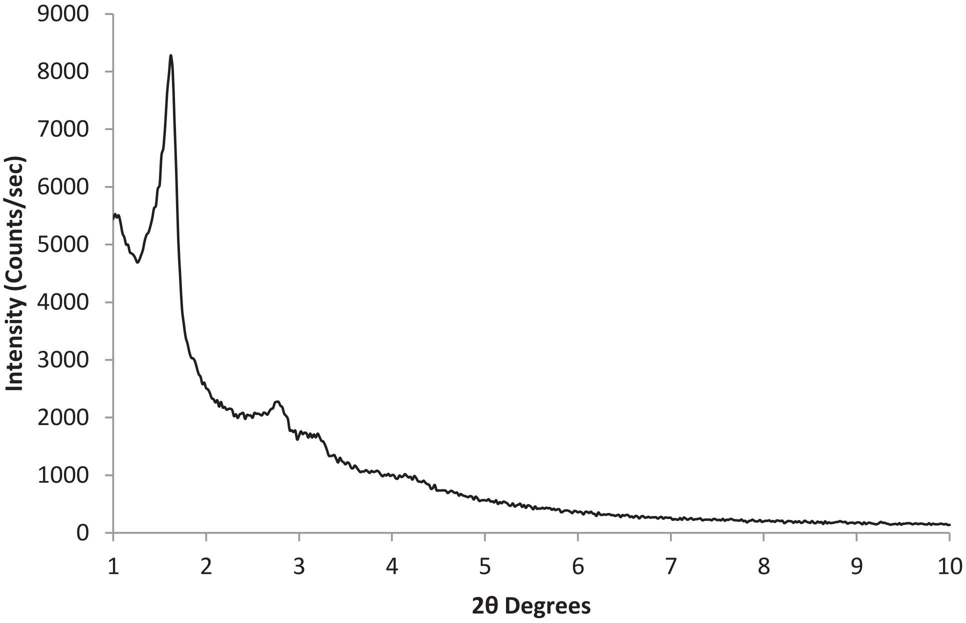

Figure S3: Small-angle X-ray diffraction pattern of **dry-Ex-MSN**.

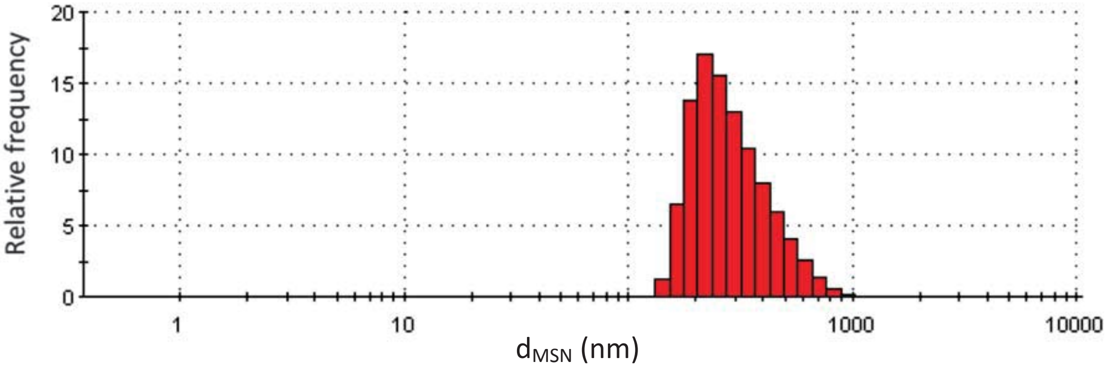

Figure S4: Particle size distribution in **Ex-MSN** measured by dynamic light scattering.

II. Uncertainties of DNP enhancement factors

For an isotope X, the enhancement factor $\varepsilon_{on/off}(X)$ is defined as

$$\varepsilon_{on/off}(X) = \frac{I_{on}(X)}{I_{off}(X)} \tag{S1}$$

where $I_{on}(X)$ and $I_{off}(X)$ are the intensities obtained with and without microwave irradiation ("µw on" and "µw off", respectively). The absolute intensity errors $\Delta I_{on}(X)$ and $\Delta I_{off}(X)$ are defined as the standard deviations of the noise in the corresponding spectra. Since these errors are not correlated, the absolute error, $\Delta\varepsilon_{on/off}(X)$, is given by

$$\Delta\varepsilon_{on/off}(X) = \varepsilon_{on/off}(X)\left\{\left[\frac{\Delta I_{on}(X)}{I_{on}(X)}\right]^2 + \left[\frac{\Delta I_{off}(X)}{I_{off}(X)}\right]^2\right\}^{1/2}, \tag{S2}$$

where $\Delta I_{on}(X)/I_{on}(X)$ and $\Delta I_{off}(X)/I_{off}(X)$ are the inverse of the signal-to-noise ratios.

III. Estimate of proton concentration in DNP samples

The ^{1}H molar concentration in **Ex-MSN**, c_H(**Ex-MSN**), impregnated with water with natural isotopic abundance was estimated from

$$c_H(\text{Ex-MSN}) = 2\frac{\rho_{H_2O}}{M(H_2O)}\frac{V_p\rho_{SiO_2}}{(1+V_p\rho_{SiO_2})}, \tag{S3}$$

where the factor of 2 accounts for the two protons in H_2O, ρ_{H_2O} and ρ_{SiO_2} are the mass densities of frozen disordered water and silica walls, $M(H_2O)$ = 18.01 $\text{g}\cdot\text{mol}^{-1}$ is the molar mass of water, and V_p = 0.59 $\text{cm}^3\cdot\text{g}^{-1}$ is the combined volume of pores and interparticle space measured by BJH desorption analysis. The protons in silanol groups and PUP substituents are disregarded. It has been shown that the frozen water confined within the mesopores of MSNs has primarily a cubic structure.[1] The densities of cubic and hexagonal ice are identical and equal to ρ_{H_2O} = 0.93 $\text{g}\cdot\text{cm}^{-3}$,[2] whereas ρ_{SiO_2} is assumed to be equal to the density of fused quartz, 2.2 $\text{g}\cdot\text{cm}^{-3}$. Using Eq. S3, we found c_H(Ex-MSN) ≈ 60 M. It follows that the ^{1}H concentration in **Ex-MSN-10** is about 6 M.

Similarly, the ^{1}H molar concentration in **S-MSN** is given by

$$c_H(\text{S-MSN}) = 42\frac{\rho_{CTAB}}{M(CTAB)}\frac{V_p\rho_{SiO_2}}{(1+V_p\rho_{SiO_2})}, \tag{S4}$$

where the factor of 42 represents the number of protons per CTAB molecule. Eq. S4 yields c_H(S-MSN) ≈ 77 M.

These concentrations are in good agreement with other DNP studies. For example, the ^{1}H concentration in [$^2H_8$]-glycerol/^2H_2O/H_2O mixture (60/30/10 w/w/w) is about 15 M. In a DNP sample consisting of 8 mg non-deuterated proteins dispersed in this mixture and placed in a 3.2-mm MAS rotor, the overall ^{1}H concentration is about 40 M.[3]

References

(1) Morishige, K.; Uematsu, H. *J. Chem. Phys.* **2005**, *122*.

(2) Arnold, G. P.; Finch, E. D.; Rabideau, S. W.; Wenzel, R. G. *J. Chem. Phys.* **1968**, *49*, 4365-4369.

(3) Bayro, M. J.; Debelouchina, G. T.; Eddy, M. T.; Birkett, N. R.; MacPhee, C. E.; Rosay, M.; Maas, W. E.; Dobson, C. M.; Griffin, R. G. *J. Am. Chem. Soc.* **2011**, *133*, 13967-13974.

PCCP

RSC Publishing

PAPER

View Article Online
View Journal | View Issue

Cite this: Phys. Chem. Chem. Phys., 2013, **15**, 5553

Analysis of sensitivity enhancement by dynamic nuclear polarization in solid-state NMR: a case study of functionalized mesoporous materials

Takeshi Kobayashi,[a] Olivier Lafon,[b] Aany S. Lilly Thankamony,[b] Igor I. Slowing,[a] Kapil Kandel,[af] Diego Carnevale,[c] Veronika Vitzthum,[c] Hervé Vezin,[d] Jean-Paul Amoureux,[b] Geoffrey Bodenhausen[ce] and Marek Pruski*[af]

Received 5th January 2013,
Accepted 29th January 2013

DOI: 10.1039/c3cp00039g

www.rsc.org/pccp

We systematically studied the enhancement factor (per scan) and the sensitivity enhancement (per unit time) in ^{13}C and ^{29}Si cross-polarization magic angle spinning (CP-MAS) NMR boosted by dynamic nuclear polarization (DNP) of functionalized mesoporous silica nanoparticles (MSNs). Specifically, we separated contributions due to: (i) microwave irradiation, (ii) quenching by paramagnetic effects, (iii) the presence of frozen solvent, (iv) the temperature, as well as changes in (v) relaxation and (vi) cross-polarization behaviour. No line-broadening effects were observed for MSNs when lowering the temperature from 300 to 100 K. Notwithstanding a significant signal reduction due to quenching by TOTAPOL radicals, DNP-CP-MAS at 100 K provided global sensitivity enhancements of 23 and 45 for ^{13}C and ^{29}Si, respectively, relative to standard CP-MAS measurements at room temperature. The effects of DNP were also ascertained by comparing with state-of-the-art two-dimensional heteronuclear $^{1}H\{^{13}C\}$ and $^{29}Si\{^{1}H\}$ correlation spectra, using, respectively, indirect detection or Carr–Purcell–Meiboom–Gill (CPMG) refocusing to boost signal acquisition. This study highlights opportunities for further improvements through the development of high-field DNP, better polarizing agents, and improved capabilities for low-temperature MAS.

1. Introduction

One of the most fundamental challenges in nuclear magnetic resonance (NMR) is its intrinsically low sensitivity. The signal-to-noise ratio (S/N) per scan in an NMR measurement depends upon, among other parameters, the gyromagnetic ratio of the observed nuclei γ_{obs}, the strength of the static magnetic field B_0, the temperature T and the apparent transverse relaxation time, T_2^*.[1] In solid-state NMR, the detection limits are further affected by inhomogeneous line broadening, which can reduce T_2^* by several orders of magnitude.

One of the main strategies for increasing the sensitivity is to begin by exciting high-γ spins and transferring their polarization to the observed low-γ nuclei. This approach is commonly used in $^{1}H \rightarrow X$ cross-polarization (CP), as a means of improving the sensitivity of hetero-nuclei ($X = {}^{13}C$, ^{29}Si, ^{15}N, *etc.*) in solids. Correspondingly larger gains of up to two orders of magnitude can be achieved by polarizing the nuclei *via* unpaired electron spins, as proposed by Overhauser and demonstrated by Slichter in the 1950s.[2,3] This idea, referred to as dynamic nuclear polarization (DNP), relies on the transfer of polarization from unpaired electrons to nuclei, which is driven by microwave (μw) irradiation near the electron spin resonance (ESR) frequency. In the 1980s and 1990s DNP was combined with $^{1}H \rightarrow X$ CP under magic angle spinning (MAS), and applied successfully to a variety of solid materials containing unpaired electrons that occur naturally or are introduced by doping.[4,5] In the past decade, advances in gyrotron technology,[6,7] the development of cryogenic MAS probes for DNP,[8] and improved biradicals or other polarizing agents[9–11] enabled researchers to perform DNP

---

[a] *U.S. Department of Energy, Ames Laboratory, Ames, Iowa 50011, USA*

[b] *Université de Lille Nord de France, 59000 Lille, CNRS UMR 8181, Unité de Catalyse et de Chimie du Solide (UCCS), Ecole Nationale Supérieure de Chimie de Lille, Université de Lille 1, 59652 Villeneuve d'Ascq, France*

[c] *Institut des Sciences et Ingénierie Chimiques, Ecole Polytechnique Fédérale de Lausanne, EPFL, Batochime, 1015 Lausanne, Switzerland*

[d] *Université de Lille Nord de France, 59000 Lille, CNRS UMR 8516, Laboratoire de Spectrochimie Infrarouge et Raman (LASIR), Université de Lille 1, 59652 Villeneuve d'Ascq, France*

[e] *Département de Chimie, Ecole Normale Supérieure, Université Pierre et Marie Curie, CNRS UMR 7203, Paris, France*

[f] *Department of Chemistry, Iowa State University, Ames, Iowa 50011, USA. E-mail: mpruski@iastate.edu*

NMR experiments at higher magnetic fields. One of the most universal polarizing agents is the biradical 1-(TEMPO-4-oxy)-3-(TEMPO-4-amino)propan-2-ol (TOTAPOL).[10] For favourably oriented molecules in frozen glasses, the two unpaired electrons of TOTAPOL exhibit ESR frequencies that differ roughly by the nuclear Larmor frequency.[12] This facilitates an efficient three-spin ''cross-effect'' involving a flip-flop process of the two unpaired electrons and a flip of the nucleus.[12–14] Significant signal enhancements can be achieved, not only in biological systems[8,15–20] but also in microcrystalline organic solids[21,22] or on surfaces and subsurfaces of silicates, aluminates, nanomaterials, and metal–organic frameworks (MOFs).[23–26]

Several studies have addressed the quantification of the sensitivity enhancement in these experiments.[21,26–30] The DNP enhancement factor is typically determined by comparing the spectra measured with μw irradiation ''on'' and ''off'', under the same conditions of static field B_0 and sample temperature T, using sufficiently long recycle delays so that relaxation effects can be neglected. In a study of DNP-enhanced ^{13}C CP-MAS NMR of a solvent-free peptide with covalently attached TOTAPOL[28] a more general enhancement factor was described which also accounts for effects of the radicals on the spin-lattice relaxation times $T_1{}^{\mathrm{H}}$ of the protons and on paramagnetic broadening ('quenching') of the signals. The influence of TOTAPOL concentration (in water/glycerol) on $T_1{}^{\mathrm{H}}$ and $T_{1\rho}{}^{\mathrm{H}}$ relaxation of protons, and the performance of ^{13}C DNP-CP-MAS NMR in proline was studied by Lange *et al.*[30] Rossini *et al.*[29] quantified sensitivity enhancements of ^{29}Si DNP-CP-MAS NMR of passivated hybrid mesoporous silica. In addition to quenching and $T_1{}^{\mathrm{H}}$ relaxation, they studied the effect of TOTAPOL on T_2' dephasing times of the ^{29}Si nuclei in $^{1}\mathrm{H} \rightarrow {}^{29}\mathrm{Si}$ CP-MAS and demonstrated that further signal enhancement is possible in DNP-CP-MAS experiments by multiple refocusing using Carr–Purcell–Meiboom–Gill (CPMG) sequences. Very recently, Takahashi *et al.*[21] compared the sensitivity of ^{13}C DNP-CP-MAS and conventional CP-MAS for [2-^{13}C]glycine and microcrystalline cellulose. These recent studies have highlighted the importance of optimizing the sensitivity, $(\mathrm{S/N})^{\mathrm{time}}$, defined as S/N per square root of unit time, rather than the enhancement per scan. Paramagnetic doping can have positive or deleterious effects: increasing the signal per observed spin and allowing for shorter recycle delays on the one hand, and quenching and broadening the signals on the other. Thus, careful sample preparation and optimization of the experimental conditions are critical.

Here, we set out to systematically assess the contributions of various experimental factors to the global sensitivity enhancement in DNP-CP-MAS NMR of both ^{13}C and ^{29}Si nuclei. We focus on mesoporous silica nanoparticles (MSNs) functionalized with 3-(*N*-phenylureido)propyl (PUP) groups. In particular, we compare signals obtained under optimized DNP conditions and signals achievable at room temperature with non-impregnated samples exposed to ambient conditions in the laboratory (hereafter, ''dry''). We take into account differences in relaxation, polarization transfer, and the chemical environment. Furthermore, we correlate these capabilities with state-of-the-art two-dimensional (2D) heteronuclear correlation (HETCOR) spectra utilizing either indirect detection of ^{13}C nuclei *via* protons,[31,32] or CPMG-enhanced ^{29}Si acquisition.[33,34] The discussion also incorporates contributions to the global sensitivity enhancement that were not addressed experimentally, stemming from potential changes in line widths, solvent effects, the Boltzmann factor, and probe characteristics. The results of this study offer additional insights into the potential of DNP for functionalized surfaces and highlight the need for further improvements.

2. Experimental

2.1. Materials

The PUP-functionalized MSNs (PUP-MSNs) were prepared using a previously reported co-condensation method.[35,36] Cetyltrimethylammonium bromide (CTAB), sodium hydroxide, aniline and mesitylene were purchased from Sigma-Aldrich. Tetraethoxysilane (TEOS) and 3-isocyanatopropyl-triethoxysilane were purchased from Gelest. All reagents were used as received. 3-Isocyanatopropyl triethoxysilane (0.50 mL) was mixed with aniline (0.25 mL) in a screw-cap vial and stirred at room temperature for 1 h to give crude 3-(*N*-phenylureido)propyl triethoxysilane. Simultaneously, CTAB (1.02 g), mesitylene (5.0 mL), NaOH (2 M, 3.5 mL), and H_2O (480 mL) were mixed in a round-bottom flask and heated at 80 °C for 1 h with vigorous stirring. To the resulting clear solution, TEOS (5.0 mL) was added drop-wise followed immediately by drop-wise addition of the crude 3-(*N*-phenylureido)propyl triethoxysilane, forming a cream-colored precipitate. The product was isolated by hot filtration, washed with copious amounts of water and methanol, and dried under vacuum at room temperature. The template was extracted by refluxing methanol in a Soxhlet extractor. The resulting surfactant-free solid product was dried under vacuum at room temperature. The concentration of PUP groups was estimated at 1.3 (±0.1) mmol/g, based on quantitative ^{29}Si NMR spectrum taken using direct polarization.

2.2. Solid-state NMR

2.2.1. Sample preparation. Dry PUP-MSN powder was mixed with 12.5 mM TOTAPOL dissolved in water with natural isotopic abundance and stirred using a glass rod. This concentration is known to result in optimal sensitivity enhancements for mesoporous silica materials.[29] After one day of impregnation at room temperature, excess TOTAPOL solution was removed by centrifugation at 12110 × *g* for 5 min. The concentration of TOTAPOL in the samples was measured on a Bruker Biospin ELEXYS E580E X-band ESR spectrometer, using 2 mW of μw power, 0.5 G amplitude modulation, and 4-amino-TEMPO as reference. The ESR spectrum was simulated with the EasySpin program[37] knowing the *g*-tensor, the hyperfine couplings with the ^{14}N nucleus, the dipolar interaction between the two electrons of TOTAPOL and the rotational correlation time, τ_c. To assess the extent of paramagnetic quenching, the PUP-MSN powder was also impregnated with pure water in natural isotopic abundance, following the same procedures. The impregnated samples were transferred to 3.2-mm sapphire rotors and weighed. Sapphire is nearly transparent to frequencies higher than 140 GHz and its excellent thermal conductivity reduces the sample heating due to μw irradiation and MAS.[38,39]

2.2.2. DNP NMR measurements. One-dimensional (1D) $^1H \rightarrow {}^{13}C$ and $^1H \rightarrow {}^{29}Si$ solid-state NMR CP-MAS spectra were obtained at B_0 = 9.4 T (400 MHz for protons) using a Bruker BioSpin DNP NMR spectrometer, equipped with a gyrotron generating a continuous-wave power of 5 W at 263 GHz. The μw irradiation was transmitted through a corrugated waveguide to a triple resonance ^{1}H/X/Y MAS probe for 3.2 mm rotors spinning at a MAS frequency ν_R = 10 kHz.[10,40] NMR spectra with μw irradiation ''on'' or ''off'' were acquired at a temperature T = 98 K, which was stabilized using a Bruker BioSpin MAS cooling system.

2.2.3. Other solid-state NMR measurements. Additional 1D $^1H \rightarrow {}^{13}C$ and $^1H \rightarrow {}^{29}Si$ CP-MAS experiments were performed at 9.4 T on a Chemagnetics Infinity spectrometer with samples in 5 mm zirconia rotors spinning at 10 kHz. Their temperature was adjusted to T = 120 or 310 K by employing the Chemagnetics variable temperature system and calibrated with ±5 K accuracy using KBr as external reference.[41] The CP transfers were optimized separately in all experiments.

All $^1H \rightarrow {}^{13}C \rightarrow {}^1H$ and $^1H \rightarrow {}^{29}Si$ 2D HETCOR spectra were recorded at room temperature on a Varian NMR spectrometer at 14.1 T (600 MHz for protons) equipped with a MAS probe with 1.6 mm rotors spinning at ν_R = 40 kHz. The sensitivity of these experiments was improved by indirect detection *via* protons for heteronuclear ^{1}H–^{13}C correlation and multiple CPMG refocusing for ^{1}H–^{29}Si correlation.[31–34]

The experimental parameters are given in the captions, using the following symbols: ν_{RF}^{X} is the magnitude of the radiofrequency (RF) magnetic field applied to X spins, τ_{CP} is the cross-polarization time, τ_{CPMG} is the delay between the rotor-synchronized π pulses in the CPMG sequence, N_{CPMG} is the number of echoes, Δt_1 is the increment of t_1 during 2D acquisition, and τ_{RD} is the recycle delay (we assume that the acquisition time of free induction decay is negligibly small compared to the recovery delay). The ^{1}H, ^{13}C and ^{29}Si chemical shifts were referenced with respect to tetramethylsilane (TMS) at 0 ppm.

3. Results

The overall concentration of TOTAPOL, c_m, in the impregnated PUP-MSNs was determined by ESR spectroscopy and is about 9.5 mM. The simulation of the X-band ESR spectrum (not shown) yields a correlation time τ_c = 410 ns,[42] which indicates that the motions of the TOTAPOL molecules are strongly restricted in the mesopores of MSNs. This observation suggests some adsorption of TOTAPOL onto the silica surface.[25] The parameters extracted from the fit of the X-band ESR spectrum were used to simulate the ESR spectrum at 263 GHz which exhibits a 1.1 GHz inhomogeneous broadening due to g-anisotropy. This greatly exceeds the ^{1}H Larmor frequency at 9.4 T and favours the cross-effect DNP mechanism involving two unpaired electrons in TOTAPOL.[12–14,39,43] The amplitude of the microwave field in the sample does not exceed a few MHz,[44] thus only a small fraction of the unpaired electrons can be saturated by the microwave irradiation in a static sample. However, in a spinning sample the ESR resonance frequencies are modulated by the sample rotation, so that a larger fraction of unpaired electrons can be affected by the microwave field, thereby contributing to the DNP enhancement.[45,46]

Table 1 Summary of samples and experimental conditions used in $^1H \rightarrow {}^{13}C$ and $^1H \rightarrow {}^{29}Si$ CP-MAS experiments at 9.4 T

Experiment[a]	Solvent	T [K]	TOTAPOL	μw
H_2O*-LT-on	H_2O	98	Yes	On
H_2O*-LT-off	H_2O	98	Yes	Off
H_2O-LT-off	H_2O	120	No	Off
Dry-LT-off	None	120	No	Off
Dry-RT-off	None	310	No	Off

[a] H_2O: samples with H_2O, dry: samples without solvent exposed to ambient conditions in the laboratory, '*': samples with TOTAPOL, LT: low temperature, RT: room temperature, 'on': with μw irradiation, 'off': without μw irradiation.

To separate various contributions to the global DNP enhancement, we carried out a series of $^1H \rightarrow {}^{13}C$ and $^1H \rightarrow {}^{29}Si$ CP-MAS experiments using the samples and experimental conditions summarized in Table 1.

Fig. 1 shows $^1H \rightarrow {}^{13}C$ and $^1H \rightarrow {}^{29}Si$ CP-MAS spectra of H_2O*-LT-on and H_2O*-LT-off. The first spinning sideband (SSB) of the aromatic carbons overlaps with aliphatic signals. Fig. 1 clearly demonstrates the DNP enhancement per scan (see eqn (1)) in both ^{13}C and ^{29}Si spectra ($\varepsilon_{\text{on/off}}^{\text{scan}} \approx 23$ for both nuclei).

As expected, the longitudinal relaxation times T_1^{H} of the proton bath, summarized in Table 2, are strongly influenced by

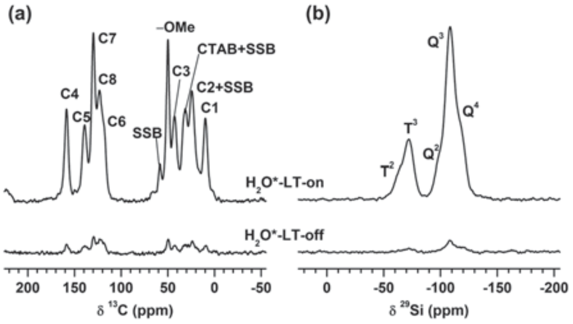

Fig. 1 (a) $^1H \rightarrow {}^{13}C$ and (b) $^1H \rightarrow {}^{29}Si$ CP-MAS spectra of PUP-MSNs impregnated with aqueous TOTAPOL solution, recorded with and without μw irradiation at $T \approx 98$ K (H_2O*-LT-on and H_2O*-LT-off, respectively). The spectra were measured using ν_R = 10 kHz, τ_{CP} = 2 ms, $\nu_{RF}^{C} = \nu_{RF}^{Si}$ = 46 kHz during CP, ν_{RF}^{H} ramped from 53 to 59 kHz during CP and ν_{RF}^{H} = 95 kHz during the π/2 pulses and SPINAL-64 ^{1}H decoupling.[47] The recycle delay was τ_{RD} = 1.3 s, 512 scans were accumulated for ^{13}C (total time = 11 min) and 1024 scans for ^{29}Si (total time = 22 min). The ^{13}C signal assignments in PUP refer to Scheme 1. ''CTAB'' denotes the CH_2 resonances of the residual cetyltrimethylammonium bromide surfactant that was not extracted from the pores, whereas ''-OMe'' represents methoxy groups due to washing with methanol. In (b), the T^n silicon signals with n = 2 or 3 represent $(SiO)_n$**Si**$R(OX)_{3-n}$ grafting sites with R = PUP, X = H or Me, whereas Q^n (n = 2, 3 and 4) corresponds to $(SiO)_n$**Si**$(OX)_{4-n}$ sites.

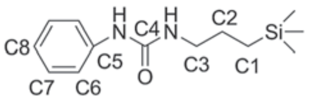

Scheme 1 The PUP functional group.

Table 2 Proton longitudinal relaxation times T_1^H at around 100 K and 9.4 T

Experiment	T_1^H (s)
H_2O*-LT-off	1.1
H_2O-LT-off	4.0
Dry-LT-off[a]	0.17
Dry-RT-off[a]	1.2

[a] Samples were handled in an ambient atmosphere.

the radicals, solvent, and temperature.[28,29] The relaxation was mono-exponential in all samples. The difference in relaxation times between dry-LT-off and dry-RT-off is attributed to the reduction of the mobility of the PUP and silanol groups at 120 K compared to 310 K.

No difference in line broadening was observed in $^1H \rightarrow {}^{13}C$ and $^1H \rightarrow {}^{29}Si$ CP-MAS spectra with and without μw irradiation (see Fig. 1). This can be ascribed to (i) the propagation of DNP-enhanced ^1H polarization *via* ^1H spin diffusion, as previously observed in organic and hybrid nano- and micro-particles,[15,22,42] and (ii) the low efficiency of CP in the vicinity of TOTAPOL, owing to short longitudinal and $T_{1\rho}^{H}$ relaxation times in the rotating frame.[30] Nuclei in the immediate proximity of TOTAPOL radicals (on the order of ~1 nm or less)[30,48] are not observable ('quenched') because of paramagnetic broadening. Furthermore, Fig. 2 shows that TOTAPOL did not broaden the visible linewidths at the concentrations used in this study. This is due both to the low CP efficiency near TOTAPOL and to the atomic-scale disorder in PUP-MSNs, producing a distribution in ^{13}C and ^{29}Si isotropic chemical shifts, which masks paramagnetic broadening.

Fig. 3 compares the intensities of $^1H \rightarrow {}^{13}C$ and $^1H \rightarrow {}^{29}Si$ CP-MAS spectra of the samples dry-RT-off, dry-LT-off and H_2O-LT-off, collected using $\tau_{RD} > 3T_1^H$. The measurements were performed at 9.4 T on a Chemagnetics spectrometer. For comparison between the two 9.4 T spectrometers, the $^1H \rightarrow {}^{13}C$ and $^1H \rightarrow {}^{29}Si$ CP-MAS spectra of the H_2O-LT-off sample were recorded on both instruments (see Fig. 2 and top spectra of Fig. 3). The RF amplitudes of the ^1H decoupling fields were 95 and ~40 kHz, respectively, on the spectrometers with and without gyrotron, hence the broadening of the aliphatic carbon signals observed without gyrotron. Fig. 3 shows that the presence of frozen water does not increase the linewidth in PUP-MSN, since the dry PUP-MSNs already exhibit atomic-scale disorder. This observation stands in contrast with organic or biological molecules in frozen solutions, where significant line broadening due to static disorder in frozen samples has been reported.[49]

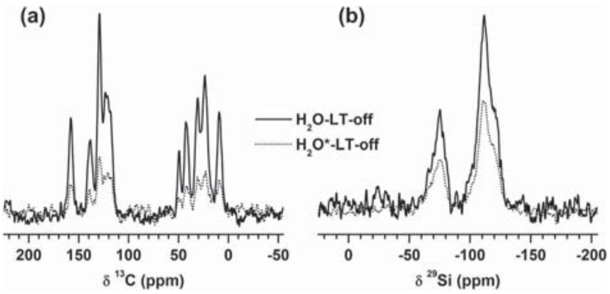

Fig. 2 (a) $^1H \rightarrow {}^{13}C$ and (b) $^1H \rightarrow {}^{29}Si$ CP-MAS spectra of PUP-MSNs without TOTAPOL (H_2O-LT-off, solid) and with TOTAPOL (H_2O*-LT-off, dotted). The recycle delays were τ_{RD} = 5 s for H_2O*-LT-off and τ_{RD}=15 s for H_2O-LT-off, with 512 scans acquired for both ^{13}C spectra and the ^{29}Si spectrum H_2O-LT-off, and 3072 scans for the ^{29}Si spectrum H_2O*-LT-off. The other experimental conditions were the same as in Fig. 1. The spectra were normalized by dividing the intensities by the number of scans to compare intensities per scan.

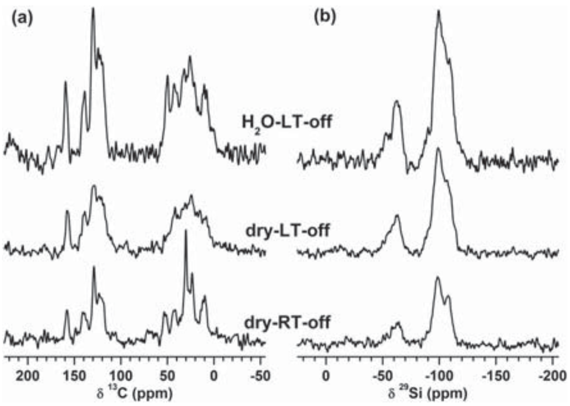

Fig. 3 (a) $^1H \rightarrow {}^{13}C$ and (b) $^1H \rightarrow {}^{29}Si$ CP-MAS spectra of H_2O-LT-off (top), dry-LT-off (middle), and dry-RT-off (bottom), acquired on a 9.4 T spectrometer without gyrotron using ν_R = 10 kHz, ν_{RF}^{H} = 40 kHz during CP and TPPM decoupling, and $\nu_{RF}^{C} = \nu_{RF}^{Si}$ = 50 kHz during CP. Other experimental conditions were: τ_{RD} = 30 s, τ_{CP} = 0.5 ms for ^{13}C and 5 ms for ^{29}Si (H_2O-LT-off); τ_{RD} = 1 s, τ_{CP} = 1 ms for ^{13}C and 5 ms for ^{29}Si (dry-LT-off); τ_{RD} = 3.5 s, τ_{CP} = 1 ms for ^{13}C and 7 ms for ^{29}Si (dry-RT-off). The spectra were normalized to compare intensities per scan.

4. Discussion

4.1. Contributions to the global DNP enhancement

When comparing DNP-CP-MAS with traditional CP-MAS measurements, one must consider not only the effect of μw irradiation on the nuclear polarization, but also the consequences of introducing the TOTAPOL solution into the pores. As noted above, TOTAPOL enhances nuclear T_1 relaxation, thereby allowing for shorter recycle delays, so that more scans can be recorded per unit time. On the other hand, the unpaired electrons can render a fraction of the nuclei unobservable due to paramagnetic broadening. The frozen solvent (water in our case) modifies the environment of the nuclei and provides an abundant pool of ^1H nuclei in the pores. This affects the longitudinal relaxation times T_1^H, as well as the efficiency of the CP process.[30] The discussion below includes several additional factors that were not confronted experimentally.

4.1.1. Enhancement per scan and per unit of time. When comparing two experiments A and B, the improvement in S/N can be characterized in terms of an enhancement factor either *per scan* ($\varepsilon^{\text{scan}}$) or *per unit of experimental time* ($\varepsilon^{\text{time}}$). The former is defined as the ratio of S/N for long recovery delays

$$\varepsilon^{\text{scan}}(\text{A};\text{B})=\frac{S_{\text{A}}(\infty)}{S_{\text{B}}(\infty)}\frac{N_{\text{B}}}{N_{\text{A}}}, \qquad (1)$$

where, N_{A} and N_{B} are the root-mean-square (rms) amplitudes of the noise in experiments A and B, $S_{\text{A}}(\infty)$ and $S_{\text{B}}(\infty)$ are the signal intensities per scan of experiments A and B measured with recycle delays $\tau_{\text{RD}}(\text{A}) > 5T_1(\text{A})$ and $\tau_{\text{RD}}(\text{B}) > 5T_1(\text{B})$, with $T_1(\text{A})$ and $T_1(\text{B})$ being the relevant time constants of the build-up of the nuclear polarization, either towards Boltzmann equilibrium, or towards the DNP-enhanced polarization. The expression of $\varepsilon^{\text{scan}}$ in the case of partial saturation ($\tau_{\text{RD}}(\text{A}) < 5T_1(\text{A})$ and $\tau_{\text{RD}}(\text{B}) < 5T_1(\text{B})$) is derived in Appendix A.1. If the rms amplitudes of the noise are identical in experiments A and B ($N_{\text{A}} = N_{\text{B}}$), $\varepsilon^{\text{scan}}(\text{A; B})$ is equal to the ratio of signal intensities, $S_{\text{A}}(\infty)$ and $S_{\text{B}}(\infty)$.

In the presence of line broadening, one should separate the contributions to the enhancement factor, $\varepsilon^{\text{scan}}$, due to the integrated intensities, $\varepsilon^{\text{integral}}$, the line widths, ε^{LW}, and the noise, $\varepsilon^{\text{noise}}$. In the Appendix A.2, we show that

$$\varepsilon^{\text{scan}}(\text{A; B}) = \varepsilon^{\text{integral}}(\text{A; B})\ \varepsilon^{\text{LW}}(\text{A; B})\ \varepsilon^{\text{noise}}(\text{A; B}). \qquad (2)$$

However, $\varepsilon^{\text{scan}}(\text{A; B})$ does not take into account the changes in T_1 relaxation between experiments A and B. To quantify this contribution, we must consider the *sensitivity enhancement per unit time*:

$$\varepsilon^{\text{time}}(\text{A};\text{B})=\frac{S_{\text{A}}(\infty)}{S_{\text{B}}(\infty)}\frac{N_{\text{B}}}{N_{\text{A}}}\sqrt{\frac{T_1(B)}{T_1(A)}}=\varepsilon^{\text{scan}}(\text{A};\text{B})\sqrt{\kappa(\text{A};\text{B})} \qquad (3)$$

as shown in Appendix A.3. In eqn (3), the factor $\kappa(\text{A; B}) = T_1(\text{B})/T_1(\text{A})$ is the ratio of longitudinal relaxation times in experiments B and A. For example, in $^1\text{H} \rightarrow \text{X}$ CP-MAS experiments, $\kappa = T_1^{\text{H}}(\text{B})/T_1^{\text{H}}(\text{A})$.

In the next paragraphs we discuss various contributions to the global sensitivity enhancement offered by DNP-CP-MAS experiments.

4.1.2. Microwave effect. The effect of μw irradiation is given by

$$\varepsilon_{\text{on/off}} = \varepsilon(\text{H}_2\text{O*-LT-on; H}_2\text{O*-LT-off}). \qquad (4)$$

In $^1\text{H} \rightarrow {}^{13}\text{C}$ and $^1\text{H} \rightarrow {}^{29}\text{Si}$ DNP-CP-MAS experiments, the factor $\varepsilon^{\text{scan}}_{\text{on/off}}$ depends on the efficiency of (i) the polarization transfer between unpaired electrons and protons located near the spin diffusion barrier,[43,50,51] and of (ii) the propagation of DNP-enhanced ^{1}H polarization *via* ^{1}H–^{1}H spin diffusion.[15,22,42] Furthermore, in our PUP-MSN samples, as can be seen in Fig. 1, the μw irradiation affects neither the full width at half maximum (FWHM) nor the noise amplitude. The enhancement per scan, $\varepsilon^{\text{scan}}_{\text{on/off}} = 23$, which is identical for both $^1\text{H} \rightarrow {}^{13}\text{C}$ and $^1\text{H} \rightarrow {}^{29}\text{Si}$ CP-MAS spectra, indicates that the ^{1}H polarization is identical near various ^{13}C and ^{29}Si nuclei.[42] We have also verified that at 98 K the time constant of the polarization build-up, τ_{DNP}, is equal to the longitudinal proton relaxation time $T_1^{\text{H}}(\text{H}_2\text{O*-LT-off})$, which is consistent with the assumption that the cross-effect is dominant in our samples (hence $\kappa_{\text{on/off}} = T_1^{\text{H}}(\text{H}_2\text{O*-LT-off})/\tau_{\text{DNP}} = 1$).[27,29,49,52] (We note that diverging values of τ_{DNP} and T_1^{H} have been observed at temperatures below 30 K in samples containing frozen glassy solutions of TEMPO radicals.[53,54]) Thus, the effect of the recycle delay τ_{RD} does not depend on μw irradiation, and the sensitivity enhancement can be obtained by direct comparison of signal intensities observed in experiments H$_2$O*-LT-on and H$_2$O*-LT-off, hence $\varepsilon^{\text{time}}_{\text{on/off}} = \varepsilon^{\text{scan}}_{\text{on/off}} = 23$ for both ^{13}C and ^{29}Si.

4.1.3. Effect of radical concentration. The incorporation of TOTAPOL reduces the longitudinal proton relaxation time T_1^{H}, but also the apparent transverse relaxation time T_2^* of nearby nuclei, leading to line-broadening known as 'quenching' since it usually prevents the observation of nuclei distant by less than a few Angstroms from unpaired electrons. Furthermore, the introduction of exogenous radicals also shortens the longitudinal relaxation times in the rotating frame, $T_{1\rho}$, of both ^{1}H and X nuclei, which affects the CP efficiency. These paramagnetic effects can be assessed globally by comparing experiments with and without radicals,

$$\varepsilon_{\text{para}} = \varepsilon(\text{H}_2\text{O*-LT-off; H}_2\text{O-LT-off}). \qquad (5)$$

As stated in the previous section (see Fig. 2), the introduction of TOTAPOL into our PUP-MSN samples affects neither the linewidths of ^{13}C and ^{29}Si signals nor the noise. However, the quenching and magnetization losses during CP due to radicals[30] are severe, resulting in $\varepsilon^{\text{scan}}_{\text{para}}(^{13}\text{C}) = 0.25$. For ^{29}Si nuclei, three independent measurements at 9.4 T yielded $\varepsilon^{\text{scan}}_{\text{para}}(^{29}\text{Si}) = 0.59$, 0.58 and 0.51. Therefore, we use the value of 0.58 here. However, the effect of quenching is partly compensated by the acceleration of the T_1^{H} relaxation, since $\kappa_{\text{para}} = T_1^{\text{H}}(\text{H}_2\text{O-LT-off})/T_1^{\text{H}}(\text{H}_2\text{O*-LT-off}) = 3.6$, so that $\sqrt{\kappa_{\text{para}}} = 1.9$. The factor $\varepsilon^{\text{time}}_{\text{para}}$ can be estimated using the measured S/N ratios and eqn (3) to be $\varepsilon^{\text{time}}_{\text{para}} = 0.25\sqrt{3.6} = 0.48$ and $0.58\sqrt{3.6} = 1.1$ for ^{13}C and ^{29}Si, respectively. Assuming that (i) the TOTAPOL molecules are homogeneously distributed in frozen water (which at the concentration of 9.5 mM corresponds to one biradical molecule per ~175 nm^3), (ii) the unpaired electrons in TOTAPOL are roughly 1 nm apart, and (iii) the quenching affects all nuclei closer than 1 nm from the unpaired electrons,[30] the expected values of $\varepsilon^{\text{scan}}_{\text{para}}$ should exceed 0.9. The fact that more significant fractions of both nuclei became ''invisible'' in our experiments can be attributed to the large pore diameter (~5 nm) of the MSNs used in this study, which enabled the penetration of TOTAPOL biradicals into the pores. Furthermore, it has been suggested that TOTAPOL radicals may be adsorbed on the surface *via* hydrogen bonds with silanol and siloxane groups.[25] Such an adsorption can amplify the quenching effect. We also note that the values of $\varepsilon^{\text{scan}}_{\text{on/off}}(^{29}\text{Si})$ and $\varepsilon^{\text{scan}}_{\text{para}}(^{29}\text{Si})$ observed for ^{29}Si nuclei in our PUP-MSN samples are in good agreement with those reported by Emsley and co-workers for a TOTAPOL concentration of ~8 mM in methyl passivated SBA-15 silica.[29] For a concentration that matches ours (~9.5 mM), they reported a higher enhancement factor $\varepsilon^{\text{scan}}_{\text{on/off}}(^{29}\text{Si}) = 33$ but a more pronounced signal loss $\varepsilon^{\text{scan}}_{\text{para}}(^{29}\text{Si}) = 0.39$ due to the radicals. The significant decrease in NMR signals owing to the presence of TOTAPOL in our samples highlights the need to avoid close contacts of TOTAPOL with the target spins.[42]

4.1.4. Effect of solvents. The presence of frozen solvent (here water) affects both the signal intensity and the $T_1{}^{\mathrm{H}}$ relaxation. These effects are quantified by the factor

$$\varepsilon_{\mathrm{solvent}} = \varepsilon(\mathrm{H_2O\text{-}LT\text{-}off;\ dry\text{-}LT\text{-}off}) \tag{6}$$

based on spectra such as shown in Fig. 3. In Fig. 3, the ^{13}C signals from aliphatic carbons in both H_2O-LT-off and dry-LT-off show increased line widths with respect to H_2O-LT-off spectra in Fig. 2, owing to insufficient amplitude of the ^{1}H decoupling field. To avoid errors due to insufficient decoupling, the enhancements per scan were evaluated using the integrated intensities of signals of aromatic carbons, which can be decoupled with weaker RF fields. In principle, the factor $\varepsilon^{\mathrm{scan}}_{\mathrm{solvent}}$ incorporates effects of sample dilution and modifications in CP efficiency due to the change in ^{1}H density around the detected nuclei. For porous solids such as PUP-MSNs, the impregnation with solvent sets a limit to the dilution and the presence of a larger ^{1}H bath of frozen water improves the CP efficiency per scan,[39] resulting in enhancement factors $\varepsilon^{\mathrm{scan}}_{\mathrm{solvent}}(^{13}\mathrm{C}) = 2.4$ and $\varepsilon^{\mathrm{scan}}_{\mathrm{solvent}}(^{29}\mathrm{Si}) = 1.6$. However, the $T_1{}^{\mathrm{H}}$ relaxation was slowed down by the presence of frozen water ($\kappa_{\mathrm{solvent}} = T_1{}^{\mathrm{H}}(\text{dry-LT-off})/T_1{}^{\mathrm{H}}(\mathrm{H_2O}\text{-LT-off}) = 0.04$ according to Table 2). Thus the sensitivity per unit time is *decreased* for both nuclei (eqn (3) yields $\varepsilon^{\mathrm{time}}_{\mathrm{solvent}}(^{13}\mathrm{C}) = 0.49$ and $\varepsilon^{\mathrm{time}}_{\mathrm{solvent}}(^{29}\mathrm{Si}) = 0.33$).

4.1.5. Enhancement with respect to low temperature CP-MAS. Since the three contributions described by eqn (4) to (6) act in concert during the DNP experiment, the enhancement per scan between H_2O*-LT-on and dry-LT-off experiments is given by

$$\varepsilon^{\mathrm{scan}}_{\mathrm{DNP}} = \varepsilon^{\mathrm{scan}}_{\mathrm{on/off}}\,\varepsilon^{\mathrm{scan}}_{\mathrm{para}}\,\varepsilon^{\mathrm{scan}}_{\mathrm{solvent}}. \tag{7}$$

The corresponding sensitivity enhancement is

$$\varepsilon^{\mathrm{time}}_{\mathrm{DNP}} = \varepsilon^{\mathrm{scan}}_{\mathrm{DNP}}\sqrt{\kappa_{\mathrm{DNP}}} \tag{8}$$

with

$$\kappa_{\mathrm{DNP}} = \kappa_{\mathrm{on/off}}\kappa_{\mathrm{para}}\kappa_{\mathrm{solvent}}, \tag{9}$$

where $\kappa_{\mathrm{DNP}} = T_1{}^{\mathrm{H}}(\text{dry-LT-off})/\tau_{\mathrm{DNP}}$. Eqn (7) yields $\varepsilon^{\mathrm{scan}}_{\mathrm{DNP}}(^{13}\mathrm{C}) = 14$ and $\varepsilon^{\mathrm{scan}}_{\mathrm{DNP}}(^{29}\mathrm{Si}) = 21$ for PUP-MSNs. Due to the short $T_1{}^{\mathrm{H}}$ in the dry-LT-off experiment, the sensitivity enhancement was reduced with respect to that per scan to $\varepsilon^{\mathrm{time}}_{\mathrm{DNP}}(^{13}\mathrm{C}) = 5.5$ and $\varepsilon^{\mathrm{time}}_{\mathrm{DNP}}(^{29}\mathrm{Si}) = 8.3$.

4.1.6. Global enhancement. Finally, the sensitivity of DNP experiments has to be compared with conventional NMR methods at room temperature, with state-of-the-art probes, fast spinning, optimal pulse sequences, and the highest available magnetic fields. The global S/N enhancement with respect to conventional NMR experiment can be evaluated as,

$$\varepsilon^{\mathrm{scan}}_{\mathrm{global}} = \varepsilon^{\mathrm{scan}}_{\mathrm{DNP}}\,\varepsilon^{\mathrm{scan}}_{\mathrm{probe}}\,\varepsilon^{\mathrm{scan}}_{\mathrm{seq}}\,\varepsilon^{\mathrm{scan}}_{\mathrm{B}}\,\varepsilon^{\mathrm{scan}}_{\mathrm{T}} \tag{10}$$

where $\varepsilon^{\mathrm{scan}}_{\mathrm{DNP}}$ is given by eqn (7) and the factors $\varepsilon^{\mathrm{scan}}_{\mathrm{probe}}$, $\varepsilon^{\mathrm{scan}}_{\mathrm{seq}}$, $\varepsilon^{\mathrm{scan}}_{\mathrm{B}}$ and $\varepsilon^{\mathrm{scan}}_{\mathrm{T}}$ account for the changes in S/N produced by differences in instrumentation, pulse sequences, static magnetic field and sample temperature when comparing DNP and conventional NMR experiments. The resulting global sensitivity enhancement per unit time is

$$\varepsilon^{\mathrm{time}}_{\mathrm{global}} = \varepsilon^{\mathrm{scan}}_{\mathrm{global}}\sqrt{\kappa_{\mathrm{global}}} \tag{11}$$

with

$$\kappa_{\mathrm{global}} = \kappa_{\mathrm{DNP}}\kappa_{\mathrm{B}}\kappa_{\mathrm{T}}, \tag{12}$$

where κ_{B} and κ_{T} account for the effects of the static magnetic field and temperature on $T_1{}^{\mathrm{H}}$ relaxation. The factor $\varepsilon^{\mathrm{scan}}_{\mathrm{probe}}$ is determined by characteristics of the coil (geometry, filling factor, quality factor Q, and temperature) and the temperature and performance of the preamplifier. The factor $\varepsilon^{\mathrm{scan}}_{\mathrm{seq}}$ is essential when comparing experiments acquired with different pulse sequences, for example with or without recording multiple echoes using the CPMG sequence. The magnetic field and the sample temperature can affect both the signal integral (*via* the Boltzmann factor) as well as the linewidth.

As an example, for PUP-MSN samples, we compared at the same static field the sensitivity of DNP-CP-MAS at low temperature and conventional CP-MAS at room temperature

$$\varepsilon_{\mathrm{global}} = \varepsilon(\mathrm{H_2O^*\text{-}LT\text{-}on;\ dry\text{-}RT\text{-}off}) \tag{13}$$

and

$$\kappa_{\mathrm{global}} = T_1{}^{\mathrm{H}}(\text{dry-RT-off})/\tau_{\mathrm{DNP}}. \tag{14}$$

In this case, $\varepsilon^{\mathrm{scan}}_{\mathrm{seq}} = 1$ while the Boltzmann factor and the $T_1{}^{\mathrm{H}}$ times are only influenced by the temperature, $\varepsilon^{\mathrm{scan}}_{\mathrm{B}} = 1$, $\varepsilon^{\mathrm{scan}}_{\mathrm{T}} = 3$, $\kappa_{\mathrm{B}} = 1$ and $\kappa_{\mathrm{T}} = T_1{}^{\mathrm{H}}(\text{dry-LT-off})/T_1{}^{\mathrm{H}}(\text{dry-RT-off}) = 7$ (using the values of Table 2). We further assumed that $\varepsilon^{\mathrm{scan}}_{\mathrm{probe}} = 1$. By inserting the appropriate relaxation times, eqn (11) yields the global enhancement factors $\varepsilon^{\mathrm{time}}_{\mathrm{global}}(^{13}\mathrm{C}) = 23$ and $\varepsilon^{\mathrm{time}}_{\mathrm{global}}(^{29}\mathrm{Si}) = 45$, respectively. The time savings in PUP-MSNs are thus given by factors $(\varepsilon^{\mathrm{time}}_{\mathrm{global}})^2 = 529$ and 2015 for ^{13}C and ^{29}Si, respectively.

In our samples, no significant changes in line widths were observed between the different experiments (under proper decoupling) since the dry-PUP-MSN samples already exhibit significant atomic-scale disorder. In general, the line widths can be affected by different factors, including paramagnetic effects, static disorder of the solvent or slower molecular motions at low temperature, as indeed observed in biological or organic molecules dispersed in glass-forming solvents or in metal-oxide frameworks.[21,26,49,55] These modifications of the line widths can lead to $\varepsilon^{\mathrm{LW}}_{\mathrm{para}}$, $\varepsilon^{\mathrm{LW}}_{\mathrm{solvent}}$, or $\varepsilon^{\mathrm{LW}}_{\mathrm{T}} < 1$. For instance, for glycine in a glass-forming solvent, $\varepsilon^{\mathrm{LW}}_{\mathrm{para}}\,\varepsilon^{\mathrm{LW}}_{\mathrm{sovent}}\,\varepsilon^{\mathrm{LW}}_{\mathrm{T}} = 0.2$ has been reported.[21] The static magnetic field often affects the line widths in solids, especially for NMR spectra of quadrupolar nuclei and protons, as well as NMR signals dominated by a distribution of isotropic chemical shifts.

The individual contributions and their origins are summarized in Tables 3 and 4. Clearly, the sensitivity enhancements will vary depending on the chemical structure and morphology of the samples, *e.g.*, pore diameter, surface passivation with nonpolar groups, concentration and accessibility of TOTAPOL, and sample treatment, *e.g.*, removal of paramagnetic oxygen that

Table 3 Quantification of the individual contributions to S/N and sensitivity enhancement when comparing experiments A and B for PUP-MSN

			$\varepsilon^{\mathrm{scan}}$		$\varepsilon^{\mathrm{time}}$	
	Experiment A	Experiment B	^{13}C	^{29}Si	^{13}C	^{29}Si
On/Off	H_2O*-LT-on	H_2O*-LT-off	23	23	23	23
Para	H_2O*-LT-off	H_2O-LT-off	0.25	0.58	0.48	1.1
Solvent	H_2O-LT-off	dry-LT-off	2.4	1.6	0.49	0.33
DNP	H_2O*-LT-on	dry-LT-off	14	21	5.5	8.3
T	dry-LT-off	dry-RT-off	1.6	2.0	4.3	5.3
Global	H_2O*-LT-on	dry-RT-off	22	43	23	45

may have a significant effect on $T_1{}^{\mathrm{H}}$ relaxation.[29,56] Whatever the details may be, the time-savings offered by DNP for ^{1}H → ^{13}C and ^{1}H → ^{29}Si CP-MAS spectra of such materials are remarkable.

4.2. Sensitivity enhancement by other techniques

The DNP enhancements have so far been compared with conventional ^{1}H → X CP-MAS experiments at around 100 and 300 K. However, several other approaches can be used to boost the sensitivity of standard NMR. In our earlier studies of organic–inorganic hybrid materials, we took advantage of ^{1}H → ^{13}C → ^{1}H indirectly detected heteronuclear correlation as well as CPMG-based detection of ^{29}Si nuclei.[33,34] Both of these approaches can be combined with DNP. Indeed, Emsley and coworkers have recently used CPMG sequences in 1D DNP-CP-MAS studies of functionalized silica, which yielded appreciable enhancements $\varepsilon^{\mathrm{scan}}_{\mathrm{seq}}$ on the order of 2 to 5.[29] The use of indirect detection would benefit from further improvements of fast spinning at low temperatures. Here, we report 2D ^{1}H–^{13}C and ^{1}H–^{29}Si heteronuclear correlation spectra of the same PUP-MSN sample taken without the assistance of DNP under the best possible conditions currently available in our laboratories.

Fig. 4 shows 1D ^{1}H → ^{13}C CP-MAS spectra and 2D ^{1}H → ^{13}C → ^{1}H spectra of the dry-RT-off sample obtained at 14.1 T. Both data sets were acquired in *the same experimental time*. As expected, the 2D experiment provides useful ^{1}H–^{13}C correlations. More surprisingly, it also yields better S/N ratios for all carbons than the corresponding 1D CP-MAS spectrum (by a factor of ∼2 in the case of C7), thus clearly demonstrating the sensitivity advantage of indirect detection. The comparison with the 1D ^{1}H → ^{13}C DNP-CP-MAS spectrum (H_2O*-LT-on, Fig. 1a) is not straightforward, due to different magnetic fields, different spinning frequencies, the presence of spinning sidebands in the DNP-enhanced spectrum, the use of two consecutive CP steps for indirect detection at room temperature,

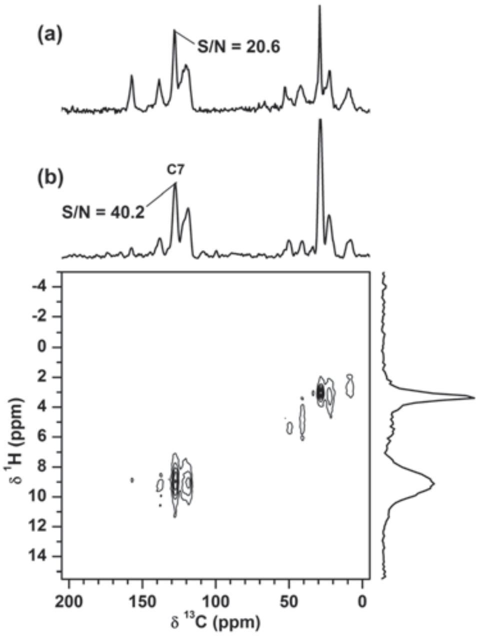

Fig. 4 (a) 1D ^{1}H → ^{13}C conventional CP-MAS spectrum and (b) indirectly detected 2D ^{1}H → ^{13}C → ^{1}H spectrum of PUP-MSNs measured at room temperature (dry-RT-off) at 14.1 T. The spectra were obtained with ν_{R} = 40 kHz, τ_{CP} = 1 ms, $\nu^{\mathrm{C}}_{\mathrm{RF}}$ = 100 kHz during short pulses and CP, $\nu^{\mathrm{H}}_{\mathrm{RF}}$ = 125 kHz during short pulses and 60 kHz during CP, recycle delay τ_{RD} = 1.5 s, $\nu^{\mathrm{H}}_{\mathrm{RF}} = \nu^{\mathrm{C}}_{\mathrm{RF}}$ = 10 kHz during SPINAL64 heteronuclear decoupling,[47] and acquisition time = 3 h 40 min in both experiments: 8600 scans in (a), and 128 increments with Δt_1 = 12.5 μs and 32 scans each in (b). The ^{1}H and ^{13}C projections in (b) are shown in 'skyline' mode, *i.e.* only the positive or negative intensities corresponding to the maximum absolute values are retained.

Table 4 Origin of the different contributions to sensitivity enhancement

	$\varepsilon^{\mathrm{integral}}$	$\varepsilon^{\mathrm{LW}}$	$\varepsilon^{\mathrm{noise}}$	κ
On/Off	(i) e$^-$–^{1}H transfer (ii) ^{1}H–^{1}H spin diffusion	1[a]	1	1[b]
Para	(i) CP transfer (ii) Quenching	Paramagnetic broadening	1	Paramagnetic relaxation
Solvent	CP transfer	Static disorder	1	Reduced mobility
Probe	(i) Filling factor (ii) *Q* factor	Field homogeneity	Thermal noise	1
Seq.	Pulse sequence efficiency	1[c]	1[c]	1
B	Boltzmann	(i) $H_Q{}^{(2)d}$ (ii) Distribution of δ_{iso} (iii) ^{1}H, ^{19}F spectra[e]	$\sqrt{B_0}$	Larmor frequency
T	(i) Boltzmann (ii) CP transfer	(i) Mobility (ii) Decoupling	1	Mobility

[a] Not necessarily when only a fraction of the sample is enhanced by DNP. [b] Valid for DNP by the 'cross-effect' and fast ^{1}H–^{1}H spin diffusion but not in all other cases.[22,52] [c] Not when the sequences differ by the RF irradiation during signal acquisition (use of hetero- or homo-nuclear decoupling, CPMG). [d] Second-order quadrupolar broadening. [e] Reduction of the line broadening due to homonuclear dipolar interactions for a larger difference in resonance frequencies.

the presence of frozen water and its rigidity at low temperatures, and different rotors with capacities of 160 and 8 μL at 9.4 and 14.1 T, respectively. Noting that the ^{13}C spectrum in Fig. 1a was acquired in just 11 min, while the spectra in Fig. 4 required 3 h and 40 min, it is clear that for 1D spectra, DNP-CP-MAS offers a sensitivity advantage over other approaches. However, the measurements of meaningful 2D correlations can be problematic under current DNP conditions because the frozen solvent affects the intermolecular interactions on the surface and, most importantly, participates in the cross-polarization process. In the best of possible worlds, one could envision a combination of indirect detection and solvent-free DNP.[57] This is worthy of pursuit and could greatly expand the limits of modern solid-state NMR.

For heteronuclear correlations of ^{1}H and ^{29}Si, it has been our experience that the sensitivity of indirect detection can be surpassed by direct CPMG-enhanced detection of ^{29}Si signals, which requires only a single CP step and takes advantage of the slow T_2' relaxation of ^{29}Si nuclei.[33,34,58,59] The 2D ^{1}H–^{29}Si CPMG-enhanced spectrum for dry-RT-off sample, processed as described earlier,[25] is shown in Fig. 5, along with 1D ^{1}H → ^{29}Si CP-MAS spectra acquired with and without CPMG under the same conditions at 300 K and 14.1 T. To avoid spectral distortions due to differences in T_2' of ^{29}Si nuclei,[34] only $N_{\mathrm{CPMG}} = 5$ echoes were used, which was sufficient to give an enhancement $\varepsilon_{\mathrm{seq}}^{\mathrm{time}}$(dry-RT-off-CPMG; dry-RT-off) = 2.3 and a good 2D spectrum within a reasonable experimental time ($\sim$18 h). Such ^{1}H–^{29}Si HETCOR spectra are useful to characterize the conformations of functional groups on the silica surfaces.[59] If only the distributions of silicon functionalities need to be characterized, 1D spectra may be sufficient. In this context, DNP enhancement is clearly beneficial, especially for qualitative characterization.[23–25] For PUP-MSN samples, a high-quality DNP-CP-MAS spectrum (Fig. 1b) could be acquired in 22 min at 9.4 T, yielding a similar S/N ratio as a conventional ^{1}H → ^{29}Si CP-MAS spectrum (Fig. 5a) acquired at 14.1 T with a much longer acquisition time of 5.5 h. The change in line shape in the DNP spectrum can be attributed to the much shorter τ_{CP} contact.

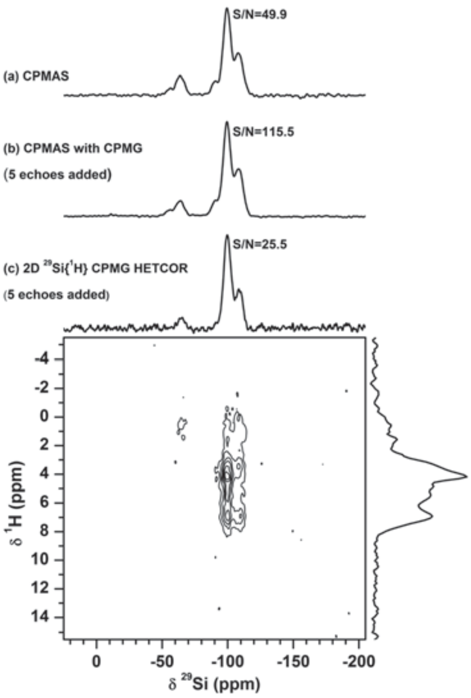

Fig. 5 The ^{1}H → ^{29}Si CP-MAS spectra for dry-RT-off obtained with (a) 1D conventional CP-MAS, (b) 1D CPMG-enhanced CP-MAS, and (c) 2D CPMG-enhanced HETCOR. The spectra were obtained at 14.1 T with $\nu_{\mathrm{R}} = 40$ kHz, $\tau_{\mathrm{CP}} = 7$ ms, $\nu_{\mathrm{RF}}^{\mathrm{Si}} = 100$ kHz during CP and π pulses, $\nu_{\mathrm{RF}}^{\mathrm{H}} = 125$ during π/2 pulse and 60 kHz during CP, $\tau_{\mathrm{CPMG}} = 5$ ms, and $N_{\mathrm{CPMG}} = 5$. The 1D spectra were acquired in 5 h 30 min each. In the 2D experiment, the acquisition involved 64 increments, with 400 scans per increment, $\Delta t_1 = 50$ μs, requiring a total acquisition time = 17 h 45 min. The ^{1}H and ^{29}Si projections are shown in the skyline mode (see caption to Fig. 4).

5. Conclusions

We assessed various contributions to the signal enhancement obtained in DNP-CP-MAS studies of functionalized mesoporous silica nanoparticles (PUP-MSNs) and compared the results with conventional room-temperature CP-MAS measurements on the same systems. When comparing 1D CP-MAS experiments performed at low temperature (around 100 K), the sensitivity enhancement factors attributable to microwave irradiation $\varepsilon_{\mathrm{on/off}}^{\mathrm{time}}(^{13}\mathrm{C}) = \varepsilon_{\mathrm{on/off}}^{\mathrm{time}}(^{29}\mathrm{Si}) = 23$ (see Table 3) exceeded the real DNP sensitivity enhancement factors corrected for quenching and changes in relaxation ($\varepsilon_{\mathrm{DNP}}^{\mathrm{time}}(^{13}\mathrm{C}) = 5.5$ and $\varepsilon_{\mathrm{DNP}}^{\mathrm{time}}(^{29}\mathrm{Si}) = 8.3$). However, the global sensitivity enhancements, adjusted for comparison with conventional 1D CP-MAS at room temperature, were even higher ($\varepsilon_{\mathrm{global}}^{\mathrm{time}}(^{13}\mathrm{C}) = 23$ and $\varepsilon_{\mathrm{global}}^{\mathrm{time}}(^{29}\mathrm{Si}) = 45$). These results confirm that DNP is useful to probe small surface areas and surface species with low concentrations. The imminent development of high-field DNP and improvements of polarizing agents will likely afford higher sensitivity gains and enable novel applications. Solvent-free approaches to DNP should eliminate perturbations due to frozen water which can affect the structure, reactivity, intermolecular interactions and dynamics on silica surfaces. Two-dimensional correlation studies of such materials, combined with indirect detection and CPMG acquisition, which recently became feasible (albeit time consuming) at room temperature should become possible at low temperatures. These techniques will necessitate faster spinning at low temperatures, and thus better control of frictional heating.[39] Possible adverse consequences of fast spinning may include quenching of spin diffusion and losses of DNP efficiency due to modulations of ESR frequencies and the resulting crossings of energy levels.[45,46]

Appendix

A.1. Enhancement factor $\varepsilon^{\mathrm{scan}}$ in the case of partial saturation

For $\tau_{\mathrm{RD}} < 5T_1$, the experimentally determined value $S(\tau_{\mathrm{RD}})$ should be corrected to account for partial saturation. Since the recycle delay τ_{RD} is much longer that the contact time and the duration of signal acquisition, the duration of each scan is roughly equal to τ_{RD} and

$$S(\tau_{\mathrm{RD}}) = S(\infty)\{1\text{-}\exp[-\tau_{\mathrm{RD}}/T_1]\}. \qquad \text{(A.1)}$$

Thus, the general expression for the enhancement per scan is given by

$$\varepsilon^{\mathrm{scan}}(\mathrm{A};\mathrm{B}) = \frac{S_{\mathrm{A}}(\tau_{\mathrm{RD}}(\mathrm{A}))}{S_{\mathrm{B}}(\tau_{\mathrm{RD}}(\mathrm{B}))}\frac{\{1-\exp[-\tau_{\mathrm{RD}}(\mathrm{B})/T_1(\mathrm{B})]\}}{\{1-\exp[-\tau_{\mathrm{RD}}(\mathrm{A})/T_1(\mathrm{A})]\}}\frac{N_{\mathrm{B}}}{N_{\mathrm{A}}}. \tag{A.2}$$

A.2. Proof of eqn (2)

The enhancement factor, $\varepsilon^{\mathrm{scan}}(\mathrm{A};\,\mathrm{B})$, defined by eqn (1), can be written as

$$\varepsilon^{\mathrm{scan}}(\mathrm{A};\,\mathrm{B}) = \varepsilon^{\mathrm{intensity}}(\mathrm{A};\,\mathrm{B})\,\varepsilon^{\mathrm{noise}}(\mathrm{A};\,\mathrm{B}), \tag{A.3}$$

where the enhancement factor for signal intensity is

$$\varepsilon^{\mathrm{intensity}}(\mathrm{A};\mathrm{B}) = \frac{S_{\mathrm{A}}(\infty)}{S_{\mathrm{B}}(\infty)} \tag{A.4}$$

and, correspondingly,

$$\varepsilon^{\mathrm{noise}}(\mathrm{A};\mathrm{B}) = \frac{N_{\mathrm{B}}}{N_{\mathrm{A}}}. \tag{A.5}$$

In the presence of line broadening, one should consider the enhancement of the integrated intensities (II)

$$\varepsilon^{\mathrm{integral}}(\mathrm{A};\mathrm{B}) = \frac{\mathrm{II}_{\mathrm{A}}(\infty)}{\mathrm{II}_{\mathrm{B}}(\infty)}. \tag{A.6}$$

For a Gaussian or Lorentzian lineshape, the integrated intensity II is proportional to the product of the intensity S and the full-width at half maximum (FWHM)

$$\mathrm{II} = \alpha \times S \times \mathrm{FWHM}, \tag{A.7}$$

where $\alpha = 0.5\sqrt{\pi/\ln 2}$ for a Gaussian lineshape and $\pi/2$ for a Lorentzian lineshape. Therefore, in order to emphasize the contributions of the line broadening to $\varepsilon^{\mathrm{scan}}(\mathrm{A};\,\mathrm{B})$, eqn (A.3) can be recast as eqn (2) with

$$\varepsilon^{\mathrm{LW}}(\mathrm{A};\mathrm{B}) = \frac{\mathrm{FWHM}_{\mathrm{B}}(\infty)}{\mathrm{FWHM}_{\mathrm{A}}(\infty)}. \tag{A.8}$$

For a Lorentzian lineshape, $\mathrm{FWHM} = \left(\pi T_2^*\right)^{-1}$ and $\varepsilon^{\mathrm{LW}}(\mathrm{A};\,\mathrm{B})$ is equal to the ratio of T_2^*'s.

A.3. Proof of eqn (3)

The sensitivity, $(\mathrm{S/N})^{\mathrm{time}}$, (*i.e.* the signal-to-noise per unit of time) is given by

$$(\mathrm{S/N})^{\mathrm{time}} = \frac{S(\tau_{\mathrm{RD}})}{N}\sqrt{\frac{1}{\tau_{\mathrm{RD}}}} = \frac{S(\infty)}{N}[1-\exp(-\tau_{\mathrm{RD}}/T_1)]\sqrt{\frac{1}{\tau_{\mathrm{RD}}}}. \tag{A.9}$$

Since the maximum $(\mathrm{S/N})^{\mathrm{time}}$ is achieved for $\tau_{\mathrm{RD}} \sim 1.3T_1$ if one uses a simple 90° excitation pulse,[60] or alternatively for CP with $\tau_{\mathrm{RD}} \sim 1.3T_1(^1\mathrm{H})$, we can define the optimal sensitivity as

$$(\mathrm{S/N})^{\mathrm{time}}_{\mathrm{opt}} = \frac{S(\infty)}{N}\frac{[1-\exp(-1.3)]}{\sqrt{1.3}}\sqrt{\frac{1}{T_1}}. \tag{A.10}$$

The sensitivity enhancement factor is defined as

$$\varepsilon^{\mathrm{time}}(\mathrm{A};\mathrm{B}) = \frac{(S_{\mathrm{A}}/N_{\mathrm{A}})^{\mathrm{time}}_{\mathrm{opt}}}{(S_{\mathrm{B}}/N_{\mathrm{B}})^{\mathrm{time}}_{\mathrm{opt}}}. \tag{A.11}$$

Substituting eqn (A.10) into eqn (A.11) leads to eqn (3).

Acknowledgements

This research was supported at the Ames Laboratory by the U.S. Department of Energy, Office of Basic Energy Sciences. Ames Laboratory is operated for the U.S. Department of Energy by Iowa State University under Contract No. DE-AC02-07CH11358. In Lille, this research was supported by the Region Nord/Pas de Calais, Europe (FEDER), the CNRS, the French Ministry of Science, FR-3050, USTL, ENSCL, Bruker BioSpin, MPNS COST Action EUROHyperPOL TD1103, and the ANR under contract 2010-JCJC-0811-01. In Lausanne, this work was supported by the Commission for Technology and Innovation (CTI), the Swiss National Science Foundation (SNSF) and the EPFL.

Notes and references

1 A. Abragam, *Principles of Nuclear Magnetism*, Oxford, NY, 1961.

2 A. W. Overhauser, *Phys. Rev.*, 1953, **92**, 411–415.

3 T. R. Carver and C. P. Slichter, *Phys. Rev.*, 1953, **92**, 212–213.

4 H. Lock, G. E. Maciel and C. E. Johnson, *J. Mater. Res.*, 1992, **7**, 2791–2797.

5 R. A. Wind, in *Encyclopedia of NMR*, ed. D. M. Grant and R. K. Harris, John Wiley, Chichester, 1996, pp. 1798–1807.

6 S. Sabchevski, T. Idehara, S. Mitsudo and T. Fujiwara, *Int. J. Infrared Millimeter Waves*, 2005, **26**, 1241–1264.

7 C. D. Joye, R. G. Griffin, M. K. Hornstein, K. N. Hu, K. E. Kreischer, M. Rosay, M. A. Shapiro, J. R. Sirigiri, R. J. Temkin and P. P. Woskov, *IEEE Trans. Plasma Sci.*, 2006, **34**, 518–523.

8 M. Rosay, J. C. Lansing, K. C. Haddad, W. W. Bachovchin, J. Herzfeld, R. J. Temkin and R. G. Griffin, *J. Am. Chem. Soc.*, 2003, **125**, 13626–13627.

9 K. N. Hu, H. H. Yu, T. M. Swager and R. G. Griffin, *J. Am. Chem. Soc.*, 2004, **126**, 10844–10845.

10 C. Song, K.-N. Hu, C.-G. Joo, T. M. Swager and R. G. Griffin, *J. Am. Chem. Soc.*, 2006, **128**, 11385–11390.

11 A. B. Barnes, M. L. Mak-Jurkauskas, Y. Matsuki, V. S. Bajaj, P. C. A. van der Wel, R. DeRocher, J. Bryant, J. R. Sirigiri, R. J. Temkin, J. Lugtenburg, J. Herzfeld and R. G. Griffin, *J. Magn. Reson.*, 2009, **198**, 261–270.

12 K.-N. Hu, C. Song, H.-H. Yu, T. M. Swager and R. G. Griffin, *J. Chem. Phys.*, 2008, **128**, 052302.

13 C. F. Hwang and D. A. Hill, *Phys. Rev. Lett.*, 1967, **19**, 1011–1014.

14 T. Maly, G. T. Debelouchina, V. S. Bajaj, K.-N. Hu, C.-G. Joo, M. L. Mak-Jurkauskas, J. R. Sirigiri, P. C. A. van der Wel, J. Herzfeld, R. J. Temkin and R. G. Griffin, *J. Chem. Phys.*, 2008, **128**, 052211.

15 P. C. A. van der Wel, K.-N. Hu, J. Lewandowski and R. G. Griffin, *J. Am. Chem. Soc.*, 2006, **128**, 10840–10846.

16 M. L. Mak-Jurkauskas, V. S. Bajaj, M. K. Hornstein, M. Belenky, R. G. Griffin and J. Herzfeld, *Proc. Natl. Acad. Sci. U. S. A.*, 2008, **105**, 883–888.

17 V. S. Bajaj, M. L. Mak-Jurkauskas, M. Belenky, J. Herzfeld and R. G. Griffin, *Proc. Natl. Acad. Sci. U. S. A.*, 2009, **106**, 9244–9249.

18 A. H. Linden, S. Lange, W. T. Franks, U. Akbey, E. Specker, B.-J. van Rossum and H. Oschkinat, *J. Am. Chem. Soc.*, 2011, **133**, 19266–19269.

19 T. Jacso, W. T. Franks, H. Rose, U. Fink, J. Broecker, S. Keller, H. Oschkinat and B. Reif, *Angew. Chem., Int. Ed.*, 2012, **51**, 432–435.

20 M. Renault, S. Pawsey, M. P. Bos, E. J. Koers, D. Nand, R. Tommassen-van Boxtel, M. Rosay, J. Tommassen, W. E. Maas and M. Baldus, *Angew. Chem., Int. Ed.*, 2012, **51**, 2998–3001.

21 H. Takahashi, D. Lee, L. Dubois, M. Bardet, S. Hediger and G. De Paepe, *Angew. Chem., Int. Ed.*, 2012, **51**, 11766–11769.

22 A. J. Rossini, A. Zagdoun, F. Hegner, M. Schwarzwalder, D. Gajan, C. Coperet, A. Lesage and L. Emsley, *J. Am. Chem. Soc.*, 2012, **134**, 16899–16908.

23 A. Lesage, M. Lelli, D. Gajan, M. A. Caporini, V. Vitzthum, P. Mieville, J. Alauzun, A. Roussey, C. Thieuleux, A. Mehdi, G. Bodenhausen, C. Coperet and L. Emsley, *J. Am. Chem. Soc.*, 2010, **132**, 15459–15461.

24 M. Lelli, D. Gajan, A. Lesage, M. A. Caporini, V. Vitzthum, P. Mieville, F. Heroguel, F. Rascon, A. Roussey, C. Thieuleux, M. Boualleg, L. Veyre, G. Bodenhausen, C. Coperet and L. Emsley, *J. Am. Chem. Soc.*, 2011, **133**, 2104–2107.

25 O. Lafon, M. Rosay, F. Aussenac, X. Lu, J. Trebosc, O. Cristini, C. Kinowski, N. Touati, H. Vezin and J.-P. Amoureux, *Angew. Chem., Int. Ed.*, 2011, **50**, 8367–8370.

26 A. J. Rossini, A. Zagdoun, M. Lelli, J. Canivet, S. Aguado, O. Ouari, P. Tordo, M. Rosay, W. E. Maas, C. Coperet, D. Farrusseng, L. Emsley and A. Lesage, *Angew. Chem., Int. Ed.*, 2012, **51**, 123–127.

27 K. R. Thurber, W.-M. Yau and R. Tycko, *J. Magn. Reson.*, 2010, **204**, 303–313.

28 V. Vitzthum, F. Borcard, S. Jannin, M. Morin, P. Mieville, M. A. Caporini, A. Sienkiewicz, S. Gerber-Lemaire and G. Bodenhausen, *ChemPhysChem*, 2011, **12**, 2929–2932.

29 A. J. Rossini, A. Zagdoun, M. Lelli, D. Gajan, F. Rascon, M. Rosay, W. E. Maas, C. Coperet, A. Lesage and L. Emsley, *Chem. Sci.*, 2012, **3**, 108–115.

30 S. Lange, A. H. Linden, U. Akbey, W. T. Franks, N. M. Loening, B.-J. van Rossum and H. Oschkinat, *J. Magn. Reson.*, 2012, **216**, 209–212.

31 Y. Ishii and R. Tycko, *J. Magn. Reson.*, 2000, **142**, 199–204.

32 J. W. Wiench, C. E. Bronnimann, V. S. Y. Lin and M. Pruski, *J. Am. Chem. Soc.*, 2007, **129**, 12076–12077.

33 J. Trebosc, J. W. Wiench, S. Huh, V. S. Y. Lin and M. Pruski, *J. Am. Chem. Soc.*, 2005, **127**, 7587–7593.

34 J. W. Wiench, V. S. Y. Lin and M. Pruski, *J. Magn. Reson.*, 2008, **193**, 233–242.

35 S. Huh, J. W. Wiench, J. C. Yoo, M. Pruski and V. S. Y. Lin, *Chem. Mater.*, 2003, **15**, 4247–4256.

36 I. I. Slowing, B. G. Trewyn and V. S. Y. Lin, *J. Am. Chem. Soc.*, 2007, **129**, 8845–8849.

37 S. Stoll and A. Schweiger, *J. Magn. Reson.*, 2006, **178**, 42–55.

38 A. B. Barnes, G. De Paepe, P. C. A. van der Wel, K. N. Hu, C. G. Joo, V. S. Bajaj, M. L. Mak-Jurkauskas, J. R. Sirigiri, J. Herzfeld, R. J. Temkin and R. G. Griffin, *Appl. Magn. Reson.*, 2008, **34**, 237–263.

39 M. Rosay, L. Tometich, S. Pawsey, R. Bader, R. Schauwecker, M. Blank, P. M. Borchard, S. R. Cauffman, K. L. Felch, R. T. Weber, R. J. Temkin, R. G. Griffin and W. E. Maas, *Phys. Chem. Chem. Phys.*, 2010, **12**, 5850–5860.

40 P. P. Woskov, V. S. Bajaj, M. K. Hornstein, R. J. Temkin and R. G. Griffin, *IEEE Trans. Microwave Theory Tech.*, 2005, **53**, 1863–1869.

41 K. R. Thurber and R. Tycko, *J. Magn. Reson.*, 2009, **196**, 84–87.

42 O. Lafon, A. S. L. Thankamony, T. Kobayashi, V. V. Carnevale, I. I. Slowing, K. Kandel, H. Vezin, J.-P. Amoureux, G. Bodenhausen and M. Pruski, *J. Phys. Chem. C*, 2013, **117**, 1375–1382.

43 K.-N. Hu, G. T. Debelouchina, A. A. Smith and R. G. Griffin, *J. Chem. Phys.*, 2011, **134**, 125105.

44 E. A. Nanni, A. B. Barnes, Y. Matsuki, P. P. Woskov, B. Corzilius, R. G. Griffin and R. J. Temkin, *J. Magn. Reson.*, 2011, **210**, 16–23.

45 K. R. Thurber and R. Tycko, *J. Chem. Phys.*, 2012, **137**, 084508.

46 F. Mentink-Vigier, U. Akbey, Y. Hovav, S. Vega, H. Oschkinat and A. Feintuch, *J. Magn. Reson.*, 2012, **224**, 13–21.

47 B. M. Fung, A. K. Khitrin and K. Ermolaev, *J. Magn. Reson.*, 2000, **142**, 97–101.

48 S. Balayssac, I. Bertini, A. Bhaumik, M. Lelli and C. Luchinat, *Proc. Natl. Acad. Sci. U. S. A.*, 2008, **105**, 17284–17289.

49 V. Vitzthum, M. A. Caporini and G. Bodenhausen, *J. Magn. Reson.*, 2010, **205**, 177–179.

50 G. R. Khutsishvili, *Sov. Phys. Usp.*, 1969, **11**, 802–815.

51 A. A. Smith, B. Corzilius, A. B. Barnes, T. Maly and R. G. Griffin, *J. Chem. Phys.*, 2012, **136**, 15101.

52 D. S. Wollan, *Phys. Rev. B: Condens. Matter Mater. Phys.*, 1976, **13**, 3671–3685.

53 D. Shimon, Y. Hovav, A. Feintuch, D. Goldfarb and S. Vega, *Phys. Chem. Chem. Phys.*, 2012, **14**, 5729–5743.

54 T. A. Siaw, S. A. Walker, B. D. Armstrong and S.-I. Han, *J. Magn. Reson.*, 2012, **221**, 5–10.

55 V. S. Bajaj, P. C. A. van der Wel and R. G. Griffin, *J. Am. Chem. Soc.*, 2009, **131**, 118–128.

56 C. A. Fyfe and D. H. Brouwer, *J. Am. Chem. Soc.*, 2004, **126**, 1306–1307.

57 A. S. Lilly Thankamony, O. Lafon, X. Lu, F. Aussenac, M. Rosay, J. Trebosc, H. vezin and J.-P. Amoureux, *Appl. Magn. Reson.*, 2012, **43**, 237–250.

58 J. W. Wiench, Y. S. Avadhut, N. Maity, S. Bhaduri, G. K. Lahiri, M. Pruski and S. Ganapathy, *J. Phys. Chem. B*, 2007, **111**, 3877–3885.

59 K. Mao, T. Kobayashi, J. W. Wiench, H.-T. Chen, C.-H. Tsai, V. S. Y. Lin and M. Pruski, *J. Am. Chem. Soc.*, 2010, **132**, 12452–12457.

60 M. Pons, M. Feliz and E. Giralt, *J. Magn. Reson.*, 1988, **78**, 314–320.

Chapter 3

DNP-enhanced ^{27}Al NMR of mesoporous alumina and metal organic frameworks

Aluminium is the third most abundant element in Earth crust (after oxygen and silicon). It is found combined in over 270 different minerals. Because of its abundance and its low toxicity, compounds with aluminium have a wide range of applications and are present in many inorganic materials. The only stable isotope of aluminium is ^{27}Al, which has a natural abundance of 100% and a spin value $I = 5/2$. ^{27}Al nuclei have a nuclear quadrupole moment arising from a non-spherical distribution of nuclear electrical charge and the quadrupolar coupling constant, C_Q, ranges between 0 and 16 MHz. These nuclear quadrupole moments interact with electric field gradients at the position of the nucleus.[1] These quadrupolar interactions lead to broadening and distortion of the spectral peaks and cause displacement from the isotropic chemical shift.[2] Furthermore, the intricate nuclear spin dynamics of the quadrupolar nuclei in the presence of rf fields and sample rotation strongly reduces the efficiency of homo- and hetero-nuclear correlation experiments, involving quadrupolar nuclei, such as ^{27}Al. Therefore, the observation of homo- and hetero-nuclear proximities with ^{27}Al can be challenging,[3] especially for diluted species, such as surface sites or defects. Here, we show how the low efficiency of advanced NMR techniques for ^{27}Al nuclei can be negated by sensitivity enhancement produced by DNP. This sensitivity enhancement is demonstrated for two advanced materials: (i) mesoporous alumina and (ii) aluminium-containing metal-organic frameworks (MOF). ^{27}Al DNP-enhanced experiments have only been reported so far for ^{1}H→^{27}Al CP and CP-MQMAS experiments on γ-alumina.

3-1. Observation of ^{27}Al-^{27}Al proximities near the surface of mesoporous alumina

Mesoporous alumina is a highly promising material for many applications, including heterogeneous catalysis or protein bioadsorption.[4-6] Mesoporous alumina benefits from a high accessibility and a high proportion of penta-coordinated Al sites, which can act as binding sites for catalytically active phase.[7] Here we show that ^{27}Al-^{27}Al proximities near the interface of mesoporous alumina can be probed by combining the DNP sensitivity enhancements and advanced ^{27}Al-^{27}Al homonuclear dipolar-mediated correlation experiments.[8] For mesoporous alumina, DNP yielded 4−5 orders of magnitude of time savings compared with conventional solid-state NMR experiments. DNP sensitivity enhancements negate the low efficiency of cross-polarization and dipolar recoupling for quadrupolar nuclei. In this study, the important presence of penta-coordinated Al in mesoporous alumina has not only been observed, but its role in bridging interfacial tetra- and hexa-coordinated Al has been determined. Such structural information, collected at low temperature (~103 K) and 9.4 T with the use of DNP, would have been impossible to obtain under standard conditions, even using a higher magnetic field. However, here it is demonstrated that this information can be obtained in only 4 h.

3-2. Observation of ^{13}C-^{27}Al proximities in aluminium-containing MOF

Metal-organic frameworks (MOFs) have attracted increasing attention owing to their high surface area and their wide range of three-dimensional (3D) architectures that exhibit different pore apertures and chemical tunabilities. These hybrid materials represent promising systems for gas storage, catalysis, capture of radioactive compounds, and drug delivery.[9,10] Amongst them, aluminium-based MOFs, such as MIL-100(Al),[11] present many advantages, including low cost, density and toxicity, remarkable thermal stability and high Lewis acidity that should allow many industrial applications.

Rational design of MOFs requires a clear understanding of structure-property relationships and hence requires characterization methods endowed with atomic resolution. In particular, solid-state NMR is well suited to assess structural models of MOF frameworks, to probe the organization of extra-framework entities[12] and to analyze atomic-level dynamics.[13,14,15,16] However, the poor sensitivity of NMR limits the observation of adsorbed species, defects, etc., particularly when the observed nuclei have low gyromagnetic ratios, low natural abundances or long longitudinal relaxation times (T_1). Besides, the observation of ^{27}Al-^{13}C proximities by NMR in Al-based MOFs has hitherto been hindered by limitations of common NMR probes, which cannot be tuned simultaneously to nearby ^{27}Al and ^{13}C Larmor frequencies.

We have reported the first observation of ^{27}Al-^{13}C proximities in MOFs using advanced NMR methods, such as *D*-HMQC and S-RESPDOR, combined with a frequency splitter. We have shown that DNP can significantly reduce acquisition times for MIL-100(Al) at 100 K. EPR spectroscopy and DNP enhancements proved that the biradical TOTAPOL enters the MIL-100(Al) cavities within tens of minutes, although its apertures are smaller than 0.88 nm. Besides, DNP-enhanced ^{27}Al-^{13}C correlation experiments demonstrated that the MIL-100(Al) framework is not altered by impregnation with a TOTAPOL solution. So far, DNP of MOFs has only been demonstrated for 1D spectra under MAS using $^{1}H\rightarrow^{13}C$ and $^{1}H\rightarrow^{15}N$ CP and 2D ^{1}H-^{13}C correlation spectroscopy of In-based MIL-68.

Thus, these works on γ-alumina and MIL100 (Al) clearly open a new avenue for the application of ss-NMR to quadrupolar nuclei and notably the atomic-scale structure determination of catalysis materials.

References:

1 K.J.D. MacKenzie and M.E. Smith, *Multinuclear Solid-State Nuclear Magnetic Resonance of Inorganic Materials*, Pergamon, 2002.
2 A.P.M. Kentgens, *Geoderma*, 1997, **80**, 271-306.
3 J.C.C. Chan, *Journal of Magnetic Resonance*, 1999, **140**, 487-490.
4 Q. Yuan, A.X. Yin, C. Luo, L.D. Sun, Y.W. Zhang, W.T. Duan, H.C. Liu and C.H. Yan, *Journal of the American Chemical Society*, 2008, **130**, 3465-3472.
5 J.P. Dacquin, J.R.M. Dhainaut, D. Duprez, S.B. Royer, A.F.Lee and K. Wilson, *Journal of the American Chemical Society*, 2009, **131**, 12896-12897.
6 S.A. El-Safty, M.A. Shenashen, M. Ismael and M. Khairy, *Chemical Communications*, 2012, **48**, 6708-6710.
7 J.H. Kwak, J. Hu, D. Mei, C.W. Yi, D.H. Kim, C.H.F. Peden, L.F. Allard and J. Szanyi, *Science*, 2009, **325**, 1670-1673.
8 D. Lee, H. Takahashi, A.S.L. Thankamony, J.P. Dacquin, M. Bardet, O. Lafon and G. De Paëpe, *Journal of the American Chemical Society*, 2012, **134**, 18491-18494.
9 J.R. Long and O.M. Yaghi, *Chemical Society Reviews*, 2009, **38**, 1213-1214.
10 H.C. Zhou, J.R. Long and O.M. Yaghi, *Chemical Reviews*, 2012, **112**, 673-674.
11 C. Volkringer, D. Popov, T. Loiseau, G. Ferey, M. Burghammer, C. Riekel, M. Haouas and F. Taulelle, *Chemistry of Materials*, 2009, **21**, 5695-5697.
12 M. Haouas, C. Volkringer, T. Loiseau, G. Ferey and F. Taulelle, *Chemistry-a European Journal*, 2009, **15**, 3139-3146.
13 S. Horike, R. Matsuda, D. Tanaka, S. Matsubara, M. Mizuno, K. Endo and S. Kitagawa, *Angew. Chem.-Int. Ed.*, 2006, **45**, 7226-7230.
14 L.C. Lin, J. Kim, X.Q. Kong, E. Scott, T.M. McDonald, J.R. Long, J.A. Reimer and B. Smit, *Angew. Chem.-Int. Ed.*, 2013, **52**, 4410-4413.
15 H.C. Hoffmann, M. Debowski, P. Muller, S. Paasch, I. Senkovska, S. Kaskel and E. Brunner, *Materials*, 2012, **5**, 2537-2572.
16 A. Sutrisno and Y.N. Huang, *Solid State Nuclear Magnetic Resonance*, 2013, **49-50**, 1-11.

J|A|C|S
JOURNAL OF THE AMERICAN CHEMICAL SOCIETY
Communication
pubs.acs.org/JACS

Enhanced Solid-State NMR Correlation Spectroscopy of Quadrupolar Nuclei Using Dynamic Nuclear Polarization

Daniel Lee,[†] Hiroki Takahashi,[†] Aany S. L. Thankamony,[‡] Jean-Philippe Dacquin,[‡] Michel Bardet,[†] Olivier Lafon,[‡] and Gaël De Paëpe*,[†]

[†]Laboratoire de Chimie Inorganique et Biologique (SCIB), UMR-E 3 CEA/UJF-Grenoble 1, Institut Nanosciences et Cryogénie (INAC), F-38054 Grenoble, France.

[‡]Université Lille Nord de France, 59000 Lille, CNRS UMR 8181, Unité de Catalyse et de Chimie du Solide (UCCS), Université de Lille 1, Bât. C7, F-59652, Villeneuve d'Ascq, France

Supporting Information

ABSTRACT: By means of a true sensitivity enhancement for a solid-state NMR spectroscopy (SSNMR) experiment performed under dynamic nuclear polarization (DNP) conditions, corresponding to 4−5 orders of magnitude of time savings compared with a conventional SSNMR experiment, it is shown that it is possible to record interface-selective ^{27}Al−^{27}Al two-dimensional dipolar correlation spectra on mesoporous alumina, an advanced material with potential industrial applications. The low efficiency of cross-polarization and dipolar recoupling for quadrupolar nuclei is completely negated using this technique. The important presence of pentacoordinated Al has not only been observed, but its role in bridging interfacial tetra- and hexacoordinated Al has been determined. Such structural information, collected at low temperature (∼103 K) and 9.4 T with the use of DNP, would have been impossible to obtain under standard conditions, even using a higher magnetic field. However, here it is demonstrated that this information can be obtained in only 4 h. This work clearly opens a new avenue for the application of SSNMR to quadrupolar nuclei and notably the atomic-scale structure determination of catalysis materials such as mesoporous alumina.

Porous materials are a cornerstone of the chemical industry since they can be employed in heterogeneous catalysis, separation processes, sensors, photonics, biomaterials, etc. However, their rational design is currently limited by the lack of applicable atomic-resolution characterization methods. NMR spectroscopy can provide detailed information on the atomic-level structure and dynamics of these heterogeneous and often disordered systems. Unfortunately, the intrinsic insensitivity of NMR spectroscopy impedes the examination of interfaces, which are crucial to the properties of porous materials.

On the basis of the pioneering work of Griffin and co-workers,[1] recent developments in the combination of solid-state NMR spectroscopy (SSNMR) under magic-angle spinning (MAS) with dynamic nuclear polarization (DNP) at high magnetic field have facilitated the acquisition of high-resolution NMR spectra with greatly enhanced signal-to-noise ratios (S/N).[2] This heralds the imagination and implementation of previously unrealistic experiments. In this work, one such experiment has been performed on technologically and catalytically important mesoporous alumina (Al_2O_3).[3] This thermally stable (800 °C) and high-surface-area material (typically 200−400 m^2 g^{-1}) possessing ordered mesopores (Figure 1 a) has a high concentration of research interest due to its catalytic significance in the production of biodiesel[4] along with many other applications.[5] Utilizing "green" and renewable fuels is forever becoming increasingly important, and understanding mesoporous alumina and its specific role in the catalysis of biodiesel production will lead to improved manufacturing methods and therefore increased system viability.

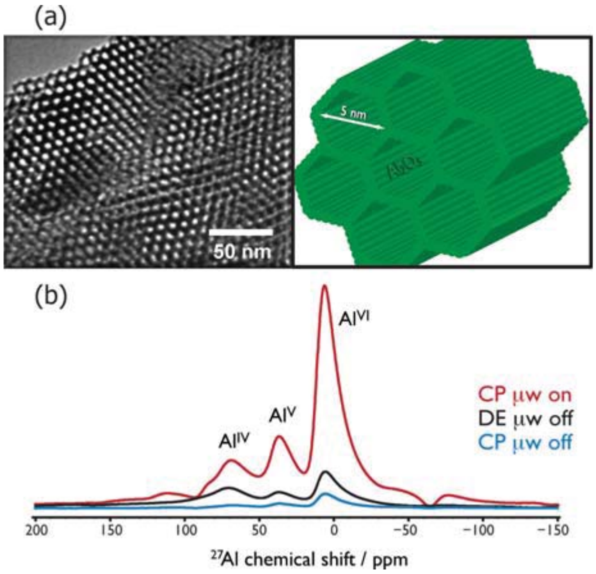

Figure 1. (a) Transmission electron micrograph (left) and associated schematic (right) showing the presence of ordered hexagonal mesopores throughout the alumina sample studied in this work. (b) ^{27}Al NMR spectra of this sample recorded with a MAS rate of 8 kHz and a sample temperature of ∼103 K.

Received: August 5, 2012
Published: October 24, 2012

dx.doi.org/10.1021/ja307755t | *J. Am. Chem. Soc.* 2012, 134, 18491−18494

A particular obstacle when knowledge of the local environment of ^{27}Al nuclei is desired is that conventional SSNMR radiofrequency (RF) irradiation sequences return very low efficiencies for quadrupolar nuclei. However, herein it is shown that in spite of the difficulties arising from the quadrupolar nature of ^{27}Al, DNP-enhanced SSNMR can be used to perform sophisticated yet fast interface-selective characterization measurements. Previous studies have shown that when protons are located only at the surface/interface of much larger systems, cross-polarization (CP) from protons to the nuclei of interest can result in a surface/interface-selective technique.[6] This technique has been combined with DNP to study surfaces with greatly improved sensitivity[7] as well as γ-alumina, where CP is very inefficient.[8]

In this work, the DNP is dominated by the cross-effect (CE)[9] between two unpaired electrons in a biradical (TOTAPOL[10]) and protons in a glass-forming solvent matrix or at the interface in the mesoporous alumina. The experiments were performed on a Bruker BioSpin DNP-SSNMR spectrometer[11] equipped with a gyrotron and connecting transmission line that is able to provide microwave (μw) irradiation at 263 GHz and ~5 W at the sample, in combination with an AVANCE III 400 MHz wide-bore NMR system and a low-temperature MAS probe capable of achieving spinning rates of up to 17 kHz for 3.2 mm rotors at sample temperatures of ~100 K.

The "DNP-ready" sample was prepared by impregnation with an excess of solution.[12] The mesoporous alumina was first heated to 408 K for 6 h to ensure that the sample, including the pores, was dry. A 46 μL aliquot of TOTAPOL solution [20 mM in a glass-forming mixture of [$^2H_6$]DMSO, H_2O, and ^2H_2O (78, 8, 14 wt %, respectively)] was added to cover 28 mg of the mesoporous alumina powder. This mixture was stirred vigorously and then left to rest at room temperature for 24 h to allow time for the impregnation of the pores by the DNP chemical matrix. A repetition of centrifuging the mixture followed by pipetting any supernatant was employed to remove the excess liquid. The remaining wet powder was added to a thin-walled zirconia 3.2 mm MAS rotor. It must be stated that unlike other systems, here it was not necessary to dissolve/disperse[1] the impregnated mesoporous alumina in the DNP matrix, allowing this system to benefit from the ability to use the maximum possible amount of the sample of interest without compromising the DNP enhancement.

The NMR signal enhancement as a result of DNP in this system can be seen in Figure 1 b. With μw irradiation, the CE enhances the polarization of protons within the sample. This polarization is then transferred to the central transition (CT) of the ^{27}Al nuclei via low-power CP under MAS (CPMAS),[13] and the resulting spectrum is recorded (red line). The experiment is repeated under the same conditions except without the μw irradiation (blue line). Here, the DNP enhancement, ε, is measured simply by comparing the intensities of the spectral peaks resulting from the CPMAS experiments with and without μw irradiation. For this system, ε was measured to be 15 for each of the ^{27}Al peaks. For comparison, the direct excitation under MAS (DEMAS) spectrum of ^{27}Al is also shown as the black line in Figure 1 b. As an aside, a similar DNP-ready sample that used an impregnation time of only 1 h was also tested and found to have $\varepsilon = 11$. Thus, it appears that longer impregnation times are necessary to facilitate the penetration of the TOTAPOL solution into the pores.

In the spectra in Figure 1 b, three discrete ^{27}Al peaks can be seen. These correspond to hexacoordinated Al^{VI} ($\delta_{^{27}Al} = 5$ ppm), pentacoordinated Al^{V} ($\delta_{^{27}Al} = 36$ ppm), and tetracoordinated Al^{IV} ($\delta_{^{27}Al} = 70$ ppm) sites. Contrary to the literature,[8] the substantial presence of Al^{V} resonances observed here indicates that the water-based DNP matrix does not significantly coordinate to these sites, and thus, this solution is applicable for the study of Al^{V} sites using DNP-enhanced SSNMR measurements of similar systems. Furthermore, this abundance of Al^{V} sites at the interface demonstrates the industrial potential for this mesoporous alumina. Not only does this system exhibit greater surface area than the more commonly employed γ-alumina, but it also appears that these Al^{V} sites, which can act as binding sites for the active phase,[14] are much more plentiful.

Not only does the impregnation solution provide the biradical necessary for DNP and the glass-forming solvents to best utilize this biradical, but this matrix also provides extra protons that enhance the CP signal, irrespective of DNP. Furthermore, the requirement of low temperatures for efficient DNP has the added advantage of increasing the nuclear relaxation times, whereas the usually fast relaxation of quadrupolar nuclei during spin-lock periods limits the success of CP for measurements at room temperature. The combination of low temperatures and the addition of these extra useful protons means that the time savings using this system for DNP-enhanced CPMAS experiments, relative to ubiquitous SSNMR systems, cannot be predicted by simply allowing for the DNP enhancement, the low-temperature gain (Boltzman factor and reduced thermal noise) while taking into account sample "bleaching",[15] and the change in relaxation times due to the paramagnetic effects of the added biradical. The only true comparison in this (and similar) system(s) is to record spectra under specific DNP conditions and under normal SSNMR conditions and compare the S/N per unit time.[16] It should be noted that resolution is also an extremely important factor, and the apparent line widths should also be taken into account. In this system, however, the line widths are dominated by disorder, and there are negligible changes between the two sets of experimental conditions. A similar CPMAS experiment was recorded under conventional SSNMR conditions (9.4 T, 298 K, 8 kHz MAS on a 3.2 mm rotor; data not shown). Comparing the S/N per unit time for the DNP-enhanced CPMAS spectrum with that for the conventional CPMAS spectrum showed that using DNP for this system gave $\varepsilon = 184$, corresponding to a time-saving factor of ~34000. This demonstrates the considerable advantage of using DNP in the study of this system.

A comparison of the DNP-enhanced CPMAS and the DEMAS NMR signal intensities for each Al coordination state can give only a very crude indication of the influence of protons on each state. The ^{27}Al^{IV}, ^{27}Al^{V}, and ^{27}Al^{VI} peaks were 2.4, 4.6, and 6.1 times larger in the DNP-enhanced CPMAS spectrum, respectively. Notably, the line widths (and thus the apparent transverse dephasing times, T_2^*) did not vary between the two spectra, and accordingly, proton couplings were not the limiting factor of these line widths. A more complete analysis of the relative influence of protons can be performed using measurements of T_2', the time constant associated with the homogeneous contribution to the transverse dephasing, which cannot be refocused with a π pulse. T_2' values were measured using a pseudo-two-dimensional (pseudo-2D) spin−echo experiment with various rotor-synchronized echo times, the pulse sequence for which is given in Figure S1 in the Supporting Information. Figure 2 shows the results of such measurements for each of the Al peaks in the mesoporous

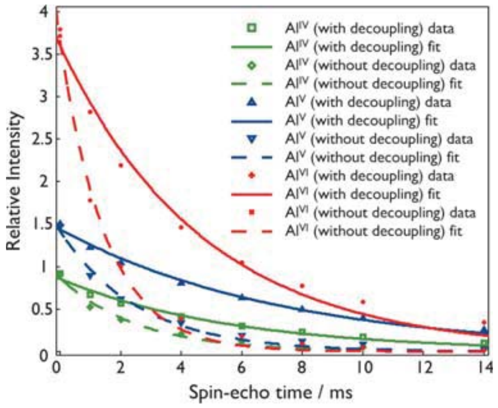

Figure 2. Normalized intensity decays for the ^{27}Al peaks with and without 100 kHz SPINAL-64 heteronuclear decoupling during a spin−echo period, as functions of the (rotor-synchronized) spin−echo time, from which T_2' values were determined. This DNP-enhanced experiment was performed using a MAS rate of 8 kHz, a sample temperature of ∼103 K, and the pulse sequence shown in Figure S1.

alumina sample with and without heteronuclear decoupling. These data demonstrate the effect protons have on each T_2' value and thus on each Al site. Notably, the employed heteronuclear decoupling was deemed sufficient in that an increase in power did not affect the value of T_2' (this was observed for optimized SPINAL-64 decoupling[17] with powers above 90 kHz; data not shown). The ratios of the T_2' value measured with decoupling to the value measured without decoupling were 2.3 for Al^{IV}, 2.9 for Al^{V}, and 3.2 for Al^{VI}. This is in agreement with the relative intensities of the CPMAS and DEMAS spectra. These corroborating observations indicate that the interfacial Al^{VI} sites are more heavily influenced by protons than the interfacial Al^{V} sites, which in turn are more heavily influenced by protons than the interfacial Al^{IV} sites. This is consistent with an increase in the number of hydroxo or aqua groups with increasing coordination number.

The lack of change in T_2^* for each spectral peak in the CPMAS and DEMAS experiments noted above could indicate that heteronuclear decoupling is not necessary. Nonetheless, as clearly shown in Figure 2, protons have a significant impact on the spin dynamics of ^{27}Al nuclei. Moreover, in this system the large influence of protons is not just limited to experiments that begin with a CP step. This realization is beyond the scope of the present work but will be discussed in detail in a future publication.

Figure 2 illustrates the importance of the heteronuclear decoupling during the spin−echo period; these periods (and thus the T_2' values) are vital in most SSNMR experiments involving J couplings.[18] A further demonstration of its importance is given in Figure S2, which compares the spectral intensities of each ^{27}Al coordination state after CP and then a spin−echo period with a total duration of 4 ms with and without ^{1}H decoupling. Globally, the intensities without decoupling are reduced by 60% relative to those with decoupling. T_2' values are also important in SSNMR experiments involving dipolar couplings (REDOR-type experiments, etc.[19]). Furthermore, other dipolar recoupling sequences experience magnetization decay times on the order of T_2' that can also be heavily affected by proton couplings. Thus, heteronuclear decoupling during these sequences can also be highly beneficial, as long as interference effects are avoided.

The supercycled symmetry-based dipolar recoupling sequence BR2$_2$[1] has been shown to be of great utility when recording homonuclear correlation spectra.[20] However, the use of this and other[21] sequences for ^{27}Al has been limited to bulk studies because of their low efficiency (∼5%), which results from the intricate spin dynamics of quadrupolar nuclei in the presence of an RF field and MAS. The entirety of the adapted pulse sequence used here for interface-selective, DNP-enhanced correlation spectroscopy of quadrupolar nuclei is given in Figure S1. This pulse sequence first transfers hyperpolarized proton magnetization to nearby half-integer-spin quadrupolar nuclei via a CP step. Next, the sequence creates double-quantum (DQ) coherences between the CTs of dipolar-coupled quadrupolar nuclei while removing DQ coherence contributions involving satellite transitions of a single ^{27}Al nucleus. The spectra resulting from this sequence then give information about the spatial proximities between neighboring nuclei. The variables of this experiment can be optimized using a one-dimensional (1D) version (no indirect-dimension increments) that can also be used to demonstrate the importance of heteronuclear decoupling during the recoupling periods and also the whole sequence (Figure S2). Moreover, demanding experiments usually require careful calibrations of pulses and delays. Here, calibrations of the parameters required for maximum efficacy of the recoupling sequence could be performed on the sample of interest in <1 h because of the huge gain in S/N due to the DNP conditions. Under conventional SSNMR conditions, these calibrations would require much longer experimental times even with model samples.

Once calibrated, the 2D version of this pulse sequence was used to record the first correlation spectra of quadrupolar nuclei using DNP. Furthermore, since the sequence begins with a CP step, the only observed correlations would be between interfacial ^{27}Al nuclei. Spectra resulting from the implementation of this sequence on the mesoporous alumina sample are shown in Figure 3. It has been shown that the BR2$_2$[1] recoupling sequence has an offset dependence,[20a] so three spectra with different offsets were recorded to remove any uncertainty in the data. Possibly the most striking point is that each spectrum took only ∼4 h to acquire. Under conventional SSNMR conditions, the acquisition of equivalent data would require over 15 years for each spectrum! It can be seen that dipolar correlations between all sites are present (including same-site correlations between different nuclei, e.g., Al^{VI}−Al^{VI} correlations), except for Al^{IV}−Al^{VI} correlations. Therefore, at the interface of this material Al^{V} sites connect Al^{IV} and Al^{VI} sites.

To summarize, DNP enhancements (ε) of ∼15 have been observed on an industrially important sample of mesoporous alumina using a 9.4 T DNP-SSNMR spectrometer. More importantly, this translates into a true sensitivity gain per unit time of 184 relative to equivalent room-temperature measurements. Transcending the sensitivity limitations of cross-polarization and also dipolar recoupling for quadrupolar nuclei, the corresponding 4−5 orders of magnitude of time savings allow not only very fast 1D CPMAS and pseudo-2D experiments but also interface-selective 2D homonuclear dipolar correlation experiments to be performed. These 1D and 2D experiments clearly demonstrate that spatial proximities involving quadrupolar nuclei can be probed using DNP-enhanced SSNMR with greatly reduced time scales. Moreover, the absence of Al^{IV}−Al^{VI} correlations combined with the presence of Al^{IV}−Al^{V} and Al^{V}−Al^{VI} correlations shows that

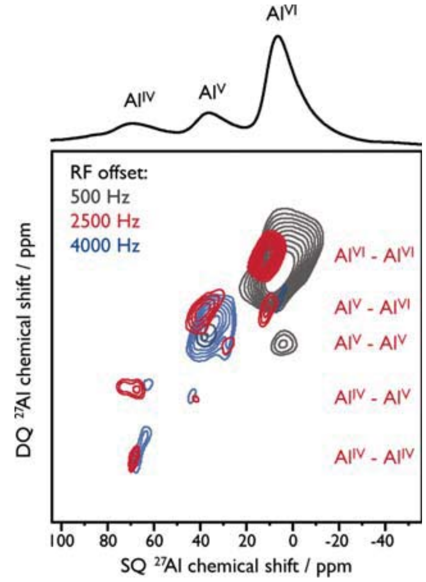

Figure 3. DNP-enhanced, interface-selective DQ−SQ ^{27}Al homonuclear dipolar correlation spectra of mesoporous alumina recorded using a MAS rate of 8 kHz, a sample temperature of ∼103 K, and the pulse sequence shown in Figure S1. The total acquisition time for each spectrum was ∼4 h. For illustrative purposes, the DNP-enhanced CPMAS spectrum (Figure 1 b), with the three different Al peaks labeled, is shown at the top.

interfacial Al^{IV} and Al^{VI} sites are bridged by interfacial Al^{V}. These structural data, together with the results of the influence of protons on the T_2' of each interfacial site, can be combined with ab initio calculations to help elucidate the surface structure of this amorphous material. This work is planned for a future publication.

■ ASSOCIATED CONTENT

Ⓢ Supporting Information

Experimental details, pulse sequence diagrams, and spectra demonstrating the importance of heteronuclear decoupling. This material is available free of charge via the Internet at http://pubs.acs.org.

■ AUTHOR INFORMATION

Corresponding Author

gael.depaepe@cea.fr

Notes

The authors declare no competing financial interest.

■ ACKNOWLEDGMENTS

This work was supported by the ANR (ANR08-CEXC-003-01) and funding from the RTB. G.D.P. was supported by EU Marie Curie (PIEF-GA- 2009-237646) for part of the work. D.L. was supported by CEA-EUROTALENTS (PCOFUND-GA-2008-228664). Dr. M. Giffard is acknowledged for the synthesis of the TOTAPOL biradical. The UCCS members are grateful for funding provided by Region Nord/Pas de Calais, Europe (FEDER), CNRS, the French Minister of Science, FR-3050, USTL, ENSCL, and ANR-2010-JCJC-0811-01. O.L. and A.S.L.T. acknowledge X. Lu, J. Trébosc, H. Vezin, and J.-P. Amoureux for helpful discussions.

■ REFERENCES

(1) Hall, D. A.; Maus, D. C.; Gerfen, G. J.; Inati, S. J.; Becerra, L. R.; Dahlquist, F. W.; Griffin, R. G. *Science* **1997**, *276*, 930.

(2) Barnes, A. B.; Paëpe, G. D.; van der Wel, P. C.; Hu, K. N.; Joo, C. G.; Bajaj, V. S.; Mak-Jurkauskas, M. L.; Sirigiri, J. R.; Herzfeld, J.; Temkin, R. J.; Griffin, R. G. *Appl. Magn. Reson.* **2008**, *34*, 237.

(3) Dacquin, J.-P.; Dhainaut, J.; Duprez, D.; Royer, S.; Lee, A. F.; Wilson, K. *J. Am. Chem. Soc.* **2009**, *131*, 12896.

(4) Wilson, K.; Lee, A. F.; Dacquin, J.-P. In *Catalysis for Alternative Energy Generation*; Springer: Berlin, 2012; pp 263−304.

(5) (a) Bejenaru, N.; Lancelot, C.; Blanchard, P.; Lamonier, C.; Rouleau, L.; Payen, E.; Dumeignil, F.; Royer, S. *Chem. Mater.* **2009**, *21*, 522. (b) Granger, P.; Parvulescu, V. I. *Chem. Rev.* **2011**, *111*, 3155.

(6) (a) Agarwal, G. K.; Titman, J. J.; Percy, M. J.; Armes, S. P. *J. Phys. Chem. B* **2003**, *107*, 12497. (b) Lee, D.; Balmer, J. A.; Schmid, A.; Tonnar, J.; Armes, S. P.; Titman, J. J. *Langmuir* **2010**, *26*, 15592.

(7) (a) Lock, H.; Maciel, G. E.; Johnson, C. E. *J. Mater. Res.* **1992**, *7*, 2791. (b) Lesage, A.; Lelli, M.; Gajan, D.; Caporini, M. A.; Vitzthum, V.; Miéville, P.; Alauzun, J.; Roussey, A.; Thieuleux, C.; Mehdi, A.; Bodenhausen, G.; Copéret, C.; Emsley, L. *J. Am. Chem. Soc.* **2010**, *132*, 15459. (c) Rossini, A. J.; Zagdoun, A.; Lelli, M.; Canivet, J.; Aguado, S.; Ouari, O.; Tordo, P.; Rosay, M.; Maas, W. E.; Copéret, C.; Farrusseng, D.; Emsley, L.; Lesage, A. *Angew. Chem., Int. Ed.* **2012**, *51*, 123.

(8) Vitzthum, V.; Miéville, P.; Carnevale, D.; Caporini, M. A.; Gajan, D.; Copéret, C.; Lelli, M.; Zagdoun, A.; Rossini, A. J.; Lesage, A.; Emsley, L.; Bodenhausen, G. *Chem. Commun.* **2012**, *48*, 1988.

(9) (a) Kessenikh, A. V.; Manenkov, A. A.; Pyatnitskii, G. I. *Sov. Phys. Solid State* **1964**, *6*, 641. (b) Hwang, C. F.; Hill, D. A. *Phys. Rev. Lett.* **1967**, *19*, 1011.

(10) Song, C.; Hu, K. N.; Joo, C. G.; Swager, T. M.; Griffin, R. G. *J. Am. Chem. Soc.* **2006**, *128*, 11385.

(11) Rosay, M.; Tometich, L.; Pawsey, S.; Bader, R.; Schauwecker, R.; Blank, M.; Borchard, P. M.; Cauffman, S. R.; Felch, K. L.; Weber, R. T.; Temkin, R. J.; Griffin, R. G.; Maas, W. E. *Phys. Chem. Chem. Phys.* **2010**, *12*, 5850.

(12) (a) Haber, J.; Block, J. H.; Delmon, B. *Pure Appl. Chem.* **1995**, *67*, 1257. (b) Lafon, O.; Rosay, M.; Aussenac, F.; Lu, X. Y.; Trebosc, J.; Cristini, O.; Kinowski, C.; Touati, N.; Vezin, H.; Amoureux, J. P. *Angew. Chem., Int. Ed.* **2011**, *50*, 8367.

(13) (a) Vega, A. J. *Solid State Nucl. Magn. Reson.* **1992**, *1*, 17. (b) Amoureux, J.-P.; Pruski, M. *Mol. Phys.* **2002**, *100*, 1595.

(14) (a) Kwak, J. H.; Hu, J. Z.; Kim, D. H.; Szanyi, J.; Peden, C. H. F. *J. Catal.* **2007**, *251*, 189. (b) Kwak, J. H.; Hu, J.; Mei, D.; Yi, C.-W.; Kim, D. H.; Peden, C. H. F.; Allard, L. F.; Szanyi, J. *Science* **2009**, *325*, 1670.

(15) (a) Thurber, K. R.; Yau, W.-M.; Tycko, R. *J. Magn. Reson.* **2010**, *204*, 303. (b) Vitzthum, V.; Borcard, F.; Jannin, S.; Morin, M.; Miéville, P.; Caporini, M. A.; Sienkiewicz, A.; Gerber-Lemaire, S.; Bodenhausen, G. *ChemPhysChem* **2011**, *12*, 2929.

(16) Takahashi, H.; Lee, D.; Dubois, L.; Bardet, M.; Hediger, S.; De Paëpe, G. *Angew. Chem., Int. Ed.* **2012**, DOI: 10.1002/anie.201206102.

(17) Fung, B. M.; Khitrin, A. K.; Ermolaev, K. *J. Magn. Reson.* **2000**, *142*, 97.

(18) (a) Fyfe, C. A.; Wong-Moon, K. C.; Huang, Y.; Grondey, H. *J. Am. Chem. Soc.* **1995**, *117*, 10397. (b) Lesage, A.; Bardet, M.; Emsley, L. *J. Am. Chem. Soc.* **1999**, *121*, 10987. (c) Lee, D.; Struppe, J.; Elliott, D. W.; Mueller, L. J.; Titman, J. J. *Phys. Chem. Chem. Phys.* **2009**, *11*, 3547.

(19) Gullion, T.; Schaefer, J. *J. Magn. Reson.* **1989**, *81*, 196.

(20) (a) Wang, Q.; Hu, B.; Lafon, O.; Trebosc, J.; Deng, F.; Amoureux, J. P. *J. Magn. Reson.* **2009**, *200*, 251. (b) Lafon, O.; Trebosc, J.; Hu, B. W.; De Paëpe, G.; Amoureux, J. P. *Chem. Commun.* **2011**, *47*, 6930.

(21) (a) Eden, M.; Zhou, D.; Yu, J. *Chem. Phys. Lett.* **2006**, *431*, 397. (b) Hansen, M. R.; Jakobsen, H. J.; Skibsted, J. *J. Phys. Chem. C* **2008**, *112*, 7210.

Supporting Information

Enhanced solid-state NMR correlation spectroscopy of quadrupolar nuclei using dynamic nuclear polarization

Extra Experimental Details.

All experiments were performed on a Bruker BioSpin 263 GHz/400 MHz solid-state DNP-NMR spectrometer. It is worth noting that the application of the microwave (μw) power required to reach the saturation limit of the DNP enhancement will slightly raise the sample temperature. In this study the increase in sample temperature due to μw irradiation is approximately 3 K. Consequently, the magic angle spinning (MAS) rate of 8 kHz used for all experiments here was coupled with an approximate sample temperature of 103 K.

A 3.2 mm diameter, thin-wall zirconia MAS rotor was used for the presented experiments. The more ubiquitous rotor for DNP-enhanced SSNMR experiments is the sapphire (empirical formula: Al_2O_3) 3.2 mm MAS rotor. This rotor permits greater penetration of the μw and thus produces better DNP-enhancement. Results (not shown) indicate that the DNP-enhancement is improved by approximately 30 % with the sapphire rotor. However, this rotor was not utilized here since it produces intense background ^{27}Al signal. Nevertheless, when considering the overall S/N returned, the inferior DNP-enhancement observed for this zirconia rotor compared to a sapphire rotor is compensated by the larger sample volumes that it can contain.

Figure 1. (b) ^{27}Al NMR spectra of the mesoporous alumina recorded with direct excitation under MAS (DEMAS), with cross-polarization under MAS (CPMAS) from protons and with μw-induced DNP of protons followed by CPMAS. 64 scans were added for each with a polarization build-up interval between scans of 10 s for the CPMAS experiments (i.e. an experimental time, ET, of 11 min) and 1 s for the DEMAS experiment (i.e. ET = 1 min). 100 kHz of SPINAL-64[i] heteronuclear decoupling was used during acquisition for each. The CPMAS experiments used a central-transition (CT)-selective low-power matching condition that required nutation frequencies of approximately 28 kHz for protons and 20 kHz for the CT of ^{27}Al nuclei (i.e. 6.7 kHz of RF irradiation). The CP contact time was 1 ms.

Figure 2. Plot of the normalized intensity decay for each ^{27}Al peak with and without 100 kHz of SPINAL-64 heteronuclear decoupling during a spin-echo period as a function of the (rotor-synchronized) spin-echo time, used to determine T_2'. 32 scans were added for each data point recorded with decoupling and 64 scans were added for each data point recorded without decoupling. A polarization build-up interval of 5 s was used between scans and the low-power CP step and acquisition-period decoupling were applied using the same parameters as given in the extended caption to Figure 1 (above). The data points were fitted to single-component exponential decays.

Figure 3. DNP-enhanced, interface-selective DQ-SQ ^{27}Al homonuclear dipolar correlation spectra of the mesoporous alumina recorded with 64 scans for each of 20 t_1 points using a polarization build-up interval of 5 s between scans (i.e. ET ~ 4 hours each). After the low-power CP step, applied using the same parameters as given in the extended caption to Figure 1 (above), 100 kHz of SPINAL-64 heteronuclear decoupling was employed for the entirety of the sequence (except during the z-filter). 1.67 kHz of RF irradiation (corresponding to a nutation frequency for the CT of ^{27}Al nuclei of 4 kHz) was used for the dipolar recoupling sequence.

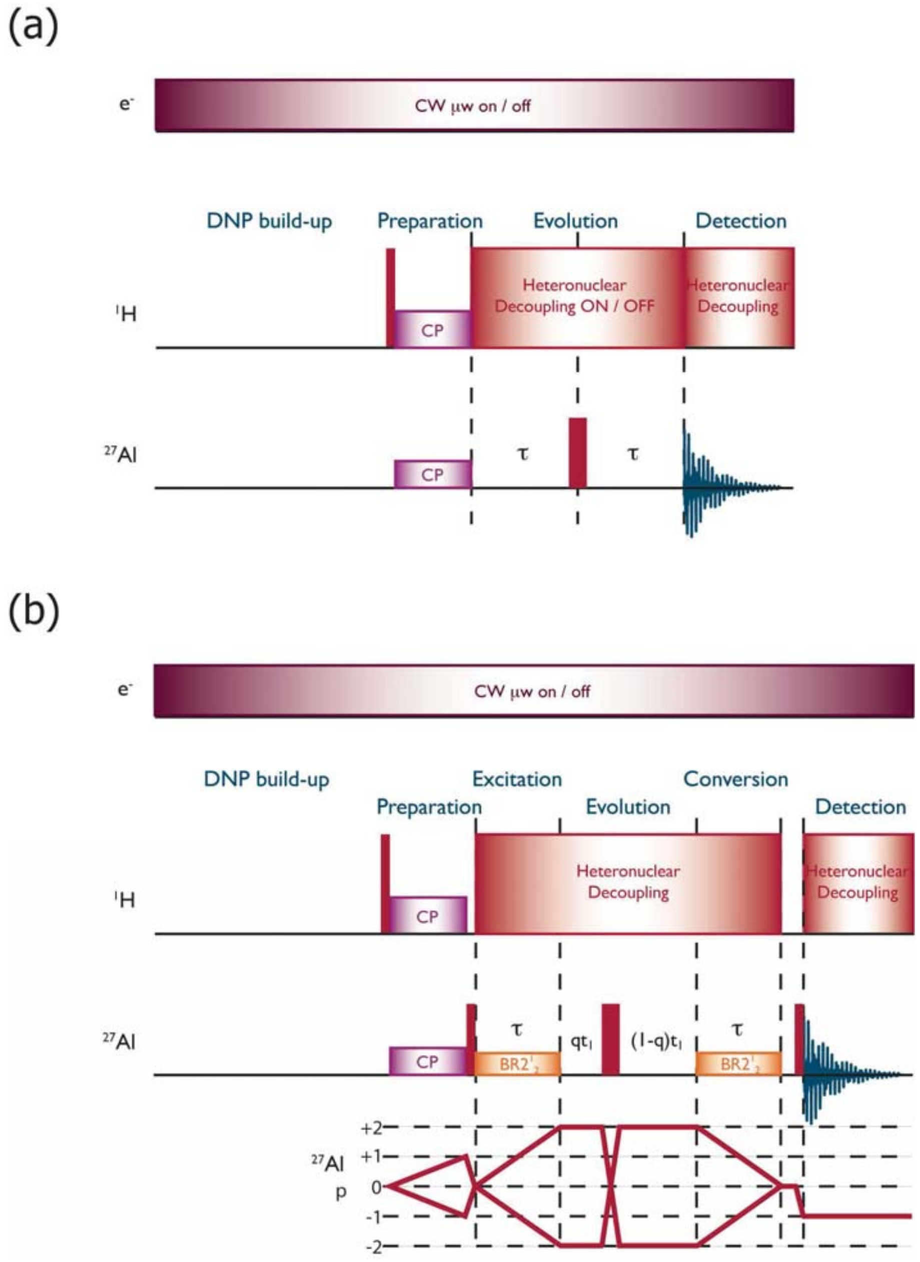

Figure S1. (a) NMR pulse sequence for the DNP-enhanced, pseudo-two-dimensional experiment used to determine the time constants associated with the homogeneous contribution to the transverse dephasing which cannot be refocused with a π-pulse (T_2'). Rotor-synchronized 'τ' times are varied to produce the pseudo-2D dataset. (b) NMR pulse sequence and corresponding coherence transfer pathway used to record DNP-enhanced, DQ-SQ homonuclear dipolar correlation spectra of quadrupolar nuclei. For both pulse sequences, thin red rectangles represent π/2-pulses and thick red rectangles represent π-pulses. For quadrupolar nuclei (i.e. ^{27}Al) the π/2- and π-pulses are CT-selective.

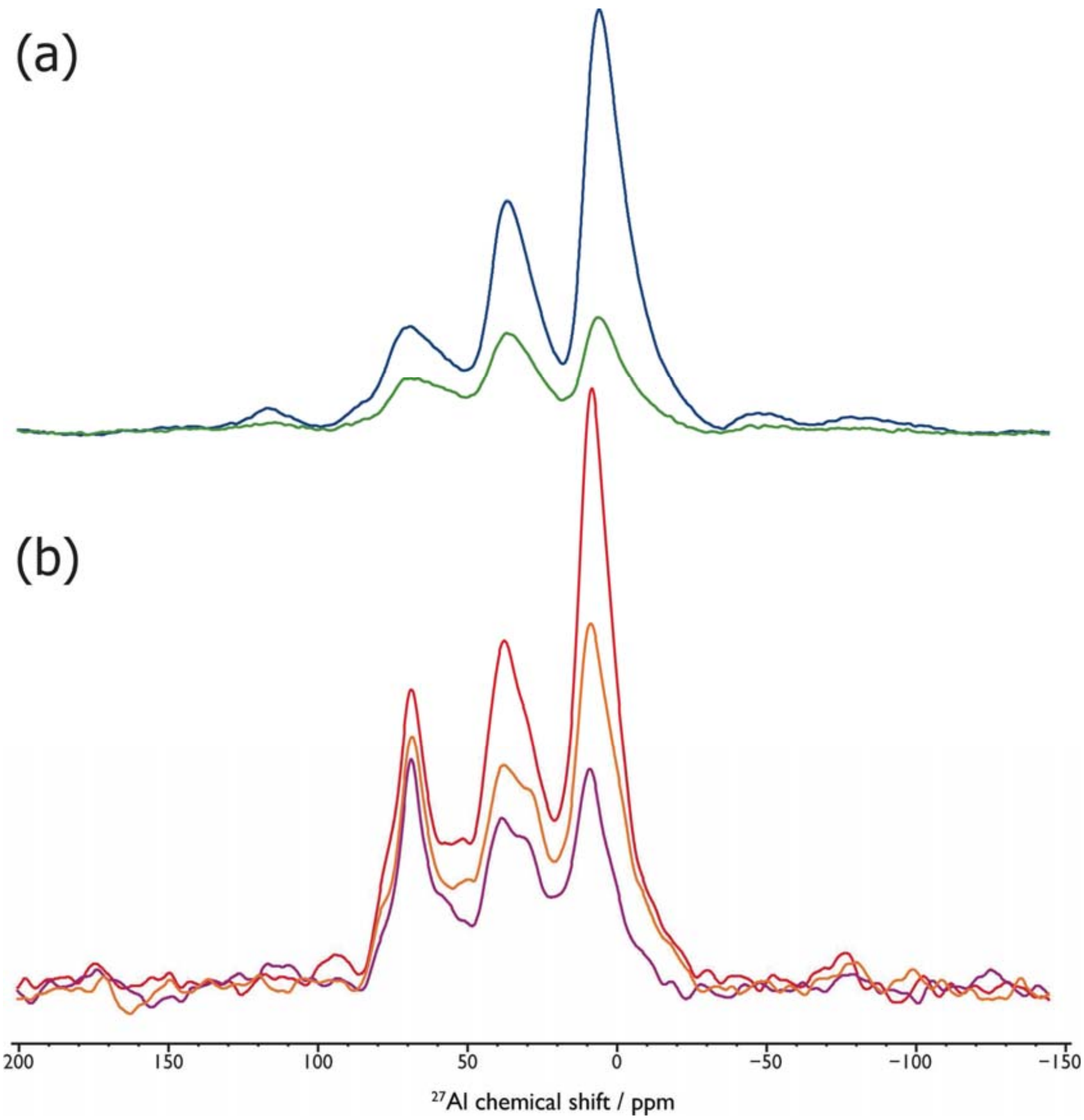

Figure S2. (a) Two DNP-enhanced interfacial-^{27}Al NMR spectra of the mesoporous alumina sample studied in this work recorded using the pulse sequence given in Figure S1(a). This pulse sequence was used in a one-dimensional fashion with a total spin-echo time (2τ) of 4 ms to record the spectra with (blue) and without (green) 100 kHz of SPINAL-64 heteronuclear decoupling. The gain in sensitivity by using the decoupling can be clearly observed. (b) DNP-enhanced interfacial-^{27}Al NMR spectra of the mesoporous alumina sample studied in this work recorded using the pulse sequence given in Figure S1(b). This pulse sequence was used in a one-dimensional fashion to demonstrate the effect of employing 100 kHz of SPINAL-64 heteronuclear decoupling during different parts of the sequence. Spectra resulting from no decoupling (purple), decoupling only during the recoupling sequence (orange) and decoupling throughout the sequence (except for during the z-filter) (red) are shown.

Comments on Figure S2(b). Firstly, like Figure S2(a), it is instantly apparent that utilizing heteronuclear decoupling returns better sensitivity. It is obvious, but it is worth stating nonetheless, that when CP is used to transfer magnetization to a second spin then this second spin must experience a coupling. Therefore, adequate decoupling must be employed if an absence of this coupling is required (for high-resolution solid-state NMR this is generally the case). This is an important point for the acquisition of spectra resulting from indirect DNP-enhancements that use a CP step to transfer hyperpolarized proton magnetization. It is also worth mentioning that the use of this recoupling sequence for quadrupolar nuclei does not prohibit the use of moderate RF heteronuclear decoupling fields since the recoupling RF field is small. Using similar RF field strengths for homonuclear recoupling and also simultaneous heteronuclear decoupling can introduce interference effects that significantly reduce recoupling transfer efficiencies. Figure S2(b) demonstrates that here this is not the case. Finally, the total experimental time for each of the 1D spectra in Figure S2(b) was approximately 11 minutes. This fast experimental time is due to the DNP conditions used here. Under conventional solid-state NMR conditions these experiments would require experimental times many orders of magnitude greater. These DNP conditions permit the careful calibration of the pulse sequence and thus allow optimum sensitivity to be obtained when performing the 2D version of this dipolar correlation experiment.

(i) Fung, B.M.; Khitrin, A.K.; Ermolaev, K. *J. Magn. Reson.* **2000**, *142*, 97.

ChemComm

COMMUNICATION

Cite this: DOI: 10.1039/c3cc47208f

Received 20th September 2013,
Accepted 14th November 2013

DOI: 10.1039/c3cc47208f

www.rsc.org/chemcomm

Probing ^{27}Al–^{13}C proximities in metal–organic frameworks using dynamic nuclear polarization enhanced NMR spectroscopy†

Frédérique Pourpoint,*[a] Aany Sofia Lilly Thankamony,[a] Christophe Volkringer,[a] Thierry Loiseau,[a] Julien Trébosc,[a] Fabien Aussenac,[b] Diego Carnevale,[c] Geoffrey Bodenhausen,[cd] Hervé Vezin,[e] Olivier Lafon*[a] and Jean-Paul Amoureux[af]

We show how ^{27}Al–^{13}C proximities in the microporous metal–organic framework MIL-100(Al) can be probed using advanced ^{27}Al–^{13}C NMR methods boosted by Dynamic Nuclear Polarization.

Metal–organic frameworks (MOFs) have attracted increasing attention owing to their high surface area and their wide range of three-dimensional (3D) architectures that exhibit different pore apertures and chemical tunabilities. These hybrid materials represent promising systems for gas storage, catalysis, capture of radioactive compounds, and drug delivery.[1] Amongst them, aluminium-based MOFs, such as MIL-100(Al),[2] present many advantages, including low cost, density and toxicity, remarkable thermal stability and high Lewis acidity that should allow many industrial applications.[3]

Rational design of MOFs requires a clear understanding of structure–property relationships and hence calls for characterization methods endowed with atomic resolution. In particular, solid-state NMR is well suited to assess structural models of MOF frameworks, to probe the organization of extra-framework entities,[4] and to analyze atomic-level dynamics.[5,6] However, the poor sensitivity of NMR limits the observation of adsorbed species, defects, *etc.*, particularly when the observed nuclei have low gyromagnetic ratios, low natural abundances or long longitudinal relaxation times (T_1). Besides, the observation of ^{27}Al–^{13}C proximities by NMR in Al-based MOFs has hitherto been hindered by limitations of common NMR probes, which cannot be tuned simultaneously to nearby ^{27}Al and ^{13}C Larmor frequencies.

We report here the first observation of ^{27}Al–^{13}C proximities in MOFs using advanced NMR methods combined with a frequency splitter.[7,8] We show that Dynamic Nuclear Polarization (DNP) can significantly reduce acquisition times for MIL-100(Al) at 100 K. EPR spectroscopy and DNP enhancements prove that the biradical TOTAPOL[9] enters the MIL-100(Al) cavities within tens of minutes, although its apertures are smaller than 0.88 nm. Besides, DNP-enhanced ^{27}Al–^{13}C correlation experiments prove that the MIL-100(Al) framework is not altered by impregnation with a TOTAPOL solution. So far, DNP of MOFs has only been demonstrated for 1D spectra under Magic-Angle Spinning (MAS) using ^{1}H → ^{13}C and ^{1}H → ^{15}N cross-polarisation (CP) and 2D ^{1}H–^{13}C correlation spectroscopy of In-based MIL-68.[10] So far, ^{27}Al DNP has only been reported for γ- and mesoporous alumina.[11]

Fig. 1d shows the EPR spectra of MIL-100(Al) impregnated with a 16 mM aqueous TOTAPOL solution (**1**). Immediately after impregnation the EPR spectrum is dominated by a triplet due to the isotropic hyperfine coupling with ^{14}N. During impregnation, an additional triplet develops mono-exponentially with a time constant of 77 min (Fig. 1f), which is consistent with the kinetics of the adsorption of organic molecules on MIL-100 from aqueous solutions.[12] This triplet is due to the anisotropic hyperfine coupling with ^{14}N and corresponds to TOTAPOL adsorbed on MIL-100(Al). So far, EPR has never been used to probe adsorption of radicals onto MOFs.

Fig. 1e and g show 1D ^{1}H → ^{13}C and ^{1}H → ^{27}Al CP-MAS spectra of **1** with and without microwave (μw) irradiation (Fig. S2a and b, ESI†). Three ^{13}C signals are resolved, which can be assigned to three sites of the benzene-1,3,5-tricarboxylate (btc) moiety, based on the ^{13}C chemical shifts of btc in solution and 2D ^{27}Al–^{13}C spectra (see below). The ^{1}H → ^{27}Al CP-MAS spectra are similar to the directly detected ^{27}Al signals of hydrated MIL-100(Al), with overlapping signals of octahedral Al sites.[13] Fig. 1e and g show DNP enhancements per scan, $\varepsilon^{\text{scan}}_{\text{on/off}} \approx 8.5$, which are identical for all ^{13}C and ^{27}Al sites. A similar enhancement is measured for the ^{1}H polarization under MAS (Fig. S3, ESI†), which is the source of the ^{27}Al and ^{13}C polarization when using CP. The radicals do not

---

[a] Université Lille Nord de France, CNRS, UMR 8181 UCCS, ENSCL, Université de Lille 1, 59652 Villeneuve d'Ascq, France. E-mail: frederique.pourpoint@ensc-lille.fr, olivier.lafon@univ-lille1.fr; Tel: +33 320436542

[b] Bruker BioSpin SA, 34, rue de l'Industrie, 67166 Wissembourg Cedex, France

[c] Institut des sciences et ingénierie chimiques, Ecole Polytechnique Fédérale de Lausanne, EPFL, Batochime, CH-1015 Lausanne, Switzerland

[d] Département de chimie, Ecole Normale Supérieure, 24, rue Lhomond, 75321 Paris cedex 05, France

[e] Université Lille Nord de France, CNRS, UMR LASIR 8516, Université de Lille 1, 59652 Villeneuve d'Ascq, France

[f] East China Normal University, Shanghai, China

† Electronic supplementary information (ESI) available: Experimental section, additional DNP and standard NMR data, spin dynamics simulations and a discussion of DNP enhancement values. See DOI: 10.1039/c3cc47208f

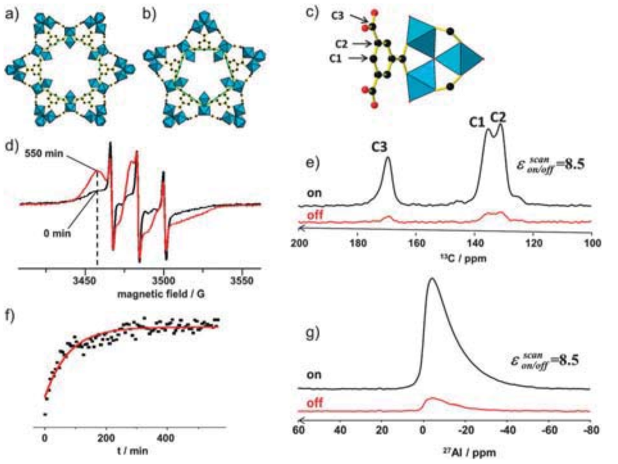

Fig. 1 Representations of the (a) hexagonal and (b) pentagonal apertures of MIL-100(Al) (Fig. S1, ESI†). (c) Representation of the btc moiety attached to Al trimers. (d) 9 GHz continuous wave EPR spectra of **1** at room temperature after an impregnation time of 0 (black) and 550 min (red). (f) Evolution of experimental EPR intensity (square symbols) at 3458 G (dashed line in d) for **1** as a function of impregnation time. The continuous line is the best mono-exponential fit. (e) ^{13}C MAS NMR spectra of **1** at 100 K with CP from ^{1}H at B_0 = 9.4 T with (black) and without (red) μw irradiation, using zirconia rotors spinning at ν_r = 10 kHz. (g) ^{27}Al MAS NMR spectra of **1** under the same conditions with CP from ^{1}H.

affect the linewidths of ^{27}Al and ^{13}C CP-MAS signals.[14] As for other biradicals, the build-up time of the DNP-induced ^{1}H polarization is equal to $T_1(^{1}\mathrm{H})$ = 0.7 s, as determined without μw irradiation in the same sample.[15] Hence, μw irradiation does not allow reducing the recovery delay, so that the enhancement per unit time is $\varepsilon^{\mathrm{time}}_{\mathrm{on/off}} = \varepsilon^{\mathrm{scan}}_{\mathrm{on/off}} \approx 8.5$. When compared to standard room-temperature CP-MAS spectra of dry MIL-100(Al), DNP-CP-MAS at 100 K provides a global sensitivity enhancement of $\varepsilon^{\mathrm{time}}_{\mathrm{global}} = 10$.[16]

The TOTAPOL molecule is approximately 1.2 nm long and 0.65 nm wide. Hence, it can enter the large cavities of MIL-100(Al) through the hexagonal apertures of 0.88 nm (Fig. 1a), but not the small cavities with pentagonal apertures of 0.54 nm (Fig. 1b). The TOTAPOL diffusion into MIL-100(Al) is confirmed by EPR and by a quantitative analysis of the DNP enhancement using a ^{1}H spin diffusion model for spherical samples (see ESI†).

The significant enhancement of $\varepsilon^{\mathrm{scan}}_{\mathrm{on/off}} \approx 13$ for direct ^{13}C polarization (with MAS but without resorting to CP) corroborates the presence of TOTAPOL in the pores of MIL-100(Al) (Fig. S4a, ESI†). The (integrated) intensities of the ^{13}C signals exhibit a stretched exponential DNP build-up where the longest time constant is a few hundreds of seconds (Fig. S6, ESI†).[14] Polarization build-up curves are identical with and without μw and $\varepsilon^{\mathrm{time}}_{\mathrm{on/off}} = \varepsilon^{\mathrm{scan}}_{\mathrm{on/off}}$ do not depend on the recovery delay. However, ^{13}C linewidths obtained by direct DNP-MAS (without CP) with short recycle delays are twice broader than with DNP-CP-MAS (Fig. S5a, ESI†),[14] since direct DNP transfer emphasizes ^{13}C nuclei that are close to TOTAPOL. In this sample, the sensitivity of $^{1}\mathrm{H} \rightarrow {}^{13}\mathrm{C}$ DNP-CP-MAS is approximately equal to direct ^{13}C DNP-MAS without CP. The disadvantage of direct polarization compared to CP-MAS is compensated by DNP. On the other hand, losses due to paramagnetic $T_{1\rho}$ relaxation during CP partly cancel sensitivity gains resulting from CP from remote protons relayed by ^{1}H spin diffusion.[16] The enhancement $\varepsilon^{\mathrm{scan}}_{\mathrm{on/off}}$ = 1.7 is modest for ^{27}Al (Fig. S4b, ESI†). Besides, the direct build-up of ^{27}Al polarization occurs within a few seconds and no line broadening is observed (Fig. S5b, ESI†).

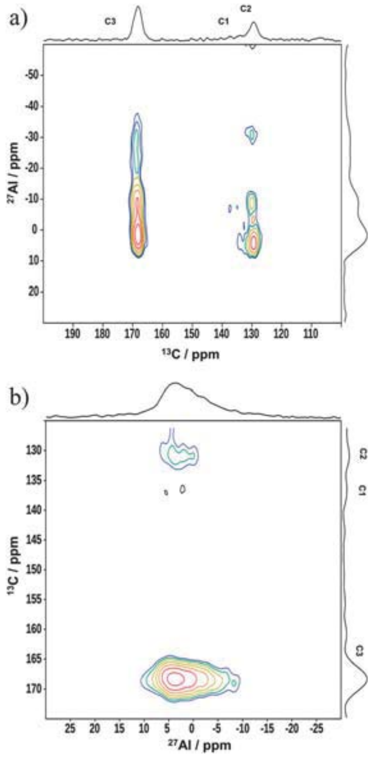

Fig. 2 DNP-enhanced (a) ^{13}C–{^{27}Al} CP-*D*-HMQC 2D spectra of **1** and (b) ^{27}Al–{^{13}C} at B_0 = 9.4 T, ν_r = 10 kHz and T = 100 K. Additional details are given in the ESI.†

The sensitivity enhancement afforded by DNP allows one to acquire 2D NMR experiments that are precluded under standard conditions. Fig. 2 shows ^{27}Al–^{13}C Dipolar-mediated Heteronuclear Multiple Quantum Correlation (*D*-HMQC) spectra of MIL-100(Al) (Fig. S2c and d, ESI†). The acquisition of these spectra was made possible by combining a frequency splitter with DNP for sensitivity enhancement.[7] Without DNP, no signal could be seen after three days in a *D*-HMQC spectrum of dry MIL-100(Al) using $^{1}\mathrm{H} \rightarrow {}^{13}\mathrm{C}$ CP excitation (CP-*D*-HMQC) and ^{13}C detection (denoted ^{13}C–{^{27}Al} hereafter), whereas the signal-to-noise ratio (S/N) of the CP-*D*-HMQC spectrum with ^{27}Al detection (denoted ^{27}Al–{^{13}C}) was S/N < 2 after 17 h (Fig. S7, ESI†). This poor sensitivity stems not only from the 1.1% natural abundance of the ^{13}C isotope but also from coherent and incoherent losses during the *D*-HMQC sequence. For instance, the efficiency of the ^{13}C–{^{27}Al} CP-*D*-HMQC spectrum relative to $^{1}\mathrm{H} \rightarrow {}^{13}\mathrm{C}$ CP-MAS is about 10%. The DNP enhancement compensates for this low efficiency, and the ^{13}C–{^{27}Al} CP-*D*-HMQC spectrum acquired in 7.1 h exhibits a S/N ≈ 30 for the C3 signal. Under DNP conditions, ^{13}C–{^{27}Al} CP-*D*-HMQC spectra are more sensitive than with ^{27}Al detection, ^{27}Al–{^{13}C}, since $^{1}\mathrm{H} \rightarrow {}^{13}\mathrm{C}$ CP-MAS is more efficient and easier to optimize than $^{1}\mathrm{H} \rightarrow {}^{27}\mathrm{Al}$ CP-MAS. Hence, ^{13}C–{^{27}Al} CP-*D*-HMQC should be preferred in this case.

Such ^{27}Al–^{13}C correlation spectra allow one to identify ^{27}Al–^{13}C proximities in MIL-100(Al). In agreement with the crystal

View Article Online
DOI: 10.1039/C3CC47208F

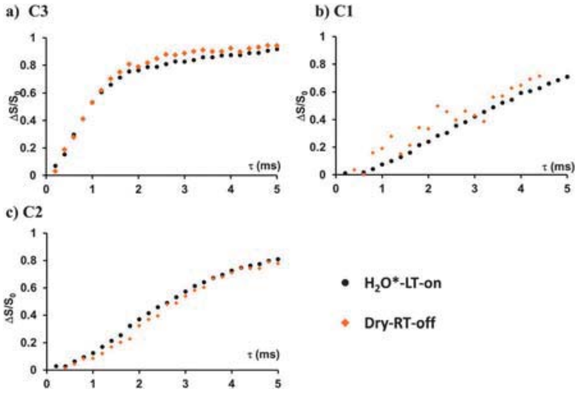

Fig. 3 Comparison of the ^{27}Al–^{13}C S-RESPDOR curves of three ^{13}C signals of (i) **1** with microwave irradiation at 100 K (black circles, denoted H_2O*-LT-on) and (ii) dry MIL-100(Al) without microwave irradiation at room temperature (orange diamonds, denoted dry-RT-off). Both experiments were recorded at 9.4 T with ν_r = 10 kHz. The total experimental time was 7 and 50 h, with and without DNP, respectively. Additional experimental details are given in the ESI.†

structure, C2 and C3 display cross-peaks with several octahedral Al sites. Weak C1 cross-peaks are also visible. The cross-peak intensities decrease with increasing ^{27}Al–^{13}C distances: I(C3) > I(C2) > I(C1) (Table S2, ESI†), thus confirming the assignment of ^{13}C signals based on isotropic chemical shifts in solution. DNP facilitates the detection of weak cross-peaks and hence of large ^{27}Al–^{13}C distances.

However, simple *D*-HMQC experiments are not suitable for a quantitative assessment of ^{27}Al–^{13}C distances. This is possible using Symmetry-based Rotational-Echo Saturation-Pulse Double-Resonance (S-RESPDOR) (Fig. S2e, ESI†).[8] However, under standard conditions, the low S/N of S-RESPDOR spectra acquired in 50 h leads to noisy dipolar dephasing curves (dry-RT-off data in Fig. 3b). DNP can help to overcome this problem, although the presence of TOTAPOL accelerates signal decay and hence decreases the efficiency of S-RESPDOR (Fig. S8, ESI†).

The DNP-S-RESPDOR curves of Fig. 3 were acquired in only 7 h. DNP is especially useful to detect slow dipolar dephasing, like for C1 and C2, which correspond to long ^{27}Al–^{13}C distances. Furthermore, there is a good agreement between the S-RESPDOR signal fractions of MIL-100(Al) obtained by DNP-NMR and conventional NMR. This result demonstrates that the impregnation with an aqueous TOTAPOL solution and freezing to low temperature do not affect the MIL-100(Al) framework. Besides, the experimental S-RESPDOR signal fractions agree with those expected from the crystal structure of MIL-100(Al) (Fig. S9, ESI†). This agreement validates crystal structures obtained from X-ray diffraction analysis.

In summary, we demonstrated by EPR and DNP experiments that TOTAPOL can diffuse into the large cavities of microporous MIL-100(Al), leading to DNP sensitivity enhancements for CP-MAS and direct polarization ^{13}C MAS experiments. We reported the first 2D ^{27}Al–^{13}C correlation experiments on MOFs and showed that the time required for these experiments can be reduced using DNP. These experiments validate the crystal structure of MIL-100(Al) and the assignment of the ^{13}C resonances. Besides, S-RESPDOR experiments demonstrate that impregnation and freezing down to 100 K do not alter the MIL-100(Al) framework. Our new ^{27}Al–^{13}C DNP-NMR methods should have implications for the characterization of other advanced materials, including alkylaluminium[7,8] and microporous organic polymers.[17] The reader is referred to ESI.†

This work was supported by the Region Nord/Pas de Calais, the European Union (FEDER), the CNRS, the French ministry of research, USTL, ENSCL, contracts ANR-2020-jcjc-0811-01 and COST TD 1103, EPFL, the Swiss National Science Foundation, the Swiss Commission for Technology and Innovation, and Bruker Biospin.

Notes and references

1 Reviews on MOFs: J. R. Long and O. M. Yaghi, *Chem. Soc. Rev.*, 2009, **38**, 1207; H. C. Zhou, J. R. Long and O. M. Yaghi, *Chem. Rev.*, 2012, **112**, 673.
2 C. Volkringer, D. Popov, T. Loiseau, G. Férey, M. Burghammer, C. Riekel, M. Haouas and F. Taulelle, *Chem. Mater.*, 2009, **21**, 5695.
3 M. Gaab, N. Trukhan, S. Maurer, R. Gummaraju and U. Muller, *Microporous Mesoporous Mater.*, 2012, **157**, 131.
4 M. Haouas, C. Volkringer, T. Loiseau, G. Férey and F. Taulelle, *Chem.–Eur. J.*, 2009, **15**, 3139.
5 S. Horike, R. Matsuda, D. Tanaka, S. Matsubara, M. Mizuno, K. Endo and S. Kitagawa, *Angew. Chem., Int. Ed.*, 2006, **45**, 7226; L. C. Lin, J. Kim, X. Q. Kong, E. Scott, T. M. McDonald, J. R. Long, J. A. Reimer and B. Smit, *Angew. Chem., Int. Ed.*, 2013, **52**, 4410.
6 H. C. Hoffmann, M. Debowski, P. Muller, S. Paasch, I. Senkovska, S. Kaskel and E. Brunner, *Materials*, 2012, **5**, 2537; A. Sutrisno and Y. N. Huang, *Solid State Nucl. Magn. Reson.*, 2013, **49–50**, 1.
7 F. Pourpoint, Y. Morin, F. Capet, J. Trébosc, R. M. Gauvin, O. Lafon and J. P. Amoureux, *J. Phys. Chem. C*, 2013, **117**, 18091.
8 F. Pourpoint, J. Trébosc, R. M. Gauvin, Q. Wang, O. Lafon, F. Deng and J. P. Amoureux, *ChemPhysChem*, 2012, **13**, 3605.
9 C. S. Song, K. N. Hu, C. G. Joo, T. M. Swager and R. G. Griffin, *J. Am. Chem. Soc.*, 2006, **128**, 11385.
10 A. J. Rossini, A. Zagdoun, M. Lelli, J. Canivet, S. Aguado, O. Ouari, P. Tordo, M. Rosay, W. E. Maas, C. Coperet, D. Farrusseng, L. Emsley and A. Lesage, *Angew. Chem., Int. Ed.*, 2012, **51**, 123.
11 D. Lee, H. Takahashi, A. S. Lilly Thankamony, J. P. Dacquin, M. Bardet, O. Lafon and G. De Paepe, *J. Am. Chem. Soc.*, 2012, **134**, 18491; V. Vitzthum, P. Mieville, D. Carnevale, M. A. Caporini, D. Gajan, C. Coperet, M. Lelli, A. Zagdoun, A. J. Rossini, A. Lesage, L. Emsley and G. Bodenhausen, *Chem. Commun.*, 2012, **48**, 1988.
12 S. H. Huo and X. P. Yan, *J. Mater. Chem.*, 2012, **22**, 7449.
13 M. Haouas, C. Volkringer, T. Loiseau, G. Férey and F. Taulelle, *J. Phys. Chem. C*, 2011, **115**, 17934.
14 O. Lafon, A. S. Lilly Thankamony, M. Rosay, F. Aussenac, X. Lu, J. Trébosc, V. Bout-Roumazeilles, H. Vezin and J. P. Amoureux, *Chem. Commun.*, 2013, **49**, 2864.
15 O. Lafon, A. S. Lilly Thankamony, T. Kobayashi, D. Carnevale, V. Vitzthum, I. I. Slowing, K. Kandel, H. Vezin, J. P. Amoureux, G. Bodenhausen and M. Pruski, *J. Phys. Chem. C*, 2013, **117**, 1375.
16 T. Kobayashi, O. Lafon, A. S. Lilly Thankamony, I. I. Slowing, K. Kandel, D. Carnevale, V. Vitzthum, H. Vezin, J. P. Amoureux, G. Bodenhausen and M. Pruski, *Phys. Chem. Chem. Phys.*, 2013, **15**, 5553.
17 Y. Xie, T.-T. Wang, X.-H. Liu, K. Zou and W.-Q. Deng, *Nat. Commun.*, 2013, **4**, 1960; F. Blanc, S. Y. Chong, T. O. McDonald, D. J. Adams, S. Pawseyn, M. A. Caporini and A. J. Cooper, *J. Am. Chem. Soc.*, 2013, **135**, 15290.

Supporting Information

Probing ^{27}Al-^{13}C Proximities in Metal-Organic Frameworks using Dynamic Nuclear Polarization enhanced NMR Spectroscopy

EPR experiments

MIL-100(Al) was synthesized following the literature procedure.[1] It was first heated at 150°C overnight to eliminate adsorbed water trapped within the pores of the material. EPR sample was prepared by adding about 15 μL of 16 mM TOTAPOL dissolved in water with natural isotopic abundance to about 20 mg of MIL-100(Al) dry powder. Just after the addition of TOTAPOL solution, 9 GHz continuous-wave EPR spectra were recorded every minute during 550 min using a Bruker Biospin ELEXYS E580E spectrometer. The spectra were recorded with 2 mW microwave power and 0.5 G of amplitude modulation.

Sample preparation for DNP measurement

The sample for solid-state DNP NMR experiments was prepared at room temperature by impregnating dry MIL-100(Al) with a 16 mM TOTAPOL dissolved in water with natural isotopic abundance. Even though other impregnation solvents and polarizing agents were tested, including (i) 90/10 (w/w) mixture of $^{2}H_2O$ and H_2O (ii) 78/14/8 (w/w/w) mixture of [$^{2}H_6$]-DMSO, $^{2}H_2O$ and H_2O, the impregnation of MIL-100(Al) with these radical solutions resulted in lower DNP enhancement. Typically an aliquot of 60 µL of radical solution was added to cover about 30 mg of MIL-100 (Al) dry powder. The mixture was stirred vigorously and kept at room temperature for one day. After this saturation, the mixture was centrifuged for 5 min at 12110×*g* and the supernatant was pipetted. The remaining wet powder was packed into a thick-walled 3.2 mm zirconia rotor. Zirconia rotors were employed to avoid ^{27}Al background signal of sapphire rotor.

DNP and standard NMR measurements at 100 K

The solid-state NMR experiments at 100 K enhanced or not by DNP were obtained at 9.4 T (400 MHz for protons) using a Bruker BioSpin Avance III DNP NMR spectrometer, equipped with a gyrotron generating a continous 263 GHz μw irradiation. The μw irradiation was transmitted through a corrugated waveguide to a triple resonance ^{1}H/X/Y MAS probe for 3.2 mm rotors. The μw power at the position of the sample was approximately 6 W. NMR spectra with μw irradiation "on" and "off" were acquired at ν_r = 10 kHz and sample temperature of ca. 100 K, which was stabilized by a Bruker BioSpin MAS cooling system.

The employed NMR pulse sequences are depicted in **Fig.S2**. The ^{1}H rf-amplitude for 90°-pulse was 89 kHz. For $^{1}\text{H}\rightarrow^{13}\text{C}$ CP-MAS transfer, the cross-polarization time was 3.2 ms, the ^{1}H rf field amplitude was linearly ramped from 42 to 85 kHz, whereas the ^{13}C rf field amplitude was constant and equal to 42 kHz. For $^{1}\text{H}\rightarrow^{27}\text{Al}$ CP-MAS transfer, the cross-polarization time was 800 μs, the ^{1}H rf amplitude was 33 kHz, whereas the ^{27}Al rf amplitude was equal to 7.6 kHz (central transition selective pulse). SPINAL-64[3] ^{1}H decoupling was applied during the acquisition of ^{13}C spectra with an rf amplitude of 89 kHz. No ^{1}H decoupling was applied during the acquisition of ^{27}Al spectra. The $^{1}\text{H}\rightarrow^{13}\text{C}$ and $^{1}\text{H}\rightarrow^{27}\text{Al}$ CP-MAS spectra typically resulted from the accumulation of 64 transients with a recovery delay of 1 s, leading to a total experimental time of 1 min. Other parameters of direct ^{1}H, ^{13}C MAS experiments and ^{27}Al Hahn-echo experiments are given in Figs.S3 and S4. The ^{1}H and ^{13}C chemical shifts were referenced to tetramethylsilane (TMS) at 0 ppm, whereas the ^{27}Al chemical shifts were referenced to 1M $AlCl_3$ aqueous solution.

DNP-enhanced ^{13}C-{^{27}Al} and ^{27}Al-{^{13}C} CP-*D*-HMQC 2D spectra and ^{27}Al-^{13}C S-RESPDOR curves were recorded with μw irradiation. SFAM-1 recoupling was chosen to reintroduce the ^{13}C-^{27}Al dipolar couplings owing to its high robustness, its large scaling factor of the recoupled dipolar interaction and the negligible ^{13}C-^{13}C dipolar couplings in natural abundance.[4] The rf field amplitude of ^{13}C 90° and 180° pulses as well as the rf peak amplitude of SFAM-1 recoupling were equal to 42 kHz. The rf field amplitude of ^{27}Al 90° and 180° CT-selective pulses was 5 kHz for CP-*D*-HMQC experiment, whereas the amplitude of ^{27}Al saturation pulse in S-RESPDOR was 46 kHz. The sum of the two SFAM-1 recoupling periods, τ, was equal to 6 ms in CP-*D*-HMQC experiment and was varied from 0 to 5 ms in *S*-RESPDOR experiments. Continuous wave ^{1}H decoupling with an rf field amplitude of 89 kHz was applied during SFAM-1 recoupling periods. SPINAL-64 ^{1}H decoupling with an rf field amplitude of 89 kHz was also applied during the indirect evolution period, t_1, of CP-*D*-HMQC experiments. The recovery delays of these experiments was 1 s. The number of transients, the number of t_1 or τ increments and the total experimental times were equal to (640, 20, 7.1 h) for ^{13}C-{^{27}Al} CP-*D*-HMQC, (640, 26, 16 h) for S-RESPDOR and (4096, 20, 39 h) for ^{27}Al-{^{13}C} CP-*D*-HMQC.

^{27}Al-^{13}C S-RESPDOR experiment at 100 K without microwave irradiation was also acquired for dry MIL-100(Al). The experimental parameters are identical to those employed for DNP-enhanced S-RESPDOR, except for the number of scans, which is 3616.

Standard solid-state NMR measurements at room temperature

^{27}Al-{^{13}C} CP-*D*-HMQC 2D spectra and ^{27}Al-^{13}C S-RESPDOR curves were also aquired at room temperature without microwave irradiation. The experimental parameters are identical to those of DNP-enhanced experiments, except the number of scans, which was equal at room temperature to 2048 and 3616, corresponding to 17 and 61 h, for CP-*D*-HMQC and S-RESPDOR, respectively.

Spin dynamics simulations

The simulated ^{27}Al-^{13}C S-RESPDOR curves in Fig.**S9** were calculated as follows. For each ^{13}C*i* signal, the simulated ^{27}Al-^{13}C S-RESPDOR curve is the sum of the eleven simulated S-RESPDOR signal fractions for the eleven crystallographically inequivalent C*i* sites contained in the unit cell. The S-RESPDOR signal fraction was simulated for each crystallographically inequivalent site using SIMPSON software[5] and a spin system consisting of one ^{13}C nucleus surrounded by its two nearest ^{27}Al neighbours in the MIL-100(Al) crystal structure. The ^{27}Al quadrupolar interaction was considered up to the second-order and the quadrupolar coupling constant, C_Q, and the asymmetry parameters of the electric field gradient, η_Q, were equal to 4.6 MHz and 0.5, respectively. The parameters of the S-RESPDOR pulse sequence were identical to the experimental ones. The powder average was calculated using 168 $\{\alpha_{MR},\beta_{MR}\}$pairs and 13 γ_{MR} angles. The 168 $\{\alpha_{MR},\beta_{MR}\}$pairs, which relate the molecular and rotor frames, were selected according to the REPULSION scheme.

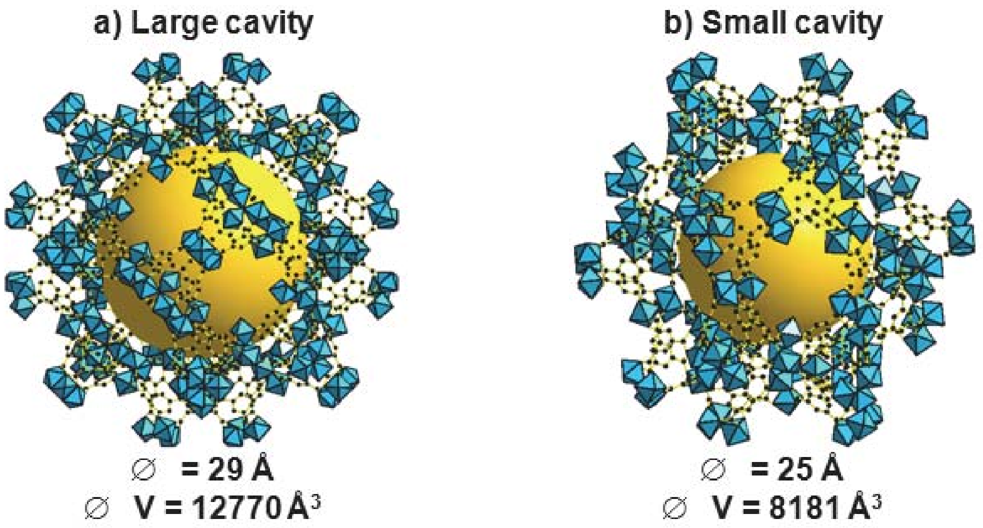

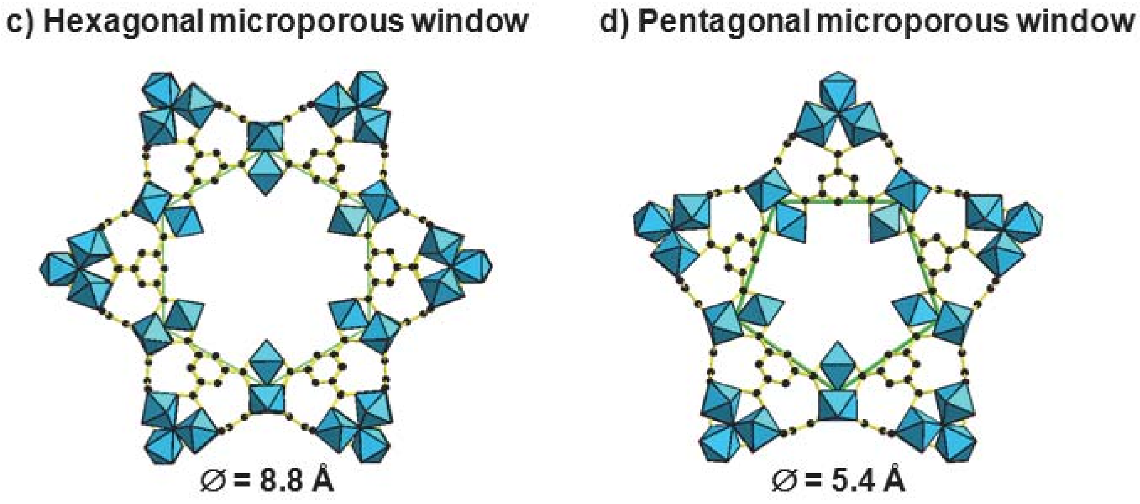

Fig. S1: Representations of the (a) large and (b) small cavities of MIL-100(Al). Large cavities display both (c) hexagonal and (d) pentagonal apertures, respectively, whereas small cavities only display pentagonal apertures. The inner diameter and the volume of the cavities are indicated below the subfigures a and b, whereas the diameter of the apertures is given below subfigures c and d.

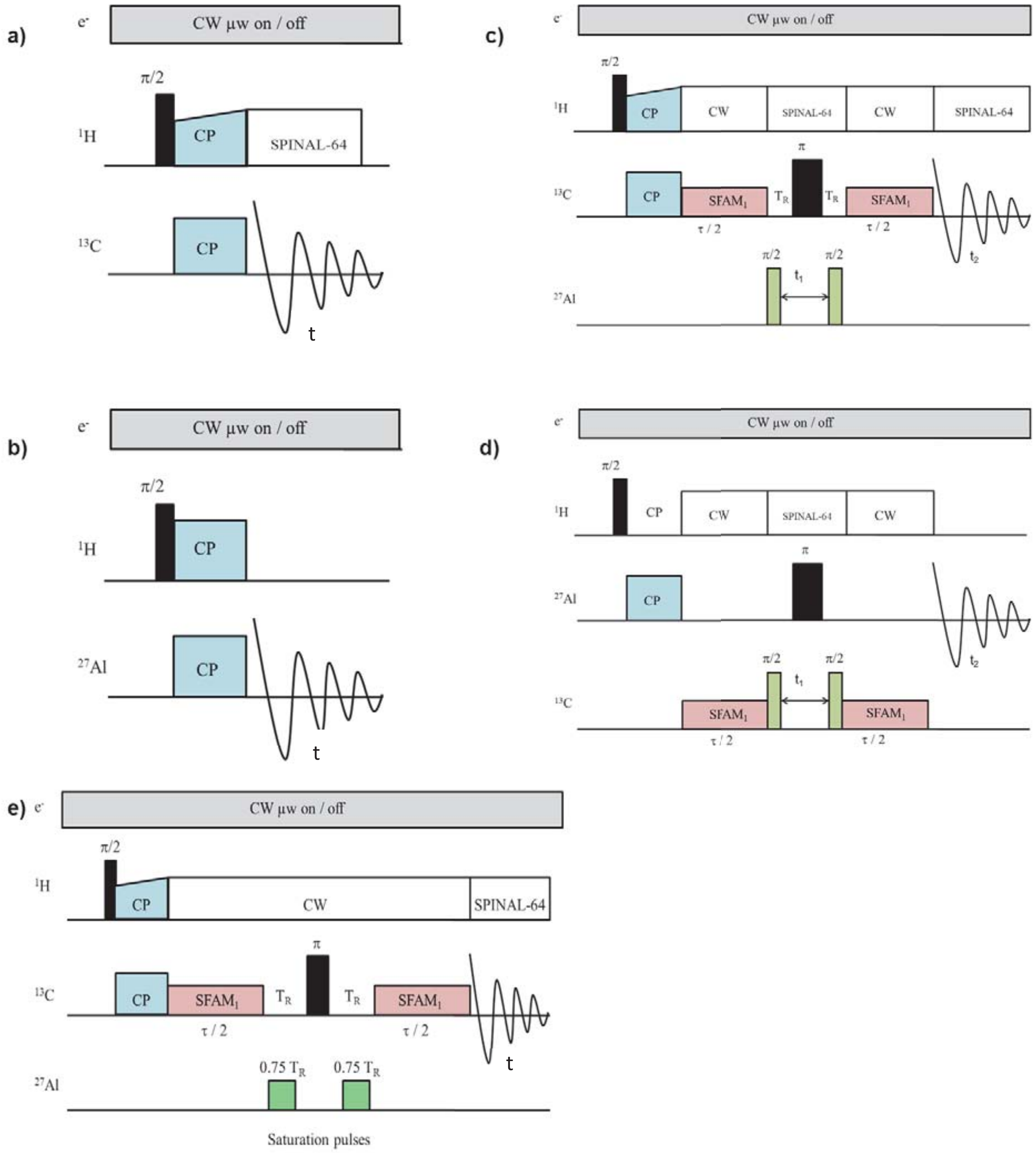

Fig.S2 NMR pulse sequences for: (a) 1D $^{1}H\rightarrow^{13}C$ CP-MAS, (b) 1D $^{1}H\rightarrow^{27}Al$ CP-MAS, (c) 2D ^{13}C-{^{27}Al} CP-*D*-HMQC, (d) 2D ^{27}Al-{^{13}C} CP-*D*-HMQC, and (e) ^{27}Al-^{13}C CP-S-RESPDOR. The phase cycling of CP-D-HMQC and CP-S-RESPDOR are given in refs [4] and [6], respectively.

DNP enhancement for CP-MAS if TOTAPOL does not enter into MIL-100(Al) cavities

To confirm the diffusion of TOTAPOL into the large cavities of MIL-100(Al), we use *reductio ad absurbum*: we assume that TOTAPOL molecules do not penetrate into the MIL-100(Al) crystals and are relagated into the interparticle voids. The ^{1}H polarization of the frozen water within the interparticle voids is assumed to be uniform and equal to $P_{\mathrm{eq}}\,\varepsilon_{on/off}^{scan}(R)$ where P_{eq} is the ^{1}H polarization at thermal equilibrium and $\varepsilon_{on/off}^{scan}(R)$ is the steady-state enhancement per scan produced by microwave irradiation for the protons within the interparticle voids. This DNP-enhanced ^{1}H polarization can only enter into the bulk of MIL-100(Al) crystals via ^{1}H-^{1}H spin diffusion. We assume an uniform proton density within the MIL-100(Al) crystals. This proton density can be estimated from the empirical formula and the unit cell volume of hydrated MIL-100(Al) to be equal to $n(^1\mathrm{H}) = 4.3\times10^2$ Å^3.

The average ^{1}H-^{1}H distance is thus equal to

$$d_{HH} = n\left(^1\mathrm{H}\right)^{-1/3} \approx 0.3 \text{ nm} \tag{S1}$$

The average dipolar coupling constant, b_{HH}, in rad.s^{-1} between two protons at a distance d_{HH} is

$$b_{HH} = -\frac{\mu_0}{4\pi}\frac{\gamma_H^2\hbar}{d_{HH}^3} \tag{S2}$$

where μ_0 is the vaccum permeability and all physical quantities are expressed in SI units. Under MAS condition, the effective dipolar coupling, ν_{d}, expressed in Hz can be estimated as[7]

$$\nu_d = \frac{b_{HH}^2}{4\pi^2\nu_r} \tag{S3}$$

The ^{1}H-^{1}H spin diffusion coefficient, D, is given by

$$D = d_{HH}^2\pi\nu_d \tag{S4}$$

Using Eqs.S1 to S4, we obtain $D = 6.8\times10^2$ nm^2.s^{-1}. This spin diffusion coefficient can be used to estimate the distribution of ^{1}H polarization within MIL-100(Al) crystals. These crystals have an octahedral shape and an average length of 1 μm.[8] However, for the sake of simplicity, the crystals are assumed to be spheres with a radius R = 500 nm and the diffusion to be radial. We also assume that all ^{1}H nuclei within the bulk MIL-100(Al) crystal have an identical longitudinal relaxation time of T_1 = 0.7 s. The ^{1}H polarization evolves under longitudinal ^{1}H relaxation and ^{1}H-^{1}H spin diffusion. Under the above assumption, the evolution of ^{1}H polarization within the bulk MIL-100(Al) crystal is given by[9]

$$\frac{\partial P(r,t)}{\partial t} = \frac{D}{r}\frac{\partial^2\left[rP(r,t)\right]}{\partial r^2} - \frac{P(r,t) - P_{eq}}{T_1}. \tag{S5}$$

Introducing $f(r,t) = r[P(r,t) - P_{eq}]$, Eq.S5 can be written as

$$\frac{\partial f(r,t)}{\partial t} = D\frac{\partial^2[f(r,t)]}{\partial r^2} - \frac{f(r,t)}{T_1} \quad \text{(S6)}$$

In the steady-state, all the physical quantities, including *f*, are time-independent and Eq.S6 becomes

$$\frac{\partial^2[f(r)]}{\partial r^2} - \frac{f(r)}{l_D^2} = 0 \quad \text{(S7)}$$

where $l_D = \sqrt{DT_1}$ is the diffusion length. Here, l_D is about 22 nm. Furthermore, the ^{1}H polarization at the center of the crystal, *P*(0), is finite, whereas it is equal to $P_{eq}\,\varepsilon_{on/off}^{scan}(R)$ at the surface of the crystal. Therefore, boundary conditions for *f* function are

$$f(0) = 0 \quad \text{and} \quad f(R) = R\left[\varepsilon_{on/off}^{scan}(R) - 1\right]P_{eq}\ . \quad \text{(S8)}$$

Solving Eq.S7 with the above boundary conditions leads to

$$P(r) = P_{eq}\left\{1 + \left[\varepsilon_{on/off}^{scan}(R) - 1\right]\frac{R}{r}\sinh\left(\frac{r}{l_D}\right)/\sinh\left(\frac{R}{l_D}\right)\right\} \quad \text{(S9)}$$

The enhancement per scan produced by μw irradiation is equal to the ratio of the polarization over the volume of the crystal with and without μw irradiation:

$$\varepsilon_{on/off}^{scan} = \frac{3}{4\pi R^3 P_{eq}}\int_0^R P(r)dR = 1 + 3\left[\varepsilon_{on/off}^{scan}(R) - 1\right]\frac{l_D}{R}\left\{\coth\left(\frac{R}{l_D}\right) - \frac{l_D}{R}\right\} \quad \text{(S10)}$$

For mesoporous systems, in which TOTAPOL molecules enter into the mesopores, we have measured enhancements per scan due to μw irradiation ranging from 11 to 30 for CP-MAS experiments.[7,9-11] Therefore, $\varepsilon_{on/off}^{scan}(R)$ value must fall within the above interval, which leads to $\varepsilon_{on/off}^{scan}$ values for MIL-100(Al) crystal ranging from 2.2 to 4.6. These estimates are not consistent with the experimental value $\varepsilon_{on/off}^{scan} = 8.5$ (see Fig.1 and S3). Hence, the TOTAPOL molecule must penetrate into the MIL-100(Al) cavities.

DNP-enhanced direct excitation experiments

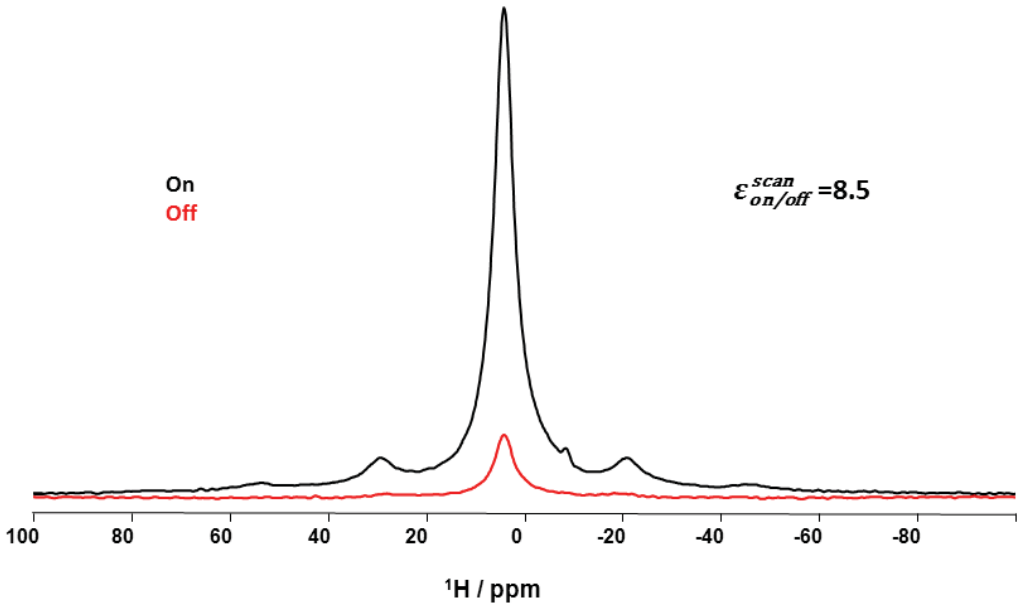

Fig.S3 ^{1}H MAS spectra of MIL-100(Al) recorded with (black) and without (red) μw irradiation. The spectra resulted from the accumulation of 64 transients with a recovery delay of 1 s, leading to a total experimental time of 1 min.

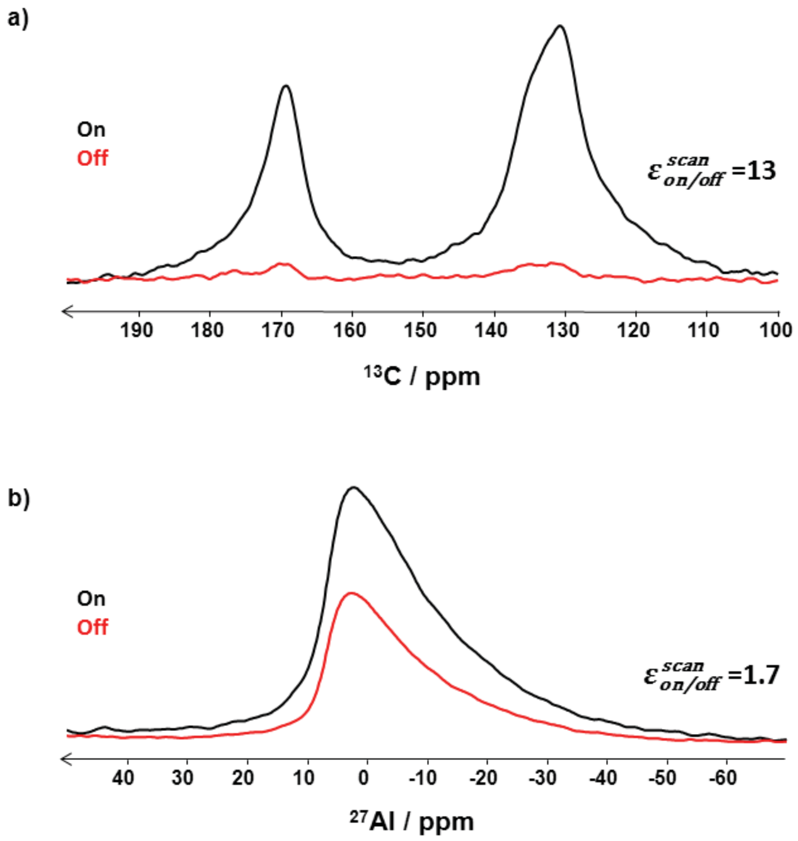

Fig.S4 (a) Direct polarization ^{13}C MAS spectra and (b) ^{27}Al Hahn echo spectra of MIL-100(Al) recorded with (black) and without (red) μw irradiation. The direct ^{13}C MAS spectra were acquired with a ^{13}C 90° pulse length of 6 μs and resulted from the accumulation of 128 transients with a recovery delay of 60 s, leading to a total experimental time of 128 min. The rf amplitude of ^{27}Al 90° and 180° CT-selective pulses was 5.5 kHz and the delay between the centers of these pulses was $\tau_r = 1/\nu_r$. The ^{27}Al Hahn echo NMR spectra resulted from the accumulation of 16 transients with a recovery delay of 1.5 s, leading to a total experimental time of 24 s.

DNP enhancement for direct ^{13}C MAS if TOTAPOL is outside MIL-100(Al) cavities

In MIL-100(Al) with natural isotopic abundance, the ^{13}C spin diffusion is vanishing and the DNP transfer is only conveyed by electron-^{13}C interaction. Therefore, the DNP transfer in direct ^{13}C MAS experiments is limited to a few nanometers.[12] Here, we consider a transfer depth of 5 nm. Assuming TOTAPOL is prevented from entering the cavities of MIL-100(Al), DNP in direct MAS experiment can only polarize the "outer" nuclei, located at a distance less than 5 nm from outer surface of MIL-100(Al) crystals. The molar fraction of "outer" ^{13}C nuclei can be estimated as[7]

$$x_{out} = 4\pi R^2 5 / \left[\frac{4}{3}\pi R^3\right] = \frac{15}{R} \tag{S11}$$

and the expected enhancement per scan due to μw irradiation is

$$\varepsilon_{on/off}^{scan} = 1 + x_{out}\left\lfloor \varepsilon_{on/off}^{scan}(R) - 1 \right\rfloor . \tag{S12}$$

With R = 500 nm and $\varepsilon_{on/off}^{scan} = 8.5$, Eqs.S11 and S12 yield $\varepsilon_{on/off}^{scan}(R) \approx 400$, which is significantly higher than DNP enhancements per scan reported for direct ^{13}C MAS at 9.4 T.[13] This inconsistency confirms again the presence of TOTAPOL within the cavities of MIL-100(Al).

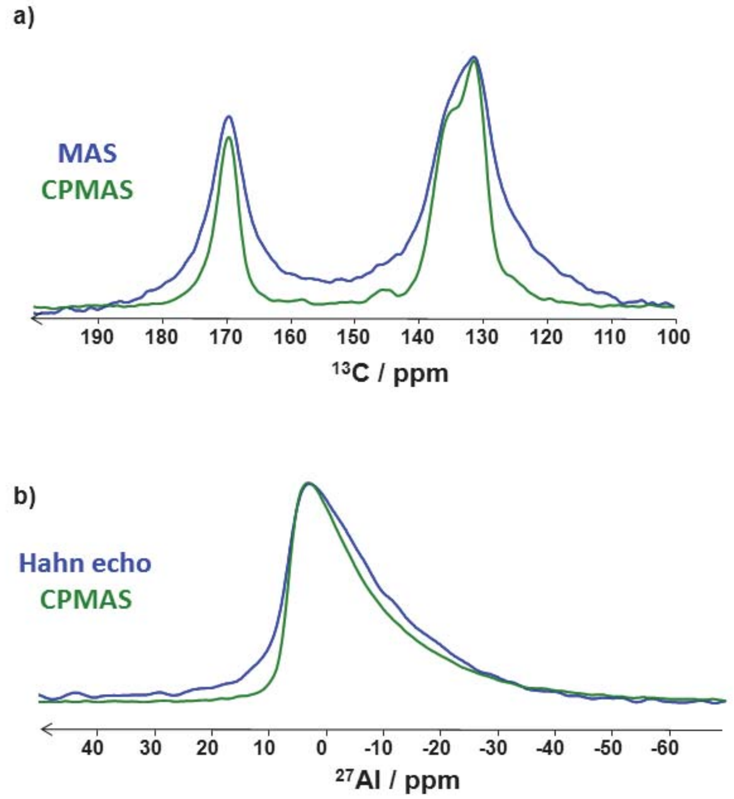

Fig.S5 (a) Comparison between direct ^{13}C MAS and ^{1}H→^{13}C CP-MAS spectra of MIL-100(Al) recorded with μw irradiation. (b) Comparison between ^{27}Al Hahn echo and ^{1}H→^{27}Al CP-MAS spectra of MIL-100(Al) recorded with μw irradiation. The CP-MAS spectra are identical to those of Fig.1 in the main text, whereas the direct ^{13}C MAS and ^{27}Al Hahn echo spectra are those of Fig.S4. Here, these spectra are scaled to the same absolute intensity to highlight changes in spectral resolution.

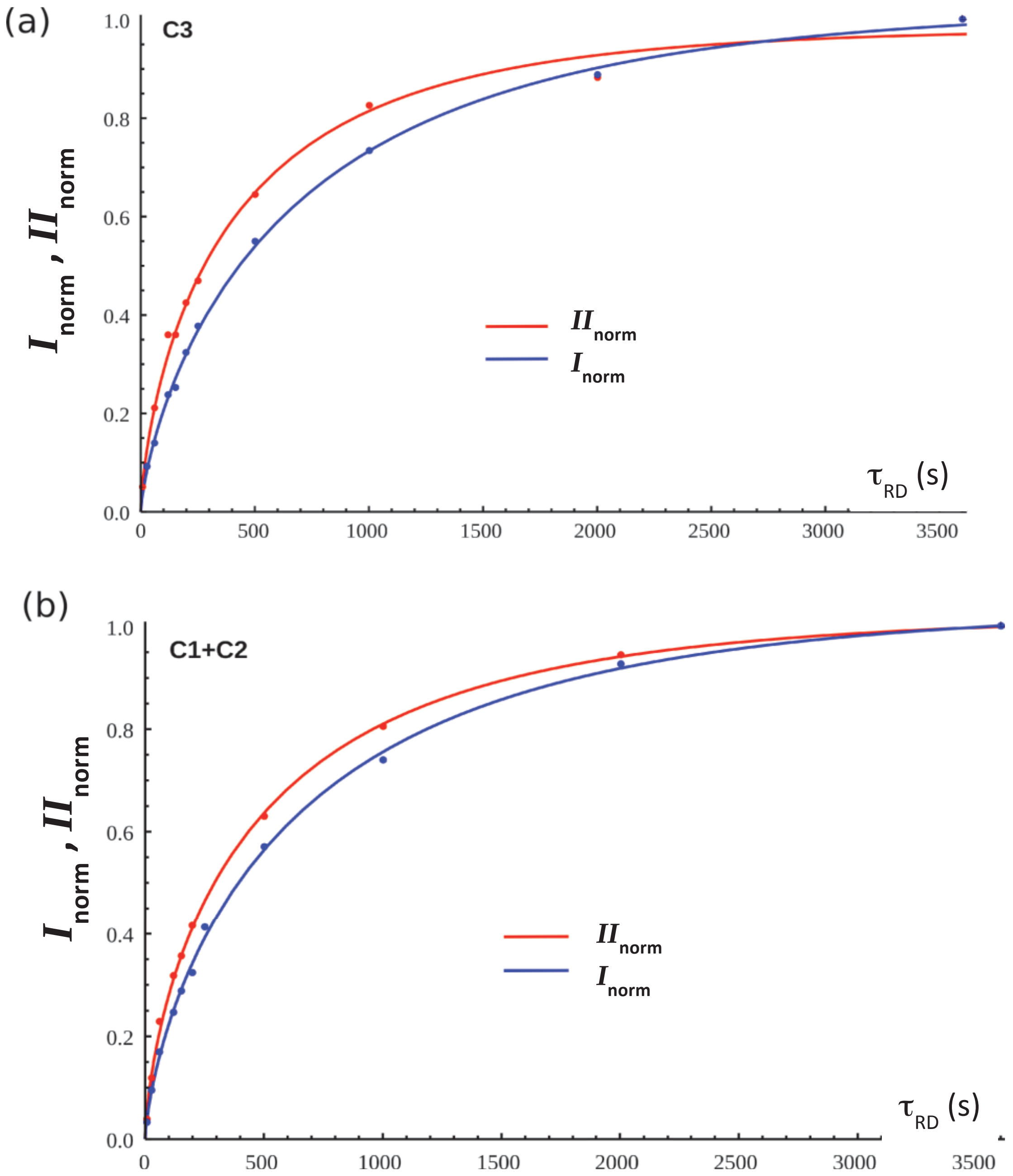

Fig.S6 Build-ups of intensity and intregrated intensity of DNP-enhanced direct ^{13}C MAS signals of (a) C3 and (b) C1,2 sites. The signal intensity, $I(\tau_{\mathrm{RD}})$, and the integrated intensity, $II(\tau_{\mathrm{RD}})$, are normalized with respect to their value at τ_{RD} = 3600 s: $X_{\mathrm{norm}}(\tau_{\mathrm{RD}}) = X(\tau_{\mathrm{RD}})/X(3600\mathrm{s})$ with $X = I$ and II. The experimental values are depicted as dots, whereas the best fit curves are displayed as continuous lines.

The buildups of I_{norm} and II_{norm} were fitted to a stretched exponential function

$$X_{\mathrm{norm}}(\tau_{\mathrm{RD}}) = X_{\mathrm{norm}}^{\infty}\left\{1 - \exp\left[-\left(\frac{\tau_{\mathrm{RD}}}{T_1}\right)^n\right]\right\} \qquad \text{(S13)}$$

Where $X = I$ or II, $X_{\mathrm{norm}}^{\infty}$ is the asymptotic value of X, n is an integer number lower than 1, is T_1 is the build-up time constant. The best fit parameters T_1 and n for the C3 and C1,2 signals are given in Table S1.

Table S1. Parameters T_1 and n for the best fits of the buildup curves of DNP-enhanced direct MAS signals of C3 and C1,2 sites.

Sites	C3		C1,2	
X	*I*	*II*	*I*	*II*
n	0.75	0.71	0.73	0.72
T_1 /s	746	449	701	747

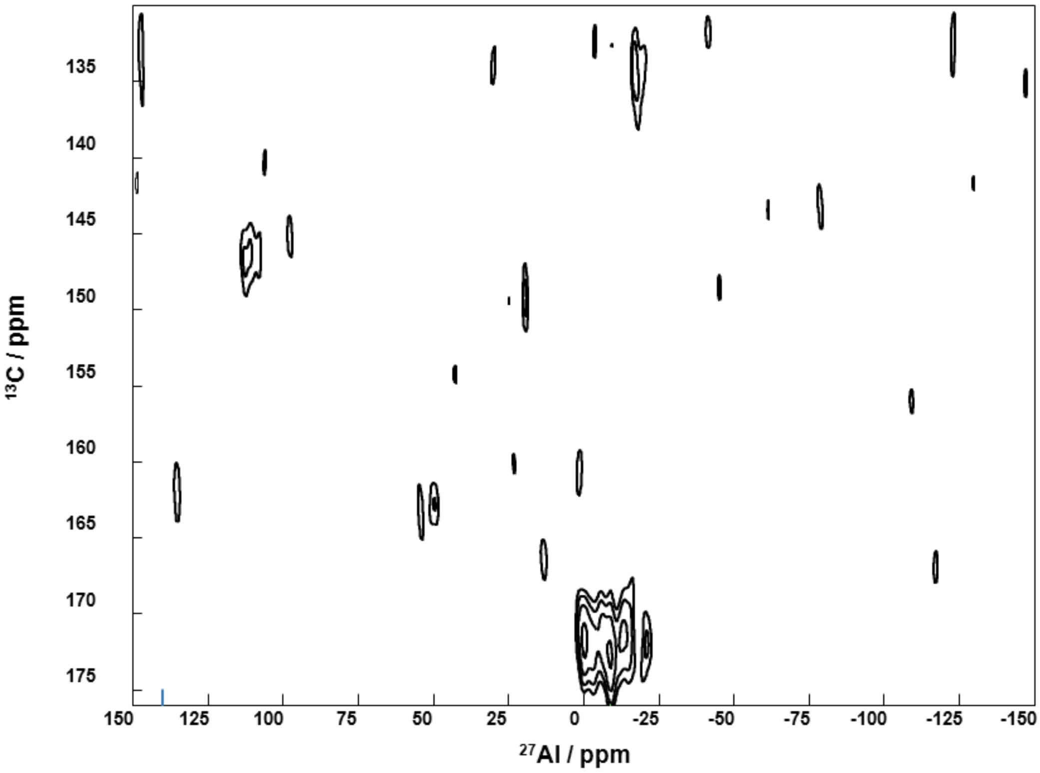

Fig.S7 ^{27}Al-{^{13}C} CP-*D*-HMQC spectrum recorded at 9.4 T, ν_r = 10 kHz and room temperature without μw irradiation.

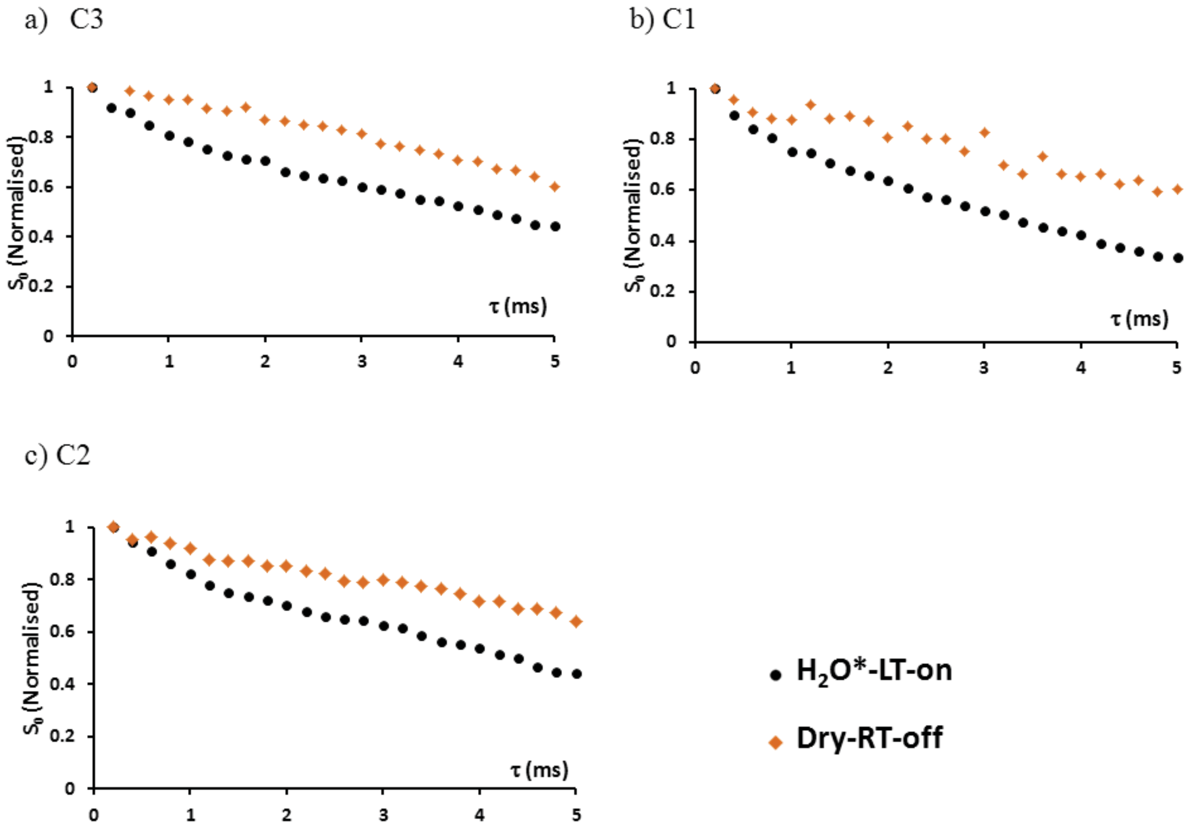

Fig.S8 Evolution of reference signals, S_0, for sites C1, C2 and C3 versus recoupling time, τ, of ^{27}Al-^{13}C S-RESPDOR experiments for experimental conditions H_2O*-LT-on (black disks) and dry-RT-off (orange diamond). For each site and condition, S_0 signal is normalized with respect to its value for $\tau = 0$.

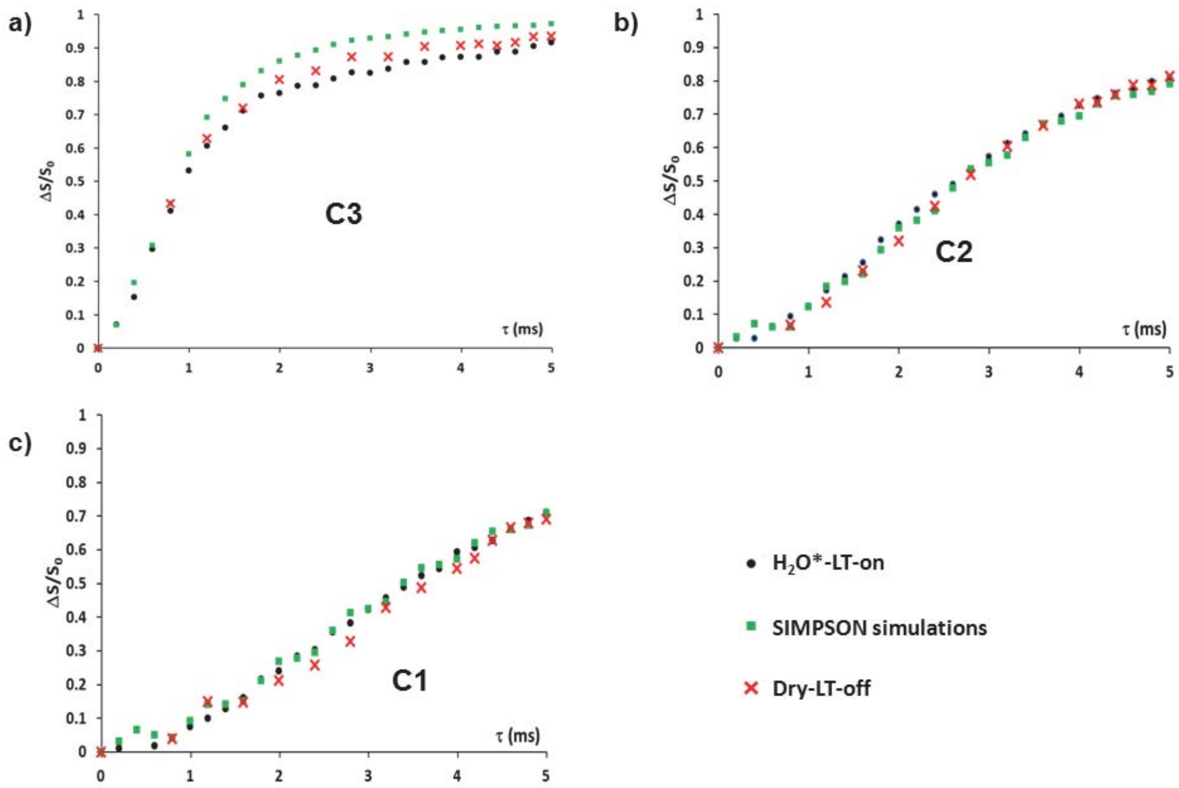

Fig.S9 Experimental ^{27}Al-^{13}C S-RESPDOR fraction curves of the three ^{13}C signals of H_2O*-LT-on (black disks) and dry MIL-100(Al) without microwave irradiation at 100 K (dry-LT-off, red crosses). ^{27}Al-^{13}C S-RESPDOR fraction curves simulated from the crystal structure of MIL-100(Al)[14] are also shown (green squares). Details about the simulation of ^{27}Al-^{13}C S-RESPDOR fraction curves are given above. There is an excellent agreement between experimental and simulated S-RESPDOR fraction curves for C1 and C2. The larger discrepancy for C3 stems from the presence of third Al neighbors, which were not included in the spin system for simulations.

Table S2. Average distances between each C*i* environment and its first and second nearest Al neighbours determined from the single crystal structure analysis of MIL-100(Al).

Site (δ_{iso} /ppm)	C3 (169)	C2 (131)	C1 (138)
d_1(C*i*-Al)^a /nm	0.284	0.417	0.452
d_2(C*i*-Al)^b /nm	0.290	0.420	0.458

^{a}Average distance between C*i* environment with i = 1, 2 and 3 and the first nearest Al neighbour. ^{b}Average distance between C*i* environment and the second nearest Al neighbour.

1 C. Volkringer, D. Popov, T. Loiseau, G. Férey, M. Burghammer, C. Riekel, M. Haouas and F. Taulelle, *Chem. Mater.*, 2009, **21**, 5695.

2 Y. Matsuki, T. Maly, O. Ouari, H. Karoui, F. Le Moigne, E. Rizzato, S. Lyubenova, J. Herzfeld, T. Prisner, P. Tordo and R. G. Griffin, *Angew. Chem.-Int. Ed.*, 2009, **48**, 4996.

3 B. M. Fung, A. K. Khitrin and K. Ermolaev, *J. Magn. Reson.*, 2000, **142**, 97.

4 O. Lafon, Q. Wang, B. W. Hu, F. Vasconcelos, J. Trébosc, S. Cristol, F. Deng and J. P. Amoureux, *J. Phys. Chem. A*, 2009, **113**, 12864; X. Lu, O. Lafon, J. Trébosc, G. Tricot, L. Delevoye, F. Mear, L. Montagne and J. P. Amoureux, *J. Chem. Phys.*, 2012, **137**.

5 M. Bak, J. T. Rasmussen and N. C. Nielsen, *J. Magn. Reson.*, 2000, **147**, 296.

6 L. Chen, X. Y. Lu, Q. A. Wang, O. Lafon, J. Trébosc, F. Deng and J. P. Amoureux, *J. Magn. Reson.*, 2010, **206**, 269.

7 O. Lafon, A. S. L. Thankamony, T. Kobayashi, D. Carnevale, V. Vitzthum, I.I. Slowing, K. Kandel, H. Vezin, J. P. Amoureux, G. Bodenhausen and M. Pruski, *J. Phys. Chem. C*, 2013, **117**, 1375.

8 C. Volkringer, D. Popov, T. Loiseau, G. Férey, M. Burghammer, C. Riekel, M. Haouas and F. Taulelle, *Chem. Mater.*, 2009, **21**, 5695.

9 S. R. Rabbani and D. T. Edmonds, *Phys. Rev. B*, 1994, **50**, 6184; A. J. Rossini, A. Zagdoun, M. Lelli, J. Canivet, S. Aguado, O. Ouari, P. Tordo, M. Rosay, W. E. Maas, C. Coperet, D. Farrusseng, L. Emsley and A. Lesage, *Angew. Chem-Int. Ed.*, 2012, **51**, 123.

10 O. Lafon, M. Rosay, F. Aussenac, X. Y. Lu, J. Trébosc, O. Cristini, C. Kinowski, N. Touati, H. Vezin and J. P. Amoureux, *Ang. Chem-Int. Ed*, 2011, **50**, 8367; D. Lee, H. Takahashi, A. S. L. Thankamony, J. P. Dacquin, M. Bardet, O. Lafon and G. De Paepe, *J. Am. Chem. Soc.*, 2012, **134**, 18491.

11 T. Kobayashi, O. Lafon, A. S. L. Thankamony, I.I. Slowing, K. Kandel, D. Carnevale, V. Vitzthum, H. Vezin, J. P. Amoureux, G. Bodenhausen and M. Pruski, *Phys. Chem. Chem. Phys.*, 2013, **15**, 5553.

12 O. Lafon, A. S. L. Thankamony, M. Rosay, F. Aussenac, X. Y. Lu, J. Trébosc, V. Bout-Roumazeilles, H. Vezin and J. P. Amoureux, *Chem. Commun.*, 2013, **49**, 2864.

13 U. Akbey, W. T. Franks, A. Linden, S. Lange, R. G. Griffin, B. J. van Rossum and H. Oschkinat, *Angew. Chem.-Int. Ed.*, 2010, **49**, 7803.

14 C. Volkringer, T. Loiseau, M. Haouas, F. Taulelle, D. Popov, M. Burghammer, C. Riekel, C. Zlotea, F. Cuevas, M. Latroche, D. Phanon, C. Knofelv, P. L. Llewellyn and G. Férey, *Chem. Mater.*, 2009, **21**, 5783.

Chapter 4

DNP NMR of nanoparticles

Nanoscience is an emerging area of research with wide applications in biomedical, optical and electronic fields, automotive industry, medical technology, cosmetics and environmental remediation.[1,2] This is because of the distinct physico-chemical properties of nanoparticles (NPs) compared to materials with the same chemical structure but larger size. These properties vary according to the particle size and the relative interfacial area of surface structure. Functionalized nanomaterial-based catalysts are very popular in the field of catalysis for many known organic and inorganic reactions.[3-5] NPs can be considered as a bridge between bulk materials and atomic or molecular structures. They have a similar chemical structure as bulk materials, but with better properties due to their decreased size and increased surface area. In particular, the activities and functions of the nanoparticles can be clarified by correlating molecular level site-specific knowledge regarding its surface and bulk regions. In order to understand the details of structure–function–property relationships of these nanomaterials, solid state DNP NMR has been accepted as an inevitable tool due to its high sensitivity. Conventional (^{1}H, ^{13}C or ^{31}P) NMR studies had been used in the past decades for studying spherical nanoparticles, where the low sensitivity remained a big challenge.[6,7] In the first chapter, application of DNP enhanced MAS NMR spectroscopy on several mesoporous silica nanoparticles has been demonstrated and showed the feasibility of the technique for studying such systems. In this chapter, we demonstrate how the ^{29}Si NMR signals of dispersed inorganic nanoparticles of laponites in a frozen solution containing TOTAPOL can be enhanced by DNP at B_0 = 9.4 T and under MAS.[8] Laponites are industrial synthetic clay NPs, with applications for hybrid materials and soft matter (cleanser, coating).[9] This protocol should become a standard for the DNP of NPs, since they are often dispersed in a liquid phase to prevent their aggregation. Hitherto, dispersion in frozen TOTAPOL solutions has only been demonstrated for indirect ^{13}C and ^{15}N DNP of biological systems, such as bacteriophage or peptide mesocrystals.[10,11] The dispersion is supplementary to impregnation and co-condensation which have been employed for high-field MAS DNP of porous solids or particle aggregates. Enhancements of ^{29}Si NMR signals in the order of 10 are reported in direct polarization (DP) and ^{1}H-^{29}Si cross-polarization (CP) experiments. This enhancement facilitates the detection of edge and defect sites. We also show the complementarity of indirect and direct ^{29}Si DNP: in indirect DNP, ^{1}H spin diffusion distributes the polarization within the whole sample, whereas direct DNP enhances the signals of ^{29}Si sites nearer to TOTAPOL. The polarization build-ups in direct and indirect DNP are compared and the polarization leakage is discussed.

References:

1 M. Wilson, K. Kannangara, G. Smith, M. Simmons and B. Raguse, *Nanotechnology: Basic Science and Emerging Technologies*, Chapman and Hall/CRC, 2002.
2 C.T. Kresge, M.E. Leonowicz, W.J. Roth, J.C. Vartuli and J.S. Beck, *Nature*, 1992, **359**, 710 - 712.
3 Y. Xia, H. Yang and C.T. Campbell, *Accounts of Chemical Research*, 2013, **46**, 1671-1672.
4 A.T. Dickschat, F. Behrends, S. Surmiak, Wei, H. Eckert and A. Studer, *Chemical Communications*, 2013, **49**, 2195-2197.
5 S. Banerjee and S. Santra, *Tetrahedron Letters*, 2009, **50**, 2037-2040.
6 X. Fang, J. Mao, E.M. Levin and K. Schmidt-Rohr, *Journal of the American Chemical Society*, 2009, **131**, 1426-1435.
7 S. Cadars, B.J. Smith, J.D. Epping, S. Acharya, N. Belman, Y. Golan and B.F. Chmelka, *Physical Review Letters*, 2009, **103**, 136802.
8 O. Lafon, A.S.L. Thankamony, M. Rosay, F. Aussenac, X. Lu, J. Trébosc, V. Bout-Roumazeilles, H. Vezin and J.P. Amoureux, *Chemical Communications*, 2012, **49**, 2864-2866.
9 S. Borsacchi, M. Geppi, L. Ricci, G. Ruggeri and C.A. Veracini, *Langmuir*, 2007, **23**, 3953-3960.
10 M. Rosay, A.C. Zeri, N. Astrof, S. Opella, J. Herzfeld and R.G. Griffin, *Journal of the American Chemical Society*, 2001, **123**, 1010-1011.
11 P.C.A. van der Wel, K.N. Hu, J.Z. Lewandowski and R.G. Griffin, *Journal of the American Chemical Society*, 2006, **128**, 10840-10846.

ChemComm

RSCPublishing

COMMUNICATION

View Article Online
View Journal | View Issue

Indirect and direct ^{29}Si dynamic nuclear polarization of dispersed nanoparticles†

Cite this: *Chem. Commun.*, 2013, **49**, 2864

Received 24th August 2012,
Accepted 3rd December 2012

DOI: 10.1039/c2cc36170a

www.rsc.org/chemcomm

Olivier Lafon,*[a] Aany Sofia Lilly Thankamony,[a] Melanie Rosay,[b] Fabien Aussenac,[c] Xingyu Lu,[a] Julien Trébosc,[a] Viviane Bout-Roumazeilles,[d] Hervé Vezin[e] and Jean-Paul Amoureux[a]

We show how the ^{29}Si NMR signals of dispersed inorganic nanoparticles of laponite® can be enhanced by Dynamic Nuclear Polarization (DNP). The direct DNP enhances the signals of ^{29}Si nuclei near unpaired electrons, whereas the indirect DNP *via* ^{1}H enhances the signals of more remote sites.

As a local and non-destructive technique, solid-state nuclear magnetic resonance (NMR) provides precious insight into the atomic-scale structure and dynamics of nanoparticles (NPs), *i.e.* materials with three external dimensions sized between 1 and 100 nm.[1,2] Nevertheless, the low sensitivity of NMR can preclude the observation of diluted species, such as the edge, corner, grafting or surface sites. The sensitivity limitation of NMR is even more acute for nuclei with long longitudinal relaxation times (T_{1n}), low natural abundance and/or low gyromagnetic ratio, such as ^{29}Si.[3,4]

Herein, we show how the NMR signals of inorganic NPs dispersed in a frozen solution containing TOTAPOL[5] can be enhanced at high static magnetic field, B^0, and under magic-angle spinning (MAS) using dynamic nuclear polarization (DNP).[3–12] Enhancements of ^{29}Si NMR signals in the order of 10 are reported in direct polarization (DP) and $^{1}\mathrm{H} \rightarrow {}^{29}\mathrm{Si}$ cross-polarization (CP) experiments for laponite® (**1**), an industrial synthetic clay NP (see Fig. 1), with applications for hybrid materials and soft matter (cleanser, coating).[13–15] Hereafter, the DP and CP experiments with microwave irradiation are referred to as direct and indirect DNP, respectively. This protocol should become a standard for the DNP of NPs, since they are often dispersed in a liquid phase to prevent their aggregation.[16] The dispersion is supplementary to impregnation[4,17] and co-condensation,[18] which have been employed for high-field MAS DNP of porous solids or particle aggregates.[3,4,17–19] Hitherto, dispersion in frozen 1-(TEMPO-4-oxy)-3-(TEMPO-4-amino)-propan-2-ol (TOTAPOL) solutions has only been demonstrated for indirect ^{13}C and ^{15}N DNP of biological systems, such as bacteriophage or peptide mesocrystals.[10,11]

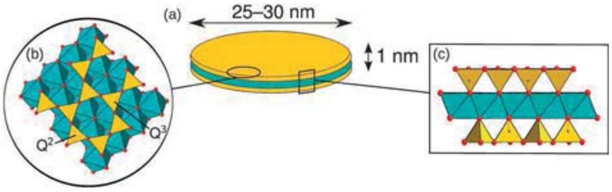

Fig. 1 (a) Schematic representation of **1** NPs, which are disk-shaped crystallites with a diameter of *ca.* 25–30 nm.[20] The specific surface area of **1** is 370 m^2 g^{-1}. (b and c) Atomic-scale structures of the circular (b) and lateral (c) surfaces. The sheet of octahedrally coordinated magnesium atoms is sandwiched by two sheets of silicate.

We also show the complementarity of indirect and direct ^{29}Si DNP: in indirect DNP, ^{1}H spin diffusion distributes the polarization within the whole sample, whereas direct DNP enhances the signals of ^{29}Si sites nearer to TOTAPOL. The polarization buildups in direct and indirect DNP are compared and the polarization leakage is discussed.

Fig. 2a shows how the indirect ^{29}Si DNP results in a 14-fold enhancement of ^{29}Si NMR signals of **1** dispersed in TOTAPOL solution. The concentration in unpaired electrons of **1** is lower than 100 nm (see the EPR spectrum in Fig. S1a, ESI†). Hence, in indirect DNP, the polarization is transferred from an exogenous TOTAPOL radical in the matrix to ^{29}Si nuclei of **1** *via* ^{1}H spin diffusion and $^{1}\mathrm{H} \rightarrow {}^{29}\mathrm{Si}$ CP. The ^{29}Si NMR spectrum enhanced by indirect DNP displays two resolved ^{29}Si NMR signals. The intense peak at −94 ppm corresponds to the $(\mathrm{SiO})_3\mathrm{Si(OMg)}$ (Q^3) sites, located inside the silicate framework, whereas the weak peak at −85 ppm is assigned to the $(\mathrm{SiO})_2\mathrm{Si(OMg)OH}$ (Q^2) sites.[15]

---

[a] Univ. Lille Nord de France, CNRS, UMR 8181 – UCCS, Univ. Lille 1, F-59652 Villeneuve d'Ascq, France. E-mail: olivier.lafon@univ-lille1.fr
[b] Bruker Biospin Corporation, 15 Fortune Drive, Billerica, MA 01821, USA
[c] Bruker Biospin SA, 34, rue de l'Industrie, 67166 Wissembourg Cedex, France
[d] Univ. Lille Nord de France, CNRS, UMR 8217 – Géosystèmes, Univ. Lille 1, F-59652 Villeneuve d'Ascq, France
[e] Univ. Lille Nord de France, CNRS, UMR 8516 – LASIR, Univ. Lille 1, F-59652 Villeneuve d'Ascq, France

† Electronic supplementary information (ESI) available: Experimental procedures, additional EPR and DNP data, location of Q^2 sites and transfer depth of direct DNP. See DOI: 10.1039/c2cc36170a

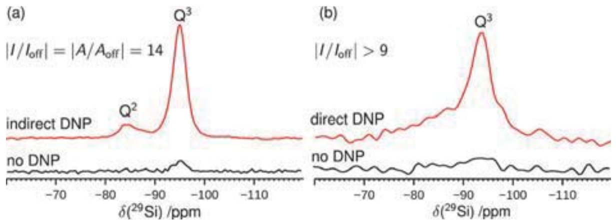

Fig. 2 Natural abundance ^{29}Si NMR spectra of **1** obtained with (a) CP-MAS and (b) DP-MAS sequences. In each subfigure, the top and bottom spectra are recorded with and without microwave irradiation, respectively. All the spectra were acquired at a MAS frequency ν_r = 8 kHz and a field B^0 = 9.391 T. The sample temperature was 98 K without microwave irradiation. The $\tau_{\mu w}$ delays are 5 s in a and 120 s in b. Additional experimental parameters are given in the ESI.†

We show in the ESI† that the Q^2 sites do not only correspond to the edges of **1**, but also to point defects in the silicate sheets, which might result from the breaking of Si–O–Si bonds and the formation of Si–OH groups. Interestingly we also show in the ESI† that the number of Q^2 sites not located at the edge of the NP is about twice the number of Li atoms.

The indirect ^{29}Si DNP is not quantitative since the integral ratio between Q^2 and Q^3 signals is about 6 in indirect DNP and 12.5 in quantitative NMR experiments. The lack of quantitativeness for indirect DNP results from the larger CP enhancement of Q^2 ^{29}Si sites, which are covalently bonded to the O^1H group.[21] No line broadening was observed between CP-MAS spectra with or without microwave irradiation and hence the DNP enhancements calculated from intensities or integrals are identical (see Fig. 3a). The absence of line broadening indicates that the indirect DNP enhancements are not higher for ^{29}Si near TOTAPOL. This nearly uniform enhancement stems from (i) the ^1H spin diffusion, which distributes the enhanced polarization among all ^1H in the sample,[11] and (ii) the low CP efficiency near the unpaired electrons owing to short longitudinal nuclear relaxation times in the rotating frame, $T_{1n\rho}$ and the paramagnetic shifts.[22]

Fig. 2b shows that direct ^{29}Si DNP using direct polarization (DP) of ^{29}Si nuclei also produces a high enhancement of the ^{29}Si signal. The enhancement cannot be determined owing to the low signal-to-noise ratio for DP without DNP. Given the maximal intensity in the DP-MAS spectrum without microwave irradiation, the DNP enhancement of intensity must be larger than 9 for direct DNP.

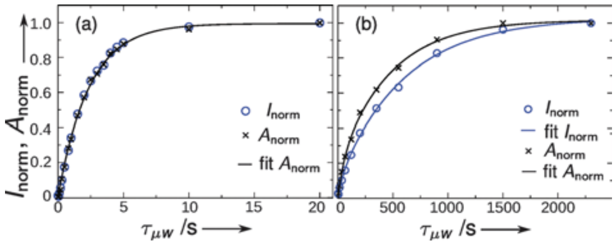

Fig. 3 Buildup curves of ^{29}Si polarization enhanced by (a) indirect and (b) direct DNP. The DNP-enhanced ^{29}Si signal intensity, $I(\tau_{\mu w})$, of Q^3 sites and the DNP-enhanced integral, $A(\tau_{\mu w})$, of all ^{29}Si signals are normalized with respect to the signal intensity and integral at $\tau_{\mu w}$ = 20 and 2300 s in a and b, respectively: $X_{\rm norm} = X(\tau_{\mu w})/X(20)$ in a and $X(\tau_{\mu w})/X(2300)$ in b with $X = I$ or A. The normalized intensities and integrals are depicted as blue circles and black crosses. The best-fit curves are displayed as continuous lines.

For a polarization delay, $\tau_{\mu w}$ = 120 s, only the Q^3 signal at −94 ppm is visible in Fig. 2b. The signal of the Q^2 site is unresolved owing to line broadening compared to the indirect DNP (see Fig. S4, ESI†). For longer $\tau_{\mu w}$ times, there is a line narrowing and the Q^2 signal is resolved. The line narrowing for increasing $\tau_{\mu w}$ stems from the slower buildup for increasing distances from TOTAPOL[9] since in direct ^{29}Si DNP, the spin diffusion is vanishing and the polarization is primarily transferred *via* electron–^{29}Si interactions.[4,8] Hence, direct DNP with short $\tau_{\mu w}$ chiefly polarizes ^{29}Si nuclei near unpaired electrons, as already observed for low-field ^{13}C direct DNP.[8] However, for $\tau_{\mu w}$ = 120 s, direct DNP already enhances signals of ^{29}Si nuclei 3.0–3.5 nm distant from TOTAPOL (see the ESI†).

For indirect ^{29}Si DNP experiments, the identical buildups of normalized intensities and integrals, $I_{\rm norm}$ and $A_{\rm norm}$, for Q^3 sites were fitted by a monoexponential function (see Fig. 3a)

$$X_{\rm norm} = X^{\infty}_{\rm norm}\left\{1 - \exp\left[-\left(\frac{\tau_{\mu w}}{\tau_{\rm DNP}}\right)^{n}\right]\right\} \qquad (1)$$

with n = 1 and a buildup time constant, $\tau_{\rm DNP}$ = 2.37 s. The $\tau_{\rm DNP}$ constant is of the same order of magnitude as the $T_1(^1H)$, as expected for a cross-effect (CE).[23] The monoexponential buildup results from the ^1H spin diffusion, which suppresses the heterogeneity of DNP buildup between ^1H nuclei experiencing different hyperfine interactions.

The direct ^{29}Si DNP buildups, shown in Fig. 3b, cannot be fitted to a monoexponential function (n = 1 in eqn (1)) owing to the longer DNP buildup time for increasing ^{29}Si–TOTAPOL distance. In the case of CE, the buildups of NMR signals are similar with and without microwave irradiation[23] and hence the direct DNP buildups were fitted to the stretched exponential function of eqn (1), in analogy with paramagnetic relaxation for vanishing spin diffusion.[24] The value n = 0.5 should be obtained when (i) the buildup is only governed by ^{29}Si–electron interactions, and (ii) there is a three-dimensional random distribution of unpaired electrons.[18,25]

The best fit parameters of buildups are n = 0.89 and $\tau_{\rm DNP}$ = 480 s for $I_{\rm norm}$ and n = 0.83 and $\tau_{\rm DNP}$ = 330 s for $A_{\rm norm}$. The shorter $\tau_{\rm DNP}$ value for $A_{\rm norm}$ stems from the faster polarization of the ^{29}Si nuclei nearer to TOTAPOL. The n value, intermediate between 0.5 and 1, indicates that the ^{29}Si nuclei do not only relax *via* electron–^{29}Si interactions but also *via* other interactions, which are independent of the electron–nucleus distance, such as ^1H–^{29}Si dipolar couplings.[24,26] This additional relaxation mode produces a leakage in ^{29}Si polarization and limits the DNP enhancement, especially for the ^{29}Si nuclei distant from TOTAPOL.

DNP experiments were also carried out on a natural clay, the bentonite (**2**), dispersed in TOTAPOL solution. The major constituents of **2** are montmorillonite NPs and nanoplates. The atomic-scale structure of montmorillonite is similar to that of **1**: a layer of Al and Mg atoms in octahedral coordination is sandwiched by two silicate layers. However, only two-thirds of octahedral sites are occupied. The EPR spectrum of **2**, shown in Fig. S1b (ESI†), indicates the presence of paramagnetic centers in **2**: isolated Fe(III) sites, Fe(III) oxide impurities and Mn(II) interlayer ions.[27] No NMR signal enhancement was measured for ^{1}H, ^{27}Al and ^{29}Si direct DNP of **2**. The absence of DNP enhancement must stem from the polarization leakage, since the nuclear relaxation *via* high-spin (S = 5/2) Fe(III) and Mn(II) must be faster than the CE DNP from TOTAPOL.

In conclusion, we demonstrated that direct and indirect DNP enhancements can be obtained for inorganic NPs dispersed in TOTAPOL solution. The DNP is especially useful for the observation of defects, such as the Q^2 sites. We also showed that the direct and indirect ^{29}Si DNP are complementary. The former allows the observation of ^{29}Si nuclei near paramagnetic centers, whereas the latter enhances remote ^{29}Si nuclei owing to ^{1}H spin diffusion and the use of CP. High MAS frequency could be beneficial for direct ^{29}Si DNP since it will improve the resolution and the sensitivity for nuclei in the vicinity of unpaired electrons. For **2**, we showed that the DNP enhancements can be quenched by endogenous paramagnetic centers. The characterization of other nano-objects by high-field DNP is currently under investigation.

The authors are grateful for funding provided by Region Nord/Pas de Calais, Europe (FEDER), CNRS, French Minister of Science, FR-3050, University of Lille 1, ENSCL, Bruker BIOSPIN, and Contract No. ANR-2010-JCJC-0811-01.

References

1 X. Fang, J. Mao, E. M. Levin and K. Schmidt-Rohr, *J. Am. Chem. Soc.*, 2009, **131**, 1426–1435.
2 S. Cadars, B. J. Smith, J. D. Epping, S. Acharya, N. Belman, Y. Golan and B. F. Chmelka, *Phys. Rev. Lett.*, 2009, **103**, 136802.
3 M. Lelli, D. Gajan, A. Lesage, M. A. Caporini, V. Vitzthum, P. Miéville, F. Héroguel, F. Rascón, A. Roussey, C. Thieuleux, M. Boualleg, L. Veyre, G. Bodenhausen, C. Copéret and L. Emsley, *J. Am. Chem. Soc.*, 2011, **133**, 2104–2107.
4 O. Lafon, M. Rosay, F. Aussenac, X. Lu, J. Trébosc, O. Cristini, C. Kinowski, N. Touati, H. Vezin and J.-P. Amoureux, *Angew. Chem., Int. Ed.*, 2011, **50**, 8367–8370.
5 C. Song, K.-N. Hu, C.-G. Joo, T. M. Swager and R. G. Griffin, *J. Am. Chem. Soc.*, 2006, **128**, 11385–11390.
6 T. R. Carver and C. P. Slichter, *Phys. Rev.*, 1953, **92**, 212–213.
7 A. Abragam, J. Combrisson and I. Solomon, *C. R. Acad. Sci.*, 1958, **246**, 1035–1037.
8 R. Wind, M. Duijvestijn, C. van der Lugt, A. Manenschijn and J. Vriend, *Prog. Nucl. Magn. Reson. Spectrosc.*, 1985, **17**, 33–67.
9 M. Afeworki, S. Vega and J. Schaefer, *Macromolecules*, 1992, **25**, 4100–4105.
10 M. Rosay, A.-C. Zeri, N. S. Astrof, S. J. Opella, J. Herzfeld and R. G. Griffin, *J. Am. Chem. Soc.*, 2001, **123**, 1010–1011.
11 P. C. A. van der Wel, K.-N. Hu, J. Lewandowski and R. G. Griffin, *J. Am. Chem. Soc.*, 2006, **128**, 10840–10846.
12 M. Rosay, L. Tometich, S. Pawsey, R. Bader, R. Schauwecker, M. Blank, P. M. Borchard, S. R. Cauffman, K. L. Felch, R. T. Weber, R. J. Temkin, R. G. Griffin and W. E. Maas, *Phys. Chem. Chem. Phys.*, 2010, **12**, 5850–5860.
13 Q. Wang, J. L. Mynar, M. Yoshida, E. Lee, M. Lee, K. Okuro, K. Kinbara and T. Aida, *Nature*, 2010, **463**, 339–343.
14 B. Ruzicka, E. Zaccarelli, L. Zulian, R. Angelini, M. Sztucki, A. Moussaïd, T. Narayanan and F. Sciortino, *Nat. Mater.*, 2011, **10**, 56–60.
15 S. Borsacchi, M. Geppi, L. Ricci, G. Ruggeri and C. A. Veracini, *Langmuir*, 2007, **23**, 3953–3960.
16 A. R. Studart, E. Amstad and L. J. Gauckler, *Langmuir*, 2006, **23**, 1081–1090.
17 A. Lesage, M. Lelli, D. Gajan, M. A. Caporini, V. Vitzthum, P. Miéville, J. Alauzun, A. Roussey, C. Thieuleux, A. Mehdi, G. Bodenhausen, C. Copéret and L. Emsley, *J. Am. Chem. Soc.*, 2010, **132**, 15459–15461.
18 A. S. Lilly Thankamony, O. Lafon, X. Lu, F. Aussenac, M. Rosay, J. Trébosc, H. Vezin and J.-P. Amoureux, *Appl. Magn. Reson.*, 2012, **43**, 237–250.
19 V. Vitzthum, P. Mieville, D. Carnevale, M. A. Caporini, D. Gajan, C. Copéret, M. Lelli, A. Zagdoun, A. J. Rossini, A. Lesage, L. Emsley and G. Bodenhausen, *Chem. Commun.*, 2012, **48**, 1988–1990.
20 H. J. M. Hanley, C. D. Muzny and B. D. Butler, *Langmuir*, 1997, **13**, 5276–5282.
21 G. Hou, S. Ding, L. Zhang and F. Deng, *J. Am. Chem. Soc.*, 2010, **132**, 5538–5539.
22 S. Lange, A. H. Linden, Ü. Akbey, W. Trent Franks, N. M. Loening, B.-J. v. Rossum and H. Oschkinat, *J. Magn. Reson.*, 2012, **216**, 209–212.
23 D. S. Wollan, *Phys. Rev. B*, 1976, **13**, 3671–3685.
24 J. S. Hartman, A. Narayanan and Y. Wang, *J. Am. Chem. Soc.*, 1994, **116**, 4019–4027.
25 D. Tse and S. R. Hartmann, *Phys. Rev. Lett.*, 1968, **21**, 511–514.
26 S. Hayashi, *J. Phys. Chem.*, 1995, **99**, 7120–7129.
27 P. L. Hall, *Clay Miner.*, 1980, **15**, 321–335.

Electronic Supporting Information for "Indirect and Direct ^{29}Si Dynamic Nuclear Polarization of Dispersed Nanoparticles"

Sample preparation

The laponite® RD (**1**) was purchased from Rockwood Additives Ltd., Widnes (UK). It is a trioctahedral 2:1 phyllosilicate with the empirical formula $Na_{0.7}$ $[Si_8Mg_{5.5}Li_{0.3}O_{20}(OH)_4]$. Samples for solid-state DNP NMR experiments were prepared by dispersing at room temperature (20 °C) about 100 mg of **1** in about 340 mg of 20 mM TOTAPOL[1] solution in $[^2H_6]$-DMSO/$^2H_2O/H_2O$ mixture (78/14/8 w/w/w). The mixture was stirred vigorously until the formation of a viscous, translucent and yellowish gel.

The bentonite (**2**) is taken from an Oxfordian (Upper Jurassic) deposit in Paris bassin and primarily consists of montmorillonite, a dioctahedral 2:1 phyllosilicate. **2** may also contain traces of feldspar, quartz, calcite, and gypsum. The empirical formula of **2** is $Ca_{0.2}(Al,Mg)_2Si_4O_{10}(OH)_2$-$4H_2O$. In **2**, the montmorillonite platelets exhibit a uniform height of 1 nm, whereas they vary in both shape and size. The longest chord inside the platelet ranges from 5 to 750 nm and its average value is about 300 nm.[2,3] Samples for solid-state DNP NMR experiments were prepared by dispersing about 100 mg of **2** in about 290 mg of 20 mM TOTAPOL solution in $[^2H_6]$-DMSO/$^2H_2O/H_2O$ mixture (78/14/8 w/w/w). **2** and the solution were stirred vigorously until the formation of a colloidal suspension. After three days, the sample was centrifuged during 5 min at a relative centrifugal force of 12,110 to remove the excess of solution.

The impregnated samples were placed into a 3.2 mm sapphire rotors for DNP experiments.

EPR experiments

X-band EPR experiments were performed using a Bruker Biospin ELEXYS E580E spectrometer. The spectra were recorded with respectively 2 mW microwave power and 0.5 G of amplitude modulation. Spin concentration of sample was determined by full spectra integration.

Figure S1a shows the EPR spectrum of **1**. The signal-to-noise ratio of this spectrum is close to 2 and hence the concentration of electron spins, $c_e[\text{spins.g}^{-1}]$, expressed in spins.g^{-1}, is comparable to the lower limit of detection of the EPR spectrometer, i.e. 10^{13} spins.g^{-1}. The concentration of electron spins, $c_e[\text{M}]$, expressed in M, is

$$c_e[\text{M}] = \frac{10^3 c_e[\text{spins.g}^{-1}]\rho_b}{N_A} \approx 2 \times 10^{-8}\ \text{M} \qquad \text{(S1)}$$

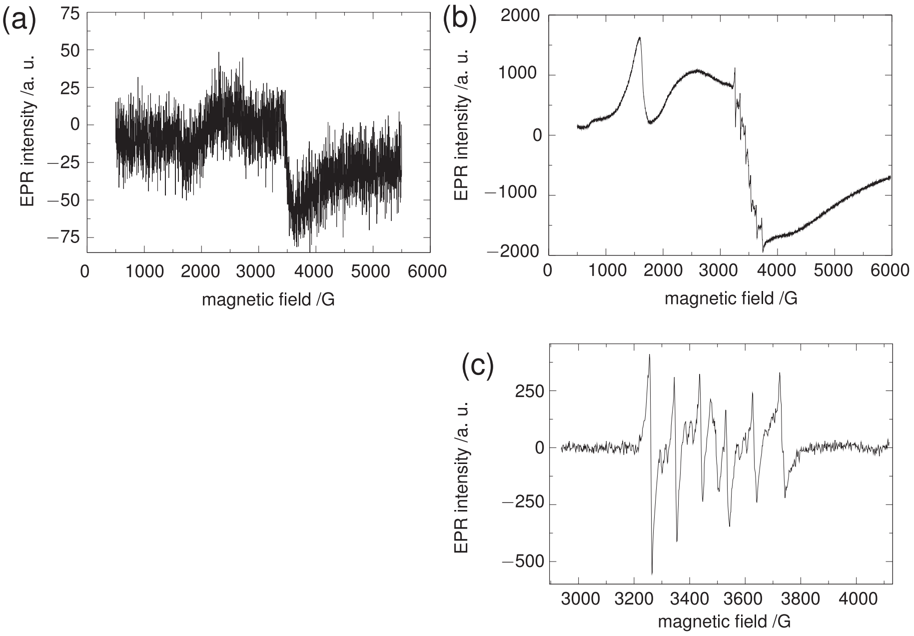

Figure S1: 9 GHz continuous wave EPR spectra of (a) **1** and (b-c) **2**. The spectrum c is an expansion of spectrum b, centered on the signal of the Mn(II) sites. The spectra were recorded at room temperature and the samples were powders. The EPR intensities are expressed in an arbitrary unit, which is identical for the three spectra.

where $\rho_b \approx 1$ kg.dm^{-3} is the bulk density of **1** and N_A is the Avogadro number.

In Figure S1b, the narrow resonance centered about $g \approx 4.3$ was attributed to octahedrally coordinated high spin ($S = 5/2$) Fe(III) atoms, which substitute Al(III) atoms in the octahedral layer of montmorillonite.[4,5] The broad resonance ($\Delta B > 10^3$ G) at about $g \approx 2$ stems from iron (III) oxides which are often present in **2** ores.[4,5] The concentration of electron spins for iron oxide was estimated to be in the order of 10^{17} spins g^{-1}. However, the unpaired electrons in iron oxide are submitted to ferromagnetic interactions, which can bias the measurement of electron spin density. In addition, narrow resonances are superimposed to the iron oxide signal. An expansion of these resonances after baseline correction is shown in Figure S1c. This spectrum is a powder lineshape centered at $g \approx 2$, which consists of six intense resonances and weaker doublets, which appear between the intense resonances. These spectral features are characteristic of high-spin ($S = 5/2$) Mn(II) sites with axial symmetry.[6] The splitting in six resonances results from anisotropic hyperfine coupling with ^{55}Mn nucleus of nuclear spin $I = 5/2$, whereas the weak doublets stem from forbidden hyperfine transitions corresponding to the changes, $\Delta m_S = \pm 1$ and $\Delta m_I = \pm 1$, in the azimuthal quantum numbers of the unpaired electron and ^{55}Mn nucleus. The Mn(II) sites in montmorillonite were ascribed to interlayer Mn(II) ions.[6] The density of electron spins corresponding to Mn(II) sites was determined using $MnCl_2$ as a reference and is equal to 2.6×10^{16} spins g^{-1}.

DNP experiments

All solid-state DNP MAS experiments were performed on a commercial Bruker BioSpin Avance III DNP spectrometer operating at a microwave frequency of 263 GHz and a ^{29}Si frequency of 79.2 MHz.[7] The wide-bore 9.4 T NMR magnet was equipped with a double resonance ^{1}H/X 3.2 mm low-temperature probe. The sample was placed in a 3.2 mm sapphire rotor. DNP experiments are usually performed at cryogenic temperatures because electron and nuclear relaxation processes slow with decreasing temperature.[7,8] Sample temperature of 98 K was achieved and controlled under MAS condition using a Bruker BioSpin low-temperature MAS cooling system. The sample temperature corresponds to the calibrated temperature with microwave off. During the DNP MAS experiment, a gyrotron generated continuous microwave irradiation, which was delivered to the sample by a corrugated waveguide. The microwave power at the position of the sample was approximately 6 W. The NMR spectra were recorded at $\nu_r = 8$ kHz and result from averaging 8 transients. A SPINAL-64 decoupling with ^{1}H radiofrequency (rf) nutation frequency of 100 kHz was applied during the acquisition.[9] The indirect DNP ^{29}Si NMR spectra were recorded using a CP-MAS pulse sequence (see Figure S2a) in order to transfer the DNP-enhanced ^{1}H polarization to the ^{29}Si nuclei.[10,11] The indirect DNP ^{29}Si NMR experiments used a microwave polarization time, $\tau_{\mu\mathrm{w}} = 5$ s, a ^{1}H 90° pulse length of 2.5 μs, a contact time of 2 ms, a constant ^{29}Si rf nutation frequency of 50 kHz and a linear ramp of ^{1}H rf nutation frequency between 30 kHz and 33 kHz. The direct DNP ^{29}Si NMR spectra were recorded using a ^{29}Si 90° pulse length of 4.2 μs and background suppression (see Figure S2b).[12] Furthermore, the background ^{29}Si signal of the probe was carefully subtracted by recording the DNP ^{29}Si NMR spectra of the empty rotor under identical experimental conditions. In direct ^{29}Si DNP experiments, the equilibrium ^{29}Si Boltzmann was eliminated by a presaturation, consisting of a train of hundred 90° pulses, separated by a delay of $\tau_{ps} = 60$ μs. The ^{29}Si chemical shifts are referenced to tetramethylsilane using the shielded resonance (−9.8 ppm) in the ^{29}Si NMR spectrum of tetrakis(trimethylsilyl)silane as a secondary reference.

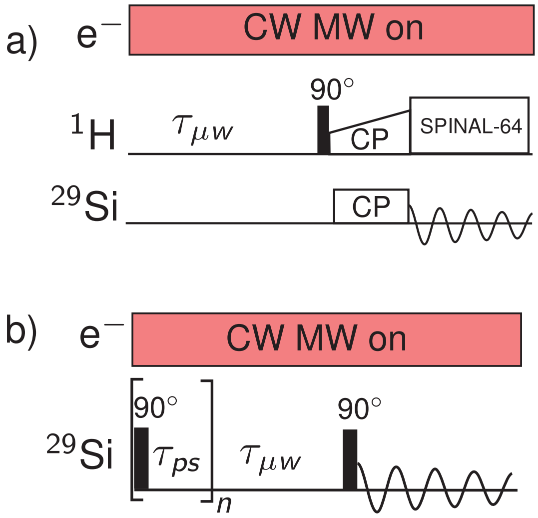

Figure S2: (a) Pulse sequence used for 1D indirect DNP MAS experiment. The longitudinal ^{1}H polarization develops during $\tau_{\mu\mathrm{w}}$ and is finally transferred to ^{29}Si nuclei using a CP step. (b) Pulse sequence used for 1D direct DNP MAS experiment. The longitudinal ^{29}Si polarization builds up during the microwave polarization time, $\tau_{\mu\mathrm{w}}$. The same experiment without microwave irradiation serves as a reference for the measurement of signal enhancement by direct DNP.

Location of Q^2 sites

We assume that (i) the silicon atoms are located on the lattice points of a hexagonal two-dimensional lattice, (ii) the NP has the shape of a regular hexagon, (iii) the silicate sites at the edge of the NP are Q^2 sites. This type of structure is depicted in Figure S3. Under these assumptions and taking into the account the two silicate disks in **1** NP, the numbers of Q^2 sites at the NP edges, $N(Q^{2\text{edge}})$, and of internal silicon atoms, $N(Q^{\text{int}})$, not located on the edges are

$$N(Q^{2\text{edge}}) = 12k \tag{S2}$$

and

$$N(Q^{\text{int}}) = 12k(k-1) \tag{S3}$$

respectively. The index k denotes the number of concentric siloxane rings. It increases from the center to the periphery of the NP. Therefore, we have

$$\frac{N(Q^{2\text{edge}})}{N(Q^{\text{int}})} = \frac{1}{k-1} \tag{S4}$$

Furthermore, the upper and lower bounds for the diameter, d, of the NP are

$$2\sqrt{3}ka \leq d \leq 4ka \tag{S5}$$

where a is the edge length of silicate tetrahedron and $2\sqrt{3}ka$ and $4ka$ are the diameters of the inscribed and circumscribed circles, respectively (see Figure S3). In the crystal structure of talc, which is structurally related to **1**, the length a varies between 2.64 and 2.66 Å.[13] Similar range for a is expected in **1**. Furthermore, using small-angle X-ray scattering and small-angle neutron scattering, the diameter of **1** nanodisks has been found in the range 25–30 nm.[14,15] Therefore, it can be deduced from Eq. S5 that the k value is in the range 24–32 and hence from Eq. S4, we have

$$\frac{N(Q^{2\text{edge}})}{N(Q^{\text{int}})} < 0.04. \tag{S6}$$

The above equation shows that the ratio $N(Q^{2\text{edge}})/N(Q^{\text{int}})$ differs from the ratio of integrals $r^A = A(Q^2)/A(Q^3) = 0.08$ in the quantitative 1D ^{29}Si NMR spectrum [not shown]. Consequently, the internal silicon atoms are not all Q^3 sites and there must be internal Q^2 sites. The number of internal Q^2

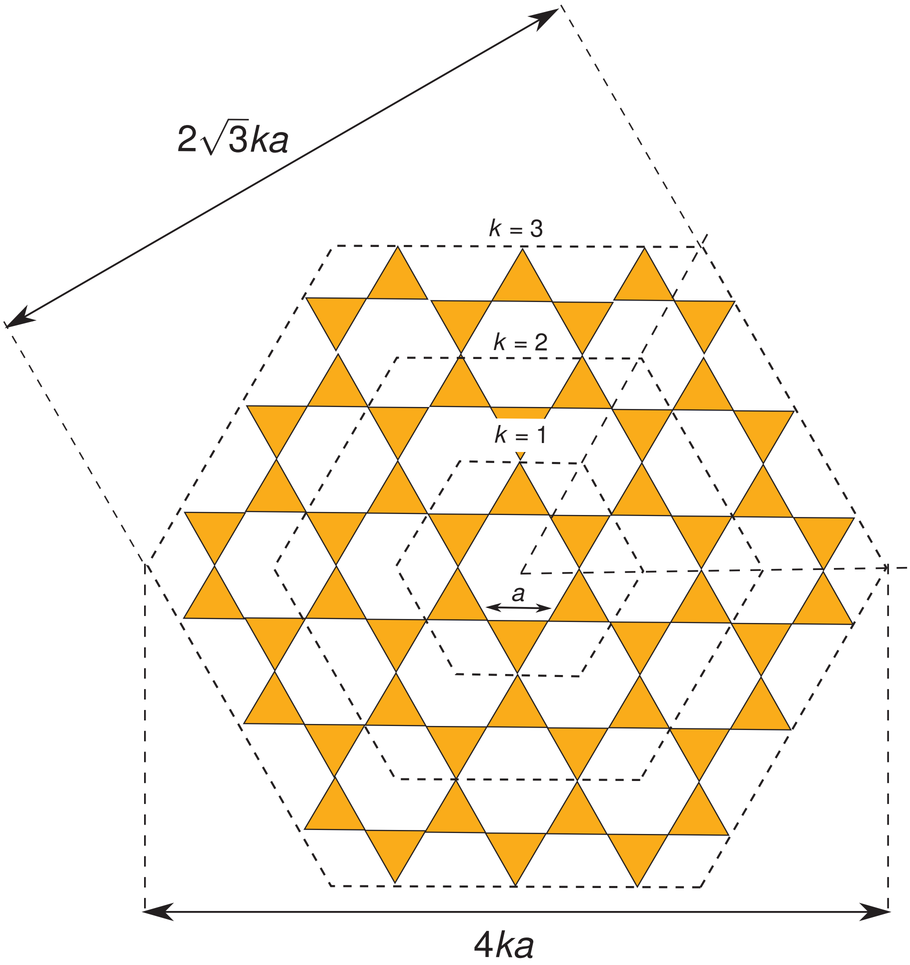

Figure S3: Silicate framework of the tetrahedral sheet in a NP of **1**. The plane of the figure corresponds to the plane of the tetrahedral sheet. The triangles are the bases of silicate tetrahedra.

sites, $Q^{2\text{int}}$, can be estimated from the k and r^A values by solving the system of linear equations, including Eqs. S2 and S3, and the following ones

$$N(Q^2) = N(Q^{2\text{edge}}) + N(Q^{2\text{int}}) \tag{S7}$$

where $N(Q^2)$ is the total number of Q^2 sites in one NP of **1**,

$$N(Q^{\text{int}}) = N(Q^{2\text{int}}) + N(Q^3) \tag{S8}$$

where $N(Q^3)$ is the number of Q^3 sites in one NP of **1**,

$$N(\text{Si}) = N(Q^2) + N(Q^3) \tag{S9}$$

where $N(\text{Si})$ is the number of silicon atom in one NP of **1**,

$$\frac{N(Q^2)}{N(Q^3)} = r^A. \tag{S10}$$

The expressions of $N(Q^{2\text{int}})$ and $N(\text{Si})$ derived from the above equations are

$$N(Q^{2\text{int}}) = 12k\frac{(k-1)r^A - 1}{r^A + 1} \tag{S11}$$

and

$$N(\text{Si}) = 12k^2, \tag{S12}$$

respectively. Consequently, the $N(Q^{2\text{int}})$ value ranges from 228 to 533, whereas the $N(\text{Si})$ value ranges from 3450 to 6150, depending on the diameter of the **1** NP. According to the empirical formula of **1**, the number of Li atoms ranges from 130 for $N(Q^{2\text{int}}) = 228$ to 230 for $N(Q^{2\text{int}}) = 533$ and hence there are about two Q^2 sites for each Li atom. The presence of the internal Q^2 sites might be related to the substitution of Mg^{2+} by Li^+. Furthermore, the amount of internal Q^2 sites is estimated at about 44–58% of the total number of Q^2 sites and at about 6.6–8.7% of the total number of silicon atom in **1**. These estimates agree with the amount of Q^2 sites that do not react during the functionalization of **1** with organic molecules.[16,17] Additional experiments and first-principle calculations will be required to determine the exact structure of the internal Q^2 sites.

Comparison of ^{29}Si NMR spectra enhanced by direct and indirect DNP

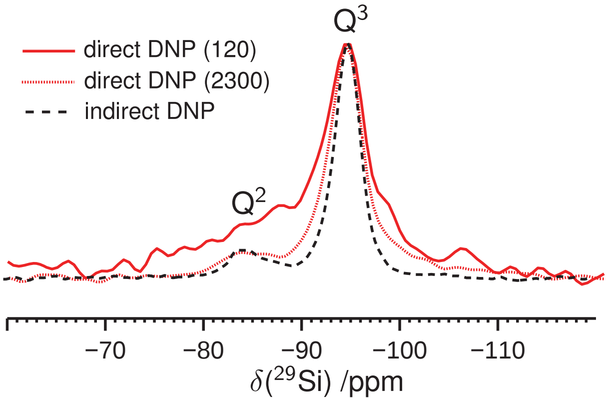

Figure S4: Natural abundance ^{29}Si NMR spectra of **1** obtained via indirect DNP and direct DNP with $\tau_{\mu\mathrm{w}} = 120$ s [direct DNP (120)] or 2300 s [direct DNP (2300)]. The indirect and direct DNP (120) spectra are identical to those of Figure 2, but they are scaled to the same absolute intensity in order to show the broadening of ^{29}Si NMR signal in direct DNP experiments. The fullwidth half-height (FWHH) of Q^3 site is 440 Hz in the direct DNP with $\tau_{\mu\mathrm{w}} = 120$ s and 300 Hz with $\tau_{\mu\mathrm{w}} = 2300$ s, whereas it is 250 Hz in spectrum enhanced by indirect DNP.

Estimate of transfer depth in direct ^{29}Si DNP

We show below that the transfer depth of direct ^{29}Si DNP can be estimated from the fullwidth at half height (FWHH) of Q^3 signals. The ^{29}Si transverse relaxation rate, $1/T_2(^{29}\text{Si})$, governed by ^{29}Si-TOTAPOL interactions represents a lower bound for FWHH. Hence, assuming an exponential decay of the ^{29}Si NMR signal, we have

$$\text{FWHH} \geq \frac{1}{\pi T_2(^{29}\text{Si})}. \tag{S13}$$

The $T_2(^{29}\text{Si})$ relaxation of Q^3 contributing to FWHH is governed by the fluctuations of the dipolar interactions between ^{29}Si and TOTAPOL[18] since (i) in solids, the Curie relaxation[19] is absent[20], (ii) the contact relaxation[21] only dominates for nuclei at a distance shorter than 4 Å from the unpaired electrons[22] and (iii) at MAS frequency of 8 kHz, the signal of nuclei at a distance of few angstroms from the TOTAPOL is quenched by electron-nucleus interactions.[23] Assuming that the point-dipole-approximation holds for the TOTAPOL-^{29}Si interaction and that the electron g-tensor is isotropic, the $1/T_2(^{29}\text{Si})$ rate via electron-nucleus dipolar interactions is given by[18,24,25,19,22]

$$\begin{aligned}\frac{1}{T_2(^{29}\text{Si})} = \frac{S\,(S+1)}{15}\left[\frac{\mu_0}{4\pi}\frac{\hbar\gamma(^{29}\text{Si})\gamma_e}{r^3}\right]^2 &\left[4T_{1e} + \frac{3T_{1e}}{1+\omega^2(^{29}\text{Si})T_{1e}^2} + \frac{6T_{2e}}{1+\omega_e^2T_{2e}^2}\right.\\ &\left. + \frac{T_{2e}}{1+[\omega(^{29}\text{Si})-\omega_e]^2T_{2e}^2} + \frac{6T_{2e}}{1+[\omega(^{29}\text{Si})+\omega_e]^2T_{2e}^2}\right],\end{aligned} \tag{S14}$$

where μ_0 is the magnetic constant, $\hbar$ is the reduced Planck constant, γ_e and $\gamma(^{29}\text{Si})$ are the gyromagnetic ratios of electron and ^{29}Si nucleus, S is the effective spin number for TOTAPOL, which is 1/2 or 1 depending on the coupling between the two unpaired electron, r is the TOTAPOL-^{29}Si distance, T_{1e} and T_{2e} times are the longitudinal and transverse electron relaxation times, $\omega(^{29}\text{Si})$ and ω_e are the ^{29}Si and electron Larmor frequencies. As $\omega(^{29}\text{Si}) = 79.4$ MHz $\ll \omega_e = 263$ GHz, Eq. S14 can be recast as[19,22]

$$\begin{aligned}\frac{1}{T_2(^{29}\text{Si})} = \frac{S\,(S+1)}{15}\left[\frac{\mu_0}{4\pi}\frac{\hbar\gamma(^{29}\text{Si})\gamma_e}{r^3}\right]^2 &\left[4T_{1e} + \frac{3T_{1e}}{1+\omega^2(^{29}\text{Si})T_{1e}^2}\right.\\ &\left. + \frac{13T_{2e}}{1+\omega_e^2T_{2e}^2}\right].\end{aligned} \tag{S15}$$

The combination of Eqs. S13 and S15 yields a lower bound for r

$$r \geq \left\{ \frac{S\,(S+1)}{15} \left[\frac{\mu_0}{4\pi} \hbar \gamma(^{29}\mathrm{Si}) \gamma_e \right]^2 \frac{1}{\pi \mathrm{FWHH}} \times \right. \\ \left. \left[4T_{1e} + \frac{3T_{1e}}{1+\omega^2(^{29}\mathrm{Si})T_{1e}^2} + \frac{13T_{2e}}{1+\omega_e^2 T_{2e}^2} \right] \right\}^{1/6}. \tag{S16}$$

The right member of the above equation depends on the electron relaxation times. EPR measurements at $B^0 = 3.35$ T on TOTAPOL in frozen solution yielded $T_{1e} = 554$ μs and $T_{2e} = 1.6$ μs.[26] For radicals in glassy organic solvents, the dominant relaxation mechanism of the electron spin is the second-order Raman process, which is independent of B^0.[27,26] Hence, the T_{1e} and T_{2e} values at $B^0 = 9.39$ T should be close to those determined at $B^0 = 3.35$ T. For $\tau_{\mu\mathrm{w}} = 120$ s, the FWHH in direct ^{29}Si spectrum is 440 Hz. Consequently the r distance must be longer than 3.0 nm for $S = 1/2$ or 3.5 nm for $S = 1$ according to Eq. S16.

References

[1] C. Song, K.-N. Hu, C.-G. Joo, T. M. Swager and R. G. Griffin, *J. Am. Chem. Soc.*, 2006, **128**, 11385–11390.

[2] L. J. Michot, I. Bihannic, K. Porsch, S. Maddi, C. Baravian, J. Mougel and P. Levitz, *Langmuir*, 2004, **20**, 10829–10837.

[3] A. Cadene, S. Durand-Vidal, P. Turq and J. Brendle, *J. Colloid Interface Sci.*, 2005, **285**, 719–730.

[4] B. A. Goodman, *Clay Miner.*, 1978, **13**, 351–356.

[5] P. L. Hall, *Clay Miner.*, 1980, **15**, 321–335.

[6] A. U. Gehring, I. V. Fry, T. Lloyd and G. Sposito, *Clays Clay Miner.*, 1993, **41**, 565–569.

[7] M. Rosay, L. Tometich, S. Pawsey, R. Bader, R. Schauwecker, M. Blank, P. M. Borchard, S. R. Cauffman, K. L. Felch, R. T. Weber, R. J. Temkin, R. G. Griffin and W. E. Maas, *Phys. Chem. Chem. Phys.*, 2010, **12**, 5850–5860.

[8] K.-N. Hu, *Prog. Nucl. Magn. Reson. Spectrosc.*, 2011, **40**, 31–41.

[9] B. M. Fung, A. K. Khitrin and K. Ermolaev, *J. Magn. Reson.*, 2000, **142**, 97 – 101.

[10] M. Lelli, D. Gajan, A. Lesage, M. A. Caporini, V. Vitzthum, P. Miéville, F. Héroguel, F. Rascón, A. Roussey, C. Thieuleux, M. Boualleg, L. Veyre, G. Bodenhausen, C. Copéret and L. Emsley, *J. Am. Chem. Soc.*, 2011, **133**, 2104–2107.

[11] O. Lafon, M. Rosay, F. Aussenac, X. Lu, J. Trébosc, O. Cristini, C. Kinowski, N. Touati, H. Vezin and J.-P. Amoureux, *Angew. Chem. Int. Ed.*, 2011, **50**, 8367–8370.

[12] D. G. Cory and W. M. Ritchey, *J. Magn. Reson.*, 1988, **80**, 128–132.

[13] J. H. Rayner and G. Brown, *Clays Clay Miner.*, 1973, **21**, 103–114.

[14] M. Morvan, D. Espinat, J. Lambard and T. Zemb, *Colloids and Surfaces A: Physicochemical and Engineering Aspects*, 1994, **82**, 193–203.

[15] H. J. M. Hanley, C. D. Muzny and B. D. Butler, *Langmuir*, 1997, **13**, 5276–5282.

[16] P. A. Wheeler, J. Wang, J. Baker and L. J. Mathias, *Chem. Mater.*, 2005, **17**, 3012–3018.

[17] S. Borsacchi, M. Geppi, L. Ricci, G. Ruggeri and C. A. Veracini, *Langmuir*, 2007, **23**, 3953–3960.

[18] I. Solomon, *Phys. Rev.*, 1955, **99**, 559–565.

[19] M. Gueron, *J. Magn. Reson.*, 1975, **19**, 58–66.

[20] G. Kervern, G. Pintacuda, Y. Zhang, E. Oldfield, C. Roukoss, E. Kuntz, E. Herdtweck, J.-M. Basset, S. Cadars, A. Lesage, C. Copéret and L. Emsley, *J. Am. Chem. Soc.*, 2006, **128**, 13545–13552.

[21] N. Bloembergen, *J. Chem. Phys.*, 1957, **27**, 572–573.

[22] J. Koehler and J. Meiler, *Prog. Nucl. Magn. Reson. Spectrosc.*, 2011, **59**, 360–389.

[23] I. Bertini, L. Emsley, M. Lelli, C. Luchinat, J. Mao and G. Pintacuda, *J. Am. Chem. Soc.*, 2010, **132**, 5558–5559.

[24] A. Abragam, *The Principles of Nuclear Magnetism*, Oxford University Press, Oxford, 1961.

[25] R. E. Connick and D. Fiat, *J. Chem. Phys.*, 1966, **44**, 4103–4107.

[26] A. Zagdoun, G. Casano, O. Ouari, G. Lapadula, A. J. Rossini, M. Lelli, M. Baffert, D. Gajan, L. Veyre, W. E. Maas, M. Rosay, R. T. Weber, C. Thieuleux, C. Copéret, A. Lesage, P. Tordo and L. Emsley, *J. Am. Chem. Soc.*, 2011, **134**, 2284–2291.

[27] A. Abragam and B. Bleaney, *Electron paramagnetic resonance of transition ions*, Oxford University Press, 1970.

Chapter 5

Development of novel methods for the observation of ^{1}H and half-integer quadrupolar nuclei in solids

The chapters 2 to 4 focused on the development of DNP NMR for the characterization of inorganic and hybrid materials. This chapter presents my PhD works related to the development of conventional NMR methods. These works include (i) the detailed analysis of tunable homo-nuclear dipolar decoupling for ^{1}H high-resolution NMR spectroscopy of solids, (ii) the development of novel CP sequence to probe hetero-nuclear proximities between half-integer spin quadrupolar isotopes.

5.1. Detailed analysis of tunable homonuclear decoupling for ^{1}H high resolution solid-state NMR

The high gyromagnetic ratio of proton as well as its 99.985 % isotopic natural abundance renders this nucleus the ideal candidate for NMR detection. ^{1}H NMR spectroscopy is routinely used in solution state. Conversely, the characterization of solids by ^{1}H NMR is often limited by poor spectral resolution due to the narrow ^{1}H chemical shift range and the extensive network of ^{1}H-^{1}H homonuclear dipolar interactions.[1] Moreover, as the ^{1}H-^{1}H homonuclear dipolar interactions are homogeneous interactions, the individual ^{1}H line-widths only decrease as the inverse of the MAS frequency. Therefore, rotation of the sample at the magic angle alone does not generally achieve very high resolution, especially at low or moderate MAS frequencies.

The resolution can be further enhanced by combining MAS with rf irradiation schemes that manipulate the spin part of the ^{1}H–^{1}H dipolar interaction.[2,3] Numerous homonuclear dipolar decoupling sequences under MAS conditions have been developed, including rotor-synchronized symmetry-based sequences and non-synchronized sequences,[4-9] such as WHH$_4$, MREV$_8$, BR$_{24}$, BLEW$_{12}$, MSHOT$_3$,[10] FSLG, PMLG and DUMBO.[11] In these sequences, both the spatial and spin parts of the homonuclear dipolar interaction are modulated and hence can interfere. Under slow MAS frequency, the modulation of spatial part is much slower than that of the spin part, which prevents any interference. Long and nested super cycles could then be applied to eliminate high-order terms of the average dipolar Hamiltonian that led to efficient pulse sequences such as BR$_{24}$ and MSHOT$_3$. At higher MAS frequencies, sequences with shorter cycle time, such as PMLG or DUMBO, are required to avoid interferences between MAS and rf irradiation.

Recently the group of Lille in collaboration with Z. Gan and P.K. Madhu has introduced tunable homonuclear decoupling sequences, denoted TIMES (TIlted Magic-Echo Sandwich) and TIMES$_0$ (TIMES with zero degree sandwich pulse), which yield high-resolution ^{1}H spectra from slow to fast MAS.[12] The TIMES sequence combines the sandwich pulses of magic echo and the tilted effective field of FSLG/PMLG. The angle (θ_p) of the effective field with respect to the z-axis and the rf and window delays can be varied so that the TIMES sequence covers three commonly used experiments for high-resolution ^{1}H spectroscopy: (i) MAS ($\theta_p = 0°$), FSLG/PMLG ($\theta_p = 54.7°$) and the magic-echo ($\theta_p = 90°$). Hence, TIMES perform at least no worse than the best of these three experiments. The optimal θ value depends on the MAS frequency since the scaling factors of the isotropic chemical shift and ^{1}H-^{1}H dipolar interaction vary with the MAS frequency. At slow MAS (up to about 10 kHz), the optimal resolution is obtained when the effective field is close to the x-axis ($\theta_p = 90°$), which corresponds to the magic-echo condition. At moderate MAS frequencies (ranging between 15 and 35 kHz), the magic-angle $\theta_p = 54.7°$ yields the highest resolution. At MAS frequencies higher than 40 kHz, the best resolution is obtained for $\theta_p < 40°$. In the regime of high MAS frequencies, the resolution gains from an increase of the chemical shift scaling factor, when the effective field is closer to the *z*-axis. The TIMES$_0$ sequence is a variant of TIMES, in which the bracketing pulses are omitted. TIMES$_0$ scheme can be seen as a re-parametrization of PMLG sequence. Compared to PMLG, TIMES$_0$ allows an independent optimization of the θ_p angle and the cycle time.

We have carefully analysed how the spectral resolution of TIMES and TIMES$_0$ 1D spectra depends on various experimental parameters: the MAS frequency, the rf field strength and the θ_p angle.[13] This systematic study has confirmed the decrease of the optimal θ_p angle for increasing MAS frequency. Furthermore, for all MAS frequencies, the highest spectral resolution is observed for rf field strength of about 120-130 kHz. Interestingly for MAS frequency higher than 60 kHz, high spectral resolution is also achieved for weaker rf field strength of about 40-50 kHz. We have also shown that at MAS frequency higher than 60 kHz, TIMES and TIMES$_0$ sequences yield comparable spectral resolution. Hence, we recommend the use of TIMES$_0$ method at high MAS frequency since it is simpler to optimize. We have also demonstrated that the spectral resolution critically depends on the rf field inhomogeneity and that long excitation pulse can improve the spectral resolution.

5.2. Probing proximities between distinct quadrupolar isotopes using multiple pulses cross polarization

The NMR observation of connectivities and proximities between quadrupolar isotopes is challenging owing to (i) the short relaxation times of coherences for the quadrupolar nuclei, (ii) the weak *J*-couplings between these isotopes, (iii) the difficult dipolar recoupling between these isotopes under MAS owing to their intricate spin dynamics in the presence of sample rotation and rf irradiation.

One-bond ^{27}Al-^{17}O connectivities have been probed via *J*-HMQC 2D experiments. Heteronuclear through-space proximities between the isotope pairs, ^{27}Al-^{17}O, ^{11}B-^{23}Na, ^{11}B-^{27}Al and ^{27}Al-^{7}Li have been probed using continuous-wave (CW) CP under static or MAS conditions.[14,15] However, the efficiency and the robustness of CW-CP transfers are limited owing to the complex spin dynamics during spin locking, which depends on several parameters, including (i) the amplitude of the electric field gradient (efg), (ii) the orientation of the efg principal axis system with respect to the rotor axis, (iii) the MAS frequency and (iv) the rf field strength. In particular, the spin locking of the central transition (CT) of a half integer spin quadrupolar nucleus requires the use of weak CT-selective rf field, at the expense of a high sensitivity to offset. Furthermore, the Rotary Resonance Recoupling (R^3) conditions should be avoided since they strongly decrease the spin locking efficiency.[16-18]

Recently the group of Lille has shown that the robustness of CP transfers between spin- 1/2 and half-integer quadrupolar nuclei can be improved by replacing the CW irradiation on the quadrupolar channel by a burst of rotor-synchronized rf-pulses.[19] The advantage of this multipulse CP (MP-CP) has also been rediscovered in the case of ^{2}H–^{13}C CP transfers using optimal control method.[20] During my PhD, we have investigated the use of MP-CP transfers to probe under MAS the proximities between half-integer quadrupolar isotopes.[21] The D-HETCOR sequence using MP-CP is more robust with respect to offsets than that based on CW-CP, because the spin-locking of the two quadrupolar magnetizations is performed with MP-CP using shorter rf-pulses with larger rf-field, instead of the long low-power rf-pulse used in CW-CP. Moreover, the Rotary Resonance Recoupling (R^3) conditions are much more separated in MP-CP than in CW-CP, also leading to an increased robustness of MP-CP transfer with respect to rf-field homogeneity.

References:

1 P. Hodgkinson and A.W. Graham, in *Annual Reports on NMR Spectroscopy*, Academic Press, 2011, vol. Volume 72, pp. 185-223.

2 J. Klinowski, E. Vinogradov, P.K. Madhu and S. Vega, in *New Techniques in Solid-State NMR*, Springer Berlin Heidelberg, 2005, vol. 246, pp. 33-90.

3 R.E. Taylor, R.G. Pembleton, L.M. Ryan and B.C. Gerstein, *The Journal of Chemical Physics*, 1979, **71**, 4541-4545.

4 M. Lee and W.I. Goldburg, *Phys. Rev. A* 1965, **140**, 1261.

5 J.S. Waugh, L.H. Huber and U. Haeberlen, *Phys. Rev. Lett.*, 1968, **20**, 180.

6 P. Mansfield, *J. Phys. C: Solid-state Physics*, 1971, 1444.

7 M. Mehring and J.S. Waugh, *Phys. Rev. B* 1972, **5**, 3459.

8 W.K. Rhim, D.D. Elleman and R.W. Vaughan, *J. Chem. Phys.*, 1973, **59**, 3740.

9 E. Vinogradov, P.K. Madhu and S. Vega, *Chem. Phys. Lett.*, 1999, **314** 443.

10 M. Hohwy, P.V. Bower, H.J. Jakobsen and N.C. Nielsen, *Chemical Physics Letters*, 1997, **273**, 297-303.

11 D. Sakellariou, A. Lesage, P. Hodgkinson and L. Emsley, *Chemical Physics Letters*, 2000, **319**, 253-260.

12 Z. Gan, P.K. Madhu, J.P. Amoureux, J. Trébosc and O. Lafon, *Chemical Physics Letters*, 2011, **503**, 167-170.

13 X. Lu, O. Lafon, J. Trébosc, A.S.L. Thankamony, Y. Nishiyama, Z. Gan, P.K. Madhu and J.P. Amoureux, *Journal of Magnetic Resonance*, 2012, **223**, 219-227.

14 D. Iuga, C. Morais, Z. Gan, D.R. Neuville, L. Cormier and D. Massiot, *Journal of the American Chemical Society*, 2005, **127**, 11540-11541.

15 L. van Wüllen, L. Züchner, W.M. Warmuth and H. Eckert, *Solid State Nuclear Magnetic Resonance*, 1996, **6**, 203-212.

16 S.E. Ashbrook and S. Wimperis, *The Journal of Chemical Physics*, 2004, **120**, 2719-2731.

17 S.E. Ashbrook and S. Wimperis, *The Journal of Chemical Physics*, 2009, **131**,

18 J.P. Amoureux and M. Pruski, *Molecular Physics*, 2002, **100**, 1595-1613.

19 B. Hu, J.P. Amoureux, J. Trébosc and S. Hafner, *Journal of Magnetic Resonance*, 2008, **192**, 8-16.

20 D. Wei, U.M. Akbey, B. Paaske, H. Oschkinat, B. Reif, M. Bjerring and N.C. Nielsen, *The Journal of Physical Chemistry Letters*, 2011, **2**, 1289-1294.

21 X. Lu, A.S.L. Tankamony, J. Trébosc, O. Lafon and J.P. Amoureux, *Journal of Magnetic Resonance*, 2013, **228**, 148-158.

Journal of Magnetic Resonance 223 (2012) 219–227

Contents lists available at SciVerse ScienceDirect

Journal of Magnetic Resonance

journal homepage: www.elsevier.com/locate/jmr

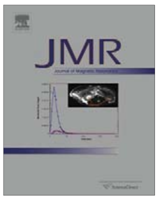

Detailed analysis of the TIMES and TIMES$_0$ high-resolution MAS methods for high-resolution proton NMR

Xingyu Lu[a], Olivier Lafon[a], Julien Trébosc[a], Aany Sofia Lilly Thankamony[a], Yusuke Nishiyama[b], Zhehong Gan[c], P.K. Madhu[d], Jean-Paul Amoureux[a,*]

[a] UCCS (CNRS-8181), University Lille North of France, Villeneuve d'Ascq 59652, France
[b] JEOL RESONANCE Inc., Musashino, Akishima, Tokyo 196-8558, Japan
[c] Center of Interdisciplinary Magnetic Resonance, NHMFL, Tallahassee, FL 32310, USA
[d] Department of Chemical Sciences, TIFR, Colaba, Mumbai 400 005, India

ARTICLE INFO

Article history:
Received 18 June 2012
Revised 19 July 2012
Available online 14 August 2012

Keywords:
Solid-state NMR
^{1}H
Ultra-fast MAS
CRAMPS
Scaling factor
TIMES methods
rf-Field homogeneity

ABSTRACT

We analyze and compare the specifications of TIMES and TIMES$_0$ proton high-resolution NMR methods for solid-state samples. This comparison is performed in terms of resolution versus magic-angle spinning (MAS) spinning speed, ν_R, rf-field amplitude, ν_1, and tilt-angle for the effective rf-field, θ_p. The chemical-shift and homo-nuclear dipolar scaling factors are calculated for both methods. For all MAS speeds, the best resolution is always observed with rf-field of $\nu_1 \approx 120$–130 kHz. At slow MAS speed ($\nu_R \leqslant 10$ kHz), the best resolution is observed for a tilt-angle of $\theta_P \approx 90°$. At moderate spinning speed ($15 \leqslant \nu_R \leqslant 35$ kHz), $\theta_P \approx 55°$ gives the best resolution. At higher MAS speed ($\nu_R \geqslant 60$ kHz), with TIMES and TIMES$_0$ the best resolution is obtained for $\theta_P \leqslant 40°$; but we then recommend TIMES$_0$, owing to its simpler set-up. We also show that in addition to the usual high rf-field regime ($\nu_1 \approx 120$–130 kHz), another low rf-regime ($\nu_1 \approx 40$–50 kHz) exists at MAS speed higher than $\nu_R \geqslant 60$ kHz, which also gives a good ^{1}H resolution. This low rf-regime should be useful for multi-dimensional analyses of bio-molecules with ^{1}H detection under high-resolution, in order to limit the heating of the sample.

1. Introduction

In solid-state nuclear magnetic resonance (NMR) of protons, the strong homo-nuclear dipolar interactions must be removed to observe ^{1}H spectra under high resolution. Homo-nuclear dipolar decoupling can be achieved by magic-angle spinning (MAS) of the sample and multiple-pulse decoupling [1–4], which average the spatial and the spin parts of the dipolar Hamiltonian, respectively. However, in the second case, MAS is also necessary to remove the broadening from proton chemical-shift anisotropy [3–6]. The goal of high-resolution proton spectra has driven the development of numerous homo-nuclear dipolar decoupling sequences [1–33], and of ultra-fast MAS commercial probes that can presently deliver spinning frequencies up to $\nu_R = 110$ kHz [34–36].

Although acquiring spectra using only ultra-fast MAS has the advantages of simplicity, high sensitivity, and artifact-free spectra over windowed multiple-pulse experiments, averaging in spin space with rf-fields far above the mechanical spinning frequency still outperforms MAS in terms of spectral resolution. Moreover, ultra-fast MAS experiments are impossible to perform in special cases, such as hetero-nuclear correlations in between ^{1}H and a low-sensitive nucleus, where a large sample volume is required for S/N reasons. However, under combined rotation and multiple-pulse spectroscopy (CRAMPS), both the spatial and spin parts of the dipolar Hamiltonian are modulated and hence can interfere with each other depending on their time scales [1,2]. In the early days of quasi-static sample conditions, the two time scales were far away from interference, which led to efficient pulse sequences such as BR-24 [5] and MSHOT [16,17]. However, since many years, increasing the spinning speed has been a general tendency of solid-state NMR. Indeed: (i) it decreases the losses in the absence of CRAMPS [33,35], (ii) it enhances the resolution, (iii) it allows using low rf-field decoupling regimes, and (iv) it increases the spectral width of indirect dimensions in rotor synchronized multi-dimensional experiments. Moreover, as increasing the speed is always obtained with decreased rotor diameters, it benefits from a better coupling of the magnetization with the coil, resulting in (v) stronger rf-fields and (vi) higher sensitivity per spin, which is an advantage for volume-limited sample, such as isotopically labeled bio-molecules. With increasing MAS frequency, windowless sequences like the frequency-switched Lee-Goldburg (FSLG) [10,12], phase-modulated Lee-Goldburg (PMLG) [18], and DUMBO [19], then became more favorable owing to their short cycle times (τ_C) for uses in proton indirectly-detected multi-dimensional spectroscopy [37–39]. However, direct acquisition of high-resolution

---

* Corresponding author. Fax: +33 3 20 43 68 14.
E-mail address: jean-paul.amoureux@univ-lille1.fr (J.-P. Amoureux).

1090-7807/$ - see front matter © 2012 Elsevier Inc. All rights reserved.
http://dx.doi.org/10.1016/j.jmr.2012.07.015

proton spectra requires insertion of short sampling window periods into these sequences. As the spinning frequency further increased, the minimum total cycle time, which is limited by the finite acquisition window and the rf-field strength, got close to the rotor period (T_R) leading to interferences causing severe resonant broadening. Nevertheless, it has been shown that even at ultra-fast MAS ($\nu_R > 60$ kHz), high-resolution proton spectra can be obtained with $\xi = T_R/\tau_C$ ratios that avoid the resonant conditions [25,26,30–33]. It has also been shown recently that two rotor-synchronized sequences, namely RN_n^ν and SAM [20,21,27–29], can yield good proton resolution. However, both sequences mostly work at fast and ultra-fast MAS frequencies.

We have recently proposed a sequence, christened TIMES (TIlted Magic-Echo Sandwich) [40], which can be tuned for high-resolution proton spectra under slow to ultra-fast MAS. The basic unit is a magic-echo sequence with effective field tilted in the rotating frame, bracketed by two sandwich pulses. The tilt-angle of the magic-echo, θ_P, can be tuned for obtaining optimal spectral resolution according to the spinning frequency. At slow MAS, the effective field is close to the transverse plane, whereas at very-fast MAS, optimal resolution is found with the effective field close to the *z*-axis resulting in a large chemical shift scaling factor, κ_{cs}. The large frequency offset under this condition increases the effective field and makes the cycle time very short. The key feature of the sequence is that the θ_P tilt-angle can be varied covering three commonly used decoupling schemes for obtaining high-resolution proton spectra: MAS-only, the FSLG and PMLG [10,12,18], and the magic-echo [16,17] experiments, corresponding to effective field close to the *z*-axis, the magic-angle, or the *xy*-plane, respectively.

We have also very recently proposed another high-resolution method for protons, called $\mathrm{TIMES_0}$ (TIMES with zero degree sandwich pulse) [35], which is a simplified version of TIMES without the two sandwich pulses. The pulse sequence of $\mathrm{TIMES_0}$ is similar to that of the most advanced windowed version of PMLG, called wPMLG_{pp}^{xx} [25,26]. However, the two basic concepts of $\mathrm{TIMES_0}$ and wPMLG_{pp}^{xx} sequences are very different and their optimizations do not only correspond to a re-parameterizations process [35].

In this article, we would like to analyze what are the specifications of TIMES and $\mathrm{TIMES_0}$, in terms of resolution, according to the MAS speed and the rf-field requirement. As a test sample, we have chosen glycine, which presents three proton resonances: one related to the NH_3 group, and the two others to the CH_2 group. As the last two resonances are difficult to resolve to the base line, the resolution of CH_2 resonances will be used as a criterion to assess the efficiency of homonuclear decoupling.

2. Pulse sequences and mathematical description of the methods

The pulse sequence of TIMES is described in Fig. 1a. Each R block is composed of two phase ramps of opposite slopes sandwiched by two pulses. The sequence is submitted to a two-steps super-cycle (R and $\underline{R}$) that makes the sum a pure *z*-rotation for the chemical shift, which eliminates false zero and image peaks. The signal is sampled during the windows situated in between the R and $\underline{R}$ blocks. Modulations by this super-cycle create sidebands at the edges of the spectral window [26].

To simplify the notations, we will always put an I, S or P subscript to all parameters describing the Initial, Sandwich or Phase-ramp pulses, respectively. The on-resonance phase-ramp with ν_{1P} amplitude is equivalent to an effective field of amplitude $\nu_{1P,\mathrm{eff}}$ and off-resonance frequency, $\nu_{P,OR}$, tilted from the z-axis with the θ_P angle:

$$\nu_{1P} = \sin\theta_P \cdot \nu_{1P,\mathrm{eff}} = \tan\theta_P \cdot \nu_{P,OR} \qquad (1)$$

The final phase of each ramp is equal to:

$$\begin{aligned}\phi_{P,\mathrm{last}}(^\circ) &= 360\cdot\tau_P\cdot\nu_{P,OR} = 360\cdot\tau_P\cdot\nu_{1P}/\tan\theta_P\\ &= 360\cdot\tau_P\cdot\nu_{1P,\mathrm{eff}}\cdot\cos\theta_P \end{aligned}\qquad (2)$$

During each ramp, the rotation angle of the magnetization about the effective field is equal to:

$$\begin{aligned}\psi_P(^\circ) &= 360\cdot\tau_P\cdot\nu_{1P,\mathrm{eff}} = 360\cdot\tau_P\cdot\nu_{1P}/\sin\theta_P\\ &= \phi_{P,\mathrm{last}}(^\circ)/\cos\theta_P \end{aligned}\qquad (3)$$

The flip-angles corresponding to each sandwich pulse and to the initial pulse are equal to:

$$\theta_S(^\circ) = 360\cdot\tau_S\cdot\nu_{1S} \quad \theta_I(^\circ) = 360\cdot\tau_I\cdot\nu_{1I} \qquad (4)$$

In the magic-echo experiment [16,17], the rotation angle is assumed to be equal to $\psi_P = 360°$, and the rf rotating frames related to the phase-ramps are switched to the *z*-axis with the sandwich pulses so that the spin operators are the same between the rf-rotation and the window periods, which leads to $\theta_P = \theta_S = \theta$. In that case, the final phase of each ramp should thus be equal to:

$$\phi_{P,\mathrm{last}}(^\circ) = 360\cdot\cos\theta \qquad (5)$$

However, the magic-echo has been proposed in the quasi-static case, and Eq. (5) may not be fulfilled, especially at ultra-fast MAS.

The $\mathrm{TIMES_0}$ pulse sequence, described in Fig. 1b, is deduced from that of TIMES by skipping the two sandwich pulses, which means that Eqs. (1)–(3) then still apply. The $\mathrm{TIMES_0}$ sequence becomes identical to that of wPMLG_{pp}^{xx} when $\theta_P = 54.736°$ [25,26].

3. Scaling factors

3.1. Scaling factors of the chemical shift

As the interaction and rotating frames coincide ($\theta_S = \theta_P$) every cycle time, $\tau_C = 2(\tau_P + \tau_S) + \tau_W$ (TIMES) or $\tau_C = 2\tau_P + \tau_W$ ($\mathrm{TIMES_0}$), the isotropic CRAMPS chemical shift factors can be calculated analytically with first-order average Hamiltonian in the static case, since this interaction is not affected by sample rotation:

$$\mathrm{TIMES}: \kappa_{cs} = (2\tau_S\sin\theta_P/\theta_P + 2\tau_P\cos\theta_P + \tau_w)/\tau_C \qquad (6)$$

$$\mathrm{TIMES_0}: \kappa_{cs} = (2\cos^2\theta_P + \tau_w/\tau_P)/(2 + \tau_w/\tau_P) \qquad (7)$$

As the pulse sequences are identical, Eqs. (6) and (7) also apply to MSHOT and $\mathrm{wPMLG}_{pp}^{x\bar{x}}$, respectively. In all cases, the scaling factor tends to 1 when the tilt-angle θ_P decreases to zero. Simulations performed with SIMPSON software [41], and shown in Figs. S1 and S2 have confirmed these equations.

3.2. Scaling factors of the homogeneous dipolar interaction

This calculation is much more complicated than the previous one on the chemical shift, because it should be performed on multi-spin systems under MAS rotation. Nevertheless, we have calculated this scaling factor in the simple case of one isolated spin-pair of protons in a static sample using first-order average Hamiltonian, when the sandwich pulses are ideal ($\theta_S = \theta_P$ with $\tau_S = 0$):

$$\mathrm{TIMES}: \kappa_D \approx [(3\cos^2\theta_P - 1) + \tau_w/\tau_p]/(2 + \tau_w/\tau_p) \qquad (8)$$

Matlab calculations performed with $\theta_P = 54.736°$, 30° and 90° have confirmed this equation (Fig. S3). When the effective field is at the magic angle, $\theta_P = 54.736°$, the homo-nuclear dipolar decoupling is perfect ($\kappa_D = 0$) when the window and sandwich pulse lengths are negligible ($\tau_W \approx \tau_S \approx 0$) (Fig. S3a). This is not the case with finite sandwich pulse length ($\tau_S \neq 0$) (Fig. S4a):

$$\mathrm{TIMES}:\kappa_D \approx [(1.5\cos\theta_P\sin\theta_P/\theta_P+0.5)\tau_S+(3\cos^2\theta_P-1)\tau_p+\tau_w]/\tau_C \qquad (9)$$

The same type of calculation, performed in static without sandwich pulses, gave:

$$\mathrm{TIMES}_0:\kappa_D = [(3\cos^2\theta_P-1)^2/2+\tau_w/\tau_p]/(2+\tau_w/\tau_p) \qquad (10)$$

This equation has been confirmed with Matlab calculations, as shown in Fig. S5. It must be noted that the larger term in the contribution of homonuclear dipolar couplings to the effective Hamiltonian is proportional to the operator T_{20} (Eqs. (8)–(10)), whereas the contributions of other operators, such as $T_{2\pm1}$, and $T_{2\pm2}$, are close to zero but not negligible. These additional contributions lead to little differences between the Matlab simulations and the analytical curves, especially when τ_w/τ_p is larger than 4 (Fig. S5b). It must be noted that Eqs. (8)–(10), also apply to MSHOT and wPMLG$^{x\bar{x}}_{pp}$, respectively.

However, it is important to remind that real CRAMPS experiments are influenced by spinning dependent interactions and are related to multi-spin ^{1}H–^{1}H couplings, and thus Eqs. (8)–(10) are only partially relevant for the TIMES and TIMES$_0$ experiments.

4. Optimization of TIMES and TIMES$_0$ experiments

Our purpose is to optimize the resolution of the two CH$_2$ resonances, and therefore the first step is to be able to quantify this resolution. We have chosen to minimize the resolution factor:

$$R_{\mathrm{CRAMPS}} = (\mathrm{CH}_{2a}+\mathrm{CH}_{2b}-2\underline{\mathrm{CH}_2})/(\mathrm{CH}_{2a}+\mathrm{CH}_{2b}) \qquad (11)$$

where CH$_{2a}$ and CH$_{2b}$ represent the amplitudes of the two CH$_2$ resonances, and $\underline{\mathrm{CH}_2}$ corresponds to that in the middle of these two resonances. This factor is normalized. Indeed, according to the fact the two resonances are not at all resolved, or resolved to the baseline, R_{CRAMPS} is equal to 0 or 1, respectively. Most of our systematic experiments (Figs. 2–7) have been performed on Bruker spectrometers either at 9.4 T with AVANCE-II console at ν_R = 10, 20, and 30 kHz (∅ = 2.5 mm), or at 18.8 T with AVANCE-III console at ν_R = 64 kHz (∅ = 1.3 mm). Those at ν_R = 80 kHz (∅ = 1 mm) (Figs. 6 and 8), have been performed at 14.1 T on a Jeol spectrometer equipped with JNM–ECA console. The chemical shift scaling factor, κ_{cs}, has been determined by fixing the middle $\underline{\mathrm{CH}_2}$ frequency to 3.55 ppm and by re-scaling the NH$_3$ resonance to 8.33 ppm. With MAS only, the resolution factor observed with 810° initial flip-angle (see below) was equal to R_{MAS} = 0, 0, 0, 0.69, 0.67 for ν_R = 10, 20, and 30 kHz (9.4 T), ν_R = 64 kHz (18.8 T), and ν_R = 80 kHz (14.1 T), respectively. These MAS only values will be used as references to quantify the resolution enhancement introduced by the decoupling pulse sequences.

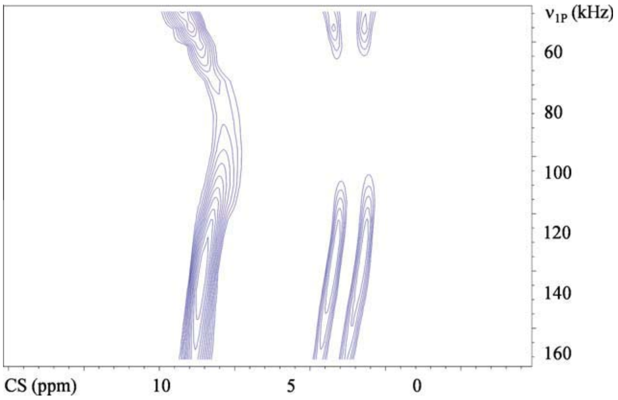

Fig. 2. TIMES$_0$: experimental ^{1}H spectra of glycine obtained at 18.8 T with ν_R = 64 kHz and θ_P = 30°, versus ν_{1P} rf-field. Two high-resolution zones are observable: $\nu_{1P} \approx 130$ and 50 kHz. Around the high-rf zone ($\nu_{1P} \approx 130$ kHz), the resonance frequencies are roughly constant, in opposite to the low-rf ($\nu_{1P} \approx 50$ kHz) zone, which is thus much more sensitive to rf-inhomogeneity.

Independently from the CRAMPS sequence and the spinning speed which are used, the best way to enhance the resolution of proton spectra is by improving the rf-homogeneity. Therefore, the

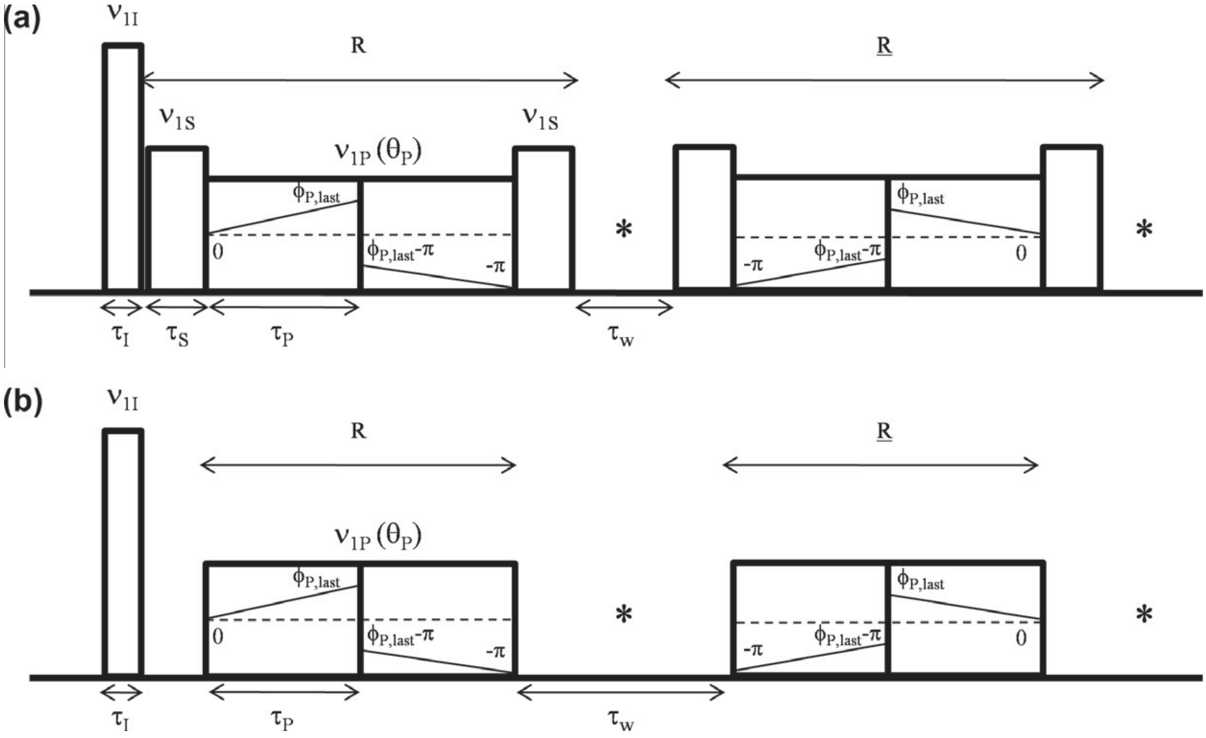

Fig. 1. (a) Pulse sequence of TIMES. This sequence becomes that of MSHOT [16,17] when the tilt-angle is equal to θ_P = 90°. (b) That of TIMES$_0$, obtained by skipping the sandwich pulses (ν_{1S}, τ_S), which becomes that of wPMLG$^{x\bar{x}}_{pp}$ when θ_P = 54.736° [25,26]. The signal is sampled in the windows (*).

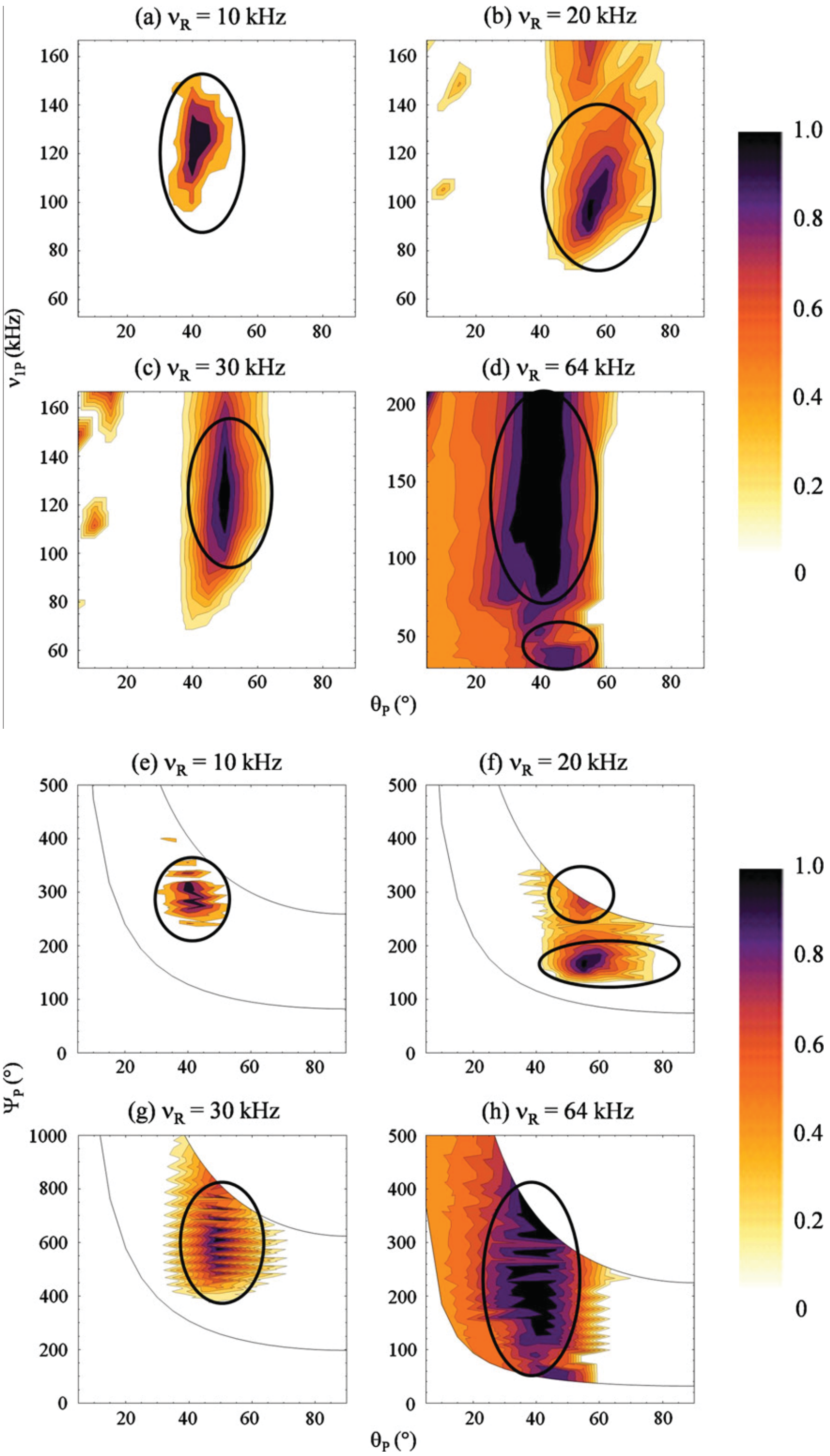

Fig. 3. TIMES: experimental resolution-maps (R_{CRAMPS}) in the low tilt-angle regime ($\theta_P < 50°$), for four different spinning speeds: $\nu_R = 10$ (a and e), 20 (b and f), 30 (c and g), and 64 (d and h) kHz. (a–d) rf-Maps (R_{CRAMPS} versus ν_{1P} and θ_P), (e–h) ψ-maps (R_{CRAMPS} versus ψ_P and θ_P). One observes that this low tilt-angle regime works better with increasing spinning speed. At very fast spinning ($\nu_R = 64$ kHz), two regimes with either high- or low-rf are observable as circled regions in (d), with $\nu_{1P} \approx 120$ or 40 kHz, respectively. To compare the resolution enhancement introduced by TIMES, it must be reminded that with MAS alone one observes $R_{MAS} = 0$ ($\nu_R = 10$ kHz, 9.4 T), 0 ($\nu_R = 20$ kHz, 9.4 T), 0 ($\nu_R = 30$ kHz, 9.4 T), and 0.69 ($\nu_R = 64$ kHz, 18.8 T).

selection of sample regions experiencing uniform rf field using either spacers and/or rf-excitation improves the spectral resolution. Several sophisticated composite sequences have been proposed to enhance the rf-homogeneity [42–49]. We have compared in detail by simulations and experiments the use of spacers, composite pulses and of a long initial pulse in the framework of their application to CRAMPS experiments (see Supplementary information). As a result, we have found that using a full-rotor sample with a long initial flip-angle (810° in our case) is the best choice for ^{1}H high-resolution CRAMPS methods, due to (i) practical simplicity, (ii) S/N ratio, and (iii) resolution enhancement. The following experiments have thus been performed using this long excitation pulse.

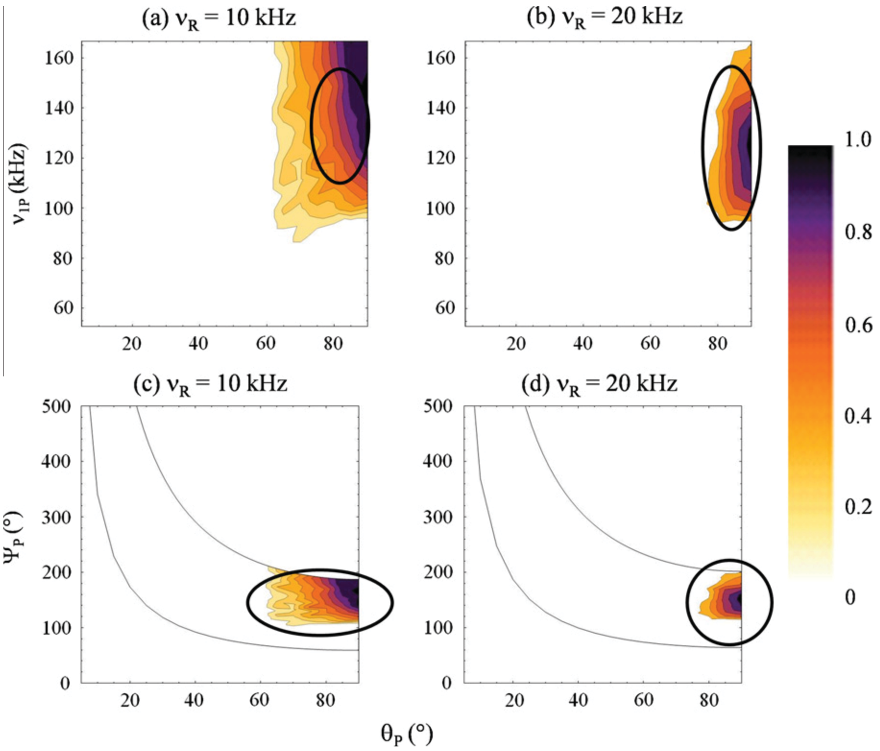

Fig. 4. TIMES: experimental resolution-maps (R_{CRAMPS}) in the high tilt-angle regime ($\theta_P > 80°$), for two different spinning speeds: $\nu_R = 10$ (a and c), and 20 (b and d) kHz. (a and b) rf-maps (R_{CRAMPS} versus ν_{1P} and θ_P), (c and d) ψ-maps (R_{CRAMPS} versus ψ_P and θ_P). This high tilt-angle regime works better with slow spinning speed. To compare the resolution enhancement introduced by TIMES, it must be reminded that with MAS alone one observes $R_{MAS} = 0$ ($\nu_R = 10$ kHz, 9.4 T), and 0 ($\nu_R = 20$ kHz, 9.4 T).

4.1. TIMES optimization

There are a priori seven parameters to be experimentally optimized with the TIMES sequence: ν_{1P}, ν_{1S}, τ_P, τ_S, $\phi_{P,last}$, τ_W (Fig. 1a) and the carrier frequency O_1. Our goal is to obtain 2D maps showing what the best experimental conditions are, especially versus ν_{1P} and θ_P (calculated from $\phi_{P,last}$ using Eq. (2)). However, before recording such maps, the other five parameters must be fixed. According to our probe and electronic consol, we have always used a sampling window of ca. $\tau_W \approx 4.5$ µs. For each spinning speed, the four remaining parameters (ν_{1S}, τ_S, τ_P, and O_1) had thus to be optimized before starting the mapping, based on the CH_2 resolution.

4.1.1. Preliminary optimization of ν_{1S}, τ_S, τ_P and O_1

Whatever the spinning speed, we have always started by fixing $\nu_{1P} \approx 120$–130 kHz, as all our experiments have shown that this is always the best rf-condition for the phase-ramp pulse. We have chosen to start the preliminary optimization with the same rf-field for the sandwich and phase-ramp pulses ($\nu_{1S} = \nu_{1P}$) for simplicity reasons.

For each spinning speed (ν_R = 10, 20, 30, 64 or 80 kHz), we have then started an optimization loop with such rf-fields, with six initial tilt-angle values: θ_{Pi} = 15°, 30°, 45°, 60°, 75° and 90°. For each of these θ_{Pi} values, the program calculated the sandwich-pulse length τ_S in order to obtain $\theta_S = \theta_{Pi}$ (Eq. (4)). We have then carefully optimized τ_P in between 1 and 17 µs, with small steps of 0.1 µs, to get the best resolution. For each τ_P value, the pulse program calculated $\phi_{P,last}$ according to Eq. (2) with $\theta_P = \theta_{Pi}$. Then, we have further optimized the resolution with τ_S, also using small steps of 0.1 µs, and the program always calculated the rf-field ν_{1S} in order to keep $\theta_S = \theta_{Pi}$ (Eq. (4)). It must be noted that the optimization of τ_S and τ_P is critical and must be performed with the purpose of obtaining a short cycle-time that avoids all recoupling ratios for $\xi = T_R/\tau_C$. Practically, this means avoiding integer ξ values for $\nu_R \leqslant 30$ kHz and $\xi = 1.5$ for $\nu_R \geqslant 50$ kHz. Finally, we optimized O1 taking care to avoid observing on the two CH_2 glycine resonances any Rotational Radio-Frequency (RRF) narrow line situated at $h\nu_R + k/\tau_c$ from the carrier frequency, where h and k are two integers including zero [2,18,22,25,26,30].

4.1.2. Resolution maps versus rf-field or rotation-angle

Thanks to the global preliminary optimization procedure, we have observed that two optimum regimes exist for θ_{Pi}: either smaller than ca. 60° or larger than ca. 80°. In the first regime ($\theta_{Pi} < 60°$) we observed three optimized τ_P values, leading (Eq. (3)) to three rotation angles $\psi_p \approx 150°$ (Fig. 3f and h), 300° (Fig. 3e, f and h) and 600° (Fig. 3g). In the second regime ($\theta_{Pi} > 80°$) we observed a single 'good' τ_P value leading to a rotation angle $\psi_p \approx 150°$ (Fig. 4c and d).

For each of the eighteen θ_P values ranging from 5° to 90° with 5° step, we have recorded the twenty three spectra that can be obtained for ν_{1P} ranging from 52 to 167 kHz with 5 kHz step. Such a 2D map is shown, before frequency re-scaling, for $\nu_R = 64$ kHz and $\theta_P = 30°$ in Fig. 2. For each map, the other parameters (ν_{1S}, τ_S, τ_P and O_1) were fixed to their previously optimized values corresponding to the closest $\theta_{Pi} \approx \theta_P$ angle. Each of these spectra has then been treated to obtain the corresponding 432 ($18 * 24$) R_{CRAMPS} values. Finally, we have represented the 2D maps showing the R_{CRAMPS} resolution factor versus θ_P and either ν_{1P} (rf-map) or ψ_P (ψ-map) for the two regimes, $\theta_{Pi} < 60°$ and $\theta_{Pi} > 80°$, in Figs. 3 and 4, respectively. The ψ_P values have been calculated with Eq. (3). In Fig. 3, the two types of maps are represented for ν_R = 10, 20, 30 and 64 kHz; whereas in Fig. 4 they are only represented at ν_R = 10 and 20 kHz because the resolution was always very poor ($R_{CRAMPS} < 0.2$) at faster speeds.

At very fast spinning speed, TIMES only works correctly with small tilt-angle ($\theta_P < 60°$) (Fig. 3d), whereas it is the contrary for slow MAS where large tilt-angle ($\theta_P > 80°$) must be used (Fig. 4a). In both cases, the optimum rf-field remains moderate $\nu_{1P} \approx 120$ kHz. However, one observes that a 'reasonable' resolution can also be observed at ultra-fast MAS with a middle tilt-angle ($\theta_P \approx 40$–$60°$) and an rf-field as small as $\nu_{1P} \approx 40$ kHz (Fig. 3d).

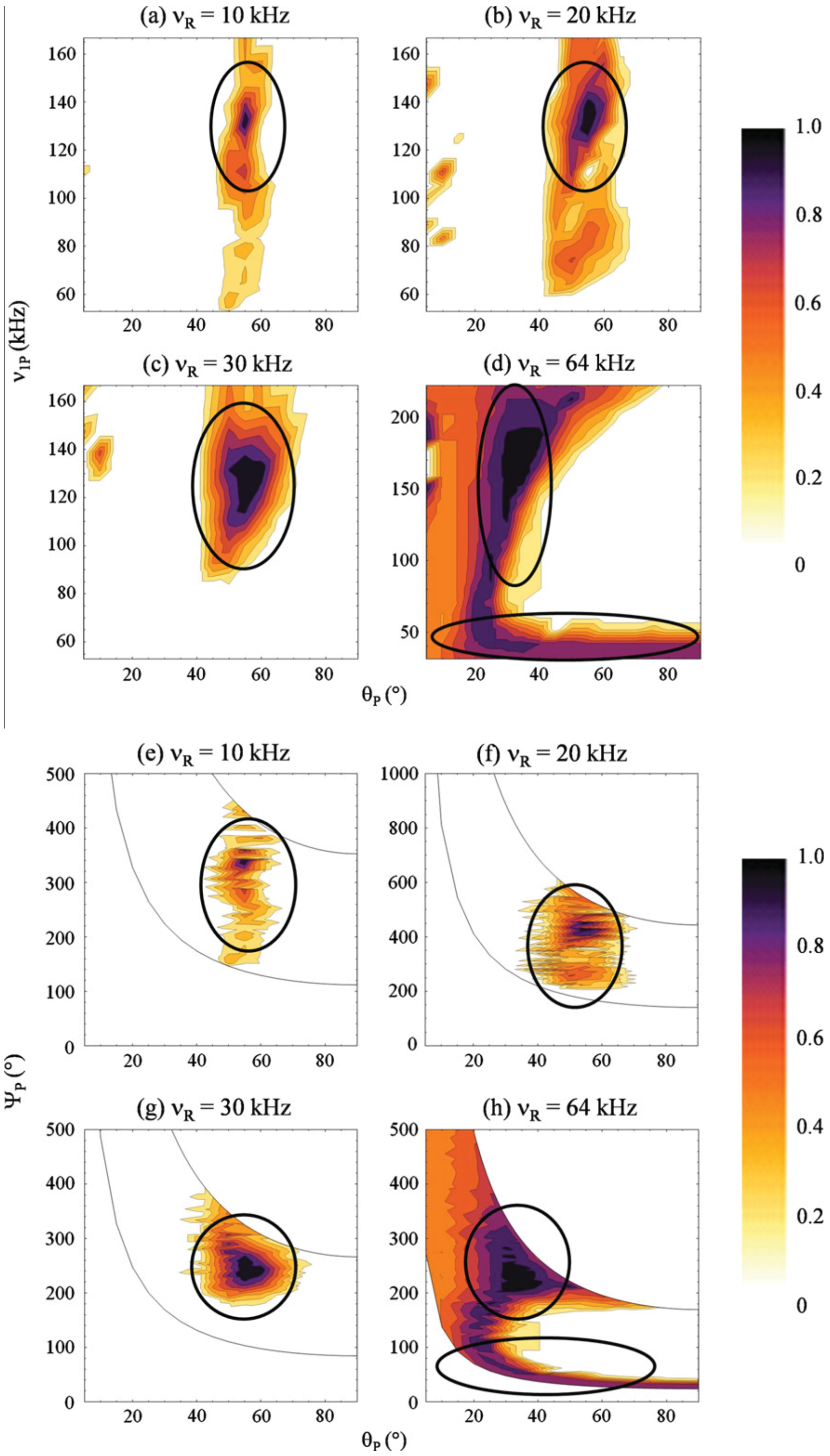

Fig. 5. TIMES$_0$: experimental resolution-maps (R_{CRAMPS}) in the low tilt-angle regime ($\theta_P < 50°$), for four different spinning speeds: ν_R = 10 (a and e), 20 (b and f), 30 (c and g), and 64 (d and h) kHz. (a–d) rf-Maps (R_{CRAMPS} versus ν_{1P} and θ_P), (e–h) ψ-maps (R_{CRAMPS} versus ψ_P and θ_P). One observes that this low tilt-angle regime works better with increasing spinning speed. At very fast spinning (ν_R = 64 kHz), two regimes with either high- or low-rf are observable as circled regions in (d), with $\nu_{1P} \approx 130$ or 50 kHz, respectively. To compare the resolution enhancement introduced by TIMES$_0$, it must be reminded that with MAS alone on observes R_{MAS} = 0 (ν_R = 10 kHz, 9.4 T), 0 (ν_R = 20 kHz, 9.4 T), 0 (ν_R = 30 kHz, 9.4 T), and 0.69 (ν_R = 64 kHz, 18.8 T).

4.2. TIMES$_0$ optimization

The initial optimization procedure of TIMES$_0$ experiment was simpler than that for TIMES, as there is no sandwich pulse and thus two parameters less: ν_{1S} and τ_S (compare Fig. 1a and b). We have represented, for ν_R = 10, 20, 30 and 64 kHz, the best rf- and ψ-maps in Fig. 5a–h, respectively. The main difference with TIMES is that amongst the six initial θ_{Pi} angles we have only observed one optimum region, which always corresponds to the 'high-speed' regime: $\theta_{Pi} < 60°$ (Fig. 5). For MAS frequencies lower or equal to 30 kHz, we have observed a single 'good' pulse-length, τ_P, which always corresponds to an rf-field of $\nu_{1P} \approx 130$ kHz (Fig. 5a–d) and a rotation

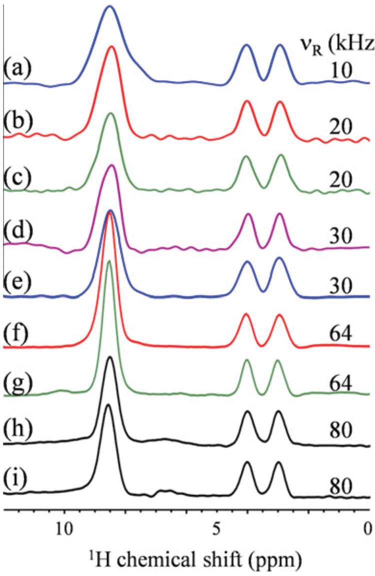

Fig. 6. Experimental best resolved re-scaled spectra of glycine observed for the five spinning speeds of ν_R = 10 (a), 20 (b and c), 30 (d and e), 64 (f and g), and 80 (h and i) kHz. The corresponding experimental parameters are described in Table 1.

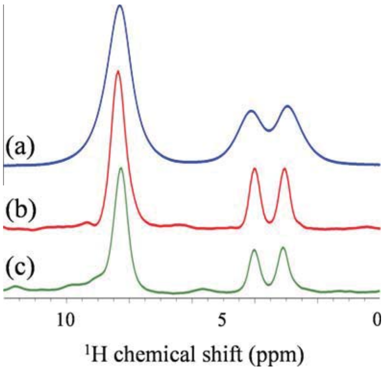

Fig. 7. Spectra of glycine observed at 18.8 T, with ν_R = 64 kHz. (a) MAS only, (b and c) TIMES$_0$ with $\theta_P \approx 30°$, and $\nu_{1P} \approx 129$ (b) or 39 (c) kHz.

angle $\psi_P \approx 300°$ (Fig. 5e–h). At very fast spinning, TIMES$_0$ only works correctly with small tilt-angle ($\theta_P \approx 20–35°$) (Fig. 5d). Again, the best resolution is achieved with $\nu_{1P} \approx 130$ kHz, but a good resolution can also be observed with an rf-field as small as $\nu_{1P} \approx 40–50$ kHz.

5. Choice of the method and experimental specification

In Fig. 6 we have represented the best re-scaled CRAMPS spectra observed at 9.4 T with ν_R = 10, 20, 30 kHz, at 18.8 T with ν_R = 64 kHz and at 14.1 T with ν_R = 80 kHz. All spectra have used a long initial pulse of θ_I = 810°. It must be first noted that whatever the spinning speed, the best resolution has always been observed with a moderate rf-field of ca. 120–130 kHz (Table 1).

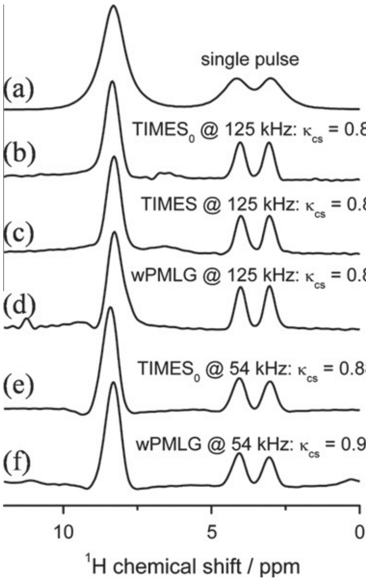

Fig. 8. Spectra of glycine observed at 14.1 T with ν_R = 80 kHz. (a) MAS only, (b) TIMES$_0$ with $\nu_{1P} \approx 125$ kHz and κ_{cs} = 0.88, (c) TIMES with $\nu_{1P} \approx 125$ kHz and κ_{cs} = 0.87, (d) wPMLG$^{xx}_{pp}$ with $\nu_{1P} \approx 125$ kHz and κ_{cs} = 0.81, (e) TIMES$_0$ with $\nu_{1P} \approx 54$ kHz and κ_{cs} = 0.88, (f) wPMLG$^{xx}_{pp}$ with $\nu_{1P} \approx 54$ kHz and κ_{cs} = 0.90.

At slow spinning speed, ν_R = 10 kHz, the best resolution is observed under TIMES, with $\theta_P \approx 90°$ and $\kappa_{cs} \approx 0.41$. These conditions correspond to the MSHOT quasi-static experiment [16,17]. At ν_R = 20 kHz, the best resolution is observed under TIMES$_0$, with $\theta_P \approx 56°$ and $\kappa_{cs} \approx 0.44$. These conditions also correspond to the wPMLG$^{xx}_{pp}$ sequence [18]. At ν_R = 30 kHz, the best resolution is observed either (i) under TIMES$_0$, with $\theta_P \approx 58°$ and $\kappa_{cs} \approx 0.55$, which also correspond to wPMLG$^{xx}_{pp}$, or (ii) under TIMES, with $\theta_P \approx 50°$ and $\kappa_{cs} \approx 0.61$ [40]. At ν_R = 64 and 80 kHz, a similar resolution is observed under TIMES and TIMES$_0$ [35], with $\theta_P \approx 25–40°$ and $\kappa_{cs} \approx 0.83–0.92$. When the spinning speed increases, the θ_P tilt-angle value decreases whereas the κ_{cs} scaling factor increases. As MAS-only spectra correspond to $\theta_P = 0$ and $\kappa_{cs} = 1$, the optimum CRAMPS conditions thus result from a compromise between the scaling factor and the homo-nuclear spatial averaging due to multiple-pulse decoupling. It must be observed that the best TIMES and TIMES$_0$ conditions are always observed with an rf-field of $\nu_{1P} \approx 120–130$ kHz, and they always correspond to a rotation of $\psi_P \approx 150°$ or 300° around the effective rf-field.

It is also very important to notice that the behavior of the CRAMPS sequences at very fast spinning is different to that observed at slow, moderate or even fast MAS. Indeed, in addition to the usual high-rf ($\nu_{1P} \approx 120–130$ kHz) regime, a second low-rf

Table 1
Experimental specifications of best resolved spectra shown in Fig. 6.

Spectrum	ν_R (kHz)	Sequence	θ_P (°)	ν_{1P} (kHz)	τ_C (μs)	κ_{cs}	B_0 (T)
(a)	10	TIMES/MSHOT	90	120	16.8	0.41	9.4
(b)	20	TIMES	59	120	17.8	0.56	9.4
(c)	20	TIMES$_0$/wPMLG$^{xx}_{pp}$	56	130	17.1	0.44	9.4
(d)	30	TIMES	50	120	12.5	0.61	9.4
(e)	30	TIMES$_0$/wPMLG$^{xx}_{pp}$	58	130	11.1	0.55	9.4
(f)	64	TIMES	40	120	15.1	0.92	18.8
(g)	64	TIMES$_0$	35	130	12.5	0.92	18.8
(h)	80	TIMES	23	125	11.5	0.87	14.1
(i)	80	TIMES$_0$	25	125	11.5	0.88	14.1

regime then exists for TIMES and TIMES$_0$, which allows observing nearly the same resolution as the high-rf regime, but with much less rf-power. This low-rf regime has been already observed in Figs. 2, 3d and 5d. It is shown explicitly for the TIMES$_0$ sequence at MAS speeds of 64 and 80 kHz, in Figs. 7c and 8e respectively. It must be noted that this low-rf regime also exists for wPMLG$_{pp}^{xx}$ as shown in Fig. 8f. As the tilt-angle of the effective field θ_P and the rf-field itself ν_{1P} are both small, this low-rf regime is close to the MAS-only regime; but it nevertheless really enhances the resolution. This effect is quite similar to that observed for hetero-nuclear dipolar decoupling [50–54]. However, it must be noted that low-rf regimes are more sensitive to rf-inhomogeneity than high-rf regimes, which is observable on the experimental spectra recorded versus rf-field (Fig. 2). Indeed, the resonance frequencies are much less affected by the rf-field when ν_{1P} is close to 120–130 kHz (high-rf regime) than when it is close to 40–50 kHz (low-rf regime). This means that in the low-rf regime, proton high-resolution spectra can be observed only if rf-inhomogeneity is controlled, e.g. with a long initial pulse. This low rf-regime could be used for multi-dimensional NMR experiments of bio-molecules with high-resolution proton detection [37,38]. At very fast spinning speed and low rf-power regime, the best resolution has been observed with $\xi = T_R/\tau_C = 1.25$ (Fig. 2), 1.25 (Fig. 7c), 1.09 (Fig. 8e), and 1.22 (Fig. 8f).

6. Conclusions

We have analyzed and compared the specifications of TIMES and TIMES$_0$ proton high-resolution NMR methods in solid-state. This comparison has been performed in terms of resolution versus spinning speed, rf-field requirement, and tilt-angle for the effective rf-field, θ_P. The chemical-shift and homo-nuclear dipolar scaling factors have been calculated for both methods. Whatever the spinning speed, the best resolution has always been observed with rf-fields of ca. 120–130 kHz. At slow MAS ($\nu_R \leqslant 10$ kHz), the best resolution was observed with a tilt-angle of $\theta_P \approx 90°$. At moderate spinning speed ($15 \leqslant \nu_R \leqslant 35$ kHz), $\theta_P \approx 55°$ gave the best resolution. At higher MAS speed ($\nu_R \geqslant 60$ kHz) the best resolution was obtained with $\theta_P \leqslant 40°$, and we then recommend TIMES$_0$, owing to its simpler set-up as two less parameters have then to be optimized with respect to TIMES. We have also shown that in addition to the usual high rf-field regime (≈120–130 kHz), another low rf-regime (≈40–50 kHz) exists at ultra-fast MAS, which also gives a very good resolution. This low rf-regime should be useful for multi-dimensional analyses of bio-molecules with ^{1}H detection under high-resolution, in order to limit the heating of the sample.

Acknowledgments

Authors would like to thank the financial support from the French TGE RMN THC FR3050 for conducting the research. X. Lu, J. Trébosc, O. Lafon, and J.P. Amoureux are grateful for funding provided by Region Nord/Pas de Calais, Europe (FEDER), CNRS, French Minister of Science, USTL, ENSCL, CortecNet, Bruker BIOSPIN, and contract ANR-2010-jcjc-0811-01.

Appendix A. Supplementary material

Supplementary data associated with this article can be found, in the online version, at http://dx.doi.org/10.1016/j.jmr.2012.07.015.

References

[1] U. Haeberlen, High Resolution NMR in Solids-selective Averaging, Academic Press, New York, 1976.

[2] E. Vinogradov, P.K. Madhu, S. Vega, Strategies for high-resolution proton spectroscopy in solid-state NMR, Topics Curr. Chem. 246 (2005) 3390.

[3] B.C. Gerstein, C. Clor, R.G. Pembleton, R.C. Wilson, Utility of pulse NMR in studying protons in coals, J. Phys. Chem. 81 (1977) 565–570.

[4] R.E. Taylor, R.G. Pembleton, L.M. Ryan, B.C. Gerstein, Combined multiple pulse NMR and sample spinning: recovery of ^{1}H chemical shift tensors, J. Chem. Phys. 71 (1979) 4541–4545.

[5] D.P. Burum, W.K. Rhim, Analysis of multiple pulse NMR in solids, J. Chem. Phys. 71 (1979) 944–956;
D.P. Burum, W.K. Rhim, An improved NMR technique for homo-nuclear dipolar decoupling in solids: application to polycrystalline ice, J. Chem. Phys. 70 (1979) 3553–3554.

[6] C.E. Bronnimann, B.L. Hawkings, M. Zhang, G.E. Maciel, Combined Rotation and Multiple Pulse Spectroscopy as an analytical proton NMR technique for solids, Anal. Chem. 60 (1988) 1743–1750.

[7] J.S. Waugh, L.M. Huber, U. Haeberlen, Approach to high-resolution NMR in solids, Phys. Rev. Lett. 20 (1968) 180–182.

[8] M. Mehring, J.S. Waugh, Magic-angle NMR experiments in solids, Phys. Rev. B 5 (1972) 3459–3471.

[9] K. Takegoshi, C.A. McDowell, A "magic echo" pulse sequence for the high-resolution NMR spectra of abundant spins in solids, Chem. Phys. Lett. 116 (1985) 100–104.

[10] A. Bielecki, A.C. Kolbert, M.H. Levitt, Frequency-switched pulse sequences: homo-nuclear decoupling and dilute spin NMR in solids, Chem. Phys. Lett. 155 (1989) 341–346.

[11] D.G. Cory, A new multiple-pulse cycle for homo-nuclear dipolar decoupling, J. Magn. Reson. 94 (1991) 526–534.

[12] M.H. Levitt, A. Bielecki, A.C. Kolbert, D.J. Ruben, High-resolution ^{1}H NMR in solids with frequency-switched multiple-pulse sequences, Solid State Nucl. Magn. Reson. 2 (1993) 151–163.

[13] M.L. Buszko, C.E. Bronnimann, G.E. Maciel, ^{1}H CRAMPS based on TREV, J. Magn. Reson. A 103 (1993) 183–187.

[14] D. Demco, S. Hafner, H.W. Spiess, Rotation-synchronized homo-nuclear dipolar decoupling, J. Magn. Reson. A 116 (1995) 36–45.

[15] S. Hafner, H.W. Spiess, Multiple-Pulse line narrowing under fast Magic-Angle Spinning, J. Magn. Reson. A 121 (1996) 160–166.

[16] M. Howhy, P.V. Bower, H.J. Jakobsen, N.C. Nielsen, A high-order and broadband CRAMPS experiment using z-rotational decoupling, Chem. Phys. Lett. 273 (1997) 297–303.

[17] M. Hohwy, N.C. Nielsen, Elimination of high order terms in multiple pulse nuclear magnetic resonance spectroscopy: application to homo-nuclear decoupling in solids, J. Chem. Phys. 106 (1997) 7571–7586.

[18] E. Vinogradov, P.K. Madhu, S. Vega, High-resolution proton solid-state NMR spectroscopy by phase-modulated Lee-Goldburg experiment, Chem. Phys. Lett. 314 (1999) 443–450.

[19] D. Sakellariou, A. Lesage, P. Hodgkinson, L. Emsley, Homo-nuclear dipolar decoupling in solid-state NMR using continuous phase modulation, Chem. Phys. Lett. 319 (2000) 253–260.

[20] P.K. Madhu, X. Zhao, M.H. Levitt, High-resolution ^{1}H NMR in the solid state using symmetry-based pulse sequences, Chem. Phys. Lett. 346 (2001) 142–148.

[21] (a) S. Paul, R.S. Thakur, P.K. Madhu, ^{1}H homo-nuclear dipolar decoupling at high magic-angle spinning frequencies with rotor-synchronized symmetry sequences, Chem. Phys. Lett. 456 (2008) 253–256;
(b) S. Paul, R.S. Thakur, M.H. Levitt, P.K. Madhu, ^{1}H homo-nuclear dipolar decoupling using rotor-synchronized pulse sequences: towards pure absorption phase spectra, J. Magn. Reson. 205 (2010) 269–275;
S. Paul, D. Schneider, P.K. Madhu, ^{1}H homo-nuclear dipolar decoupling using symmetry-based pulse sequences at ultra fast magic-angle spinning frequencies, J. Magn. Reson. 206 (2010) 241–245.

[22] E. Vinogradov, P.K. Madhu, S. Vega, Phase modulated Lee-Goldburg magic angle spinning proton nuclear magnetic resonance experiments in the solid state: a bimodal Floquet theoretical treatment, J. Chem. Phys. 115 (2001) 8983–9000.

[23] A. Lesage, D. Sakellariou, S. Hediger, B. Eléna, P. Charmont, S. Steuernagel, L. Emsley, Experimental aspects of proton NMR spectroscopy in solids using phase-modulated homo-nuclear dipolar decoupling, J. Magn. Reson. 163 (2003) 105–113.

[24] B. Eléna, G. de Paepe, L. Emsley, Direct spectral optimization of proton–proton homo-nuclear dipolar decoupling in solid-state NMR, Chem. Phys. Lett. 398 (2004) 532–538.

[25] M. Leskes, S. Steuernagel, D. Schneider, P.K. Madhu, S. Vega, Homo-nuclear dipolar decoupling at magic-angle spinning frequencies up to 65 kHz in solid-state nuclear magnetic resonance, Chem. Phys. Lett. 466 (2008) 95–99.

[26] M. Leskes, P.K. Madhu, S. Vega, Super-cycled homo-nuclear dipolar decoupling in solid-state NMR: toward cleaner ^{1}H spectrum and higher spinning rates, J. Chem. Phys. 128 (2008) 052309.

[27] J.P. Amoureux, B. Hu, J. Trebosc, Enhanced resolution in proton solid-state NMR with very-fast MAS experiments, J. Magn. Reson. 193 (2008) 305–307.

[28] J.P. Amoureux, B. Hu, J. Trébosc, F. Deng, Homo-nuclear dipolar decoupling schemes for fast MAS, Solid State Nucl. Magn. Reson. 35 (2009) 19–24.

[29] O. Lafon, Q. Wang, B. Hu, J. Trébosc, F. Deng, J.P. Amoureux, Proton-proton homo-nuclear dipolar decoupling in solid-state NMR using rotor-synchronized *z*-rotation pulse sequences, J. Chem. Phys. 130 (2009) 014504.

[30] M. Leskes, P.K. Madhu, S. Vega, Why does PMLG proton decoupling work at 65 kHz MAS?, J Magn. Reson. 199 (2009) 208–213.

[31] E. Salager, R.S. Stein, S. Steuernagel, A. Lesage, B. Eléna, L. Emsley, Enhanced sensitivity in high-resolution ^{1}H solid-state NMR spectroscopy with DUMBO

dipolar decoupling under ultra-fast MAS, Chem. Phys. Lett. 469 (2009) 336–341.

[32] E. Salager, J.N. Dumeza, R.S. Stein, S. Steuernagel, A. Lesage, B. Elena-Herrmann, L. Emsley, Homo-nuclear dipolar decoupling with very large scaling factors for high-resolution ultra-fast magic angle spinning ^{1}H solid-state NMR spectroscopy, Chem. Phys. Lett. 498 (2010) 214–220.

[33] K. Mao, M. Pruski, Homonuclear dipolar decoupling under fast MAS: resolution patterns and simple optimization strategy, J. Magn. Reson. 203 (2010) 144–149.

[34] Y. Nishiyama, Y. Endo, T. Nemoto, H. Utsumi, K. Yamauchi, K. Hioka, T. Asakura, Very fast magic angle spinning ^{1}H–^{14}N 2D solid-state NMR: sub-micro-liter sample data collection in a few minutes, J. Magn. Reson. 208 (2011) 44–48 (Also, poster from the Jeol Company at 53rd ENC, Miami-USA, 15–20 April 2012).

[35] Y. Nishiyama, X. Lu, J. Trébosc, O. Lafon, Z. Gan, P.K. Madhu, J.P. Amoureux, Practical choice of ^{1}H–^{1}H decoupling schemes in through-bond ^{1}H-{X} HMQC experiments at ultra-fast MAS, J. Magn. Reson. 214 (2012) 151–158.

[36] A. Samoson, T. Tuherm, Z. Gan, High-field high-speed MAS resolution enhancement in ^{1}H NMR spectroscopy of solids, Solid State Nucl. Magn. Reson. 20 (2001) 130–136.

[37] D.H. Zhou, G. Shah, M. Cormos, C. Mullen, D. Sandoz, C.M. Rienstra, Proton-detected Solid-State NMR spectroscopy of fully protonated proteins at 40 kHz Magic-Angle Spinning, J. Am. Chem. Soc. 129 (2007) 11791–11801.

[38] B.J. van Rossum, H. Foerster, H.J.M. de Groot, High-field and high-speed CP-MAS ^{13}C NMR hetero-nuclear dipolar-correlation spectroscopy of solids with frequency-switched Lee-Goldburg homo-nuclear decoupling, J. Magn. Reson. 124 (1997) 516–519.

[39] S. Cavadini, V. Vitzthum, S. Ulzega, A. Abraham, G. Bodenhausen, Line-narrowing in proton-detected nitrogen-14 NMR, J. Magn. Reson. 202 (2010) 57–63.

[40] Z. Gan, P.K. Madhu, J.P. Amoureux, J. Trébosc, O. Lafon, A tunable homo-nuclear dipolar decoupling scheme for high-resolution proton NMR of solids from slow to fast magic-angle spinning, Chem. Phys. Lett. 503 (2011) 167–170.

[41] M. Bak, J.T. Rasmussen, N.C. Nielsen, SIMPSON: a general simulation program for solid-state NMR spectroscopy, J. Magn. Reson. 147 (2000) 296–330.

[42] M.R. Bendall, R.E. Gordon, Depth and refocusing pulses designed for multi-pulse NMR with surface coils, J. Magn. Reson. 53 (1983) 365–385.

[43] D.G. Cory, W.M. Ritchey, Suppression of signals from the probe in Bloch decay spectra, J. Magn. Reson. 80 (1988) 128–132.

[44] S. Wimperis, Broadband, narrow-band and pass-band composite pulses for use in advanced NMR experiments, J. Magn. Reson. A 109 (1994) 221–231.

[45] R. Tycko, A. Pines, Spatial localization of NMR signals by narrowband inversion, J. Magn. Reson. 60 (1984) 156–160;
R. Tycko, A. Pines, Iterative schemes for broad-band and narrow-band population inversion in NMR, Chem. Phys. Lett. 111 (1984) 462–467.

[46] J. Baum, R. Tycko, A. Pines, Spatially selective NMR with broad-band radiofrequency pulses, Chem. Phys. 105 (1986) 7.

[47] A.J. Shaka, R. Freeman, A composite 180° pulse for spatial localization, J. Magn. Reson. 63 (1985) 596–600.

[48] A.J. Shaka, R. Freeman, Pre-pulses for spatial localization, J. Magn. Reson. 64 (1985) 145–150.

[49] S. Odedra, S. Wimperis, Improved background suppression in ^{1}H MAS NMR using composite pulses, J. Magn. Reson. 221 (2012) 41–50.

[50] M. Ernst, A. Samoson, B.H. Meier, Low-power decoupling in fast magic-angle spinning NMR, Chem. Phys. Lett. 348 (2001) 293–302.

[51] M. Ernst, A. Samoson, B.H. Meier, Low-power XiX decoupling in MAS NMR experiments, J. Magn. Reson. 163 (2003) 332–339.

[52] M. Kotecha, N.P. Wickramasinghe, Y. Ishii, Efficient low-power hetero-nuclear decoupling in ^{13}C high-resolution solid-state NMR under fast magic angle spinning, Magn. Reson. Chem. 45 (2007) S221–S230.

[53] M. Weingarth, G. Bodenhausen, P. Tekely, Low-power decoupling at high spinning frequencies in high static fields, J. Magn. Reson. 199 (2009) 238–241.

[54] M. Weingarth, J. Trébosc, J.P. Amoureux, G. Bodenhausen, P. Tekely, Efficiency at high spinning frequencies of hetero-nuclear decoupling methods designed to quench rotary resonance, Solid State Nucl. Magn. Reson. 40 (2011) 21–26.

Supplementary Information

Detailed analysis of the TIMES and TIMES$_0$ high-resolution MAS methods for high-resolution proton NMR

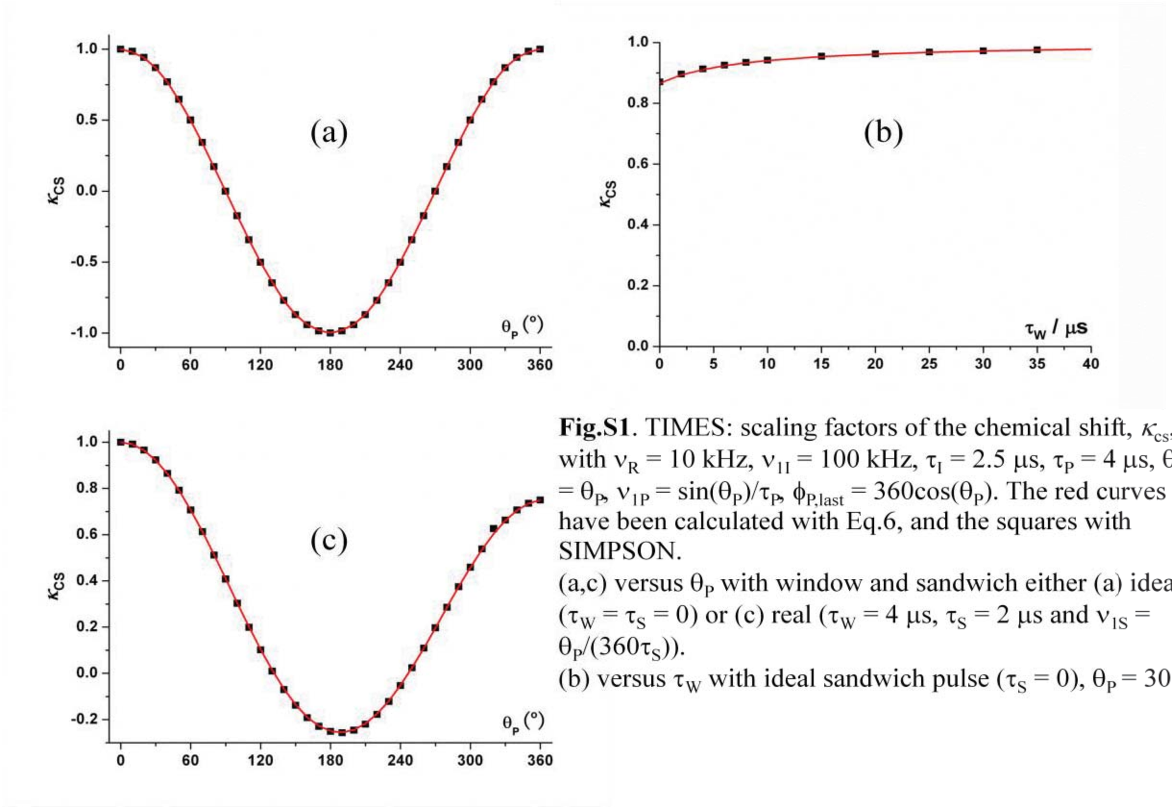

Fig.S1. TIMES: scaling factors of the chemical shift, κ_{cs}, with $\nu_R = 10$ kHz, $\nu_{1I} = 100$ kHz, $\tau_I = 2.5$ µs, $\tau_P = 4$ µs, $\theta_S = \theta_P$, $\nu_{1P} = \sin(\theta_P)/\tau_P$, $\phi_{P,last} = 360\cos(\theta_P)$. The red curves have been calculated with Eq.6, and the squares with SIMPSON.
(a,c) versus θ_P with window and sandwich either (a) ideal ($\tau_W = \tau_S = 0$) or (c) real ($\tau_W = 4$ µs, $\tau_S = 2$ µs and $\nu_{1S} = \theta_P/(360\tau_S)$).
(b) versus τ_W with ideal sandwich pulse ($\tau_S = 0$), $\theta_P = 30°$.

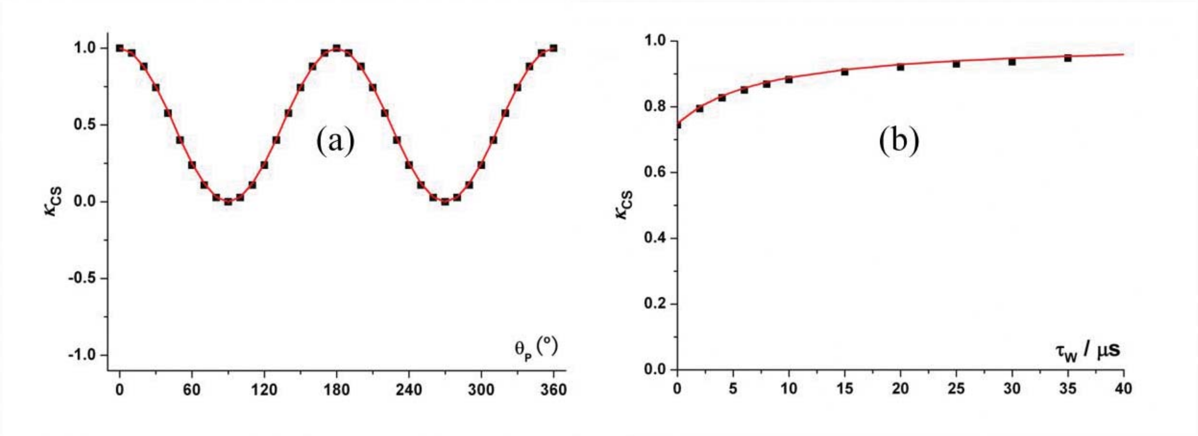

Fig.S2. TIMES$_0$: scaling factors of the chemical shift, κ_{cs}, with $\nu_R = 10$ kHz, $\nu_{1I} = 100$ kHz, $\tau_I = 2.5$ µs, $\tau_P = 4$ µs, $\nu_{1P} = \sin(\theta_P)/\tau_P$, $\phi_{P,last} = 360\cos(\theta_P)$. (a) versus θ_P with $\tau_W = 0$. (b) versus τ_W with $\theta_P = 30°$. The red curves have been calculated with Eq.7, and the squares with SIMPSON.

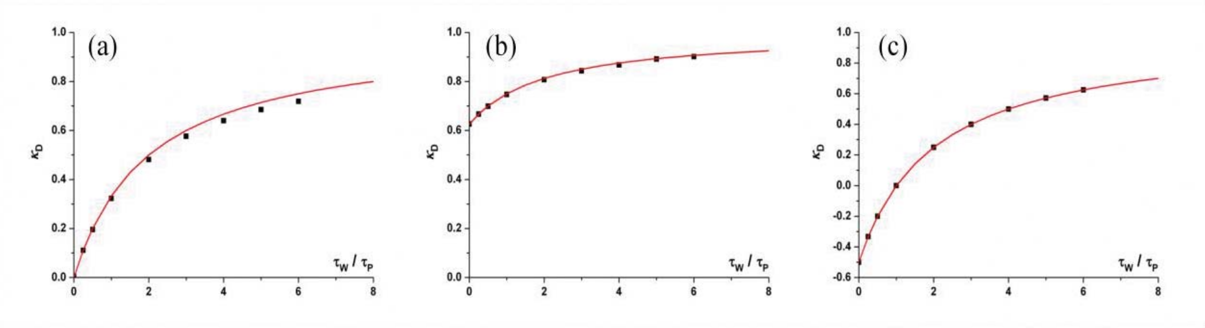

Fig.S3. TIMES: scaling factors of the homo-nuclear dipolar interaction, κ_D, for static samples, with $|b_{H\text{-}H}|/2\pi = 10$ kHz, $\tau_P = 4$ µs, (a) $\theta_S = \theta_P = 54.736°$, $\nu_{1P} = \sin(\theta_P)/\tau_P = 204$ kHz, $\phi_{P,last} = 360\cos(\theta_P) = 208°$, (b) $\theta_S = \theta_P = 30°$, $\nu_{1P} = \sin(\theta_P)/\tau_P = 125$ kHz, $\phi_{P,last} = 360\cos(\theta_P) = 312°$, (c) $\theta_S = \theta_P = 90°$, $\nu_{1P} = \sin(\theta_P)/\tau_P = 250$ kHz, $\phi_{P,last} = 360\cos(\theta_P) = 0°$. The red curves have been calculated with Eq.8, and the squares with Matlab assuming ideal ($\tau_S = 0$) sandwich pulses.

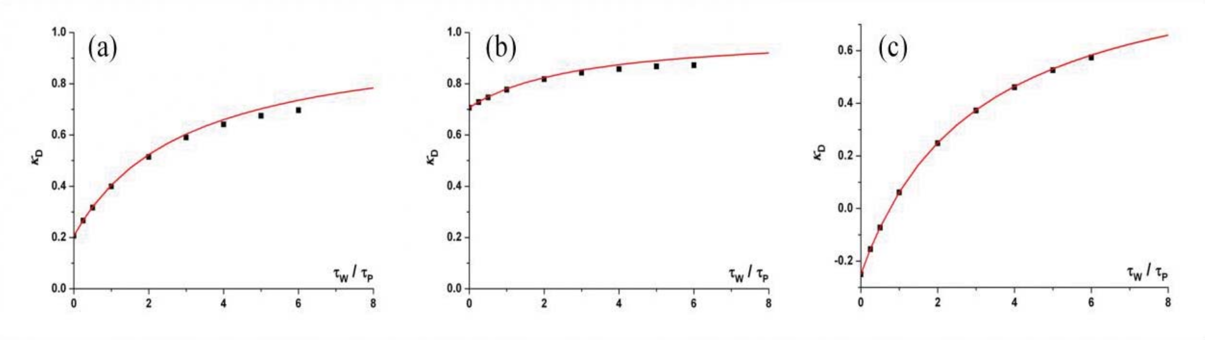

Fig.S4. TIMES: scaling factors of the homo-nuclear dipolar interaction, κ_D, for static samples, with $|b_{H\text{-}H}|/2\pi = 10$ kHz, $\tau_P = 4$ µs, (a) $\theta_S = \theta_P = 54.736°$, $\nu_{1P} = \sin(\theta_P)/\tau_P = 204$ kHz, $\phi_{P,last} = 360\cos(\theta_P) = 208°$, (b) $\theta_S = \theta_P = 30°$, $\nu_{1P} = \sin(\theta_P)/\tau_P = 125$ kHz, $\phi_{P,last} = 360\cos(\theta_P) = 312°$, (c) $\theta_S = \theta_P = 90°$, $\nu_{1P} = \sin(\theta_P)/\tau_P = 250$ kHz, $\phi_{P,last} = 360\cos(\theta_P) = 0°$. The red curves have been calculated with Eq.9, and the squares with Matlab employing real ($\tau_S = 2$ µs, $\nu_{1S} = \theta_P/(360\tau_S) = 76$ kHz) sandwich pulses.

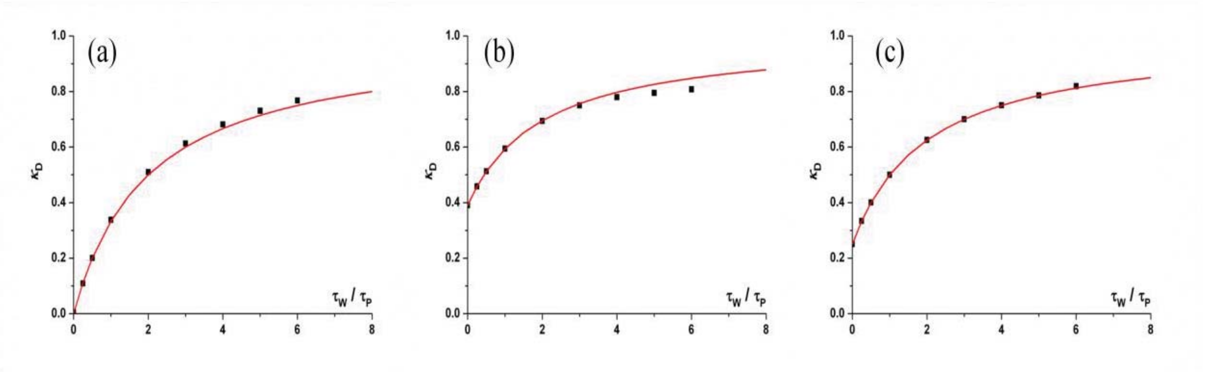

Fig.S5. TIMES$_0$: scaling factors of the homo-nuclear dipolar interaction, κ_D, for static samples, with $|b_{H\text{-}H}|/2\pi = 10$ kHz, $\tau_P = 4$ µs, (a) $\theta_P = 54.736°$, $\nu_{1P} = \sin(\theta_P)/\tau_P = 204$ kHz, $\phi_{P,last} = 360\cos(\theta_P) = 208°$, (b) $\theta_P = 30°$, $\nu_{1P} = \sin(\theta_P)/\tau_P = 125$ kHz, $\phi_{P,last} = 360\cos(\theta_P) = 312°$, (c) $\theta_P = 90°$, $\nu_{1P} = \sin(\theta_P)/\tau_P = 250$ kHz, $\phi_{P,last} = 360\cos(\theta_P) = 0°$. The red curves have been calculated with Eq.10, and the squares with Matlab.

Practical tools to enhance the ^{1}H resolution in CRAMPS experiments

Independently from the CRAMPS sequence and the spinning speed which are used, the best way to enhance the resolution of proton spectra is by improving the rf-homogeneity. This leads to using a limited part of the sample, which can be selected with spacers and/or by rf-excitation.

I. Spacers

In the early days of slow MAS CRAMPS, proton spectra were recorded using a restricted sample with spherical shape for best resolution.[1-5] However, it is important to notice that it is presently difficult to pack spherical samples with spacers when using very small rotor diameters ($\varnothing \leq 1.3$ mm) for ultra-fast MAS rotation. In Fig.**S6a** we show two glycine TIMES spectra recorded at 9.4 T using a 2.5 mm diameter rotor with ν_R = 10 kHz. One spectrum has been obtained with a full rotor, which means a sample length of 8 mm; whereas the second spectrum has been recorded with two cylindrical spacers of 3 mm length each, thus only leaving 2 mm of cylindrical sample in the middle of the rotor. Two facts can be deduced from this figure. First, the ratio for the amplitudes is only of ca. two, instead of four as the ratio of the sample volumes. This means that approximately half of the rotor length is not active in CRAMPS experiments due to rf-inhomogeneity, and that these types of sequences select by themselves a part of the sample which presents a good rf-homogeneity. Second, one observes in Fig.**S6b** showing the re-normalized spectra, that cylindrical spacers only slightly enhance the resolution of the CH_2 peaks.

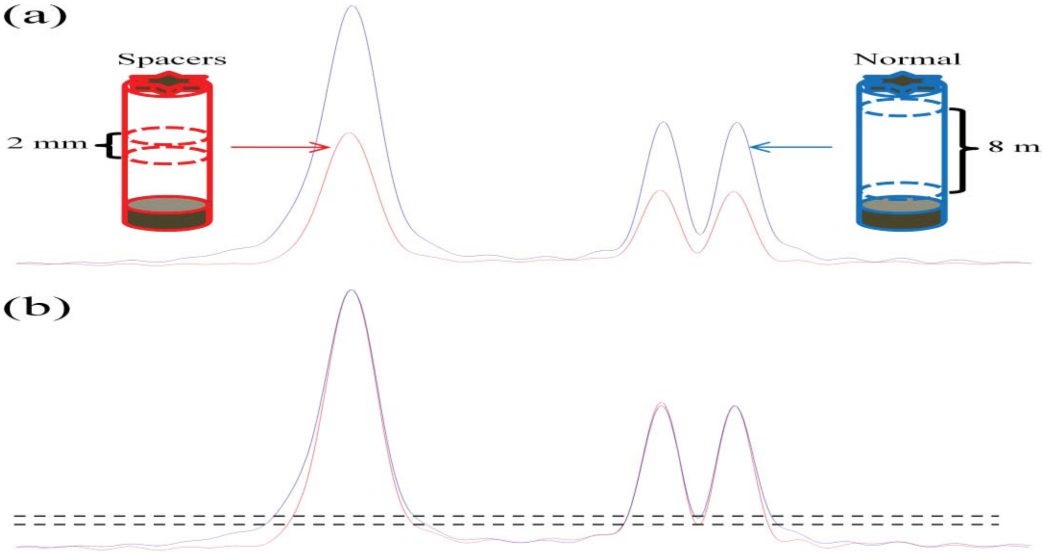

Fig.S6. (a) Experimental ^{1}H TIMES spectra of glycine obtained at 9.4 T, with ν_R = 10 kHz, with (red) and without (blue) cylindrical spacers. (b) Same spectra renormalized vertically to show the small resolution enhancement on the two CH_2 resonances.

This weak resolution enhancement is due (i) to the fact the zone where the rf-field is approximately constant is rarely situated exactly at the center of the rotor, (ii) that even in the optimum homogeneous zone with respect to the rotor axis, the rf-field is also submitted to a gradient perpendicularly to this axis, and (iii) that the cylindrical shape of the restricted sample leads to differences of magnetic susceptibility. So, even with a restricted cylindrical sample, spins are always submitted to a B_1 inhomogeneity.

II. Long initial pulse

Another way to enhance the resolution is to use an initial pulse with a long θ_I flip-angle (Fig.1), instead of the usual short pulse with θ_I = 90°. By doing so, the rf-field itself selects the 'good' region of the sample where it can be considered as approximately constant, by virtue of the dephasings of spins during the nutation. The rf-selection is then performed not only along but also perpendicularly to the rotor axis, and there is no difference of magnetic susceptibility. This is demonstrated in Fig.**S7a**, where one observes simultaneously a decrease of the amplitude and a resolution enhancement when increasing θ_I from 90° to 1170°. In Fig.**S7b**, we have represented the same spectra renormalized to the same intensity for the CH_2 resonances. Two facts are observable in this figure. First, the 'renormalized' amplitude of NH_3 resonance increases with θ_I value, which means that this resonance is much less affected by rf-inhomogeneity that CH_2 resonances for which ^1H-^1H interactions are very strong. Second, the CH_2 resolution seems to only slightly improve when $\theta_I \geq$ 810°, but the signal amplitude continues to decrease with the initial pulse length. This means that θ_I = 810° seems to be a good compromise, ***at least on our spectrometer***, between resolution and S/N ratio.

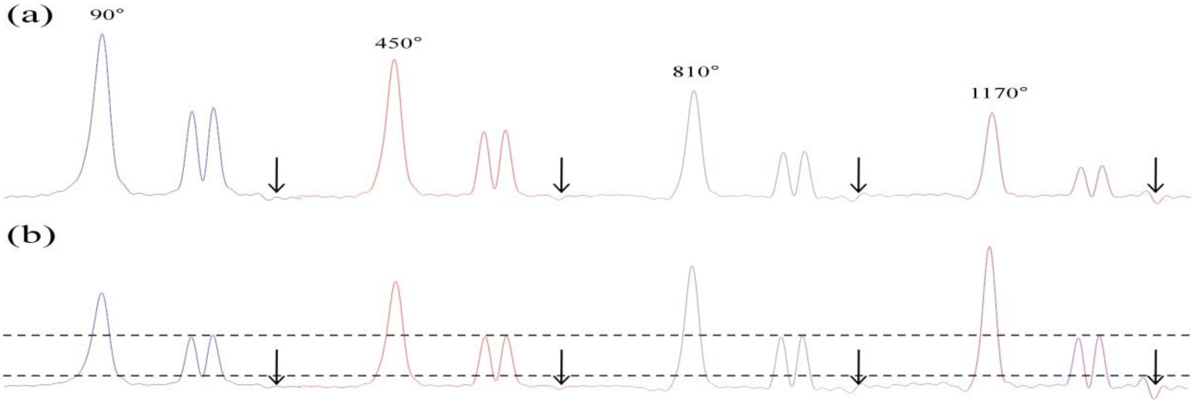

Fig.S7. (a) Experimental ^1H TIMES spectra of glycine obtained at 9.4 T, with ν_R = 10 kHz, versus the initial flip-angle θ_I. (b) Same spectra renormalized vertically onto the CH_2 resonances, to show the resolution enhancement on these two resonances, and the relative increase of the NH_3 resonance with respect to CH_2. The arrows show the carrier frequency.

One question may arise: is this resolution enhancement related to a better B_1 homogeneity, or is it related to the rf-selection of certain crystallite orientations in the powder sample that lead to weak ^1H-^1H dipolar interactions. In the second case, these selected crystallites should mainly contain inter-nuclear ^1H-^1H vectors close to the rotor axis, thus corresponding to dipolar interactions weaker than with θ_I = 90° initial pulse that selects all orientations. To answer this question, we have recorded several one-pulse spectra versus θ_I for three different rf-fields: ν_{1I} = 50, 100 and 200 kHz at ν_R = 30 (Fig.**S8a**) and 64 (Fig.**S8b**) kHz, with B_0 = 9.4 and 18.8 T, respectively. The amplitude of the spectra decreases with increasing θ_I values, but the line-shapes remain completely independent of the θ_I value (Fig.**S8c**). We can therefore conclude that using a long initial pulse only changes the rf-homogeneity, not the involved dipolar interactions. This is the same conclusion as that recently drawn in the framework of combining such a long initial pulse with the DEPTH sequence to improve the suppression of probe background signals.[6]

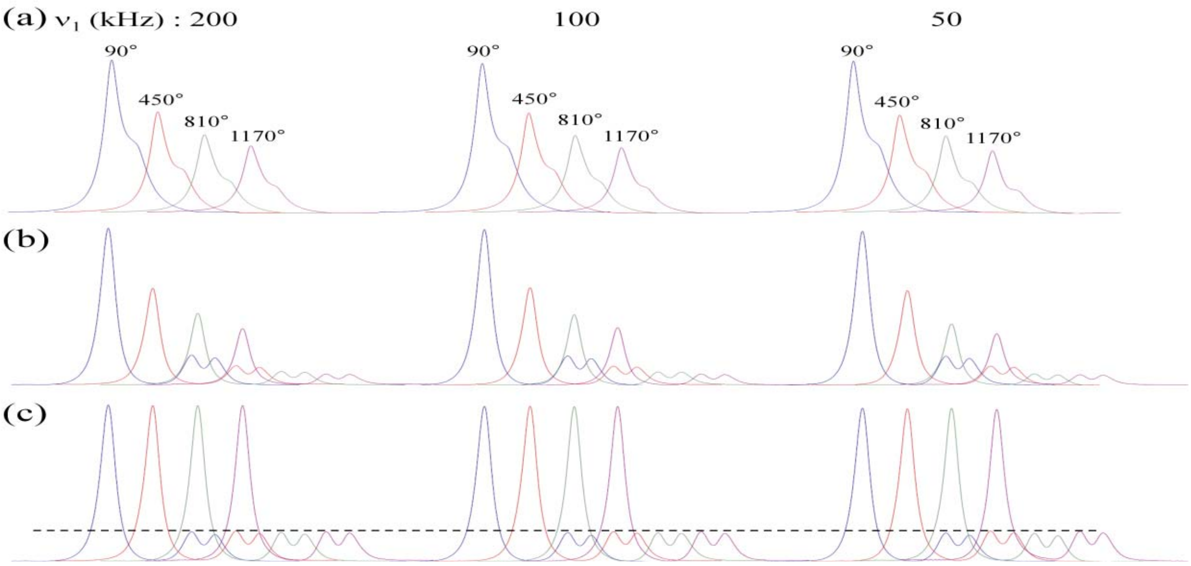

Fig.S8. Experimental one-pulse ^{1}H spectra of glycine obtained at (a) 9.4 T with ν_R = 30 kHz, and (b) 18.8 T with ν_R = 64 kHz, for four initial flip-angle θ_I (90°, 450°, 810°, 1170°) and three rf-field amplitudes (50, 100, 200 kHz). (c) Same spectra as in (b) renormalized vertically onto the CH_2 resonances, to show that the line-shapes are fully identical

One may wonder if we can still improve the resolution by combining spacers with a long initial pulse. To answer this question, we have recorded several TIMES spectra with different θ_I values either with a full rotor (Fig.**S9a**) or with two cylindrical 3 mm long spacers (Fig.**S9b**). One observes that the best resolution is experienced for the full rotor sample with $\theta_I \geq 810°$ (Fig.**S9a**), which confirms that cylindrical spacers do not select the best slice within the rotor. With the restricted sample one also observes a small decrease of amplitudes with increasing θ_I values (Fig.**S9b**), which evidences the rf-inhomogeneity perpendicularly to the rotor axis.

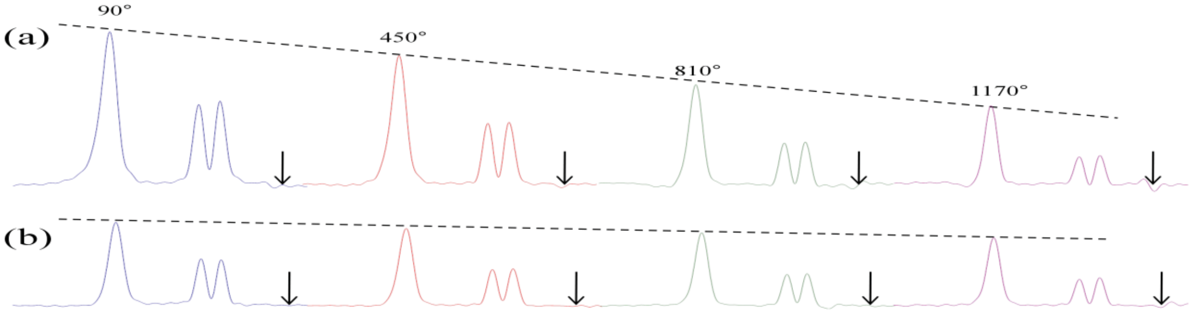

Fig.S9. Experimental ^{1}H TIMES spectra of glycine obtained at 9.4 T with ν_R = 10 kHz, for four initial flip-angle θ_I (90°, 450°, 810°, 1170°) without (a) and with (b) spacers. On our sample, rotor and spectrometer, the best compromise between resolution and S/N ratio is observed without spacer (a) and with θ_I = 810°. The arrows show the carrier frequency.

III. Composite initial pulse

III.1 With 'one-pulse' type of experiments

Several more sophisticated composite sequences have been proposed to enhance the rf-homogeneity in 'one-pulse' type of experiments.[7-13] They can be classified in two categories depending on the position of the 90° pulse transferring the magnetization to the xy plane: the DEPTH sequence which uses two π-pulses after the initial 90° pulse (90, 180, 180),[7] and the other sequences which start with a composite pulse which inverts the magnetization from +z to –z, and then rotate this magnetization to the xy plane with a 90° pulse (Inv, 90).[8-13] In the second case, the B_1-selected signal is obtained by difference with the signal recorded without the inverting composite pulse. In Fig.**S10**, we have represented the modulus of the signal that can be obtained when the pulse-lengths are calculated with a nominal rf-field of 80 kHz, versus the actual rf-field (ν_1 = 0 ↔ 160 kHz) and the offset (-10 ↔ 10 kHz). We have selected seven composite sequences proposed in this purpose, and one observes that all of them are more B_1 selective in 'one pulse' type of experiment than the simple 90° pulse.

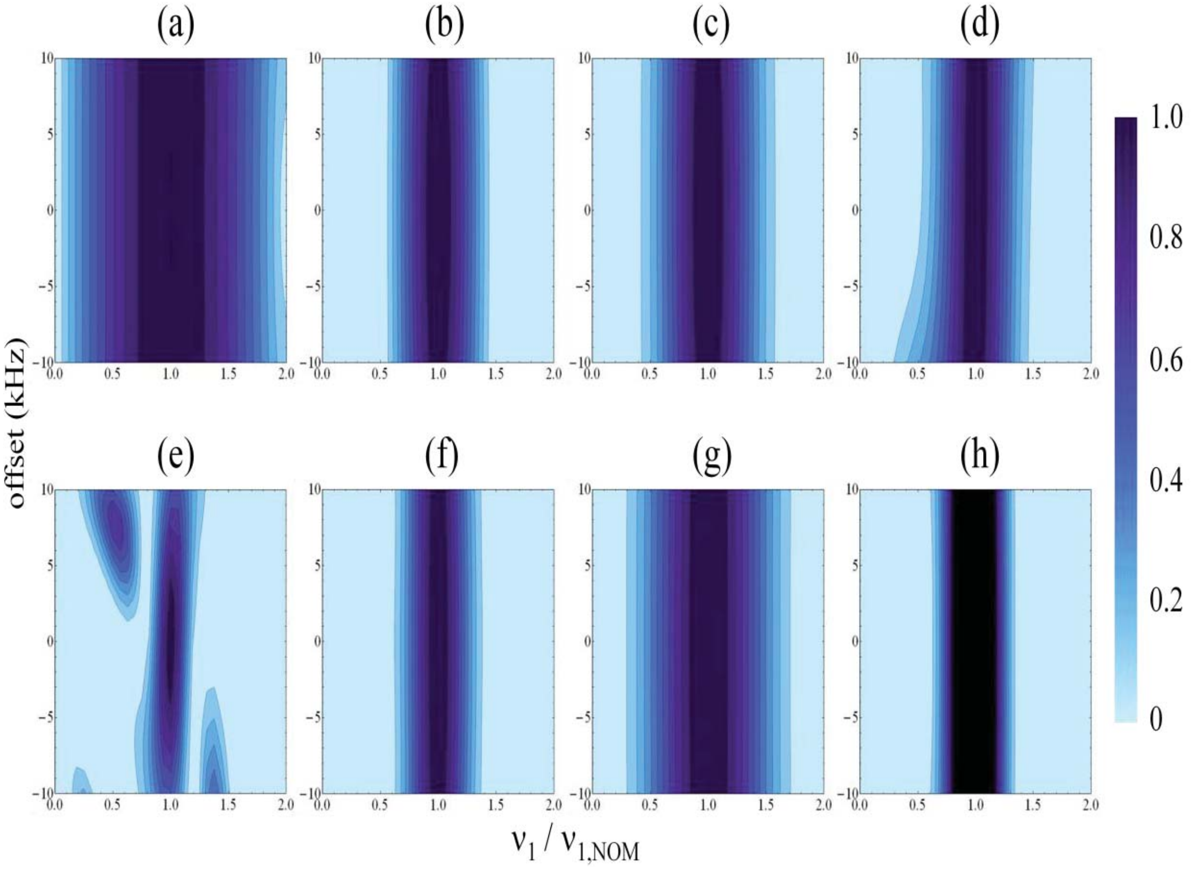

Fig.S10. Simulations showing the modulus of the signal that can be observed in 'one-pulse' experiments versus the actual rf-field (0-160 kHz) and offset (± 10 kHz), with a single pulse (a) and seven composite sequences using the same X = 90° pulse to transfer the magnetization in the xy plan: (b) DEPTH,[7] (c) pre-pulse,[8] (d) Wimperis,[9] (e) Tycko-84,[10] (f) Tycko-86,[11] (g) Shaka-85a,[12] (h) Shaka-85b.[13] The pulse-lengths are calculated with a nominal rf-field of 80 kHz.

III.2 With CRAMPS experiments

We have then replaced the initial 90° pulse in Fig.**1** by these composite sequences to start recording a high-resolution CRAMPS spectrum of glycine. The spectra, re-normalized on the CH_2 resonances, are shown in Fig.**S11**. They all show similar CH_2 resolution, but that obtained with the sequence proposed[10] by R. Tycko and A. Pines is slightly better (Fig.**S11e**) than the other ones.

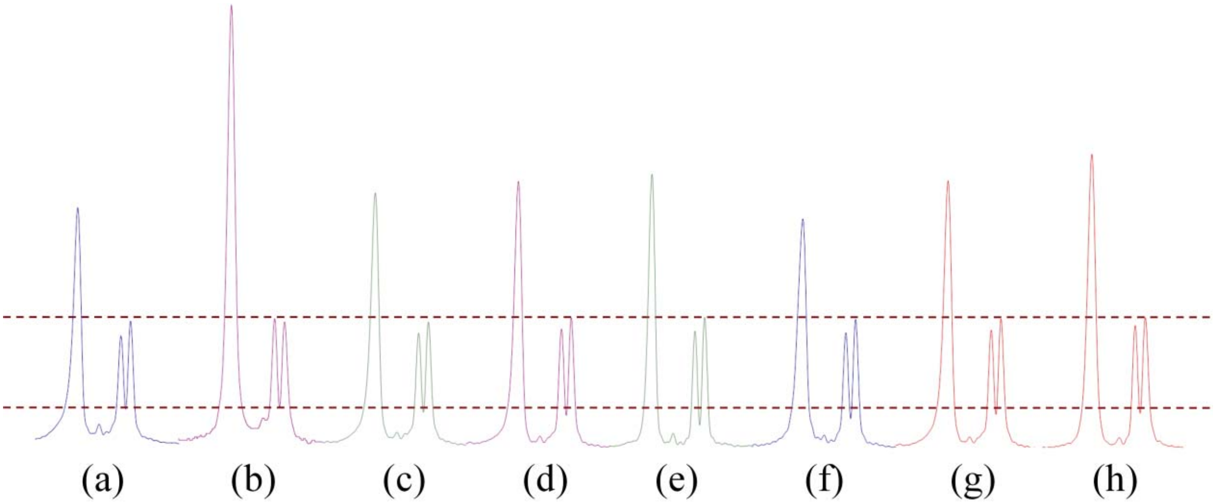

Fig.S11. Experimental TIMES spectra of glycine re-normalized on the CH_2 resonances, with B_0 = 9.4 T and ν_R = 30 kHz. The initial 90° pulse used in (a), has been replaced by a composite sequence using also a 90° pulse to rotate the magnetization to the xy plane: (b) DEPTH,[7] (c) pre-pulse,[8] (d) Wimperis,[9] (e) Tycko-84,[10] (f) Tycko-86,[11] (g) Shaka-85a,[12] (h) Shaka-85b.[13]

However, it is important to note that all these spectra are less resolved than those shown in Fig.S7 for $\theta_I > 90°$. One may thus wonder if we can still improve the resolution by replacing in the composite sequences the X = 90° pulse transferring the magnetization to the xy plane with a longer X pulse. In 'one-pulse' experiments, the selectivity of the composite pulse with respect to B_1 is then greatly increased with increasing X value (Fig.S12).

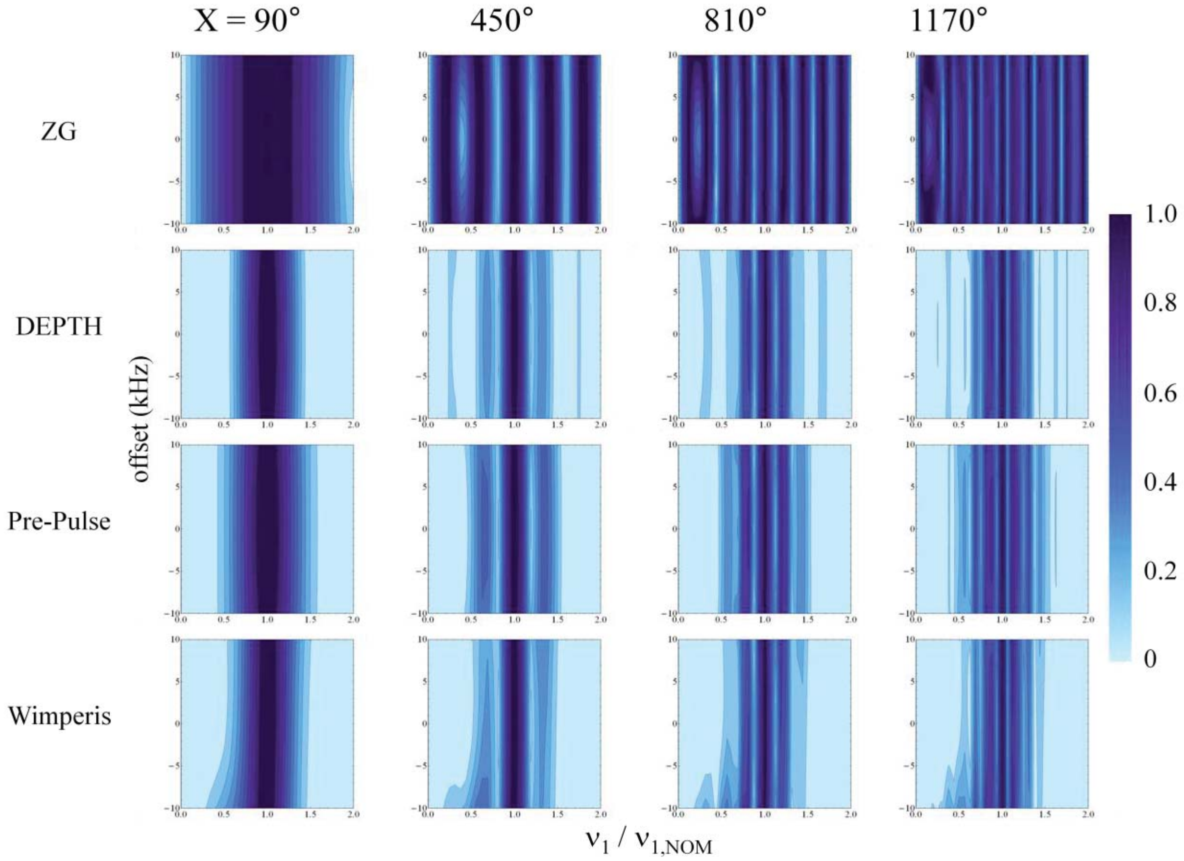

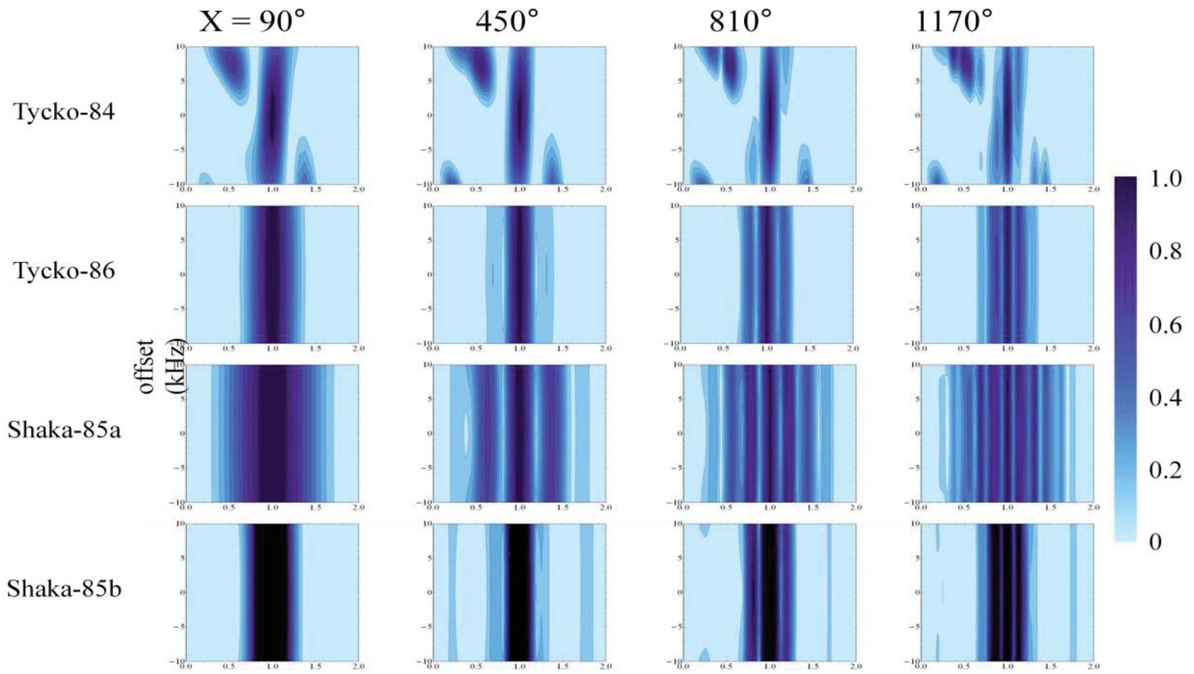

Fig.S12. Simulations showing the modulus of the signal that can be observed in 'one-pulse' experiments versus the actual rf-field (0-160 kHz) and offset (± 10 kHz), with a single pulse (a) and seven composite sequences using the same X pulse to transfer the magnetization in the xy plan: (b) DEPTH,[7] (c) pre-pulse,[8] (d) Wimperis,[9] (e) Tycko-84,[10] (f) Tycko-86,[11] (g) Shaka-85a,[12] (h) Shaka-85b.[13] X = 90°, 450°, 810°, or 1170°, for the 1st, 2nd, 3rd, or 4th column, respectively. The pulse-lengths are calculated with a nominal rf-field of 80 kHz.

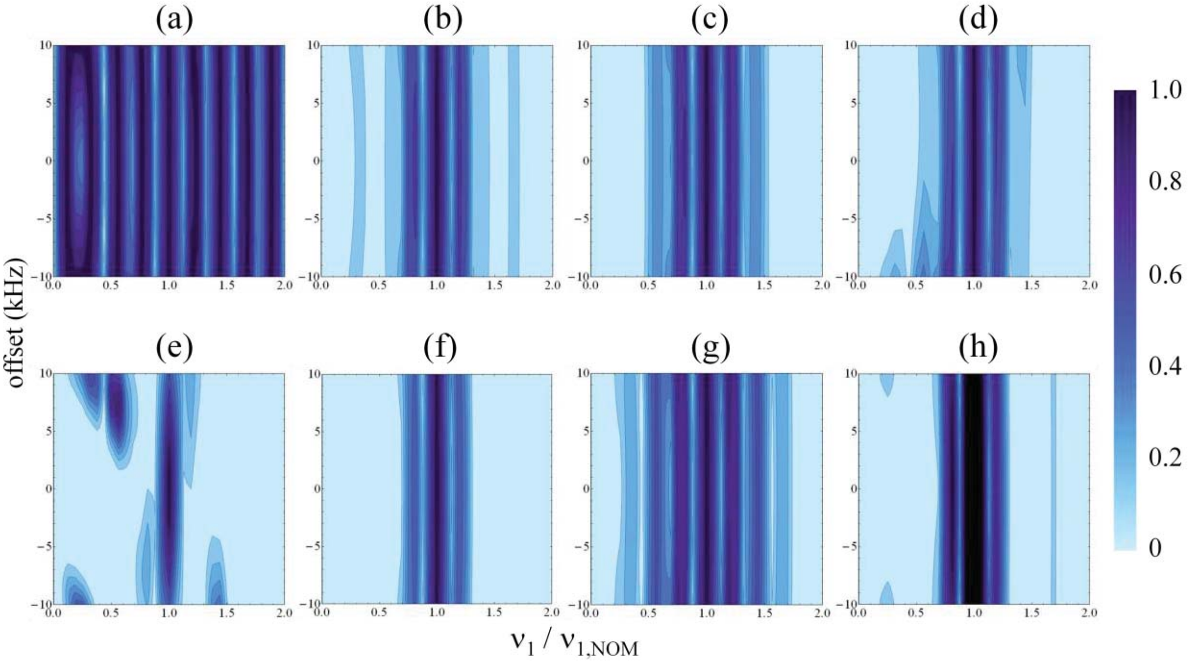

Fig.S13. Simulations showing the modulus of the signal that can be observed in 'one-pulse' experiments versus the actual rf-field (0-160 kHz) and offset (± 10 kHz), with a single pulse (a) and seven composite sequences using the same X = 810° pulse to transfer the magnetization in the xy plan: (b) DEPTH,[7] (c) pre-pulse,[8] (d) Wimperis,[9] (e) Tycko-84,[10] (f) Tycko-86,[11] (g) Shaka-85a,[12] (h) Shaka-85b.[13] The pulse-lengths are calculated with a nominal rf-field of 80 kHz.

The results for a X = 810° long pulse are shown in Fig.S13, to be compared with those shown in Fig.S10. However, the experimental results recorded with a ^{1}H high-resolution CRAMPS sequence using a composite initial pulse with a long pulse (X = 450°, 810°, 1170°) (not shown) never provided a better resolution than those observed with a simple long initial pulse (Fig.S7). This comes from the fact that three B_1-filters are then simultaneously acting: the long X pulse, the composite sequence, and the high-resolution CRAMPS method. As a result, the composite sequence does not introduce any additional resolution enhancement because the long X pulse and the high-resolution method have already selected the sample volume with best B_1 homogeneity. Very recently, a new DEPTH sequence has been proposed for improved background suppression in 'one-pulse' type of experiments.[14] However, when used with CRAMPS methods, its resolution was not as good as with a simple long initial pulse.

As a conclusion, using a full-rotor sample with a long initial flip-angle seems to be the best choice for ^{1}H high-resolution CRAMPS methods, due to (i) practical simplicity, (ii) S/N ratio, and (iii) resolution enhancement. The following experiments have thus been performed with this choice, with 810°.

References

[1] B.C. Gerstein, C. Clor, R.G. Pembleton, R.C. Wilson, Utility of pulse NMR in studying protons in coals, *J. Phys. Chem*. 81 (**1977**) 565-570.

[2] R.E. Taylor, R.G. Pembleton, L.M. Ryan, B.C. Gerstein, Combined multiple pulse NMR and sample spinning: recovery of ^{1}H chemical shift tensors, *J. Chem. Phys*. 71 (**1979**) 4541-4545.

[3] D.P. Burum, W.K. Rhim, Analysis of multiple pulse NMR in solids, *J. Chem. Phys*. 71 (**1979**) 944-956; D.P. Burum, W.K. Rhim, An improved NMR technique for homo-nuclear dipolar decoupling in solids: application to polycrystalline ice, *J. Chem. Phys*. 70 (**1979**) 3553-3554.

[4] M. Howhy, P.V. Bower, H.J. Jakobsen, N.C. Nielsen, A high-order and broadband CRAMPS experiment using z-rotational decoupling, *Chem. Phys. Lett*. 273 (**1997**) 297-303.

[5] M. Hohwy, N.C. Nielsen, Elimination of high order terms in multiple pulse nuclear magnetic resonance spectroscopy: application to homo-nuclear decoupling in solids, *J. Chem. Phys*. 106 (**1997**) 7571-7586.

[6] J. Feng, J.A. Reimer, Suppression of probe background signals via B1 field inhomogeneity, *J. Magn. Reson*. 209 (**2011**) 300-305.

[7] M.R. Bendall, R.E. Gordon, Depth and refocusing pulses designed for multi-pulse NMR with surface coils, *J. Magn. Reson*., 53 (**1983**) 365-385.

[8] D.G. Cory, W.M. Ritchey, Suppression of signals from the probe in Bloch decay spectra, *J. Magn. Reson.,* 80 (**1988**) 128-132.

[9] S. Wimperis, Broadband, narrow-band and pass-band composite pulses for use in advanced NMR experiments, *J. Magn. Reson*. A, 109 (**1994)** 221-231.

[10] R. Tycko, A. Pines, Spatial localization of NMR signals by narrowband inversion, *J. Magn. Reson*., 60 (**1984**) 156-160; R. Tycko, A. Pines, Iterative schemes for broad-band and narrow-band population inversion in NMR, *Chem. Phys. Lett*., 111 (**1984**) 462-467.

[11] J. Baum, R. Tycko, A. Pines, Spatially selective NMR with broad-band radiofrequency pulses, *Chem. Phys.* 105 (**1986**) 7.

[12] A. J. Shaka, R. Freeman, A composite 180° pulse for spatial localization, *J. Magn. Reson*., 63 (**1985**) 596-600.

[13] A. J. Shaka, R. Freeman, Pre-pulses for spatial localization, *J. Magn. Reson*., 64 (**1985**) 145-150.

[14] S. Odedra, S. Wimperis, Improved background suppression in ^{1}H MAS NMR using composite pulses, *J. Magn. Reson*., in press. http://dx.doi.org/10.1016/j.jmr.2012.05.010.

Journal of Magnetic Resonance 228 (2013) 148–158

Contents lists available at SciVerse ScienceDirect

Journal of Magnetic Resonance

journal homepage: www.elsevier.com/locate/jmr

Probing proximities between different quadrupolar isotopes using multi-pulse cross-polarization

Xingyu Lu, Aany Sofia Lilly Tankamony, Julien Trébosc, Olivier Lafon, Jean-Paul Amoureux *

UCCS, CNRS, UMR-8181, University Lille North of France, Villeneuve d'Ascq 59652, France

ARTICLE INFO

Article history:
Received 19 September 2012
Revised 3 December 2012
Available online 20 December 2012

Keywords:
Solid-state NMR
Quadrupolar nuclei
Through-space proximity
D-HETCOR
CPMAS

ABSTRACT

We present a novel cross-polarization MAS NMR pulse sequence to probe proximities between half-integer quadrupolar isotopes. This sequence employs a multi-pulse cross-polarization (MP-CP) transfer, instead of the previous continuous-wave CP (CW-CP) transfer. With respect to CW-CP transfers, our sequence is more robust with respect to offsets and Rotary Resonance Recoupling detrimental effects, especially when taking into account rf-inhomogeneity. Moreover, by using a frequency splitter and a single channel MAS probe, this MP-CP sequence may allow analyzing the through-space connectivities between two isotopes with half-integer spin values and close Larmor frequencies.

1. Introduction

Solid-state Nuclear Magnetic Resonance (NMR) is a powerful spectroscopy, which allows probing the short-range order in crystalline, disordered or amorphous solid samples. This short-range order can be determined by the analysis of through-space or through-bond NMR correlation spectra, using coherence transfers via dipolar or *J*-scalar couplings, respectively. Herein, we consider the observation of correlations between different half-integer spin quadrupolar isotopes. Transfers of coherences between quadrupolar isotopes are not efficient owing to: (i) the short relaxation times of these coherences, (ii) the weak *J*-couplings of these nuclei, and (iii) the difficult dipolar recoupling under Magic-Angle Spinning (MAS) condition owing to the intricate spin dynamics of quadrupolar nuclei in the presence of sample rotation and radio-frequency (rf) field.

One-bond connectivities between quadrupolar nuclei have been probed using two-dimensional (2D) *J*-mediated Heteronuclear Multiple Quantum Correlation (*J*-HMQC) spectroscopy in between ^{27}Al and ^{17}O in ^{17}O-enriched crystalline grossite ($CaAl_2O_4$) [1], and ^{27}Al and ^{43}Ca in ^{43}Ca-enriched Ca-aluminate or Ca-alumino-silicate glasses [2]. To the best of our knowledge, the observation of heteronuclear correlation (HETCOR) spectra via two-bonds scalar-coupling has been precluded by the small magnitude of these ^2J-couplings compared to the transverse relaxation rate, $1/T'_2$, in spin-echo experiments.

Heteronuclear through-space proximities between quadrupolar nuclei (^{27}Al–^{17}O, ^{11}B–^{23}Na, ^{11}B–^{27}Al, ^{27}Al–^{7}Li) have been probed using continuous-wave cross-polarization (CW-CP), first in static samples [3,4], and more recently under MAS [5–9]. In particular, proximities between the different ^{11}B and ^{27}Al sites in magnesium alumino-borate glasses have been probed using 2D ^{11}B–{^{27}Al} dipolar-mediated heteronuclear correlation (*D*-HETCOR) with CW-CP coherence transfer [6,7]. High-resolution along the indirect ^{27}Al spectral dimension has even been achieved by combining in *D*-HETCOR experiment a CW-CP transfer with a multiple-quantum (MQ) quadrupolar filter [8]. However, the efficiency and the robustness of CW-CP transfers are limited owing to the complex spin dynamics during spin-locking, which depends on several parameters, including: (i) the amplitude of the electric field gradient (efg), and (ii) the orientation of its principal axis systems (PAS_Q) with respect to a rotor-fixed frame, (iii) the MAS frequency, ν_R, and (iv) the rf-field amplitude, ν_1. First, depending on the orientation of the PAS_Q with respect to the rotor-fixed frame, the instantaneous quadrupolar splitting changes of sign ('zero crossing') twice or four times per rotor period. Second, in CW-CP experiments, the spin-locking of the central transition (CT) of a half-integer quadrupolar nucleus requires the use of weak CT-selective rf-field, at the expense of a high sensitivity to offsets on this channel [10,11]. Third, the Rotary Resonance Recoupling (R^3) conditions [10–13] should be avoided since they have a detrimental effect on the spin-locking efficiency. In the case of CW-CP transfer between two half-integer spin quadrupolar isotopes, twice more energy-level zero-crossings occur every rotor period, and the sensitivity to offsets extends to both channels. As a conclusion, the lack of robustness of CW-CP involving two quadrupolar isotopes has limited its applications.

---

* Corresponding author. Fax: +33 3 20 43 68 14.
E-mail address: jean-paul.amoureux@univ-lille1.fr (J.-P. Amoureux).

1090-7807/$ - see front matter © 2012 Published by Elsevier Inc.
http://dx.doi.org/10.1016/j.jmr.2012.12.005

We have shown that the robustness of CP transfers between spin-1/2 and half-integer quadrupolar nuclei can be improved by replacing the CW irradiation on the quadrupolar channel by a burst of rotor-synchronized rf-pulses [14]. The advantage of this multi-pulse CP (MP-CP) has also been rediscovered in the case of ^{2}H–^{13}C CP transfers using optimal control method [15].

In this article, we propose the use of MP-CP transfers to probe under MAS the proximities between half-integer quadrupolar nuclei. The *D*-HETCOR sequence with MP-CP is more robust with respect to offsets than with CW-CP, because the spin-locking of the two quadrupolar magnetizations is performed with MP-CP using shorter rf-pulses with larger rf-field, instead of a long low-power rf-pulse used with CW-CP. Moreover, the R^3 conditions are much more separated in MP-CP than in CW-CP, also leading to an increased robustness of MP-CP transfer with respect to rf-field homogeneity.

2. MP-CP MAS *D*-HETCOR sequence and extended Hartmann–Hahn conditions

The 2D MP-CP MAS *D*-HETCOR sequence dedicated to half-integer quadrupolar nuclei is shown in Fig. 1. In the following, the indirectly detected isotope is denoted *I*, whereas *S* is the observed isotope. It is based on the conventional CP scheme, in which the two continuous-wave spin-lock irradiations in CW-CP are replaced by two trains of rotor-synchronized rf-pulses in MP-CP [14]. The rotor-synchronization means that the centers of two consecutive rf-pulses applied to a given isotope are separated by an integer number of rotor period, T_R. In the present work, we only employ rf-pulses separated by one rotor period. The phases of rf-pulses on each channel are constant in MP-CP, and they are shifted by 90° relative to the initial 90° CT-selective excitation pulse on the *I* channel. The sequence only uses weak rf-amplitudes in order to selectively manipulate the CTs of both isotopes, which thus behave under this condition as two fictitious spin-1/2 nuclei. Indeed, a low rf-field in the order of a few kHz does not affect satellite transitions and thus avoids uncontrollable transfers to satellite coherences. The signal observed in the *S* channel is the sum of that excited by the pulse train on this channel and that arising from the CP transfer. In order to disentangle these two contributions, we used a 'spin temperature inversion' phase cycling [16]. In this two-step phase cycling, the phases of the receiver and the initial excitation 90° pulse on *I* channel are cycled over 0° and 180°, whereas the phases of rf-pulse trains on *I* and *S* channels are unchanged.

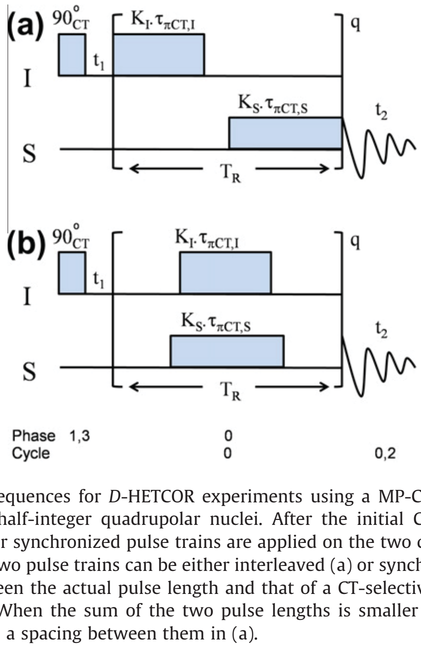

Fig. 1. Pulse sequences for *D*-HETCOR experiments using a MP-CP MAS transfer between two half-integer quadrupolar nuclei. After the initial CT-selective 90° pulse, two rotor synchronized pulse trains are applied on the two channels during $\tau_{CP} = qT_R$. The two pulse trains can be either interleaved (a) or synchronous (b). *K* is the ratio between the actual pulse length and that of a CT-selective π-pulse with same rf-field. When the sum of the two pulse lengths is smaller than one rotor period, there is a spacing between them in (a).

In Fig. 1a, all rf-pulses are interleaved to avoid any simultaneous irradiation on the two channels. This is mandatory when using an over-coupled resonator that provides two tuning and matching conditions in a single channel in order to cross-polarize two nuclei with close Larmor frequencies [17]. On the contrary, the sequence shown in Fig. 1b uses two synchronous pulse trains, and hence can only be utilized, with selective filters, when both Larmor frequencies are very different. During the two CT-selective pulse trains, the dephasings related to first-order anisotropic interactions are averaged out by MAS over full rotor periods, while rotor-synchronized pulses act in average as spin-lock irradiations. Indeed, in both channels the successive rf-pulses rotate the CT magnetizations about the rf-fields. The projections of the magnetizations along these two rf-fields are therefore constant, which lead to their spin-locking. Of course, this is true only: (i) if non-refocusable transverse relaxation times (instead of longitudinal relaxation times in the rotating frame, $T_{1\rho}$, in CW-CP) are long enough to avoid signal decay during the spin-lock period, $\tau_{CP} = qT_R$, where *q* is the number of rf-pulses in the MP-CP pulse trains, (ii) if R^3 conditions are avoided, and (iii) if dephasings produced by offsets are not too large. Globally, the continuous spin-locking of both magnetizations in CW-CP is thus replaced in MP-CP by a spin-locking 'in average' obtained by rotating each CT magnetization about its applied effective rf-field.

The lengths of MP-CP pulses on *I* and *S* channels, τ_I and τ_S, respectively, can be defined with respect to those of the CT-selective π-pulses using the same rf-field, $\tau_{\pi CT,I}$ and $\tau_{\pi CT,S}$, respectively:

$$\tau_I = K_I \tau_{\pi CT,I} \quad \text{and} \quad \tau_S = K_S \tau_{\pi CT,S} \tag{1}$$

with

$$\tau_{\pi CT,I}\,[\mu s] = 500/\{(I+1/2)\nu_{1,I}\} \quad \text{and}$$
$$\tau_{\pi CT,S}\,[\mu s] = 500/\{(S+1/2)\nu_{1,S}\} \tag{2}$$

where $\nu_{1,I}$ and $\nu_{1,S}$ are the actual nutation rf-fields given in kHz, measured in the absence of quadrupole interaction, e.g. in a liquid sample. As example, for a spin-5/2 nucleus, if the rf-pulse specifications are: $\tau_I = 8.33\ \mu s$ and $\nu_{1,I} = 10$ kHz ($\tau_{\pi CT,I} = 16.67\ \mu s$), then $K_I = 0.5$.

The original CW-CP Hartmann–Hahn (H–H) matching condition for spin-1/2 nuclei in static solids [18], has been first extended to samples under MAS rotation [19], and then to half-integer quadrupolar nuclei submitted to weak CT-selective pulses [20]:

$$(S+1/2)\nu_{1,S} = \varepsilon(I+1/2)\nu_{1,I} + J\nu_R \tag{3}$$

where $\varepsilon = +1$ for the zero-quantum (ZQ: 'flip–flop') or $\varepsilon = -1$ for the double-quantum (DQ: 'flop–flop') terms of heteronuclear dipolar interaction [21,22]. These terms lead to CP transfers of opposite signs. The last term, with $J = 0, \pm1, \pm2, \pm3, \ldots$, is related to the sample rotation, and at ultra-fast MAS, transfers related to $J = \pm1$ or ±2 are the most efficient. Eq. (3) has been adapted to MP-CP MAS transfers including one spin-1/2 and one half-integer quadrupolar nuclei [14]. To do so, the continuous rf-field in CW-CP has been replaced in MP-CP by the effective rf-field which takes into account the rf pulse lengths described in Eq. (1) [14]. It can easily be extended to include two half-integer quadrupolar nuclei submitted to weak CT-selective pulses:

$$K_S = \varepsilon K_I + 2J \tag{4}$$

A partial signal cancelation occurs when there is one CT-selective π-pulse sent in each channel every rotor period (Eq. (1): $K_I = K_S = 1$) because simultaneous transfers via zero-quantum ($\varepsilon = +1$, $J = 0$) and double-quantum ($\varepsilon = -1$, $J = 1$) coherences occur and the

S magnetizations produced by these two transfers have opposite signs. This cancelation mainly occurs at slow to moderate spinning speeds, condition under which the efficiency of MP-CP transfers corresponding to $J = 0$ are not negligible.

We also define the duty-cycles, p_I and p_S, which are equal to the ratio between the pulse-lengths and the rotor-period:

$$\begin{aligned} p_I &= \tau_I/T_R = K_I\nu_R/[(2I+1)\nu_{1,I}] \quad \text{and} \\ p_S &= \tau_S/T_R = K_S\nu_R/[(2S+1)\nu_{1,S}] \end{aligned} \tag{5}$$

The rf-amplitudes must always be chosen in order to avoid any R^3 recoupling [10–13]. In case of a continuous constant weak irradiation, this R^3 effect occurs when the nutation frequency corresponding to CT-selective excitation is equal to $n\nu_R$, with $n = 0.5$, 1, 2, 3... The homonuclear dipolar interactions are reintroduced under the $n = 0.5$ and 1 R^3 conditions; the chemical shift anisotropies (CSA) and heteronuclear dipolar interactions are reintroduced under $n = 1$ and 2; and the quadrupole interactions, including the second-order terms, are reintroduced under $n = 1, 2, 3, 4, 5, 6,\ldots$ In the case of multi-pulse rotor-synchronized CT-selective irradiation, the R^3 conditions can be extended by taking into account the rf duty-cycles (Eq. (5)):

$$\begin{aligned} \nu_{1,I} &= n\nu_R/[p_I(I+1/2)] \quad \text{and} \\ \nu_{1,S} &= n\nu_R/[p_S(S+1/2)] \quad \text{with} \quad n = 0.5, 1, 2, 3, 4, 5\ldots \end{aligned} \tag{6}$$

3. Simulations

3.1. Simulation parameters

The simulations were performed using SIMPSON software [23]. The powder averaging was accomplished using 2184 orientations: 168 $\{\alpha_{PR},\beta_{PR}\}$-pairs × 13$\gamma_{PR}$-angles. The 168 $\{\alpha_{PR},\beta_{PR}\}$-pairs, which relate the PAS_Q and rotor frames, were selected according to the REPULSION algorithm [24]. Simulations presented in Figs. 2–6, 8a, S1, and S2 were performed at $B_0 = 9.4$ T with either $\nu_R = 10$ kHz for Figs. 2–4, 6, 8a, and S1 or $\nu_R = 20$ kHz for Figs. 5 and S2. The inter-nuclear vector was aligned with the two uniaxial ($\eta_{Q,I} = \eta_{Q,S} = 0$) PAS_Q tensors, the CSAs were zero, and the dipolar coupling constant was $|b_{IS}|/(2\pi) = 400$ Hz, a classical value for an Al–O covalent bond. The spin-lock efficiency was calculated for an isolated ^{17}O nucleus with a quadrupolar coupling constant, $C_{Q,O} = 5$ MHz (Fig. 6a), whereas the MP-CP transfers were simulated for the following spin pairs: ^{23}Na → ^{11}B (Figs. 2a, 3, 4, and S1 with $C_{Q,Na} = C_{Q,B} = 2$ MHz; except Fig. 4 where different $C_{Q,B}$ values were used), ^{27}Al → ^{17}O (Figs. 2b and 8a with $C_{Q,Al} = C_{Q,O} = 5$ MHz), and ^{27}Al → ^{11}B (Figs. 5 and S2 with $C_{Q,Al} = 7$ MHz, $C_{Q,B} = 2.6$ MHz). The carrier frequencies were set 'on-resonance' (except in Fig. 5c and d), including the quadrupolar-induced shifts, which affect the centers of gravity of the MAS powder pattern. The efficiency has always been defined with respect to a standard acquisition with a CT-selective 90° pulse. All simulations shown in the article have been performed with interleaved pulse trains (Fig. 1a). However, those obtained with simultaneous pulse trains (Fig. 1b) are very similar (not shown).

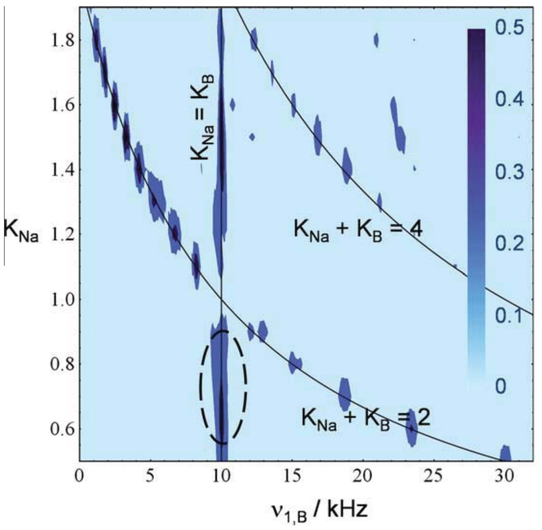

Fig. 3. Simulated efficiency of the ^{23}Na → ^{11}B MP-CP MAS transfer, calculated versus K_{Na} and $\nu_{1,B}$ values, with $\tau_{Na} = \tau_B = K_{Na}\tau_{pCT,Na}$ (Eq. (1)), $B_0 = 9.4$ T, $\nu_R = \nu_{1,Na} = 10$ kHz, $\tau_{CP} = 5$ ms, $C_{Q,Na} = C_{Q,B} = 2$ MHz, and $|b_{Na-B}|/(2\pi) = 400$ Hz. Straight vertical line ($K_{Na} = K_B$) and curves ($K_{Na} + K_B = 2$ or 4) correspond to H–H matching conditions described in Eq. (4). At slow to moderate MAS speed, the circled vertical zone ($K_{Na} \approx K_B \approx 0.6$–$0.8$) is a good compromise between efficiency and offset robustness on both channels. At ultra-fast MAS it is the curve $K_{Na} + K_B = 2$.

3.2. MP-CP Hartmann–Hahn matching conditions

In Fig. 2, we have represented the efficiency of the CP transfer that can be obtained for a pair of spin-3/2 (Fig. 2a) or spin-5/2 (Fig. 2b) nuclei, with $\nu_R = \nu_{1,I} = \nu_{1,S} = 10$ kHz, versus the K_I and K_S parameters of Eq. (1). The rotor period and the CT-selective π-pulse lengths are: $T_R = 100$ μs and $\tau_{\pi CT} = 25$ or 16.7 μs for spin-3/2 or 5/2, respectively. Therefore, the K_I and K_S parameters can extend up to 4

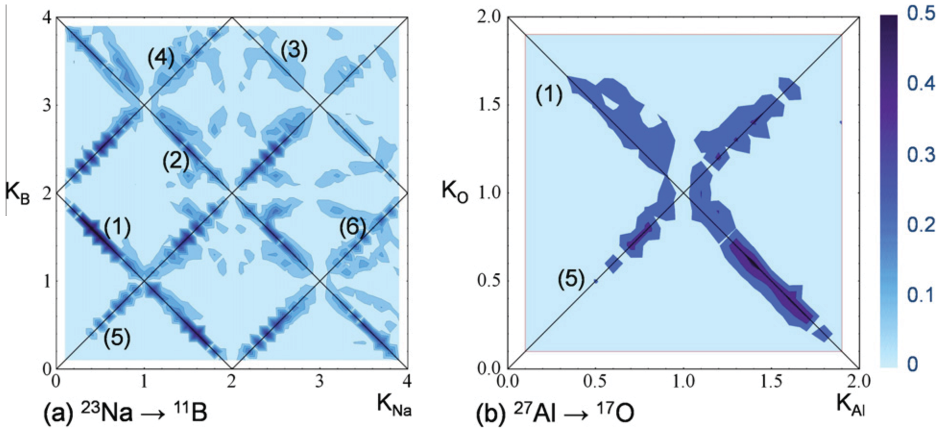

Fig. 2. Simulated efficiency of the $I \to S$ MP-CP MAS transfer, calculated versus K_I and K_S parameters, with $B_0 = 9.4$ T, $\nu_R = \nu_{1,I} = \nu_{1,S} = 10$ kHz, $\tau_{CP} = 5$ ms, $|b_{IS}|/(2\pi) = 400$ Hz. (a) ^{23}Na → ^{11}B with $C_{Q,Na} = C_{Q,B} = 2$ MHz. (b) ^{27}Al → ^{17}O with $C_{Q,Al} = C_{Q,O} = 5$ MHz. Straight lines correspond to H–H matching conditions $K_B = \varepsilon K_{Na} + 2J$ (Eq. (4)) with: (1) $\varepsilon = -1$, $J = 1$; (2) $\varepsilon = -1$, $J = 2$; (3) $\varepsilon = -1$, $J = 3$; (4) $\varepsilon = 1$, $J = 1$; (5) $\varepsilon = 1$, $J = 0$; (6) $\varepsilon = 1$, $J = -1$.

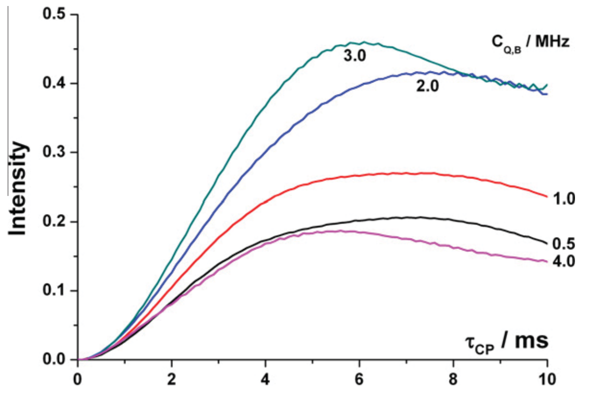

Fig. 4. Simulated efficiency of the ^{23}Na → ^{11}B MP-CP MAS transfer, calculated versus the contact time $\tau_{CP} = qT_R$, for five different quadrupolar constants: $C_{Q,B} = 0.5$, 1, 2, 3, 4 MHz, with $C_{Q,Na} = 2$ MHz, $B_0 = 9.4$ T, $\nu_R = \nu_{1Na} = \nu_{1B} = 10$ kHz, $\tau_{Na} = \tau_B = 17.5$ µs ($p_{Na} = p_B = 0.175$, $K_{Na} = K_B = 0.7$), $|b_{Na-B}|/(2\pi) = 400$ Hz.

(3/2) or 6 (5/2), values corresponding to a continuous irradiation with a CW-CP transfer. However, in Fig. 2b, we only show K_I and K_S values in the 0–2 range, because the efficiencies are much smaller out of this range. Extended H–H multi-pulse matching conditions corresponding to Eq. (4) are represented in Fig. 2 as straight lines and they correspond to the zones of good efficiencies. The spinning speed is moderate, so transfers corresponding to all J values may a priori exist (Eqs. (3) and (4)).

In Fig. 3, we have represented the efficiency that can be observed for a ^{23}Na → ^{11}B transfer on a spin-pair, performed at $\nu_R = 10$ kHz with two equal pulse lengths, $\tau_{Na} = \tau_B$, versus K_{Na} and the rf-field on the boron nucleus ($\nu_{1,B} = 0$–32 kHz), the rf-field of pulses on ^{23}Na channel being fixed to $\nu_{1,Na} = 10$ kHz. In Fig. S1 of the Supplementary information, a similar simulation is shown for a larger $\nu_{1,B}$ range, extending from 0 to 100 kHz. Fig. S1 shows that the CP-transfer is only efficient for rf-fields lower than ca. 20 kHz, which correspond to CT-selective pulses, as we assumed in the derivation of Eqs. (1)–(6). The two pulses lengths, $\tau_{Na} = \tau_B = K_{Na}\tau_{\pi CT,Na} = 25K_{Na}$ (µs) (Eqs. (1) and (2)), increase from 12.5 ($K_{Na} = 0.5$) to 47.5 µs ($K_{Na} = 1.9$) from bottom to top of the figure. From Eqs. (1) and (2), we obtained $K_B = 0.1K_{Na}\nu_{1,B}$ (kHz). The insertion of the above relation in Eq. (4) leads to extended Hartmann–Hahn conditions adapted to this particular case:

$$\nu_{1,B}\,[\mathrm{kHz}] = 10\varepsilon + 20J/K_{Na} \quad \text{with } J = 0,\ \pm1,\ \pm2, \pm3, \ldots \tag{7}$$

In Fig. 3, the three most efficient transfers correspond to ($I = {}^{23}$Na and $S = {}^{11}$B):

Vertical line $(\varepsilon = +1,\ J = 0)$:

$$\nu_{1,B}\ (\mathrm{kHz}) = \nu_{1,Na} = 10, \quad \text{equivalent to } K_I = K_S \tag{8a}$$

Left curve $(\varepsilon = -1,\ J = 1)$:

$$\nu_{1,B}\ (\mathrm{kHz}) = -10 + 20/K_{Na}, \quad \text{equivalent to } K_I + K_S = 2 \tag{8b}$$

Right curve $(\varepsilon = -1,\ J = 2)$:

$$\nu_{1,B}\ (\mathrm{kHz}) = -10 + 40/K_{Na}, \quad \text{equivalent to } K_I + K_S = 4 \tag{8c}$$

Globally, taking into account the transfer efficiency and the robustness to offsets on both nuclei, which is proportional to the rf-fields, similar rf-amplitudes on both channels seem to be a good compromise: $\nu_{1,I} \approx \nu_{1,S}$ with $K_I \approx K_S \approx 0.6$–0.8 (surrounded zone along the vertical line in Fig. 3). From Eq. (5), the condition $K_I \approx K_S$ is equivalent to:

$$(2I+1)\nu_{1,I}p_I \approx (2S+1)\nu_{1,S}p_S \tag{9}$$

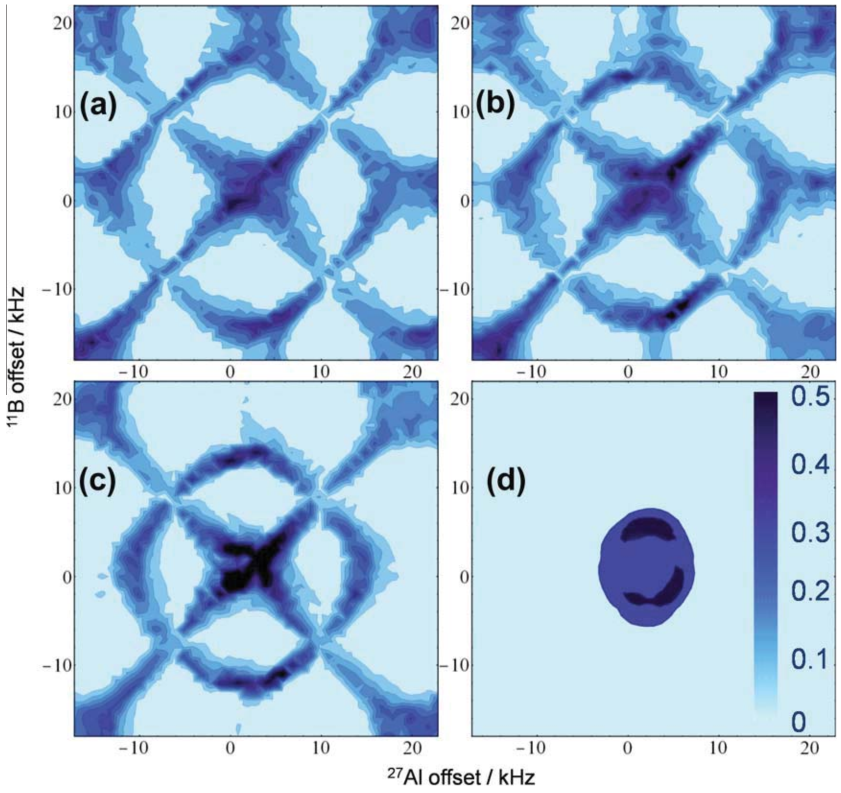

Fig. 5. Simulated efficiency modulus of the ^{27}Al → ^{11}B MP-CP (a–c) and CW-CP (d) MAS transfer, calculated versus ^{27}Al and ^{11}B offsets, with $B_0 = 9.4$ T, $\nu_R = 20$ kHz, $\tau_{CP} = 10$ ms, $C_{Q,Al} = 7$ MHz, $C_{Q,B} = 2.6$ MHz, and $|b_{Al-B}|/(2\pi) = 400$ Hz. (a) $p_{Al} = p_B = 0.1$ ($K_{Al} \approx K_B \approx 0.5$), $\nu_{1,Al} = 16$ kHz, $\nu_{1,B} = 24$ kHz; (b) $p_{Al} = p_B = 0.2$ ($K_{Al} \approx K_B \approx 0.6$), $\nu_{1,Al} = 10$ kHz, $\nu_{1,B} = 15$ kHz; (c) $p_{Al} = p_B = 0.4$ ($K_{Al} \approx K_B \approx 0.7$), $\nu_{1,Al} = 6$ kHz, $\nu_{1,B} = 9$ kHz; (d) $p_{Al} = p_B = 1$, $\nu_{1,Al} = 2.5$ kHz, $\nu_{1,B} = 5.5$ kHz.

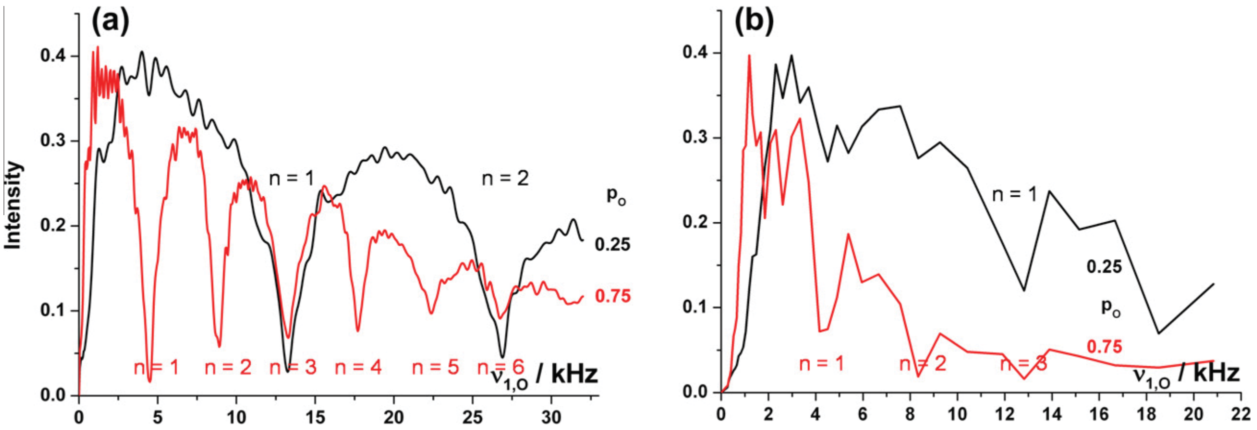

Fig. 6. (a) Simulated amplitude of the ^{17}O magnetization versus the ^{17}O rf-field of a multi-pulse spin-locking applied during $\tau = 2$ ms, for duty-cycles of $p_O = 0.25$ ($\tau_O = 25$ µs) and 0.75 ($\tau_O = 75$ µs), with $B_0 = 9.4$ T, $C_{Q,O} = 5$ MHz, $\eta_{Q,O} = 0$, and $\nu_R = 10$ kHz. (b) Experimental spin-locked amplitude of the ^{17}O magnetization in Al_2O_3, with same specifications as in (a), a recycle delay of 0.1 s and NS = 8000.

However, this condition is mainly efficient with slow to moderate spinning speed, as it is related to $J = 0$ (Eqs. (3) and (4)). At high MAS frequencies, the $J = \pm 1$ and ± 2 excitations are the two most efficient, and then the condition $K_I + K_S = 2$ should be the best compromise (Fig. 3).

3.3. Influence of quadrupolar interaction magnitude on MP-CP transfer

In Fig. 4, we have represented the efficiency build-up curve of ^{23}Na → ^{11}B MP-CP transfer for five different $C_{Q,B}$ values. The spin system is a ^{23}Na–^{11}B spin pair with $C_{Q,Na} = 2$ MHz. The rf-fields during MP-CP are $\nu_{1,Na} = \nu_{1,B} = \nu_R = 10$ kHz and the ^{23}Na and ^{11}B MP-CP pulses last $\tau_{Na} = \tau_B = 17.5$ µs ($p_{Na} = p_B = 0.175$), which leads to $K_{Na} = K_B = 0.7$, the $J = 0$ condition in Eqs. (3) and (4). The highest MP-CP transfer efficiency is obtained for $C_{Q,B} = 3$ MHz. This optimum value results from a compromise between the amplitudes of rf-fields and quadrupole interactions. On one hand, rf-fields must be low enough with respect to the quadrupole frequencies so that the MP-CP pulses are CT-selective hence allowing the selective manipulation of the magnetizations corresponding to the CT transitions. On the other hand, rf-fields must be high enough to cover the entire breadth of the CT pattern, which is solely influenced by second-order anisotropic quadrupolar broadening. In Fig. 4, for weak quadrupole interactions (e.g. $C_{Q,B} = 0.5$ MHz), the rf-field $\nu_{1,B}$ is too high for the fictitious spin-1/2 approximation to be valid and the ^{11}B pulses are not CT-selective. Conversely, for large quadrupole interactions (e.g. $C_{Q,B} = 4$ MHz), the second-order CT frequency spread is too large at 9.4 T to be fully covered by $\nu_{1,B} = 10$ kHz. This phenomenon also occurs in the case of CW-CP transfers. For spin-3/2 nuclei, moderate C_Q values in the order of 1.5–3 MHz lead to the best efficiency at this field of 9.4 T. Fig. 4 also shows that the optimum contact time τ_{CP}^{opt} is little dependent on the C_Q value.

3.4. Robustness to offset

Fig. 5 shows the variation of ^{27}Al → ^{11}B MP-CP efficiency as function of ^{27}Al and ^{11}B resonance offsets for different duty cycles on ^{27}Al and ^{11}B channels. As seen in Fig. 5d, CW-CP experiment, which corresponds to $p_{Al} = p_B = 1$, exhibits significant efficiency only when the ^{27}Al and ^{11}B carrier frequencies, ν_0^{Al} and ν_0^{B}, do not differ from the ^{27}Al and ^{11}B quadrupolar induced shifts, ν_{QIS}^{Al} and ν_{QIS}^{B}, by more than a few kHz. For MP-CP (p_{Al} and $p_B < 1$), other regions of high transfer efficiency are observed (see Fig. 5a–c). Each pulse train of the MP-CP sequence corresponds to Delays Alternating with Nutations for Tailored Excitations (DANTE) scheme [25]. Introduced in solution-state NMR for selective excitation, DANTE turns out to be useful for broadband excitation in solid-state NMR for samples undergoing MAS [26–28]. Each DANTE pulse train of MP-CP can be described as an infinite 'comb' of rectangular pulses with a period, T_R, multiplied by a boxcar function of length, qT_R. The Fourier transform of such pulse train is hence a comb of rf-spikelets separated by ν_R [27], leading to regions of high efficiencies for MP-CP transfer when $\nu_0^{Al} = \nu_{QIS}^{Al} + j_{Al} \cdot \nu_R$ and $\nu_0^{B} = \nu_{QIS}^{B} + j_B \cdot \nu_R$, where j_{Al} and j_B are integers. These predictions are consistent with the simulated MP-CP efficiency for short ^{27}Al and ^{11}B pulses (see Fig. 5a corresponding to $p_{Al} = p_B = 0.1$). For longer ^{27}Al and ^{11}B pulses, the regions of high transfer efficiency deviate from those predicted using Fourier transform (see Fig. 5c, corresponding to $p_{Al} = p_B = 0.4$). This is consistent with a nonlinear response, obtained when each MP-CP pulse tilts the CT magnetization by large angles [29]. Therefore, in MP-CP experiments, the ^{27}Al and ^{11}B offset regions exhibiting high transfer efficiency can be adjusted to resonance frequencies of different sites by changing the MAS frequency and the MP-CP pulse lengths. This possible adjustment of MP-CP rf-pulses to the sample offsets is more visible in Fig. S2. Therefore, MP-CP transfers can circumvent the offset sensitivity of CW-CP involving two half-integer quadrupolar isotopes.

3.5. Avoiding R^3 conditions

In Fig. 6a, we show the magnetization that is observed, versus the multi-pulse spin-locking rf-field amplitude, after a spin-lock time of $\tau = 2$ ms on an isolated spin-5/2 nucleus, ^{17}O, with a quadrupolar coupling constant of $C_{Q,O} = 5$ MHz. As the spin system is only composed of one isolated ^{17}O nucleus, there is no homonuclear dipolar interaction and the $n = 0.5$ R^3 condition cannot be observed in Fig. 6a. This figure shows that the minimum rf-value to cover the entire breadth of the CT pattern and hence to spin-lock efficiently is inversely proportional to the duty-cycles: $\nu_{1,O}^{min} \approx 1$ and 3 kHz for $p_O = 0.75$ and 0.25, respectively. The dips observed in the curves describing the spin-locking efficiency versus $\nu_{1,O}$ are related to R^3 effects due to quadrupole interactions. Simulations, displayed for $\nu_{1,O}$ up to 32 kHz for the two duty-cycles, perfectly agree with Eq. (6) with $n = 1$ and 2 ($p_O = 0.25$) and $n = 1$–6 ($p_O = 0.75$). In practice, efficient CP transfers require efficient spin-lockings, and they can thus only be achieved when the rf-fields on both channels do not match the R^3 conditions. When taking into account the rf-inhomogeneity in the rotor, Fig. 6a

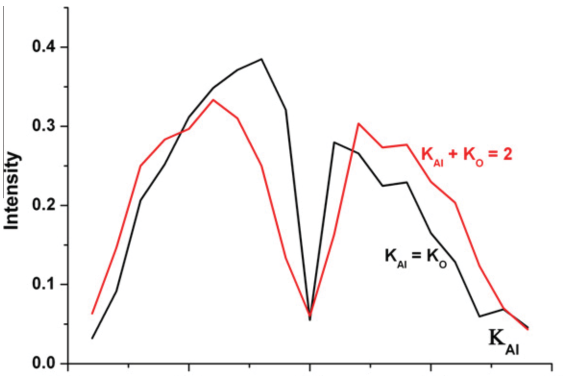

Fig. 7. Experimental efficiency of the $^{27}Al \rightarrow {}^{17}O$ MP-CP MAS transfer in Al_2O_3 corresponding either to $K_{Al} = K_O$ (black curve) or $K_{Al} + K_O = 2$ (red curve). The experiments were performed at $B_0 = 9.4$ T, with $\nu_R = 10$ kHz, $\nu_{1,Al} \approx \nu_{1,O} \approx 3.5$ kHz, and $\tau_{CP} = 2$ ms. The recycle delay is 0.1 s, NS = 8000. (For interpretation of the references to color in this figure legend, the reader is referred to the web version of this article.)

demonstrates that the R^3 detrimental effects can more easily be avoided with $p_O = 0.25$ than with $p_O = 0.75$. These effects are even worse for CW-CP MAS spin-locking because they then occur every $\nu_R/(S + ½)$, which implies that a large part of the sample has a poor transfer efficiency.

4. Experimental verifications

All experimental verifications have been performed at 9.4 T on a Bruker 400 MHz spectrometer equipped with Avance-II console, using a triple resonance probe with either a 2.5 or 3.2 mm ∅ rotor, spinning at $\nu_R = 10$ or 20 kHz. Three samples have been used: amorphous ^{17}O-enriched Al_2O_3 for $^{27}Al \rightarrow {}^{17}O$ CP-transfers, so that Mg–Al–B glass and crystalline boron aluminate of empirical formula $9Al_2O_3{\cdot}2B_2O_3$ (A_9B_2) for $^{27}Al \rightarrow {}^{11}B$ CP-transfers. We have used VPI-5, H_2O and $NaBH_4$, as chemical shift references for ^{27}Al, ^{17}O and ^{11}B isotopes, respectively.

4.1. ^{27}Al ($I = 5/2$) → ^{17}O ($S = 5/2$)

In Fig. 6b, we have represented the spin-locked ^{17}O magnetization versus the rf-amplitude observed on Al_2O_3 sample, with $\nu_R = 10$ kHz and $\tau_{CP} = 2$ ms, for the duty-cycles of $p_O = 0.25$ and 0.75. These experimental results show the dips concerning the R^3 effect predicted from Eq. (6) and simulated in Fig. 6a. As example, one finds the ratio of ca. 3 for the minimum rf-field able to spin-lock correctly the full second-order line-width with $p_O = 0.25$ and 0.75. However, the dips observed with $\nu_{1,O} \approx 13$ ($p_O = 0.25$) or 4.3, 8.6 and 13 kHz ($p_O = 0.75$) are less pronounced than those simulated in Fig. 6a. This may be due to the rf-inhomogeneity, and to the fact that only few steps for the rf-field were used.

There are three aluminum and one oxygen resonances in Al_2O_3 (Fig. S3). The quadrupolar parameters (C_Q (MHz), η_Q) have been estimated to be: (5.1, 0.5), (4.4, 0.5), (3, 0.6) and (3, 0) for Al_{IV}, Al_V, Al_{VI} and O, respectively (Fig. S3). The sample has been ca. 30% ^{17}O-enriched.

In Fig. 7, we have represented the experimental efficiency of the $^{27}Al \rightarrow {}^{17}O$ MP-CP MAS transfer in Al_2O_3 with $\nu_R = 10$ kHz and $\nu_{1,Al} \approx \nu_{1,O} \approx 3.5$ kHz, corresponding either to $K_{Al} = K_O$ or $K_{Al} + K_O = 2$. In both cases, when $K_{Al} = K_O = 1$, which means two CT-selective π-pulses of $\tau_{Al} \approx \tau_O \approx 48$ μs every rotor period, one on each channel, a partial signal cancelation occurs. This partial cancelation is related to the two coincidental matching conditions of zero-quantum ($\varepsilon = +1$, $J = 0$) and double-quantum ($\varepsilon = -1$, $J = 1$) transfers, which are of opposite signs. This cancelation is also observable in Fig. 2b.

In Fig. 8a, we have represented the simulated build-up curve that should be observed in the case of an isolated $^{27}Al \rightarrow {}^{17}O$ spin-pair with $|b_{Al-O}|/(2\pi) = 400$ Hz, $\nu_R = 10$ kHz, $\nu_{1,Al} \approx \nu_{1,O} \approx 3.5$ kHz, $\tau_{Al} = 24$ μs, ($K_{Al} \approx 0.5$, $p_{Al} = 0.24$) and $\tau_O = 71$ μs ($K_O \approx 1.5$, $p_O = 0.71$). The experimental and simulated maxima are observed at the same contact time of $\tau_{CP} \approx 2$ ms, but the experimental maximum is flatter than the simulated one. This difference stems from the fact that in the sample, the ^{27}Al nuclei are coupled to several ^{17}O nuclei. In Fig. 8b, we have represented the $^{27}Al \rightarrow {}^{17}O$ MP-CP HETCOR 2D spectrum of Al_2O_3, recorded with $\nu_R = 10$ kHz, $\nu_{1,Al} \approx \nu_{1,O} \approx 3.5$ kHz and $\tau_{Al} = \tau_O = 33$ μs, corresponding to $K_{Al} \approx K_O \approx 0.7$. The MAS spectrum at 9.4 T (shown vertically on

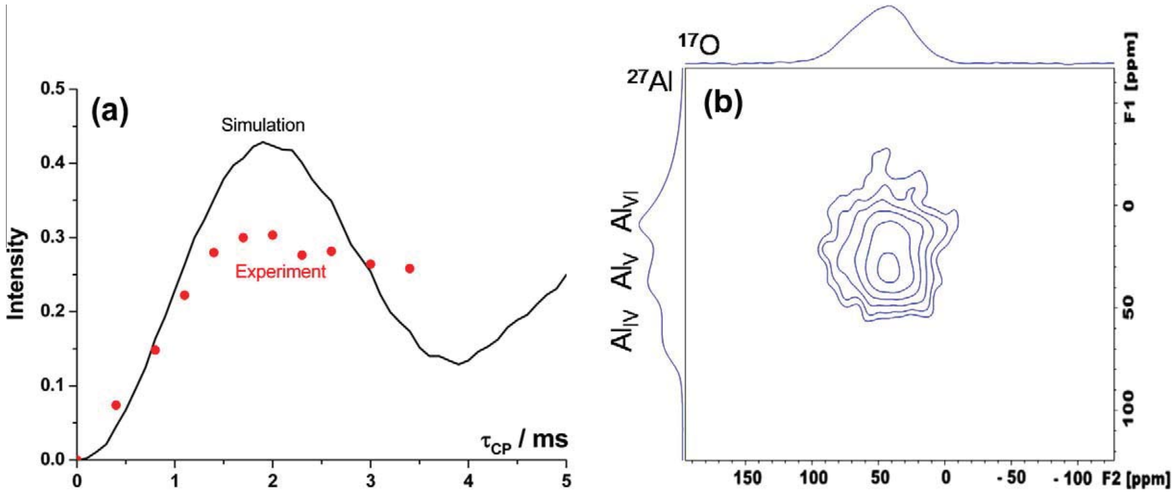

Fig. 8. (a) $^{27}Al \rightarrow {}^{17}O$ MP-CP MAS transfer efficiency versus contact time, τ_{CP}, with $B_0 = 9.4$ T, $\nu_R = 10$ kHz, $\nu_{1,Al} \approx \nu_{1,O} \approx 3.5$ kHz, $\tau_{Al} \approx 24$ μs ($K_{Al} = 0.5$), $\tau_O \approx 71$ μs ($K_O = 1.5$), NS = 8000, recycle delay = 0.1 s. The continuous black curve has been calculated with SIMPSON for one isolated ^{27}Al–^{17}O spin-pair with $|b_{Al-O}|/(2\pi) = 400$ Hz, $C_{Q,Al} = C_{Q,O} = 5$ MHz. The red points are the experimental results observed on Al_2O_3. (b) $^{27}Al \rightarrow {}^{17}O$ MP-CP MAS 2D HETCOR spectrum of Al_2O_3 with $\tau_{CP} = 2$ ms, $\tau_{Al} = \tau_O = 33$ μs ($K_{Al} \approx K_O \approx 0.7$). Other parameters are those of (a). MAS spectra are shown on the top (^{17}O) and vertically on the left (^{27}Al). Recycling delay = 0.25 s, NS = 20,000, experiment time = 58 h. The carrier frequencies were in the middle of the peak for ^{17}O, and on Al_V for ^{27}Al. (For interpretation of the references to color in this figure legend, the reader is referred to the web version of this article.)

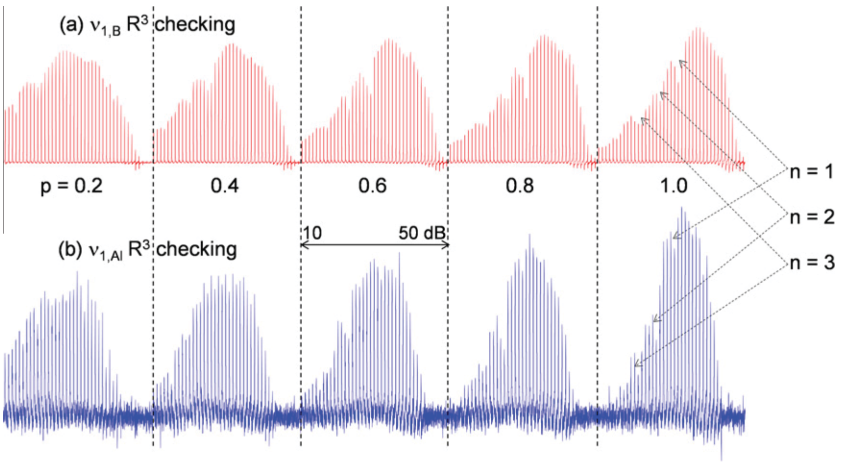

Fig. 9. Optimization of the spin-locking rf-fields on ^{11}B (a) and ^{27}Al (b) for Mg–Al–B glass sample. For the five duty-cycles (p = 0.2, 0.4, 0.6, 0.8, 1.0), the related optimal rf-fields are (kHz): $\nu_{1,B}$ = 17.6, 9.9, 7.9, 6.3, 5.6 and $\nu_{1,Al}$ = 10, 10, 8.9, 7.9, 7.1. The magnetizations have been recorded versus the rf-fields changed from 10 to 50 dB (100–0.8 kHz), with B_0 = 9.4 T, ν_R = 20 kHz, τ = 3 ms, recycle delay = 6 s, and NS = 16.

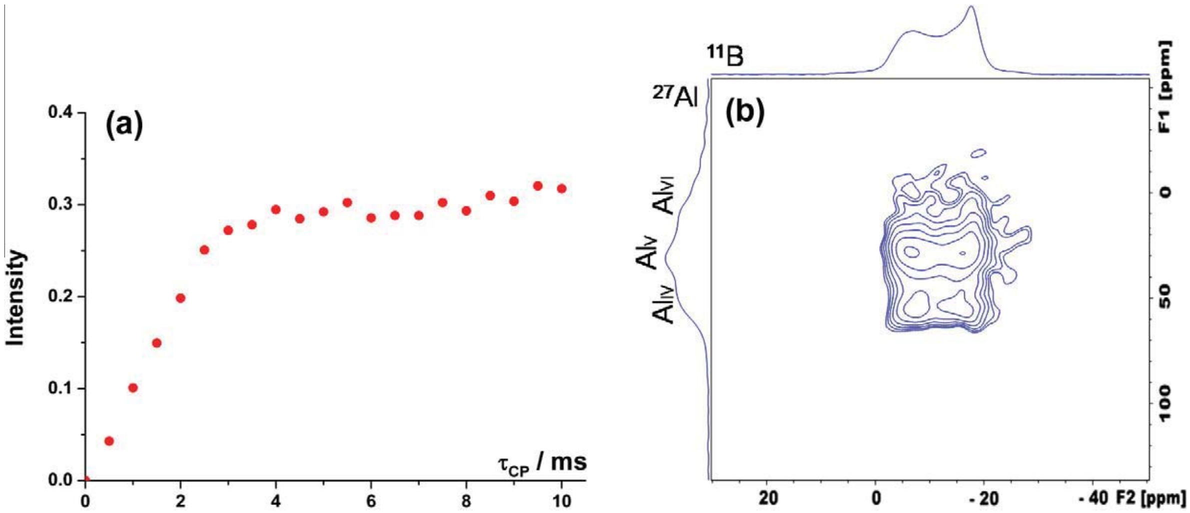

Fig. 10. Mg–Al–B glass sample. $^{27}Al \rightarrow {}^{11}B$ MP-CP MAS with B_0 = 9.4 T, ν_R = 20 kHz, $p_{Al} \approx 0.7$, $p_B \approx 0.56$ ($K_{Al} \approx K_B \approx 0.7$), $\nu_{1,Al} \approx 3.3$ kHz, $\nu_{1,B} \approx 6.3$ kHz, recycle delay = 1 s. (a) Optimization of the contact time τ_{CP}, with NS = 512. (b) *D*-HETCOR spectrum recorded with τ_{CP} = 4 ms, NS = 2048, and experimental time of 24 h. 1D MAS spectra are shown on top (^{11}B, NS = 32) and vertically on the left (^{27}Al, NS = 128).

the left) is less resolved than that recorded at 18.8 T (Fig. S3). By comparing it with the 2D spectrum, one observes that the magnetizations of the Al_V and Al_{VI} resonances are transferred to the oxygen atoms. However, the Al_{IV}–O correlation is missing. We were not able to obtain a similar MP-CP HETCOR spectrum using $^{17}O \rightarrow {}^{27}Al$ CP transfer, as the longitudinal relaxation time of ^{17}O is very long, which leads to a very poor S/N ratio.

4.2. ^{27}Al (I = 5/2) → ^{11}B (S = 3/2)

4.2.1. Mg–Al–B glass sample

In glass samples, there is no long-range order, and thus diffraction methods cannot be used for their structural characterization. For these samples, only solid-state NMR allows for analysis of the local order, and this is mainly achieved with through-space *D*-HETCOR spectra. Therefore, it is important to verify if MP-CP MAS experiments described in Fig. 1 work correctly for two half-integer quadrupolar nuclei in inorganic glasses. The sequence was thus applied to a magnesium alumino-borate glass with a $40MgO–10Al_2O_3–50B_2O_3$ molar composition. This material, proposed for the development of sealing glasses [30], has been prepared using the melt quenching procedure. Mixture of reagent grade magnesium carbonate, aluminum hydroxide and boric acid has been melted at 1300 °C during 20 min before being quenched. It is noteworthy that the spatial proximity between Al and B ions in a glass structure has been previously investigated by the TRAPDOR technique [31], but correlation maps have never been edited to our knowledge. In this Mg–Al–B glass sample, there is only one distributed boron site (Fig. S4b), but three different aluminum species are observable after shearing data processing [32] of the MQMAS z-filter [33] 2D spectrum shown in Fig. S4a: one tetra-coordinated (Al_{IV}), one pentavalent (Al_V), and one hexa-coordinated (Al_{VI}). We have analyzed the $^{27}Al \rightarrow {}^{11}B$ MP-CP MAS transfers observable in this sample with ν_R = 20 kHz. As explained previously, the first step of the optimization procedure is to search for the rf-field ranges that avoid any R^3 effect during the spin-lock processes. This has been done by observing the ^{27}Al and ^{11}B magnetizations after 3 ms spin-locking versus rf-amplitudes for five duty-cycles ranging from p = 0.2 to 1, as shown in Fig. 9. Due to rf-inhomogeneity, R^3 'dips' in spin-lock efficiency observed in this figure are less deep than those shown previously in Fig. 6a. We have chosen duty-cycles of p_{Al} = 0.7 and p_B = 0.56, and the corresponding optimized

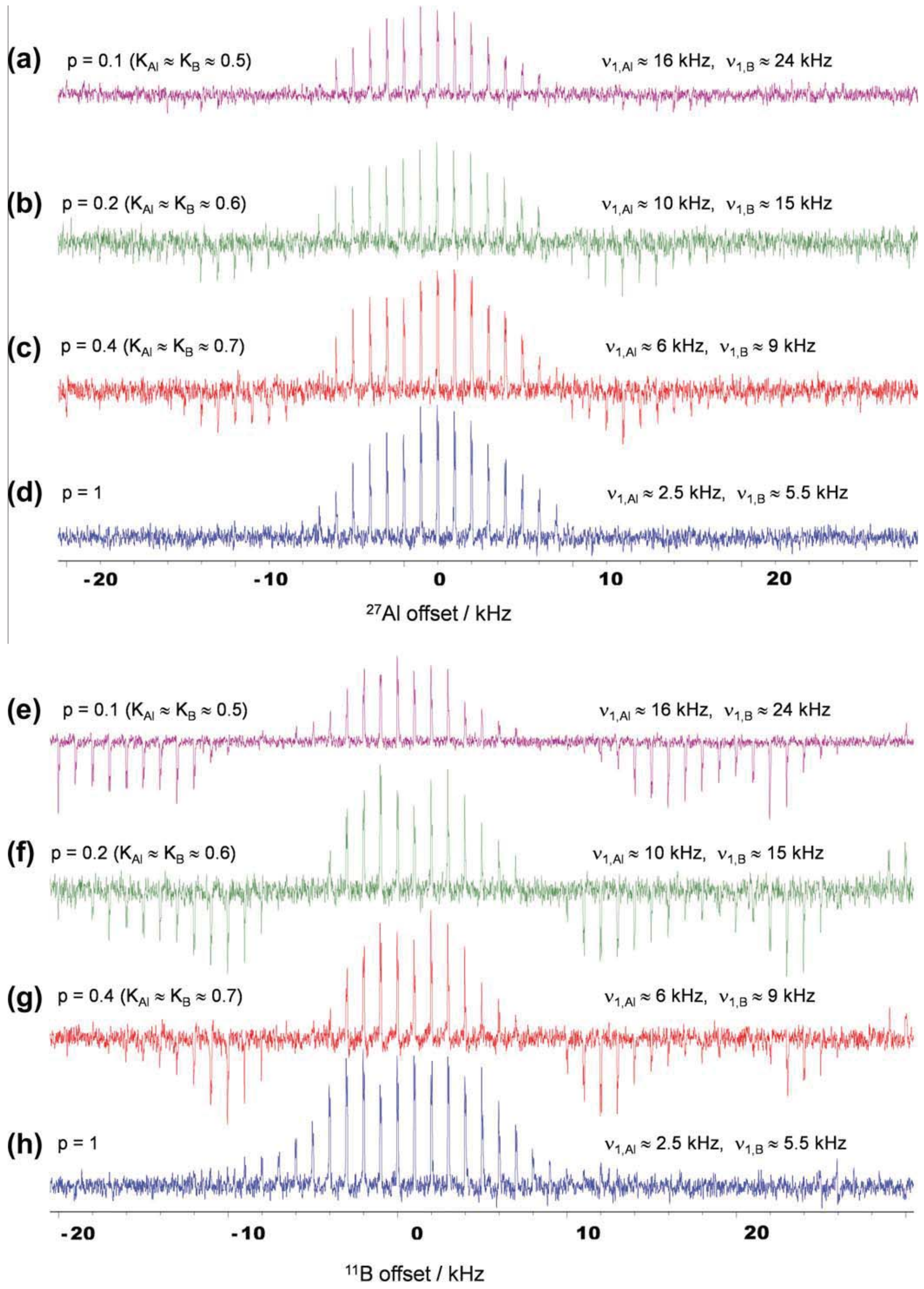

Fig. 11. A_9B_2 sample. Efficiency of the ^{27}Al → ^{11}B MP-CP MAS transfer versus the offset on the ^{27}Al channel (a–d) and ^{11}B channel (e and f), with $B_0 = 9.4$ T, $\nu_R = 20$ kHz, $\tau_{CP} = 10$ ms, $p = p_{Al} = p_B$. Spectra have been acquired with NS = 128 (a and e) or 32 (b–d, f–h), but they are normalized each others. The recycle delay is 1.1 s.

rf-fields deduced from Fig. 9, $\nu_{1,Al} = 3.3$ kHz and $\nu_{1,B} = 6.3$ kHz ($K_{Al} \approx K_O \approx 0.7$), which led to $\tau_{Al} = 35$ μs and $\tau_B = 28$ μs. With these rf values the MP-CP contact time was optimized to $\tau_{CP} = 4$ ms (Fig. 10a). Then, we have recorded the ^{27}Al → ^{11}B *D*-HETCOR spectrum of this sample (Fig. 10b). This 2D spectrum displays the three ^{27}Al–^{11}B correlations indicating that all aluminum sites are close to the boron site. This is often observed in glasses.

4.2.2. Sensitivity to offsets with A_9B_2

$9Al_2O_3{\cdot}2B_2O_3$ (A_9B_2) is a binary oxide that has previously been studied by ^{27}Al and ^{11}B solid-state NMR [34,35]. This compound presents one boron site ($C_{Q,B} = 2.6$ MHz, $\eta_{Q,B} = 0$, $\delta_{cs,B} = 16$ ppm) (Fig. S5a) and four aluminum sites: one Al_{IV} site ($C_{Q,Al} = 9.1$ MHz, $\eta_{Q,Al} = 0.44$, $\delta_{cs,Al} = 71$ ppm), two Al_V sites ($C_{Q,Al} = 8.0$ MHz, $\eta_{Q,Al} = 0.70$, $\delta_{cs,Al} = 44$ ppm; and $C_{Q,Al} = 6.8$ MHz, $\eta_{Q,Al} = 0.08$, $\delta_{cs,Al} = 52$ ppm), and one Al_{VI} site with double intensity ($C_{Q,Al} = 5.75$ MHz, $\eta_{Q,Al} = 0.39$, $\delta_{cs,Al} = 8$ ppm) (Fig. S5b).

The experiments were performed at 9.4 T with a 2.5 mm rotor spinning at $\nu_R = 20$ kHz. In a first step, they were optimized 'on-resonance', which means that the two rf-carrier frequencies were situated in the middle of the powder patterns. Similarly to Mg–Al–B glass, the rf-amplitudes were first optimized to avoid any R^3 effect during the spin-locking for five distinct duty cycles and a spin-lock time of 8 ms (Fig. S6). Then the MP-CP contact time

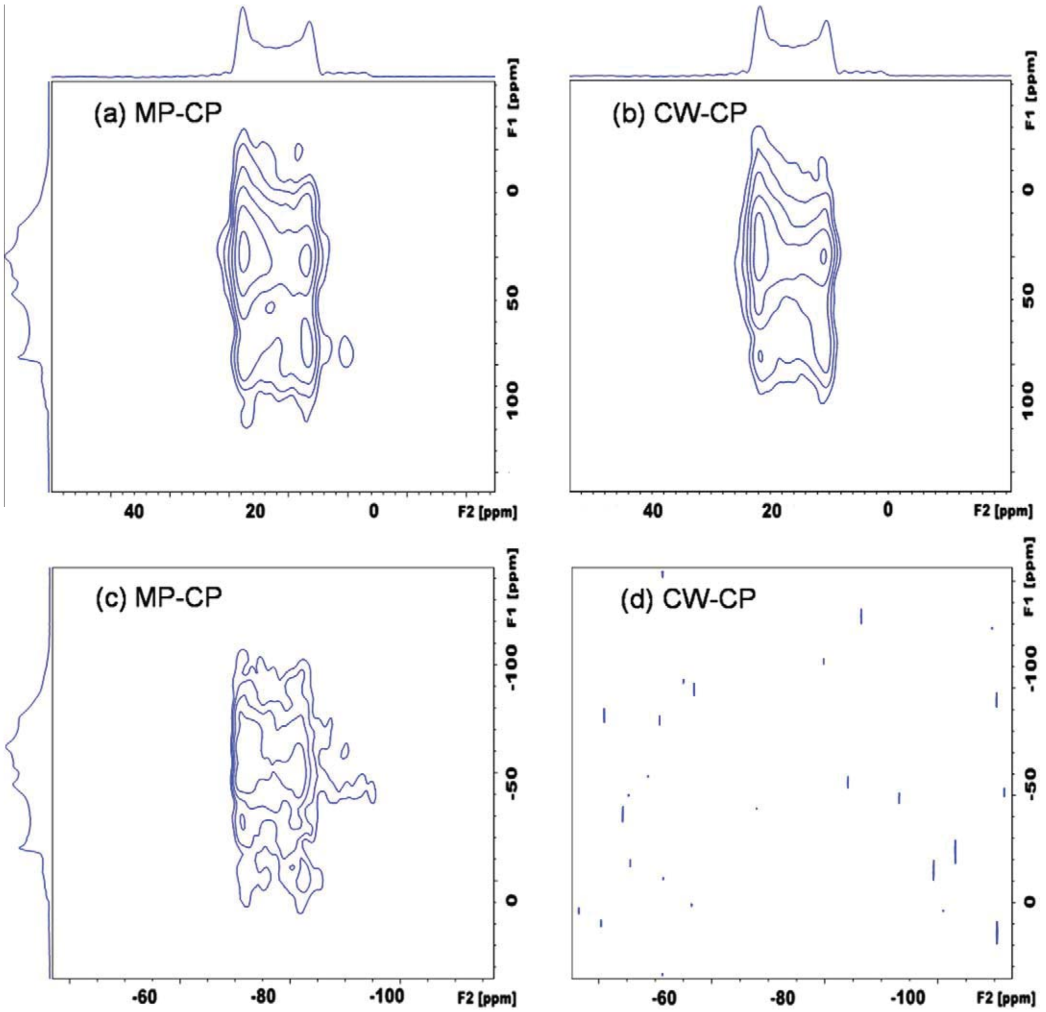

Fig. 12. A_9B_2 sample. $^{27}Al \rightarrow {}^{11}B$ MP-CP (a and c) and CW-CP (b and d) *D*-HETCOR spectra recorded at $B_0 = 9.4$ T, with $\nu_R = 20$ kHz, $\tau_{CP} = 10$ ms, recycle delay = 1.1 s, NS = 256, experiment time = 2.5 h. On ^{27}Al and ^{11}B channels, the irradiations were either on resonance (a and b), or with an offset of 12 kHz (c and d). (a and c) $p_{Al} = p_B = 0.4$ ($K_{Al} \approx K_B \approx 0.7$), $\nu_{1,Al} \approx 6$ kHz, $\nu_{1,B} \approx 9$ kHz; (b and d) $\nu_{1,Al} \approx 2.5$ kHz, $\nu_{1,B} \approx 5.5$ kHz. 1D MAS spectra (NS = 1024) are shown on the top (^{11}B) and vertically on the left (^{27}Al).

was optimized with two identical pulse lengths, $\tau_{Al} = \tau_B = 10$ µs ($K_{Al} \approx K_B \approx 0.6$), with $\nu_{1,Al} \approx 10$ kHz and $\nu_{1,B} \approx 15$ kHz, and its optimum value was found to be $\tau_{CP} \approx 10$–20 ms (Fig. S7). With these parameters optimized for 'on-resonance' irradiations, a 1D experimental analysis of the offset effects was then performed for four different duty cycles, $p_{Al} = p_B = 0.1$, 0.2, 0.4, and 1 (CW-CP), on the ^{27}Al (Fig. 11a–d) and ^{11}B (Fig. 11e–h) channels. These figures show that MP-CP achieves efficient $^{27}Al \rightarrow {}^{11}B$ transfers, for which CW-CP is inefficient. Furthermore, the offset ranges exhibiting significant MP-CP transfer efficiency depends on the duty cycle. For decreasing duty-cycle, the MP-CP transfer is efficient for larger offset, due to larger rf-fields. This is especially apparent for the ^{11}B offset (see Fig. 11e–h). Nevertheless, the MP-CP transfer efficiency cancels for some offset values. These zero-crossings are fixed by τ_{CP} length. Furthermore, the improved robustness to offset for decreasing duty-cycle comes at the expense of a slightly decreased S/N ratio (compare Fig. 11a and b–d, as well as Fig. 11e and f–g). The best compromise between S/N ratio and sensitivity to offsets is then obtained for $p \approx 0.2$–0.4. However, when using weak rf-fields and moderate spinning speed, the ratios $(2I+1)\nu_{1,I}/\nu_R$ and $(2S+1)\nu_{1,S}/\nu_R$ are smaller than one, and K parameters are then smaller than *p* values (Eq. (5)). The experimental optimization then results from a compromise in between small duty-cycles ($p = 0.2$–0.4) for robustness with respect to offsets, and larger duty-cycles for efficient MP-CP transfers ($K_I \approx K_S \approx 0.6$–$0.8$) (Fig. 3 with Eq. (8a)), and one may use duty-cycles in the $p = 0.4$–0.6 range. The above experimental results are consistent with the simulated results displayed in Fig. 5. It must be noted that the signal can be negative with MP-CP. However, this does not hamper the structural investigation via *D*-HETCOR spectra, as their analysis can be performed either by taking also into account the negative parts, or by representing the modulus of the signal.

The higher robustness of MP-CP to offset has also been verified experimentally by recording *D*-HETCOR 2D spectra of A_9B_2 (Fig. 12). The *D*-HETCOR spectra recorded at $\nu_R = 20$ kHz are quasi identical with CW-CP and MP-CP transfers when both irradiations are sent 'on resonance' (Fig. 12a and b) However, the signal is negligible for CW-CP when the offsets become larger than a few kHz on both channels (Fig. 12d). Conversely, Fig. 12c shows that MP-CP allows the observation of all ^{27}Al–^{11}B correlations, even for offset of about 12 kHz.

5. Conclusions

We have presented a new cross-polarization MAS NMR pulse sequence which allows analyzing spatial proximities between two half-integer quadrupolar isotopes. This sequence is based on a multi-pulse cross-polarization (MP-CP) transfer, instead of the previous continuous-wave CP (CW-CP) transfer. Even if the spin dynamics involved in the CP transfers between two quadrupolar nuclei remains a difficult problem, our sequence is more robust than the previous one based on CW-CP transfers. Indeed, spin-locking two quadrupolar nuclei under MAS requires using two weak rf-fields, which lead to a large sensitivity to offsets. This sensitivity is a very important limitation with CW-CP transfers, whereas it is less with MP-CP. This improvement is really useful, especially at high magnetic fields, which are recommended to improve the NMR sensitivity and resolution for half-integer quadrupolar nuclei.

Another important limitation of CW-CP is related to Rotary Resonance Recoupling (R^3) detrimental effects, which always occur with full rotor samples, when taking into account rf-inhomogeneity. These effects are decreased when replacing CW-CP by MP-CP transfers. Indeed, the robustness to R^3 effects then becomes roughly inversely proportional to the duty-cycle of the rotor-synchronized pulses. This leads to a larger robustness of *D*-HETCOR experiments using MP-CP transfer.

The way to set up the MP-CP experiment is first by optimizing the two spin-lock rf-fields as shown in Fig. 9. In case of samples with nuclei presenting large offsets, small duty-cycles of ca. $p = 0.2–0.4$ should be preferred as they provide the best robustness to offsets (Fig. 11). In case of samples presenting moderate offsets, larger duty-cycles of ca. $p = 0.4–0.6$ may be used to increase the efficiency of the MP-CP transfer. With these values of rf-fields and pulse lengths, the contact time should then be optimized.

By using a frequency splitter and a single channel MAS probe, this MP-CP sequence may allow analyzing the through-space proximities between two nuclei with close Larmor frequencies [17]. These two nuclei may have any half-integer spin value, and they even may be two quadrupolar nuclei, such as ^{45}Sc, ^{93}Nb, ^{27}Al, ^{51}V, and ^{23}Na. This is technically impossible with a CW-CP transfer, as most such frequency splitters do not allow irradiating the two channels simultaneously. However, in this case, the sum of the two pulse lengths must be smaller than the rotor period.

It is important to remind that, in spite of its improved robustness with respect to CW-CP, MP-CP cannot allow obtaining quantitative analyses of spatial proximities in between two quadrupolar nuclei, and that the results only remain qualitative. The MP-CP transfer could be combined with an MQMAS [36,37] or STMAS [38] 2nd-order quadrupolar filter on the *I* nuclei, in order to obtain a 2D *D*-HETCOR spectrum presenting a high-resolution along F_1, in the same way it has been demonstrated with CW-CP transfer [39].

Acknowledgments

Authors are grateful for funding provided by Region Nord/Pas de Calais, Europe (FEDER), CNRS, French Minister of Science, USTL, ENSCL, CortecNet, Bruker BIOSPIN and Contract ANR-2010-jcjc-0811-01. Financial support from the TGIR RMN THC (FR-3050) for conducting the research is gratefully acknowledged. Drs. D. Massiot (A_9B_2), G. Tricot (Mg–Al–B) and J. Fonseca with N. Bion (^{17}O-enriched Al_2O_3) are acknowledged for providing the samples. Authors would like to thank one of the reviewers for the very detailed analysis of the article, so that for his numerous advices.

Appendix A. Supplementary material

Supplementary data associated with this article can be found, in the online version, at http://dx.doi.org/10.1016/j.jmr.2012.12.005.

References

[1] D. Iuga, C. Morais, Z. Gan, D.R. Neuville, L. Cormier, D. Massiot, NMR heteronuclear correlation between quadrupolar nuclei in solids, J. Am. Chem. Soc. 127 (2005) 11540–11541.

[2] S.K. Lee, M. Deschamps, J. Hiet, D. Massiot, S.Y. Park, Connectivity and proximity between quadrupolar nuclides in oxide glasses: insights from through-bond and through-space correlations in solid-state NMR, J. Phys. Chem. B 113 (2009) 5162–5167.

[3] J. Haase, M.S. Conradi, E. Oldfield, Single- and double-resonance experiments of quadrupolar nuclei in solids using sensitivity enhancement of the central transition, J. Magn. Reson. A 109 (1994) 210–215.

[4] J. Haase, E. Oldfield, Aluminum to oxygen cross-polarization in α-Al_2O_3 (corundum), Solid State Nucl. Magn. Reson. 3 (1994) 171–175.

[5] L. van Wüllen, L. Züchner, W. Müller-Warmuth, H. Eckert, ^{11}B–{^{27}Al} and ^{27}Al–{^{11}B} double-resonance experiments on a glassy sodium alumino-borate, Solid State Nucl. Magn. Reson. 6 (1996) 203–212.

[6] J.C.C. Chan, M. Bertmer, H. Eckert, Double-quantum cross-polarization between half-integer quadrupolar spin systems: $^{11}B \leftrightarrow ^{23}Na$ and $^{11}B \leftrightarrow ^{27}Al$, Chem. Phys. Lett. 292 (1998) 154–160.

[7] J.C.C. Chan, M. Bertmer, H. Eckert, Site connectivities in amorphous materials studied by double-resonance NMR of quadrupolar nuclei: high-resolution $^{11}B \leftrightarrow ^{27}Al$ spectroscopy of alumino-borate glasses, J. Am. Chem. Soc. 121 (1999) 5238–5248.

[8] J.C.C. Chan, High-resolution heteronuclear correlation between quadrupolar nuclei, J. Magn. Reson. 140 (1999) 487–490.

[9] M.A. Eastman, Examples of Hartmann–Hahn match conditions for CW-CPMAS between two half-integer quadrupolar nuclei, J. Magn. Reson. 139 (1999) 98–108.

[10] J.P. Amoureux, M. Pruski, Theoretical and experimental assessment of single- and multiple-quantum cross-polarization in solid-state NMR, Mol. Phys. 100 (2002) 1595–1613.

[11] (a) S.E. Ashbrook, S. Wimperis, Spin-locking of half-integer quadrupolar nuclei in nuclear magnetic resonance of solids: creation and evolution of coherences, J. Chem. Phys. 120 (6) (2004) 2719–2731;
(b) S.E. Ashbrook, S. Wimperis, Spin-locking of half-integer quadrupolar nuclei in nuclear magnetic resonance of solids: second-order quadrupolar and resonance offset effects, J. Chem. Phys. 131 (2009) 194509.

[12] T.G. Oas, R.G. Griffin, M.H. Levitt, Rotary resonance recoupling of dipolar interactions in solid-state nuclear magnetic resonance spectroscopy, J. Chem. Phys. 89 (1988) 692–695.

[13] S.M. De Paul, M. Ernst, J.S. Shore, J.F. Stebbins, A. Pines, Cross-polarization from quadrupolar nuclei to silicon using low radio-frequency amplitudes during magic-angle spinning, J. Phys. Chem. B 101 (1997) 3240–3249.

[14] B. Hu, J.P. Amoureux, J. Trébosc, S. Hafner, Through-space MP-CP MAS experiments between spin-1/2 and half-integer quadrupolar nuclei in solid-state NMR, J. Magn. Reson. 192 (2008) 8–16.

[15] D. Wei, U. Akbey, B. Paaske, H. Oschkinat, B. Reif, M. Bjerring, N.C. Nielsen, Optimal ^{2}H rf pulses and ^{2}H–^{13}C cross-polarization methods for solid-state ^{2}H MAS NMR of perdeuterated proteins, J. Phys. Chem. Lett. 2 (2011) 1289–1294.

[16] M. Goldman, Spin Temperature and Nuclear Magnetic Resonance in Solids, Clarendon Press, Oxford, 1970.

[17] F. Pourpoint, J. Trébosc, R.M. Gauvin, Q. Wang, O. Lafon, F. Deng, J.P. Amoureux, Measurement of aluminum-carbon distances using S-RESPDOR NMR experiment, Chem. Phys. Chem. 13 (2012) 3605–3615.

[18] S.R. Hartmann, E.L. Hahn, Nuclear double resonance in the rotating frame, Phys. Rev. 128 (1962) 2042–2053.

[19] (a) A. Pines, M.G. Gibby, J.S. Waugh, Proton-enhanced nuclear induction spectroscopy: a method for high resolution NMR of dilute spins in solids, J. Chem. Phys. 56 (1972) 1776–1777;
(b) E.O. Stejskal, J. Schaefer, J.S. Waugh, Magic-angle spinning and polarization transfer in proton-enhanced NMR, J. Magn. Reson. 28 (1977) 105–112.

[20] A.J. Vega, MAS NMR spin-locking of half-integer quadrupolar nuclei, J. Magn. Reson. 96 (1992) 50–68;
A.J. Vega, CPMAS of quadrupolar $S = 3/2$ nuclei, Solid State Nucl. Magn. Reson. 1 (1992) 17–32.

[21] B.H. Meier, Cross polarization under fast magic angle spinning: thermodynamical considerations, Chem. Phys. Lett. 188 (1992) 201–207.

[22] D. Marks, S. Vega, A theory for cross-polarization NMR of non-spinning and spinning samples, J. Magn. Reson. A 118 (1996) 157–172.

[23] M. Baks, J.T. Rasmussen, N.C. Nielsen, SIMPSON: a general simulation program for solid-state NMR spectroscopy, J. Magn. Reson. 147 (2000) 296–330.

[24] M. Baks, N.C. Nielsen, REPULSION: a novel approach to efficient powder averaging in solid-state NMR, J. Magn. Reson. 125 (1997) 132–139.

[25] G. Bodenhausen, R. Freeman, G.A. Morris, A simple pulse sequence for selective excitation in Fourier transform NMR, J. Magn. Reson. 23 (1976) 171–175.

[26] V. Vitzthum, M.A. Caporini, S. Ulzega, G. Bodenhausen, Broadband excitation and indirect detection of nitrogen-14 in rotating solids using delays alternating with nutation (DANTE), J. Magn. Reson. 212 (2011) 234–239.

[27] V. Vitzthum, M.A. Caporini, S. Ulzega, J. Trébosc, O. Lafon, J.P. Amoureux, G. Bodenhausen, Uniform broadband excitation of crystallites in rotating solids using interleaved sequences of delays alternating with nutation, J. Magn. Reson. 223 (2012) 228–236.

[28] D. Carnevale, V. Vitzthum, O. Lafon, J. Trébosc, J.P. Amoureux, G. Bodenhausen, Broadband excitation in solid-state NMR of paramagnetic samples using delays alternating with nutation for tailored excitation ('Para-DANTE'), Chem. Phys. Lett. 553 (2012) 68–76.

[29] W.S. Warren, Effects of arbitrary laser or NMR pulse shapes on population inversion and coherence, J. Chem. Phys. 81 (1984) 5437–5448.

[30] R.K. Brow, D.R. Tallant, Structural design of sealing glasses, J. Non-Cryst. Solids 222 (1997) 396–406.

[31] L. van Wüllen, S. Wegner, G. Tricot, Structural changes above the glass transition and crystallization in alumniophosphate glasses: an in situ high-temperature MAS NMR study, J. Phys. Chem. B 111 (2007) 7529–7534.

[32] J.P. Amoureux, C. Fernandez, Triple, quintuple and higher-orders MQMAS NMR of quadrupolar nuclei, Solid State Nucl. Magn. Reson. 10 (1998) 211–223;
J.P. Amoureux, C. Huguenard, F. Engelke, F. Taulelle, Unified representation of MQMAS and STMAS NMR of half-integer quadrupolar nuclei, Chem. Phys. Lett. 356 (2002) 497–504.

[33] J.P. Amoureux, C. Fernandez, S. Steuernagel, Z-filtering in MQ-MAS NMR, J. Magn. Reson. A 123 (1996) 116–118.

[34] D. Massiot, F. Fayon, M. Capron, I. King, S. Le Calvé, B. Alonso, J.O. Durand, B. Bujoli, Z. Gan, G. Hoatson, Modelling one- and two-dimensional solid-state NMR spectra, Magn. Reson. Chem. 40 (2002) 70–76.

[35] H. Deters, J.F. de Lima, C.J. Magon, A.S.S. de Camargo, H. Eckert, Structural models for yttrium aluminium borate laser glasses: NMR and EPR studies of the system $(Y_2O_3)_{0.2}$–$(Al_2O_3)_x$–$(B_2O_3)_{0.8-x}$, Phys. Chem. Chem. Phys. 13 (2011) 16071–16083.

[36] L. Frydman, J.S. Harwood, Isotropic spectra of half-integer quadrupolar spins from bidimensional magic-angle-spinning NMR, J. Am. Chem. Soc. 117 (1995) 5367–5368;
A. Medek, J.S. Harwood, L. Frydman, Multiple-quantum magic angle spinning NMR: a new method for the study of quadrupolar nuclei in solids, J. Am. Chem. Soc. 117 (1995) 12779–12787.

[37] C. Fernandez, J.P. Amoureux, 2D multi-quantum MAS-NMR spectroscopy of ^{27}Al in alumino-phosphate molecular sieves, Chem. Phys. Lett. 242 (1995) 449–454.

[38] Z.H. Gan, Isotropic NMR spectra of half-integer quadrupolar nuclei using satellite transitions and magic-angle-spinning, J. Am. Chem. Soc. 122 (2000) 3242–3243.

[39] C. Fernandez, L. Delevoye, J.P. Amoureux, D. Lang, M. Pruski, ^{27}Al and ^{27}Al–{^{1}H} cross polarization 3QMAS NMR, J. Am. Chem. Soc. 119 (1997) 6858–6862.

Conclusion

My PhD work was focused on the development of novel NMR techniques, including (i) the extension of DNP NMR for the characterization of inorganic materials, (ii) the development of novel solid-state NMR pulse sequences.

My work on DNP encompasses (i) the application of DNP-NMR for inorganic materials, (ii) the introduction of new protocols for the incorporation of radical into the system of interest, (iii) the investigation of polarization transfer during DNP experiments, (iii) the combination of DNP with advanced NMR pulse sequences and (iv) the use of DNP sensitivity enhancement to extract novel structural information. We have shown that the co-condensation (functionalization of materials with nitroxide radicals) is supplementary to post-synthesis impregnation for the incorporation of DNP polarizing agents into inorganic materials. Using this protocol, the ^{29}Si NMR signals of functionalized mesoporous silica TEMPO was enhanced by high-field direct ^{29}Si DNP and proved the feasibility of solvent free DNP for porous materials. The polarization build-ups with and without microwave irradiation observed were fast and this fast build-up is promising for DNP experiments below 100 K, since the T_{1n} times are usually long at low temperatures. Mesoporous silica functionalized with nitroxide radicals can also be useful for the polarization of metabolites, as shown recently by Gajan et al[1].

A quantitative analysis of the signal enhancements in mesoporous silica nanoparticles (MSN) with and without surfactant were studied and proved that the mechanism is based on a one-dimensional proton spin diffusion model. It was also shown that in samples spinning at the magic angle, DNP can enhance ^{13}C and ^{29}Si signals of nuclei located within the functionalized mesoporous silica nanoparticles, despite the inability of TOTAPOL to penetrate into the mesopores.

Moreover, we assessed various contributions to the signal enhancement obtained in DNP-CP-MAS studies of functionalized mesoporous silica nanoparticles (PUP-MSNs) and compared the results with conventional room- temperature CP-MAS measurements on the same systems. The results confirmed that DNP is useful to probe small surface areas and surface species with low concentrations. Apart from this, a systematic analysis of the enhancement factor (per scan) and the sensitivity enhancement (per unit time) in ^{13}C and ^{29}Si CP-MAS NMR boosted by DNP of functionalized MSNs was done. Specifically, we separated contributions due to: (1) microwave irradiation, (2) quenching by paramagnetic effects, (3) the presence of frozen solvent, (4) the temperature, as well as changes in (5) relaxation and (6) cross polarization behaviour.

We showed also that the ^{29}Si NMR signals of synthetic clay nanodisks can be enhanced by DNP-NMR. The DNP sensitivity enhancement has allowed an easy observation of defects located on the edges or the surfaces of the nanoparticles. We demonstrated also for this system the complementarities of DNP cross-polarization (CP) and direct polarization (DP): The direct DNP enhances the signals of ^{29}Si nuclei near unpaired electrons, whereas the indirect DNP via ^{1}H enhances the signals of more remote sites.

Besides ^{13}C and ^{29}Si DNP NMR, we demonstrated the 1D and 2D experiments to probe the spatial proximities between quadrupolar nuclei DNP NMR with greatly reduced time scales. We recorded the ^{27}Al–^{27}Al two-dimensional dipolar correlation spectra on mesoporous alumina. The low efficiency of cross-polarization and dipolar recoupling for quadrupolar nuclei is completely negated using this technique. The absence of $\mathrm{Al^{IV}}-\mathrm{Al^{VI}}$ correlations combined with the presence of $\mathrm{Al^{IV}}-\mathrm{Al^{V}}$ and $\mathrm{Al^{V}}-\mathrm{Al^{VI}}$ correlations shows that interfacial $\mathrm{Al^{IV}}$ and $\mathrm{Al^{VI}}$ sites are bridged by interfacial $\mathrm{Al^{V}}$ sites. Such structural information, collected at low temperature (∼103 K) and 9.4 T with the use of DNP, was obtained in only 4 h. Furthermore, we detected for the first ^{27}Al-^{13}C proximities in MIL-100(Al) by solid-state NMR and showed that the duration of these experiments can be significantly reduced using DNP. Using EPR and DNP experiments it was shown that TOTAPOL can diffuse into the large cavities of microporous MIL-100(Al), leading to significant DNP sensitivity enhancements for CP-MAS and direct polarization ^{13}C MAS experiments. These experiments validate the crystal structure of MIL-100(Al) and the assignment of the ^{13}C resonances. Besides, S-RESPDOR experiments demonstrated that impregnation and low temperature do not alter the MIL-100(Al) framework.

My PhD work led also to the development of conventional solid-state NMR methods to achieve high resolution ^{1}H spectra in solids and to probe the proximities between two quadrupolar nuclei. We analyzed and compared the specifications of TIMES and TIMES0 proton high- resolution NMR methods in solid-state. This comparison was performed in terms of resolution versus spinning speed, rf-field requirement, and tilt-angle for the effective rf-field, θ_P. The chemical-shift and homo-nuclear dipolar scaling factors were calculated for both methods. Furthermore, we introduced a novel cross-polarization MAS NMR pulse sequence which allowed analyzing spatial proximities between two half-integer quadrupolar isotopes. This sequence is based on a multi-pulse cross-polarization (MP-CP) transfer, instead of the continuous-wave CP (CW-CP) transfer. MP-CP sequence is more robust than the CW-CP transfers. Indeed, spin locking the two quadrupolar nuclei under MAS require using two weak rf-fields, which lead to a large sensitivity to offsets. This sensitivity is a very important limitation for CW-CP transfers, whereas it is less with MP-CP. This improvement is really useful at high magnetic fields, which are recommended to improve the NMR sensitivity and resolution for half-integer quadrupolar nuclei.

My PhD work will open new avenues for the characterization of nanostructured materials (micro- and meso- porous hybrid solids, nanoparticles...). DNP offers new opportunities for the study of organic−inorganic hybrid materials, including the self-cooperative assembly of surfactants and the properties of catalytic centers. The solvent free DNP shows that the direct DNP will be useful for systems featuring high atomic mobility or high concentration in unpaired electrons and it should eliminate perturbations due to frozen water which can affect the structure, reactivity, intermolecular interactions and dynamics on silica surfaces. The other works on DNP clearly opens a new avenue for the essential understanding in structure−property relationships for different materials, applications of SSNMR to quadrupolar nuclei and notably the atomic-scale structure determination of catalysis materials in the future. The MP-CP transfer could be combined with an MQMAS or STMAS 2nd-order quadrupolar filter on the I nuclei, in order to obtain a 2D D-HETCOR spectrum presenting a high-resolution. For homonuclear dipolar decoupling, the next step will be to incorporate it into advanced correlation experiments.

Reference:

1 D. Gajan, M. Schwarzwälder, M. P. Conley, W. R. Grüning, A. J. Rossini, A. Zagdoun, M. Lelli, M. Yulikov, G. Jeschke, C. Sauvée, O. Ouari, P. Tordo, L. Veyre, A. Lesage, C. Thieuleux, L. Emsley and C. Copéret, *Journal of the American Chemical Society*, 2013, **135**, 15459-15466.